PhD Thesis

UNIVERSITAT POLITÈNICA DE CATALUNYA (UPC)
ESCOLA T.S. D´ENGINEYERS DE CAMINS, CANALS I PORTS
(Technical University of Catalonia)
(School of Civil Engineering)

Department of Geotechnical Engineering and Geosciences

Numerical modelling of delayed and progressive failure in stiff clays with two-stage softening behaviour

by

Zhifeng Zhan

Advisor

Antonio Gens Solé

Barcelona, May, 2012

Chapter 6. Analysis of Aznalcóllar dam failure mechanism with post-rupture strength concept and progressive failure

In this section, both the post-rupture strength concept and the two-stage softening model are applied to simulate practical geotechnical cases. A well known case—the Aznalcóllar dam failure (Olalla & Cuéllar, 2001; Alonso & Gens, 2006a; Gens & Alonso, 2006; Zabala & Alonso, 2011) has been attributed to progressive failure in Guadalquivir blue clay (Tsige, et al., 1995; Tsige et al., 1996; Tsige et al., 1997 and Tsige, 1999) and it is therefore suitable to be taken as a realistic application example.

6.1 Introduction to dam geometry and construction process

Aznalcóllar tailings dam failed catastrophically on 25 April 1998 inducing the worst-ever environmental disaster in the vicinity of Aznalcóllar village in the province of Seville, Spain. The location of the dam is shown in the satellite image (Fig. 6.1). The dam was built in the Aznalcóllar mine region which is located in the north of the Guadalquivir basin—an open sea in Miocene times and filled by thick deposits of carbonated marine high plasticity clays (known often as “Guadalquivir blue clays”).

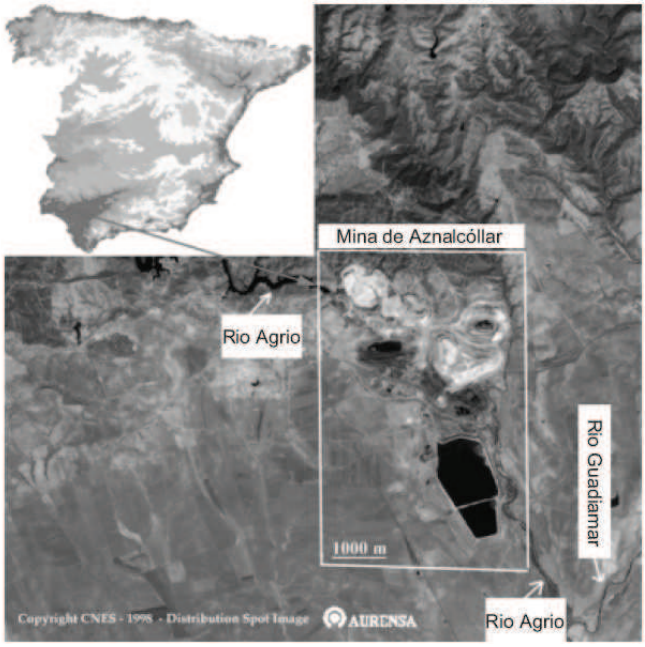

Fig. 6.1 Location of Aznalcóllar tailings deposit (Alonso & Gens, 2006a)

Fig. 6.2 shows the plan view of the tailings deposit and a representative cross section of the dam facing the Agrio river prior to the failure. A perimeter dam of increasing height was built over the years, as the volume of tailings increased.

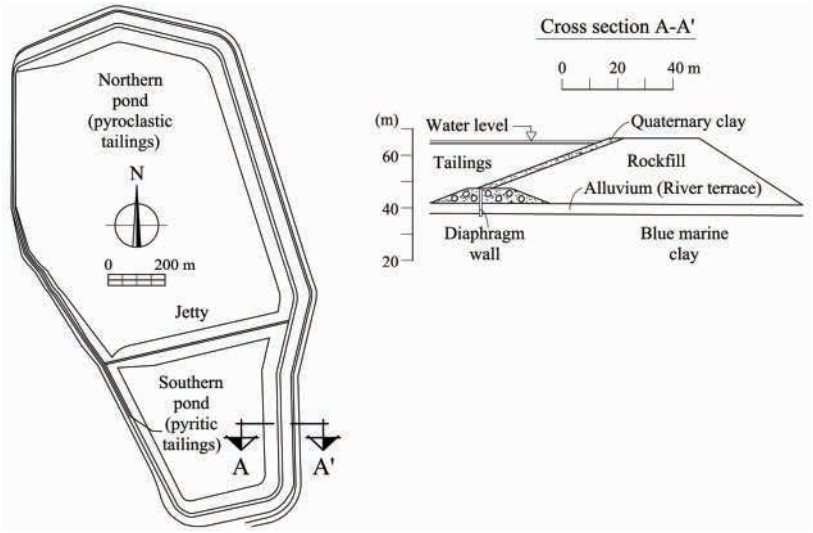

Fig. 6.2 Plan view of the Aznalcóllar tailings deposit and representative cross section of the failed dam (Alonso & Gens, 2006a)

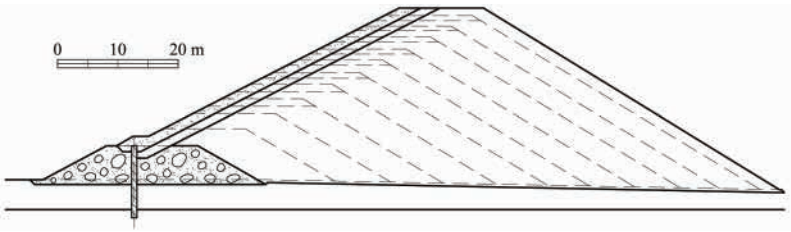

Fig. 6.3 Original dam design (Alonso & Gens, 2006a)

The dam was initially designed in 1978 in accordance with customary geotechnical engineering procedures. A representative cross-section of the initial design is shown in Fig. 6.3. The dam was built in a "forward manner". The height and lateral extension of the embankment increased continuously for 20 years, as the accumulated volume of mine tailings increased. A small upstream embankment was first constructed. Then a bentonite–cement wall, which penetrates into Guadalquivir blue clay, was built to provide an impervious barrier. The dam was built in phases of increasing height, advancing in the downstream direction. The structure is actually a rockfill dam with an upstream impervious blanket of low-plasticity red clay. This blanket is connected with the vertical cement–bentonite upstream diaphragm wall. This was designed to ensure the imperviousness of the embankment. Upstream and downstream slopes were defined in the original project as 1V:1.9H and 1V:1.75H respectively ($27.8°$ and $29.9°$ with respect to the horizontal).

The dam actually built did not follow all the design specifications. A representative cross-section of the failed dam is shown in Fig. 6.4. A significant change was introduced in 1985, when the downstream slope increased from the projected value of 30° (1V:1.75H) to 39° (1V:1.24H). The downstream slope was maintained unchanged thereafter. A second significant change took place in 1990: the width of the crest of the dam increased from the planned value of 14 m to 36.50 m. At that time, the height of the cross section was 21 m over foundations. Other changes are of minor significance. In 1990 the width of the base of the dam reached a maximum value of 130 m. Subsequent changes in dam height did not modify this base width.

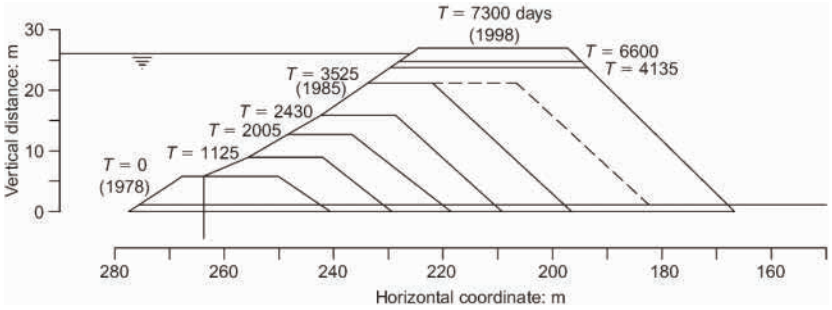

Fig. 6.4 Evolution of representative cross-section of the dam actually built (east side) (Gens & Alonso, 2006)

6.2 Description of the failure

Sometime during the early morning of the 25th of April, 1998 a failure took place affecting a section of the confining embankment. As a result, several millions of cubic meters of highly acidic liquefied tailings poured into the Agrio and Guadiamar valleys. Twenty-four kilometers of the Guadiamar river were affected by the mudflow. Fig. 6.5 shows aerial photographs of the breached embankment, the inundated valley of the Agrio river and the pond area, partially emptied and eroded, which were taken in the morning of April 25th 1998.

The failure surface was located inside the Guadalquivir blue clays. A detailed analysis of the borehole cores proved it to be practically horizontal and flat in the main movement zone, lying about 14 m below the alluvial layer. The displaced mass included the embankment, the alluvium terrace and a slab of clay, having an approximate thickness of 10 m. Fig. 6.6a shows the cross section of the slide at the position of Profile 4, defined by the boreholes S4-1, S4-2 and S4-3. The section in Fig. 6.6a includes the data provided by all the boreholes shown in the figure. The boreholes located upstream of the embankment provided a precise position of the failure surface since the tailings were found in direct contact with the clay in some of them. In several boreholes it was also possible to identify the position of the sliding surface when a highly polished surface could be found. Fig. 6.6b provides a reconstruction of the original position of the sliding surface before failure displacements. The inclination (1.5º-2º) and the planar nature of the basal sliding surface may be a strong indication that it followed a sedimentation plane.

Alonso & Gens (2006a) concluded that the Aznalcóllar dam failure is an unusual case of deep translational sliding involving the entire dam, which displaced a large distance (50 m in the central part) as a rigid body and suffered only minor distortions. The failure affected only the south-eastern embankment and not the northern one.

Fig. 6.5 Two views of the breached dam a few hours after the failure (Alonso & Gens, 2006a)

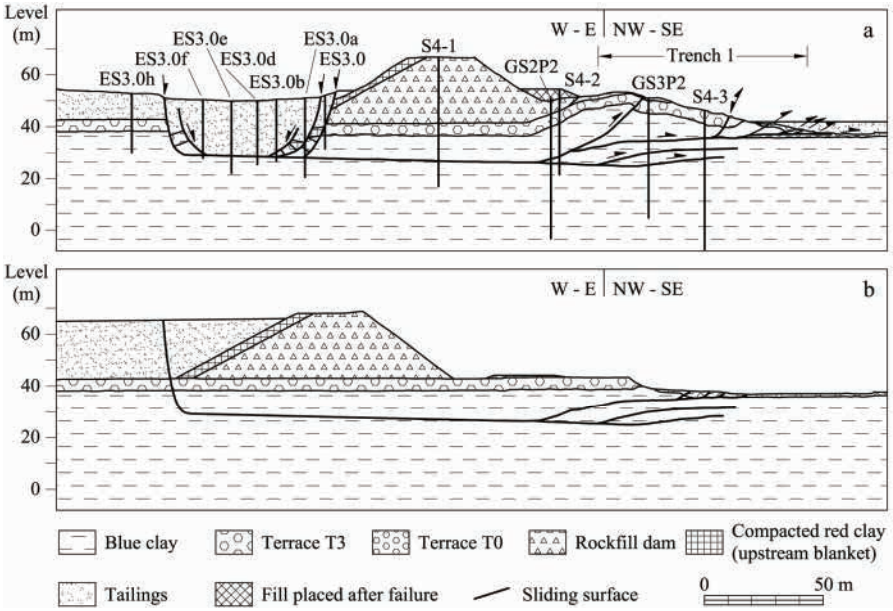

Fig. 6.6 Cross-section of the slide at the position of Profile 4. (a) Geometry after the slide as interpreted from borehole results and surface topography (b) Reconstruction of the position of the sliding surfaces before the failure (Alonso & Gens, 2006a)

6.3 Geotechnical properties of foundation materials

The failure was described in Alonso & Gens (2006a) as a translational motion of the rockfill dam, which slid on a plane of high-plasticity Miocene carbonate clay (Guadalquivir blue clay). The failure did not involve any shearing of the tailings or the rockfill which are materials with a high friction angle. The stability was basically controlled by one material: the highly plastic and brittle Guadalquivir blue clay. Therefore, only the properties of Guadalquivir blue clay are given in length here.

Alonso & Gens (2006a) presented a comprehensive study on the geotechnical properties of the foundation clay, i.e. Guadalquivir blue clay, in Aznalcóllar dam failure through basic identification, mineralogy and structure examination such as X-ray diffraction tests and scanning electron microscope observation, direct shear tests, ring shear tests, unconfined compression and triaxial tests and oedometer tests.

6.3.1 Basic identification

The Guadalquivir blue clay samples exhibit a high percentage of clay sizes (< 2μm) using standard sedimentation techniques. The clay fraction CF varies between 47% and 58% (average: 53%). They classify as MH or CH (LL=62-67%; IP=31%-35%). The activity is therefore moderate (A=0.62). Of importance, as shown in Table 2.2, the mean liquidity index (IL) of Guadalquivir blue clay is 0.03 which is quite smaller than 0.5—the limit for stiff clays. It is evident that Guadalquivir blue clay is a representative stiff overconsolidated clay with high plasticity.

The Guadalquivir blue clay has very low permeability (10^{-6} to 10^{-7} m/s).

6.3.2 Mineralogy

X-ray diffraction tests show that calcite and potassium smectite constitute the bulk of the clay mineral content.

In all the scanning electron microscope observations the clay minerals were seen to occur in aggregates of irregular ellipsoidal shape.

6.3.3 Results from direct shear tests

All the direct shear tests showed a brittle behaviour of Guadalquivir blue clay. As stated by Alonso & Gens (2006a), peak strength was found for displacements of 0.5–1.5 mm for a range of vertical stresses of 100–400 kPa. Beyond peak the strength initially drops very rapidly, then more gradually (shown in Fig. 6.7). Olalla & Cuéllar (2001) found similar results (Fig. 6.8).

Alonso & Gens (2006a) introduced a cementation loss index (CL) to measure the rapid sudden drop of shear strength. This is important to determine the post-peak strength, especially the post-rupture strength, of stiff clays.

The relevant brittle behaviour is described by the following parameters: peak strength, τ_p; displacement to reach the peak, d_p; strength at the end of the test (for a displacement of 4–6 mm), τ_f; rapid drop of resistance post-peak: $\Delta\tau_b$. An additional

reference strength, the residual strength, τ_{res}, may be calculated for a given vertical stress once the residual friction angle is known.

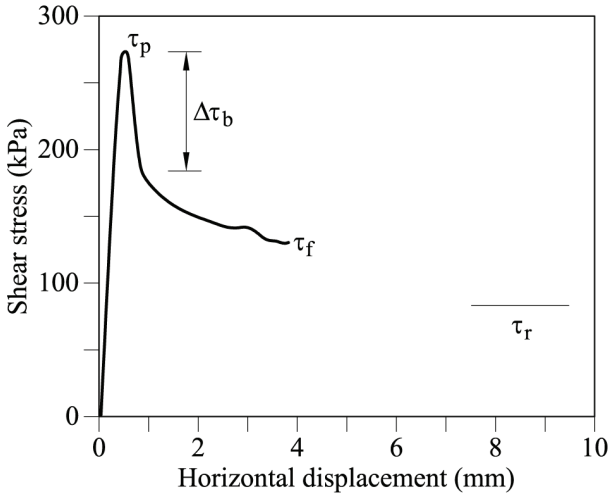

Fig. 6.7 Direct shear test on specimen of Guadalquivir blue clay from borehole sample at Aznalcóllar dam (Normal effective stress: 400 kPa) (Alonso & Gens, 2006a)

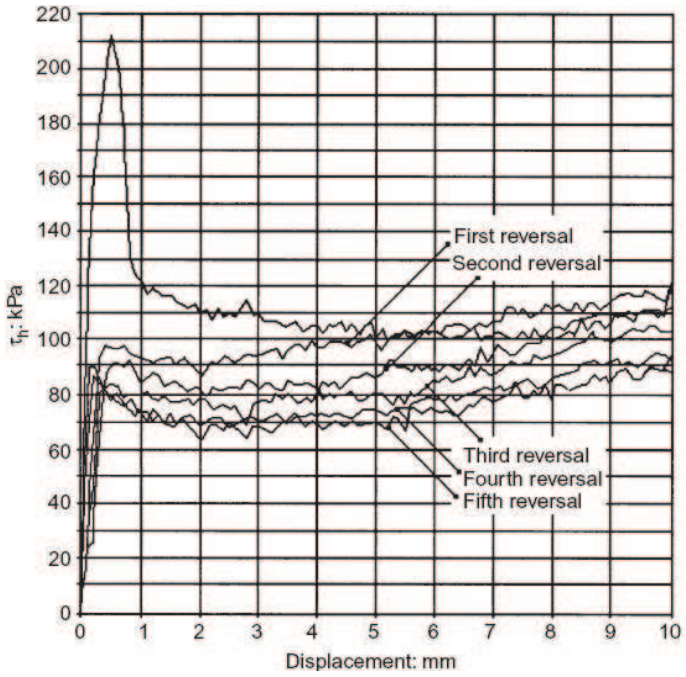

Fig. 6.8 Data from direct shear test with shear direction reversals on Guadalquivir blue clay (Olalla & Cuéllar, 2001)

Two brittleness indices I_f and I_B have been defined in Eq.(2.4) and Eq.(2.5).

In addition, a measure of the rapid loss of strength after the peak is given by two *cementation loss indices* CL_f and CL_B defined in Eq.(2.10) and Eq. (2.11). They have been associated with the shear-induced loss of cementation of the clay. Again, the first *cementation loss index* is larger than the second one, i.e. $CL_f > CL_B$.

Alonso & Gens (2006a) found that the displacement at peak, d_p, does not change with applied normal effective stress. The average value of d_p is 1 mm.

As seen in Fig. 6.9, the *cementation loss indices* are plotted against the vertical stress. No apparent effect of vertical stresses is observed. The average values ($\overline{CL}_f = 0.55$; $\overline{CL}_B = 0.35$) are very significant because they indicate that a large proportion of the peak strength is lost immediately. If the residual strength is taken as the final reference minimum strength value, it is suggested that 35% of the loss of strength after peak is due to the loss of cementation, and a further reduction of 65% is associated with changes of the fabric of the clay (particle reorientation).

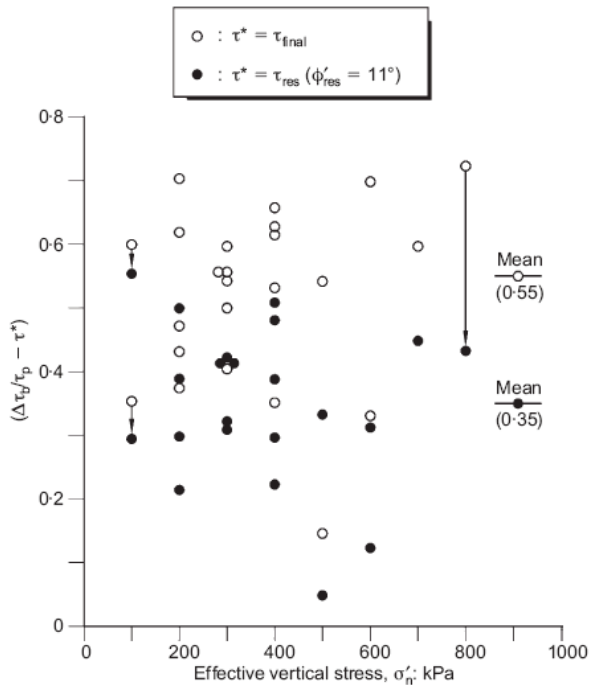

Fig. 6.9 Normalised loss of strength of Guadalquivir blue clay, immediately post-peak, as a function of vertical stress (Alonso & Gens, 2006a)

The two brittleness indices I_f and I_B are also plotted in Fig. 6.10 against the vertical stress. A single I_B line is plotted because the residual strength corresponds in all cases to a common residual friction angle and peak strength values derive from a common peak strength envelope. Points in Fig. 6.10 represent the I_f index determined for each of the shear tests performed, and this leads to the scatter observed. The dashed line provides the mean value of I_f. A reduction of brittleness with vertical stress is observed, a common finding also in other soils (Fig. 6.11). The important point is that Guadalquivir blue clay is highly brittle (I_B varies between 0.8 and 0.7 for effective vertical stress between 100 kPa and 400 kPa). Measured brittleness indices are similar to the values found for blue London clay (Bishop et al., 1971; Fig. 6.11).

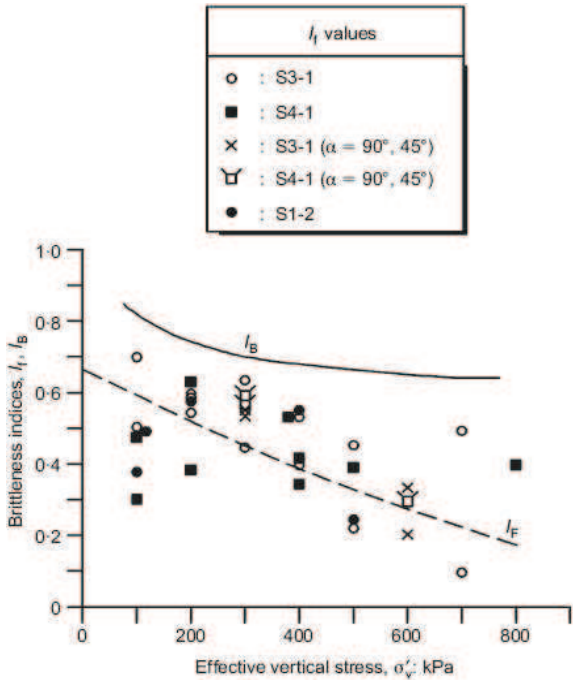

Fig. 6.10 Variation of brittleness indices I_f and I_B of Guadalquivir blue clay with effective vertical stress (Alonso & Gens, 2006a)

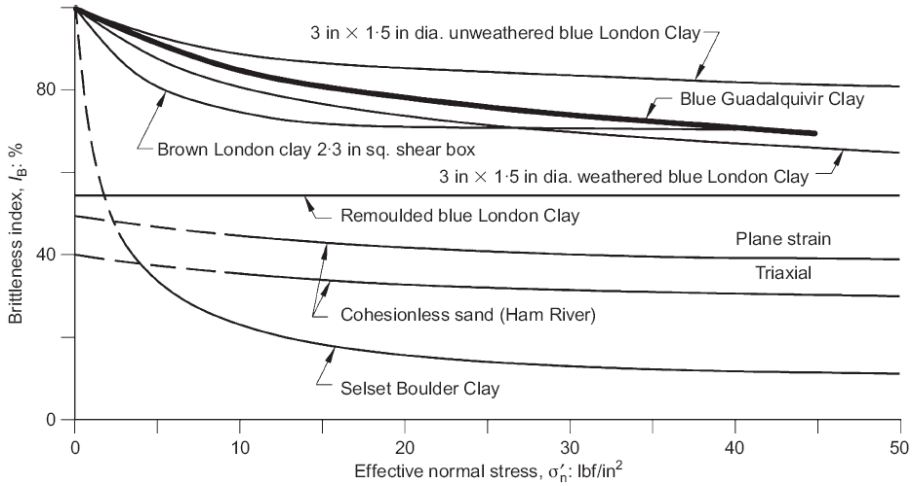

Fig. 6.11 Comparison of brittleness index I_B with other values reported by Bishop et al. (1971) (Alonso & Gens, 2006a)

Measured peak strengths are plotted in Coulomb diagram and some scatter is observed. Average peak strength values correspond to the drained parameters $c' = 65$kPa, ϕ'=24.1°. It is of interest that if the strengths measured at the end of the direct shear test (for displacements of 4–6 mm) are considered, an average limiting curve with $c' = 0$kPa, ϕ'=20° is obtained (Fig. 6.12). This curve is neither the post-rupture strength nor the residual strength. It just implies the progressive deterioration of the strength of Guadalquivir blue clay. Moreover, Alonso & Gens (2006a) also stated that no clear indication of anisotropy of the clay matrix was found for Guadalquivir blue clay and peak parameters determined from horizontal shearing may represent average peak strength values.

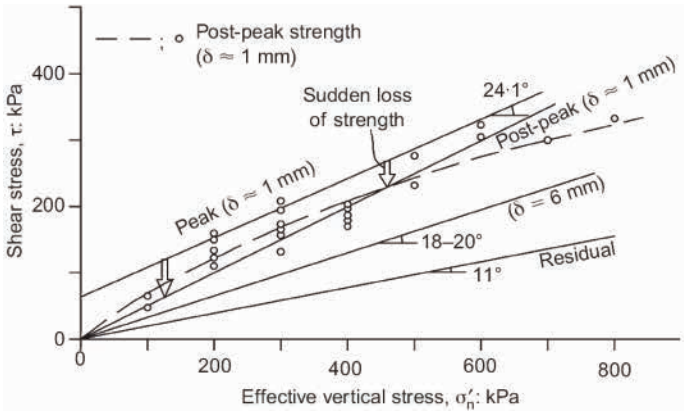

Fig. 6.12 Direct shear strength envelopes for Guadalquivir blue clay (Alonso & Gens, 2006a)

Residual strength was investigated using two types of test: ring shear tests on remoulded specimens, and direct shear tests on natural discontinuities. Twelve ring shear tests were performed at normal stresses of either 200 kPa or 700 kPa. An average residual friction angle of 13° was measured. Direct shear tests on the discontinuity gave residual strength parameters as $c' = 0$kPa, $\phi'_{res} = 11°$ for vertical stresses in the range 200–400 kPa after displacements in excess of 60 mm were achieved (Fig. 6.12). Considering the quite large displacement occurring in the Aznalcóllar dam failure, the smaller value is adopted in this thesis. At the same time, according to Fig. 2.1 and Fig. 2.2, the shearing mode for Guadalquivir blue clay (average CF=53%) is considered to be sliding shear with similar fabric of shear surface to that observed in Happisburg-London Clay mixture (CF=48%).

Finally, Alonso & Gens (2006a) synthesized all the results of direct shear tests which are summarised in Fig. 6.12. The average peak strength is obtained for a shear displacement of 1 mm. The open symbols in Fig. 6.12 correspond to the strength measured immediately after the peak at essentially the same displacement. The curved strength envelope is a reasonable approximation to the measured values. A straight line is also fitted to the points. The important result is that the sudden loss of strength results in a destruction of the effective cohesion. An accumulation of shear displacements of 6 mm implies a drop of friction angle down to $18-20°$. Finally, the residual friction envelope, associated with further additional displacements, is also plotted in Fig. 6.12.

Now we turn to the main objective of this thesis—the post-rupture strength. As described in Chapter 2, the cohesion of post-rupture strength for stiff clays ranges from 0 kPa to 10 kPa. In Aznalcóllar dam case, the cohesion of specimen changes from 65 kPa at peak to 0 kPa at the end of shear test (Fig. 6.12). An average value 5 kPa is used, which may be considered a reasonable initial value. Moreover, from Fig. 6.12, we can also see that the friction angle of post-rupture strength varies from 24° at peak to an intermediate value 20° at the end of shear test. Because generally there is very little reduction of friction angle from peak state to post-rupture state, an average value 22° may be considered as a reasonable estimation of the friction angle of post-rupture strength for Guadalquivir blue clay. This may be also confirmed in Fig. 2.3 based on which the fully softened friction angle can be deduced to be about 22.5° in line with average liquidity limit LL=64.5 of Guadalquivir blue clay.

Theoretically, all the strengths including peak, post-rupture and residual ones and relevant displacements can be obtained from Fig. 6.7 and Fig. 6.12 based on laboratory tests. The shear strengths for Guadalquivir blue clay are summarized in Table 6.1.

Table 6.1 Shear strengths for Guadalquivir blue clay

Average peak strength	$c'_p = 65\text{kPa}$, $\phi'_p = 24°$
Average post-rupture strength	$c'_{pr} = 5\text{kPa}$, $\phi'_{pr} = 22°$
Residual strength	$c'_r = 0\text{kPa}$, $\phi'_r = 11°$

6.3.4 Structure of Guadalquivir blue clay

Fig. 6.13 Slickensides exposed on a sedimentation plane. River bank of Agrio river (Alonso & Gens, 2006a)

Gens & Alonso (2006) performed back-analysis of Aznalcóllar dam failure with limit equilibrium methods and found that the failure might be significantly affected not only by progressive failure phenomena but also structural conditions (critical bedding plane).

Two main types of discontinuities were found in the Miocene clay: subhorizontal sedimentary planes and a vertical jointing system. When freshly cut surfaces are exposed to the atmosphere and partially dried, some jointing laminations and alignments of pyrite micronucleus reveal the sedimentation planes. In exposed outcrops, the weathered clay exhibits the sedimentation planes more clearly. A dip of 2º-4º towards the SSE was measured in outcrops and trenches. The state of pre-shearing of the sedimentation planes is difficult to identify. Observations in bedding planes, both in outcrops and in cores, revealed some shear striations and some shear zones similar to those described in Chandler et al. (1998). Two examples are given in Fig. 6.13 and Fig. 6.14. However, these phenomena were not generalised and in other cases the sedimentation planes appeared closely sealed and intact. Bedding planes were observed to concentrate in relatively thin bands at 2.0-2.5 m intervals. The joints and bedding surfaces in Guadalquivir blue clays are not conductive features.

Fig. 6.14 Slickensides observed in a core recovered in borehole S1-3 at 13.5 m depth (Alonso & Gens, 2006a)

6.4 Reported numerical analyses of Aznalcóllar dam failure

6.4.1 Numerical results from Olalla and Cuéllar (2001)

The first numerical analyses were conducted by Olalla & Cuéllar (2001) with both finite element and limit equilibrium methods.

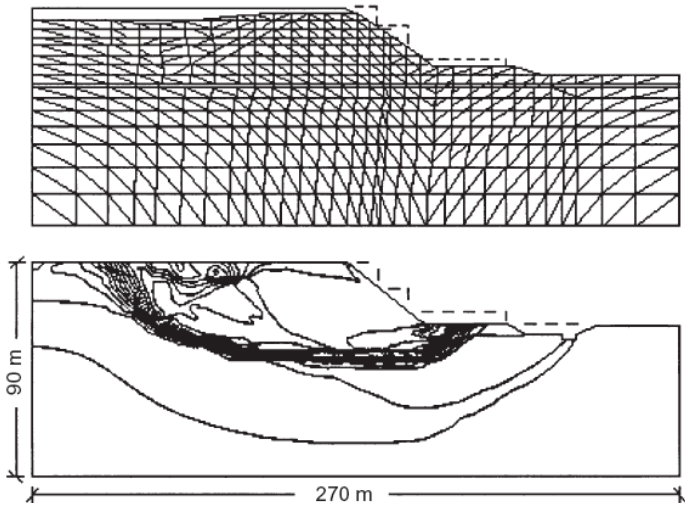

Fig. 6.15 Slip band obtained using the finite element technique (Olalla & Cuéllar, 2001)

They used a plain strain finite element algorithm to perform a parametric study assuming a five-stage construction process and Mohr-Coulomb model for all the materials. Homogeneous and isotropic behaviour was assumed. An attempt was made to incorporate the brittle behaviour of the material at the end of each one of the five construction stages, by modifying the strength parameters of Guadalquivir blue clay from peak values to residual ones in every element where failure of the material was detected. Fig. 6.15 shows the overall movements at the end of the calculation process, and the slip band itself.

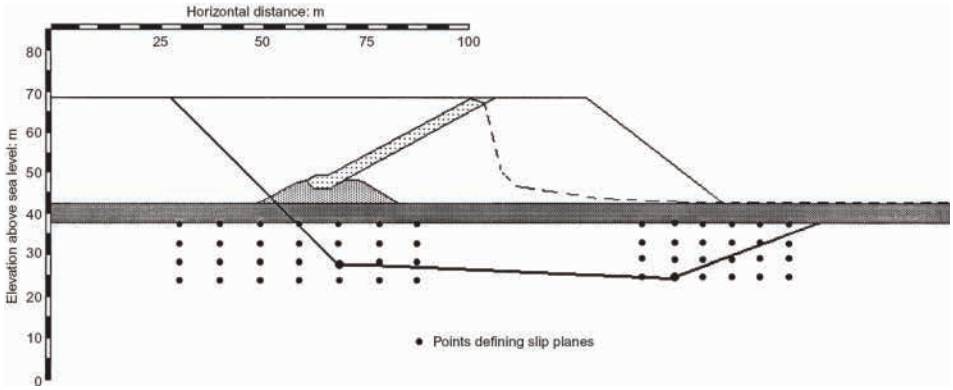

Fig. 6.16 Most unfavourable slip plane obtained from limit equilibrium analysis (Olalla & Cuéllar, 2001)

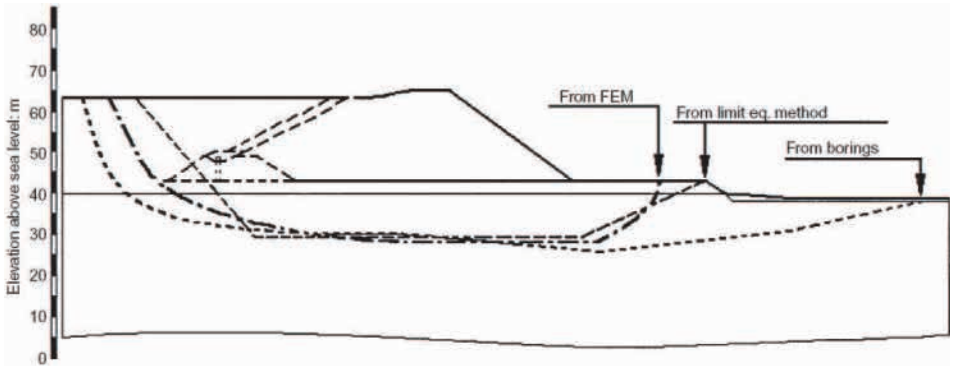

Fig. 6.17 Comparison of slide surfaces obtained from different methods (Olalla & Cuéllar, 2001)

Although the modelling results are, to some extent, consistent with the real failure state, it did not simulate the real construction process as described by Alonso & Gens (2006a). Furthermore, the way used to simulate the progressive reduction of Guadalquivir blue clay strength is not an ideal procedure to model progressive failure.

Fig. 6.16 shows the most unfavourable slip plane obtained from limit equilibrium analysis where an operational angle of friction of approximately 19° with zero cohesion was applied.

Finally failure slip planes obtained from boreholes, finite element and limit equilibrium methods were obtained systematically as shown in Fig. 6.17. It can be seen that if the foundation ground is considered to be a homogeneous medium, both the limit equilibrium calculations and the finite element method give slip surfaces that are reasonably consistent with the surface derived from the borings made in the vertical wall of the dam.

6.4.2 Numerical results from Gens & Alonso (2006)

In the study of Gens & Alonso (2006), a consolidation analysis of the foundation clay during the history of the dam and lagoon construction provides insights into the rupture mechanism. They also provide the results of conventional limit equilibrium and elastoplastic finite element analysis.

Before describing the results, it can be noted that the dam design in 1978 was performed by a standard slope stability program using the Morgenstern–Price method

and circular sliding surfaces in order to estimate the stability of the dam and the reservoir tailings against a critical downstream failure. The critical failure circle was found to be a deep circle. A safety factor F=1.30 computed for this circle was deemed to be acceptable.

In 1996 the safety of the dam was reviewed to evaluate the possibility of raising the final height of the dam by 2 m. A stability analysis was again performed for the updated geometry of the dam. The drained strength parameters were modified: the friction angle was reduced to $\phi' = 22°$, but an effective cohesion $c' = 20$ kPa was introduced. A modified Bishop method was used this time in stability calculations. For the 'low' and 'high' phreatic level assumptions, safety factors of 1.31 and 1.17 were calculated respectively.

It is apparent that conventional stability calculations assuming Guadalquivir blue clay to be fairly homogeneous and intact massive deposit predict a rotational failure mode, which was clearly not the real case. In contrast, in the limit equilibrium analysis conducted by Olalla & Cuéllar (2001), a weak layer at the same depth as real failure surface was presumed thus giving more realistic results.

A simplified consolidation analysis of the construction was performed in which the pore pressure and stress ratio on the failure plane were determined. The calculation showed that the pore pressures on the failure plane prior to failure were high, certainly much higher than the values assumed in design. It is believed that this simplified analysis developed in terms of elastic solutions and consolidation theory provides an interesting interpretation of the damage mechanisms that presumably took place before the actual final failure. It provides also a reasonable explanation for the position of the future failure surface.

Subsequently, several limit equilibrium analyses considering the actual position of the failure surface were performed. Back-analysis of failure with limit equilibrium method inferred a friction angle $\phi' = 17°$ which is intermediate between the peak friction angle in direct shear tests ($24°$) and the residual value ($11°$) suggesting the existence of progressive failure.

Both stress analysis, in terms of the maximum stress ratio along the potential failure surface, with simplified consolidation analysis of the construction process and stability analysis with limit equilibrium method demonstrate that the minimum safety factor is not achieved at the time of failure but at an earlier time. These results are interpreted as providing an additional indication that progressive failure has played an important role in the development of the instability. Available shear strength must have reduced, probably as a result of the accumulation of deformations along the failure surface, due to the construction of the embankment. It is also implied that no pre-existing very low-strength failure surface could possibly exist, as in that case failure would have been taking place many years before the actual event.

In addition, limit equilibrium analysis introducing the Agrio river meander illustrated that the meander has a very limited effect in the development of the failure. So in the numerical analyses, the geometry as shown in Fig. 6.4 instead of that used by Olalla & Cuéllar (2001) (shown in Fig. 6.15-Fig. 6.17) was adopted.

Finally, finite element analyse were performed. Elastoplastic coupled flow–deformation analyses were carried out with the purpose of increasing the understanding of the mechanisms leading to failure. In a first analysis a homogeneous

clay deposit was considered. The process of dam construction and tailings impoundment was simulated in 11 steps. Each step was, in turn, divided into an undrained application of loading and a subsequent partial dissipation of the pore pressures until the next undrained unloading is applied. A total of 21 stages of calculation are thus defined. A Mohr–Coulomb elastic perfectly plastic model was adopted for all materials.

If peak strength parameters are adopted for the clay ($c' = 65$ kPa and $\phi' = 24°$) no plastic points are obtained during the whole construction process. It is concluded that, in order to explain the embankment failure, some zones within the clay must have exhibited reduced strengths. In order to simulate failure for homogeneous conditions, a progressive reduction of strength parameters is introduced. In this way, the rupture mechanism shown in Fig. 6.18 is found (contours of equal shear strains are represented). A circular failure is predicted (as in the limit equilibrium type of analysis for homogeneous clay properties).

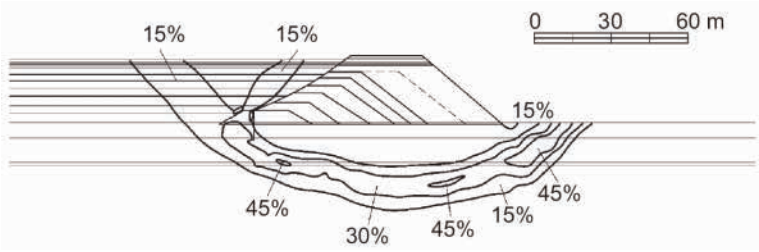

Fig. 6.18 Contours of equal shear strain calculated at failure in a 2-D elastoplastic finite element analysis: homogeneous clay (Gens & Alonso, 2006)

In a second type of analysis a discontinuity with reduced strength characteristics was located at the position of the sliding plane. This is an interesting problem because, if the reduced parameters are chosen to reproduce the final condition, failure is predicted at a much earlier date (at phase 11, out of the total 21 phases). This result is consistent with previous findings, both in the simplified consolidation analysis and in the limit equilibrium calculation. It was necessary to adopt two sets of parameters: a 'more resistant' set for the first part of the analysis, and a 'weaker' set for subsequent calculations. This is not a procedure to simulate progressive failure, but it provides a strong indication of the need to reduce the available strength of the clay if the actual rupture mechanism is to be approximated. The following strength parameters were adopted for the analysis with a discontinuity plane:

(a) Plane of discontinuity: c' variable between 1 kPa and 15 kPa; $\phi' = 21.5°$.

(b) Clay above and below the critical plane: $c' = 65$ kPa and $\phi' = 24°$ (mass properties).

A drained cohesion, 15 kPa, was assumed to correspond to the initial phases, and $c' = 1$ kPa was a further reduction of cohesion for the subsequent phases.

This FE analysis also provided data relating to the evolution of pore water pressures in the foundation that will be discussed later in this Chapter.

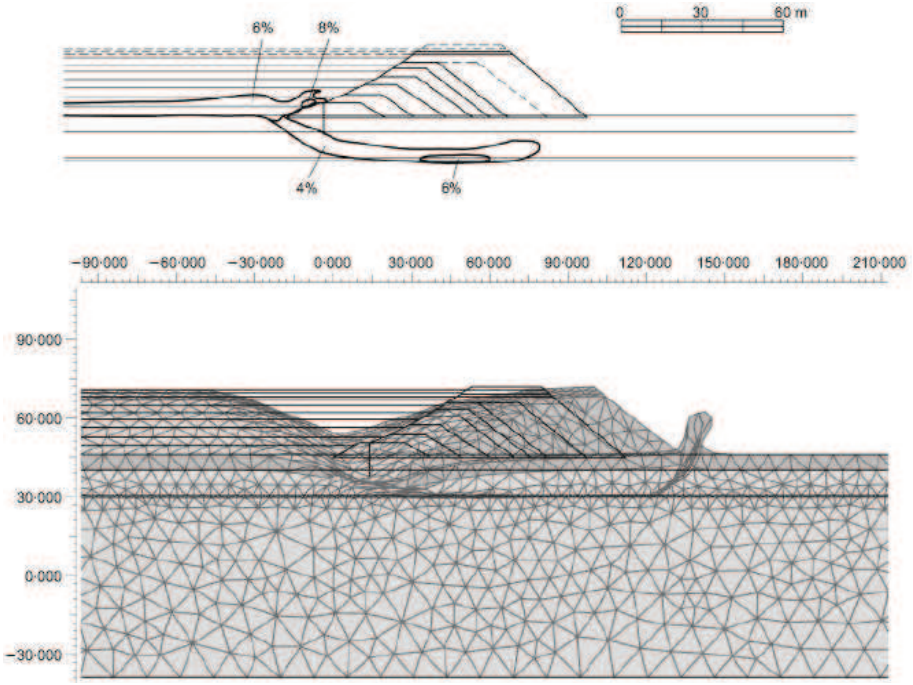

Fig. 6.19 (a) Contours of accumulated shear deformations from origin of calculations (maximum deformation 22.35%) (b) mesh deformation during failure process (Gens & Alonso, 2006)

Fig. 6.19 shows the development of an active state in the tailings and upstream of the dam, and a passive wedge at the downstream toe. The former is not supported by observations but the position of the passive wedge, immediately downstream of the dam, is close to real conditions. In Fig. 6.19, horizontal coordinates start at the upstream toe.

The analysis also confirms that the shear deformations accumulate on the potential failure plane, and they extend as the embankment construction advances (Fig. 6.19a). The rupture mechanism, identified by means of the mesh deformation (Fig. 6.19b), is similar to the actual failure mechanism described by Alonso & Gens (2006a).

6.4.3 Numerical results from Zabala & Alonso (2011)

Zabala & Alonso (2011) used the material point method to simulate the construction and failure of the Aznalcóllar dam. The model predicts the development of a localised shearing band associated with a progressive failure mechanism. The shape and position of the failure surface reproduce actual field observations.

6.5 Simulation of Aznalcóllar dam failure with the two-stage constitutive model

6.5.1 General description of numerical simulation

Although the finite element analysis by Gens & Alonso (2006) reproduced the real dam construction process and failure, the manner to model clay softening is not a

procedure to simulate progressive failure because they adopted different sets of soil parameters for the first and second parts of calculation.

As presented early in this Thesis, the modified elastoplastic non-linear strain-hardening and strain-softening model implemented in *FLAC* can be used to simulate the mechanical behaviour of Guadalquivir blue clay. In this way, progressive failure can be properly modelled.

The modelling procedure of Azanalcóllar dam failure is described in detail in Table 6.2. The procedure is divided into 7 stages. Stage 1—stage 3 establish the grid and set the soil parameters. Stage 4 calculates the initial state of stress, strain and pore pressure. Stages 5-7 (steady-flow calculation, tailings and dam loading and consolidation) are performed for each construction phase.

Table 6.2 General modelling procedure

Modelling Stage	Stage description
1	Grid generation
2	Group setting
3	Model parameters setting
4	Initial state calculation
5	Steady-flow calculation to determine phreatic surface and saturation
6	Tailings and dam loading
7	Consolidation

Table 6.3 presents the modelling phases during the construction of Aznalcóllar dam, which lasted 20 years from April, 1978 till April, 1998 (failure of dam). The whole construction process is consistent with that described in Section 6.1. In total, 35 phases are set in the numerical model. The height at failure is 26.60 m.

The initial grid before dam construction is shown in Fig. 6.20. The whole model mesh including all soils and construction groups is seen in Fig. 6.21 and Fig. 6.22. Both sides are restrained in horizontal direction and the base is also fixed vertically. The small strain setting is used in the modelling because the large deformation at and after failure may induce highly distorted element and result in the premature abortion of calculating process. The diaphragm wall is simulated by a *beam* element combined with interface setting.

Table 6.3 Modelling phases (from April, 1978 till April, 1998)

Phase	Description	Dam state		Time
		Height (m)	Width (m)	(days)
1	Grid generation	-	-	-
2	Group setting	-	-	-
3	Model parameter setting and model assignment	-	-	-
4	Initial state	0.00	0.00	0
5	Steady-flow calculation			
6	Dam 1 + Tailings	5.50	17.50	
7	Consolidation			548
8	Steady-flow calculation			
9	Dam 2 + Tailings	8.60	13.70	
10	Consolidation			1125
11	Steady-flow calculation			
12	Dam 3 + Tailings	12.40	11.71	
13	Consolidation			2005

14	Steady-flow calculation			
15	Dam 4 + Tailings	15.40	13.80	
16	Consolidation			2430
17	Steady-flow calculation			
18	Dam 5 + Tailings	18.08	12.61	
19	Consolidation			3130
20	Steady-flow calculation			
21	Dam 6 + Tailings	20.75	11.93	
22	Consolidation			3525
23	Dam 7 + Tailings	20.75	27.58	
24	Consolidation			3830
25	Steady-flow calculation			
26	Dam 8 + Tailings	23.10	36.80	
27	Consolidation			4135
28	Steady-flow calculation			
29	Dam 9 + Tailings	24.10	34.10	
30	Consolidation			6600
31	Steady-flow calculation			
32	Dam 10 + Tailings	25.35	30.50	
33	Consolidation			7300
34	Steady-flow calculation			
35	Dam 11 + Tailings	26.60	27.00	

Table 6.4 Basic soil geotechnical properties

Name	Density (kg/m^3)	Young's modulus E (Pa)	Poisson's ratio ν	Porosity n	Permeability k (m/day)	K_0
Tailings	3100	3e6	0.3	0.5	1.555e-3	-
Rockfill	2000	4e7	0.3	0.5	1.555e-3	-
Red clay	2000	4e7	0.3	0.2	0.0	-
Alluvium	2000	2e7	0.3	0.5	1.555e-3	0.426
Blue clay	2100	4e7	0.3	0.35	1.555e-6	1.0

The basic soil parameters shown in Table 6.4. are the same as those adopted by Gens & Alonso (2006). Mohr-Coulomb model is applied to tailings, rock fill, red clay and alluvium in all analyses and the model parameters are given in Table 6.5.

Table 6.5 Soil models and parameters

Material	Model type	c (kPa)	ϕ (°)	ψ (°)
Tailings	Mohr	1	37	0
Rockfill	Mohr	10	50	0
Red clay	Mohr	10	50	0
Alluvium	Mohr	1	35	0

Section 6.3 has presented the strength parameters for blue clay mass (Table 6.1). The plastic shear strain threshold values (γ_p, γ_{pr} and γ_r) may be also acquired from direct shear test (Fig. 2.20). It should be noted that the equivalent *FLAC* plastic shear strain is half of that calculated from direct shear test results.

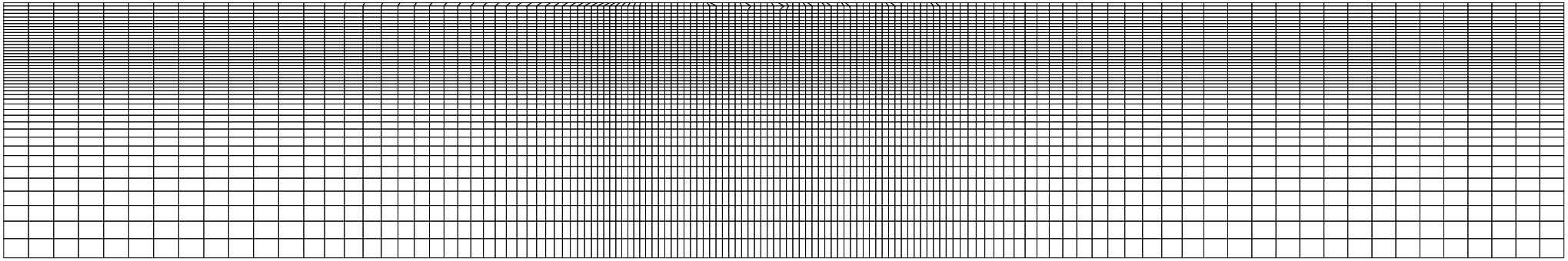

Fig. 6.20 Initial grid

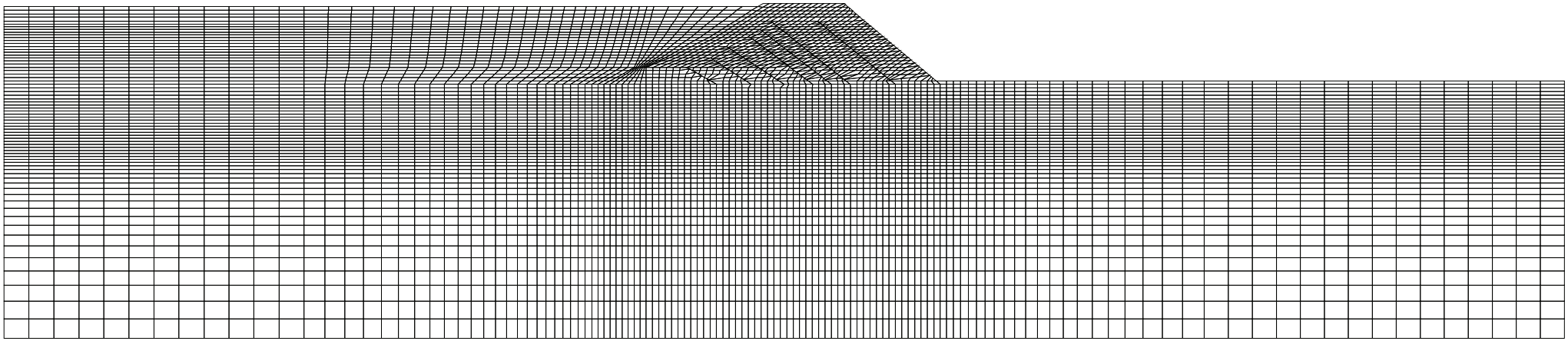

Fig. 6.21 Whole grid

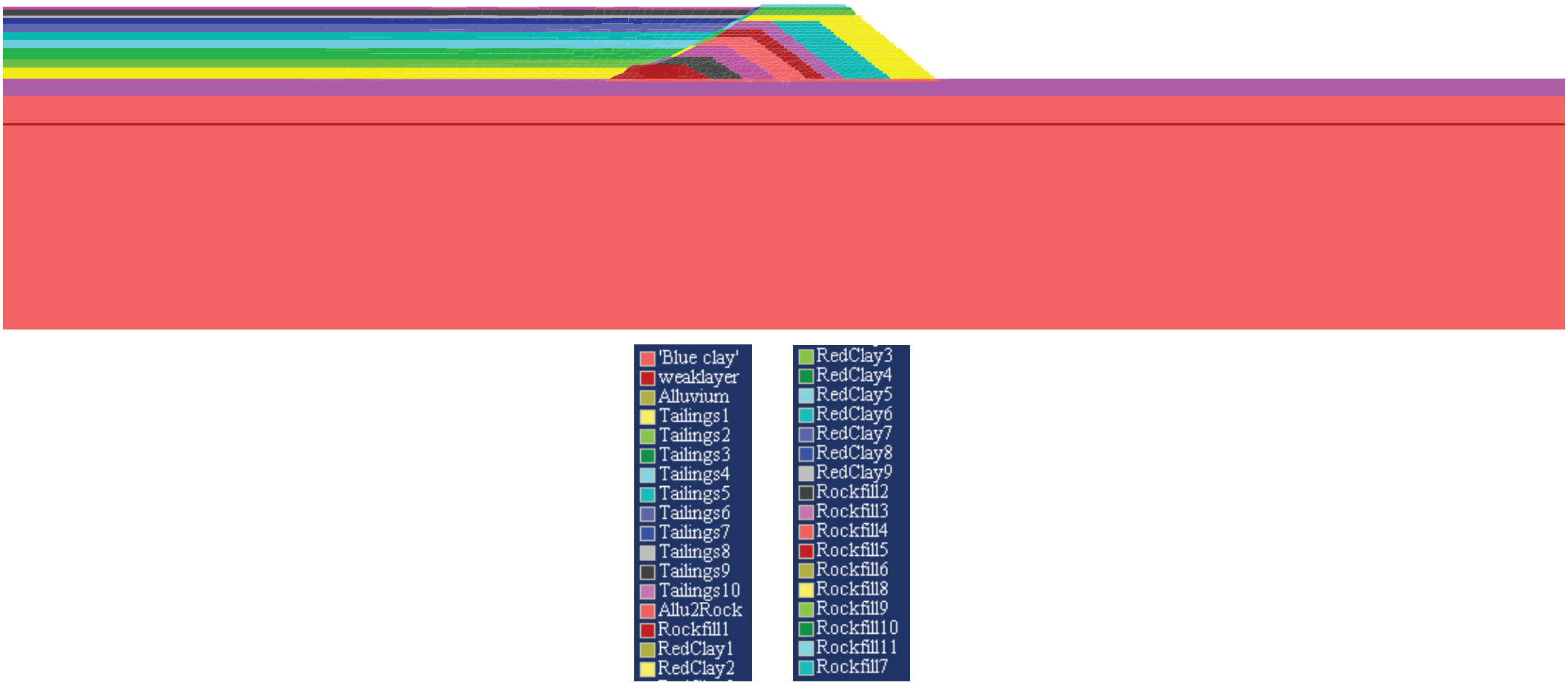

Fig. 6.22 Material and construction groups

6.5.2 Two hypotheses of numerical simulation

6.5.2.1 Inhomogeneous hypothesis

As described in Section 6.3, the sliding plane could have followed a bedding plane could be also an indication that the strength of the clay formation was not homogeneous. Some initial 'damage' was probably present in the bedding planes. The striated surfaces discovered in some of the boreholes and outcrops also favor this interpretation. Therefore a reduced available initial strength along bedding planes and the mechanisms of progressive failure are two factors that probably contributed to a reduction of the available mean strength of the clay to resist the driving forces induced by dam and tailings.

The stability analysis performed (finite elements) (Gens & Alonso, 2006) also suggested that some strength loss was initially present along the bedding planes. As suggested by the interpretation given to the results of drained direct shear strength tests (Alonso & Gens, 2006a), the effective cohesive term of the strength of bedding plane is lost first. Thereafter, the failure surface along critical bedding plane behaves as a frictional contact whose friction coefficient reduces towards an ultimate residual value when the clay structure along the critical bedding plane is oriented in the direction of sliding. Therefore, Gens & Alonso (2006) argued that, if the failure initiated along a bedding plane, the post-rupture strength may be more relevant as the initial strength of the material. So in the numerical modelling, the post-rupture strength may be applied to the critical bedding plane as an initial value.

In this hypothesis, inhomogeneous blue clay mass combined with a weak clay layer is considered. The two-stage softening model is adopted for the intact clay mass and one-stage softening model for the weak clay layer where the post-rupture strength is assumed to be the initial peak strength.

6.5.2.2 Homogeneous hypothesis

In the second hypothesis, Guadalquivir blue clay is considered as completely homogeneous medium modelled by two-stage strain-softening model with more rapid strain-softening rates.

6.5.3 Analysis with inhomogeneous hypothesis

In this section, analysis L is denoted as the one with inhomogeneous hypothesis. The model parameters (shown in Table 6.6 and Table 6.7) adopted in analysis L were obtained from direct shear test and the same plastic shear strains were applied to the elements in the numerical model.

In analysis L, the intact clay mass was modelled with two-stage strain-softening model expressing the softening process from peak state through post-rupture strength to ultimate residual condition. The peak, post-rupture and residual strengths with the corresponding plastic shear strain limits are given in Table 6.6. It is noted that γ_{pr} is very small compared with γ_r indicating the rapid loss of strength from peak value to post-rupture one.

The softening relationships of cohesion and friction angle with plastic shear strain for blue clay mass and weak layer are plotted in Fig. 6.23-Fig. 6.26.

Table 6.6 Shear strength parameters and plastic shear strain limits for blue clay mass

Peak state	$c'_p = 65\text{kPa},\ \phi'_p = 24°,\ \gamma_p = 0$
Post-rupture state	$c'_{pr} = 5\text{kPa},\ \phi'_{pr} = 22°,\ \gamma_{pr} = 0.005$
Residual state	$c'_r = 0\text{kPa},\ \phi'_r = 11°,\ \gamma_r = 0.135$

Table 6.7 Shear strength parameters and plastic shear strain limits for weak layer

Initial strength	$c'_p = 5\text{kPa},\ \phi'_p = 22°,\ \gamma_p = 0$
Final residual state	$c'_r = 0\text{kPa},\ \phi'_r = 11°,\ \gamma_r = 0.130$

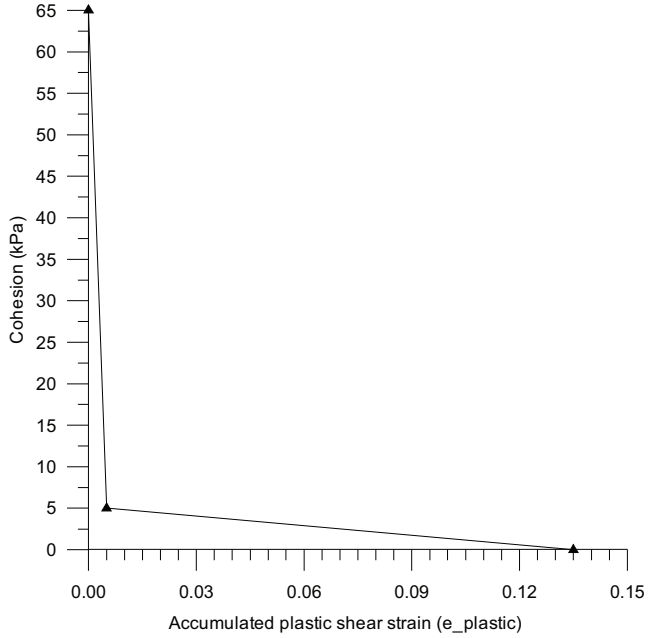

Fig. 6.23 Softening of cohesion with plastic shear strain for blue clay mass

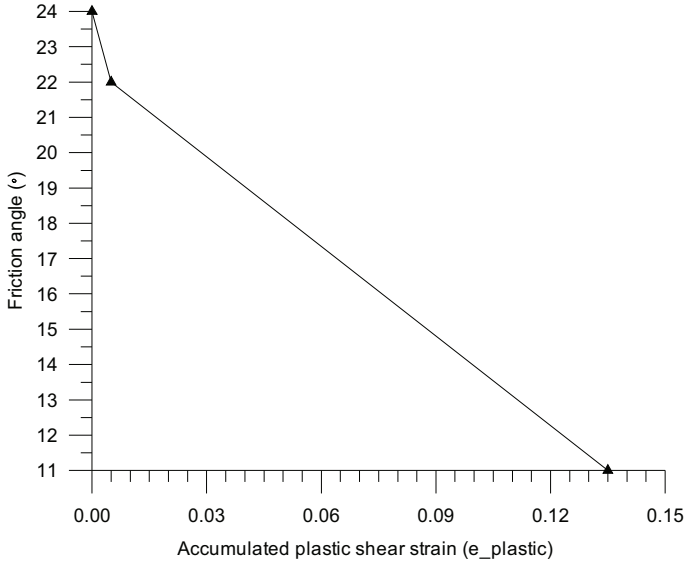

Fig. 6.24 Softening of friction angle with plastic shear strain for blue clay mass

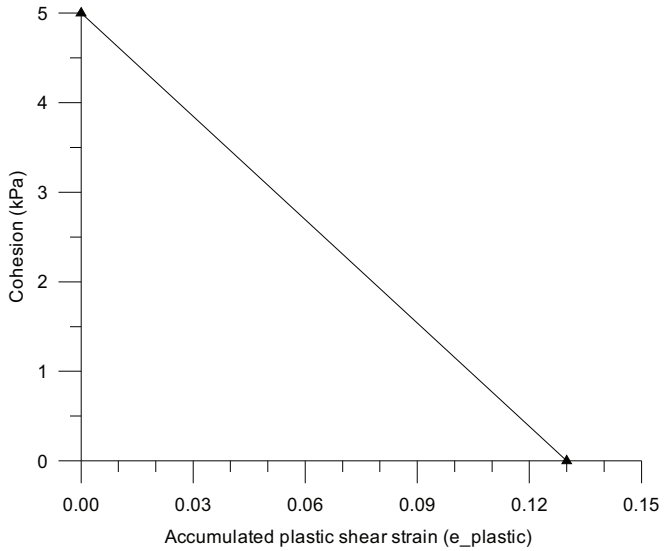

Fig. 6.25 Softening of cohesion with plastic shear strain for weak layer

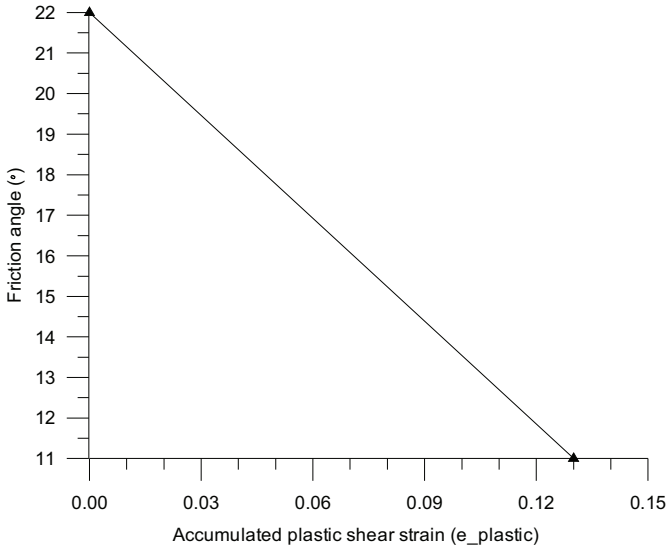

Fig. 6.26 Softening of friction angle with plastic shear strain for weak layer

A thin weak layer (Fig. 6.27) was set at depth 10m from the top of Guadalquivir blue clay mass to simulate the critical bedding plane. As described above, the strength of the bedding plane is smaller than peak value and the post-rupture strength can be considered as the initial strength of the weak layer. The one-stage strain-softening model was used indicating the strength loss from the post-rupture value to the residual one. The relevant model parameters are shown in Table 6.7.

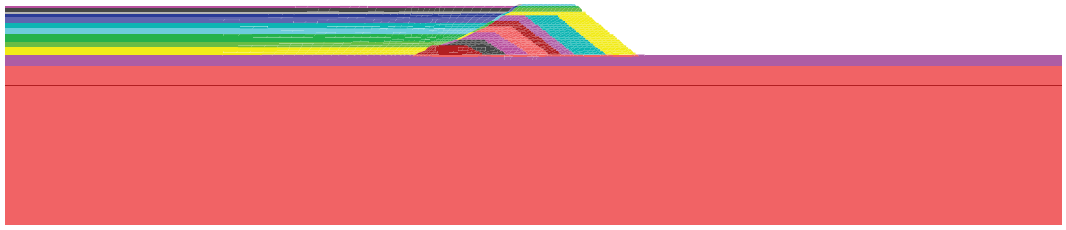

Fig. 6.27 Position of weak clay layer in the numerical model

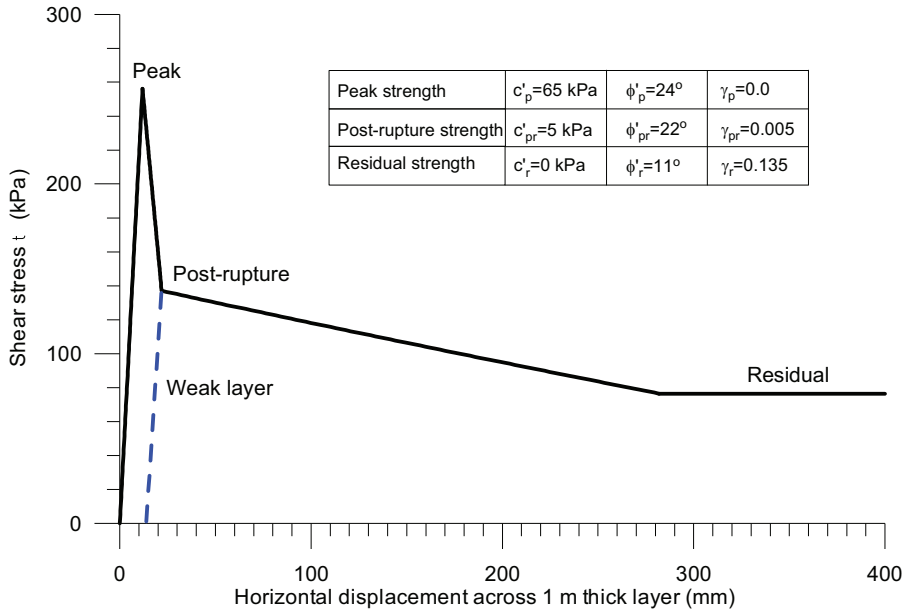

Fig. 6.28 Stress displacement relationship adopted for intact clay mass and weak layer

Fig. 6.28 shows the stress displacement relationship adopted for intact clay mass and weak layer across 1 m thick layer which corresponds to the typical model mesh size ($1\text{m}\times1\text{m}$). This relationship is calculated via the procedure presented in Appendix IV.

6.5.3.1 Description of pre-failure, initial failure and post-failure phases

General dam failure is indicated by calculation without convergence in *FLAC* using ***solve*** command. This also implies that no equilibrium will be reached and the calculation will not stop once initial failure initiates. However, there is another option (***step*** command) in *FLAC* through which detailed post-failure evolution information can be extracted.

The modelling phases have been stated in Table 6.3. In analysis L, the initial failure is defined at phase 35 with 3000 steps calculation after phase 34 and denoted as phase 35P1 with total step number equal to 939103. The post-failure phases are defined and presented in Table 6.8 together with the step number of calculation. The final post-failure modelling terminates at phase 35P11 with total step number as 1018000.

Table 6.8 Modelling step of pre-failure, initial failure and post-failure phases

Phase No.	Step number
6	24838
9	119986
12	247662
15	363744
18	455798
21	543491
23	587500
26	649650
29	862710
32	915875
35P1	939103

35P2	950656
35P3	955656
35P4	973000
35P5	984000
35P6	994000
35P7	997000
35P8	1003000
35P9	1006000
35P10	1010000
35P11	1018000

6.5.3.2 Development of shear strain rate and shear strain increment

As seen in Fig. 6.29, the shear strain rate development of Aznalcóllar dam failure demonstrates well the progressive failure process from the beginning of initial failure at phase 35P1. Moreover, shear strain increment development of Aznalcóllar dam failure (see Fig. 6.30) indicates that the shear strain concentration became gradually evident only at the final failure phases.

Phase 34 just before final construction phase 35

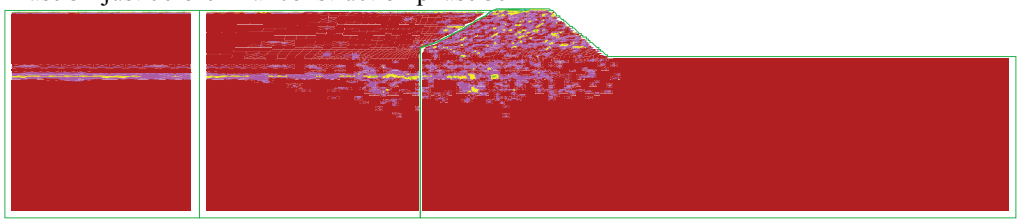

Phase 35P1

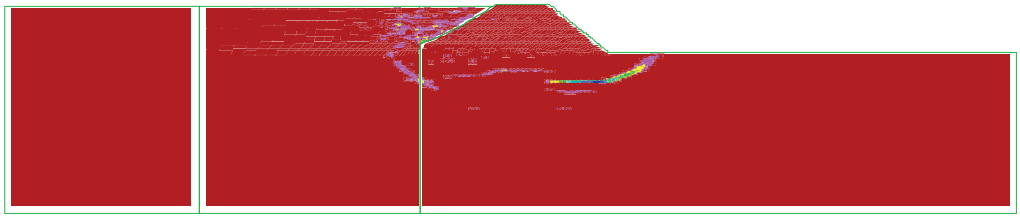

Phase 35P2

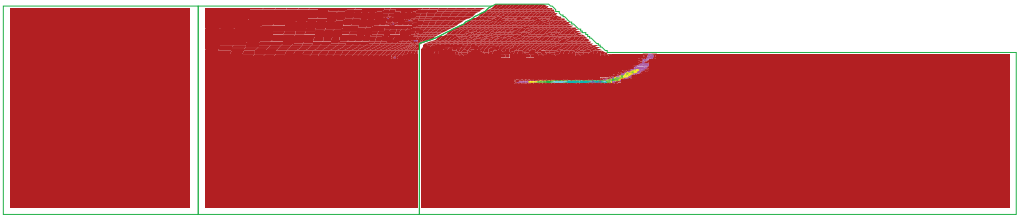

Phase 35P5

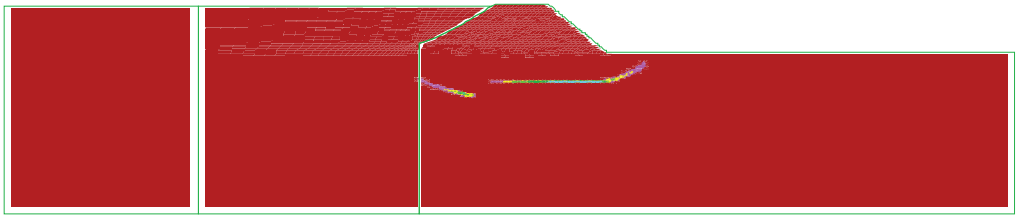

Phase 35P7

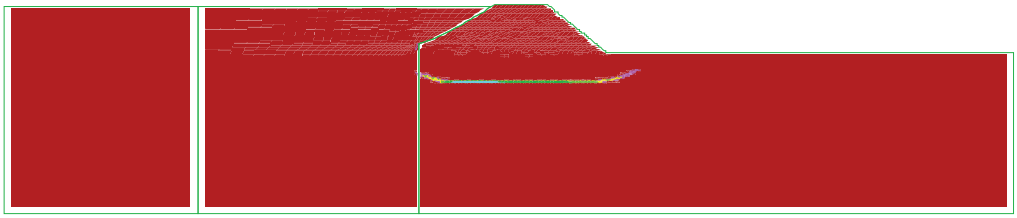

Phase 35P8

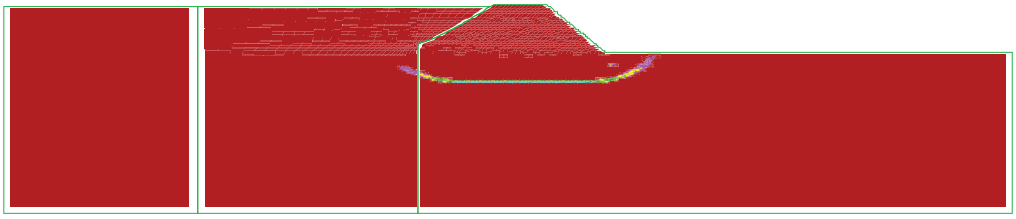

Phase 35P9

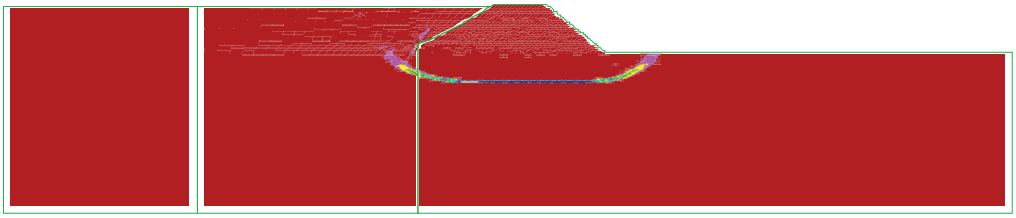

Phase 35P11

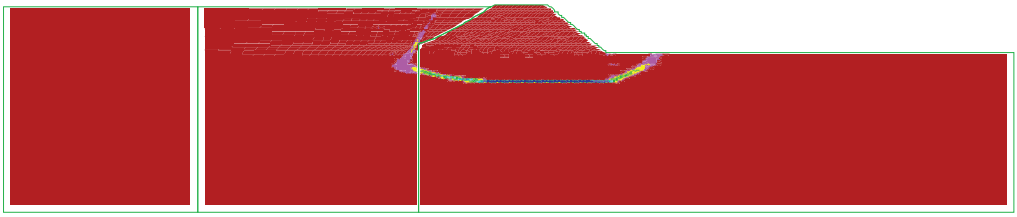

Fig. 6.29 Shear strain rate development of Aznalcóllar dam failure

Phase 35P5

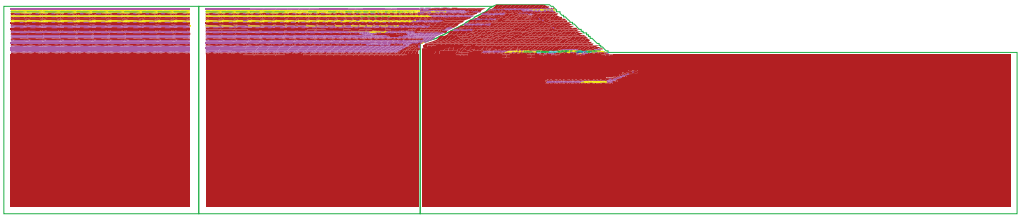

Phase 35P6

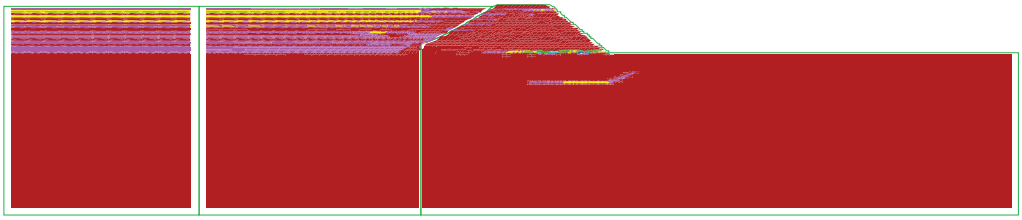

Phase 35P7

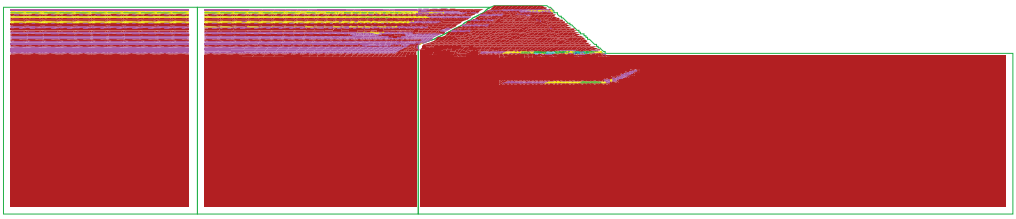

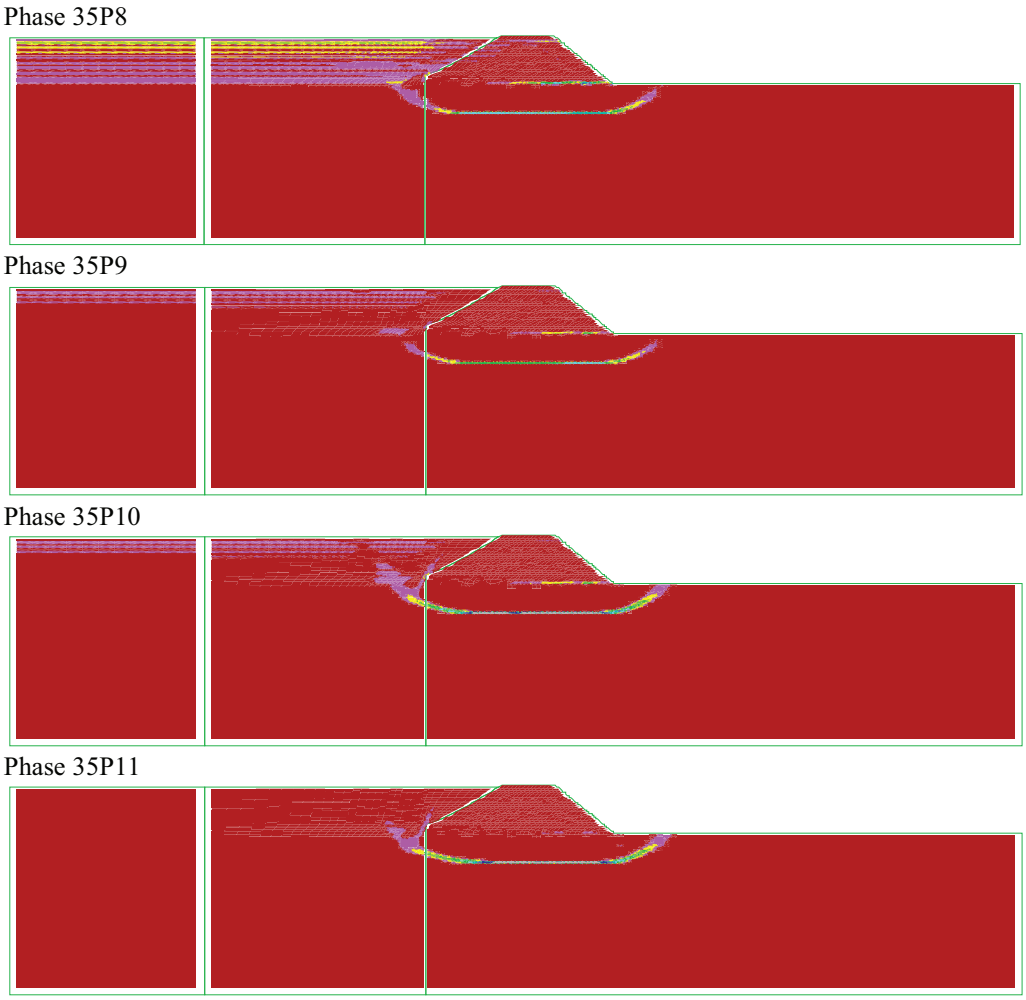

Fig. 6.30 Shear strain increment development of Aznalcóllar dam failure

In Fig. 6.29 and Fig. 6.30, the failure initiated at first in softening zones at the downstream close to the toe and at the horizontal weak layer part beneath the downstream dam toe. Then the failure extended toward the upstream along the horizontal weak layer. At the same time, failure turned up at softening zones surrounding the toe of the diaphragm wall. Afterwards the two parts were joined together and a continuous failure surface formed.

The mechanism is naturally the same as that inferred from the development of plastic zones but it is evident that shear strain rate is more suitable for capturing the progressive failure mechanism.

6.5.3.3 Development of velocity and total displacement

The velocity development (i.e. the equivalent of displacement increment) of Aznalcóllar dam failure shown in Fig. 6.31 also illustrates the whole process of the formation of a continuous slip surface.

Phase 18

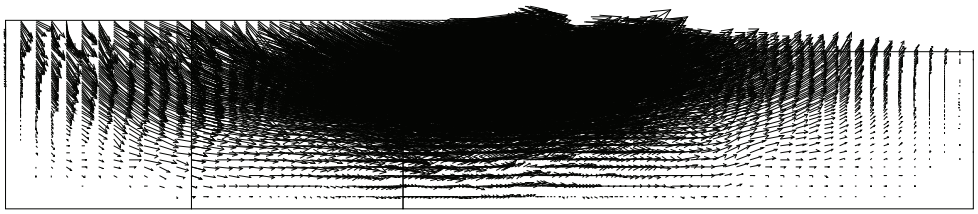

Phase 26

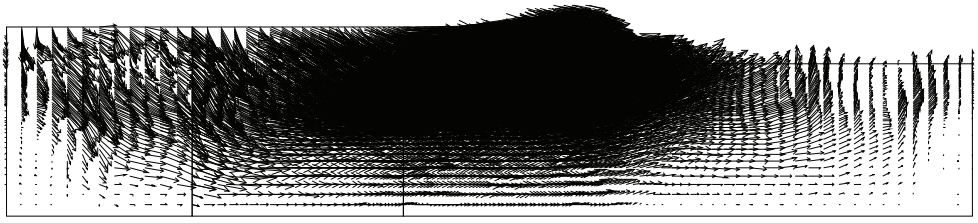

Phase 32

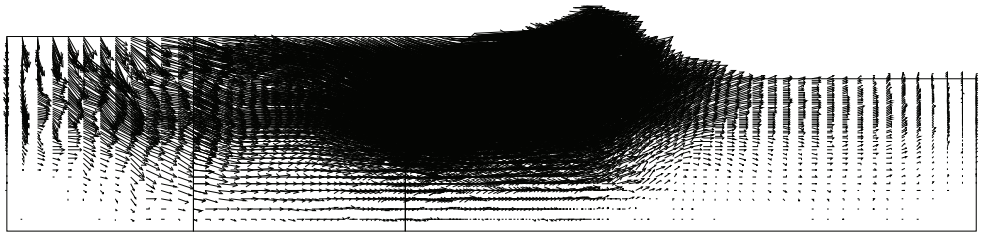

Phase 35P1

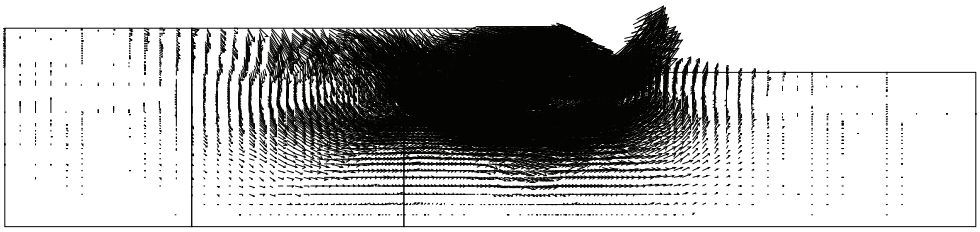

Phase 35P3

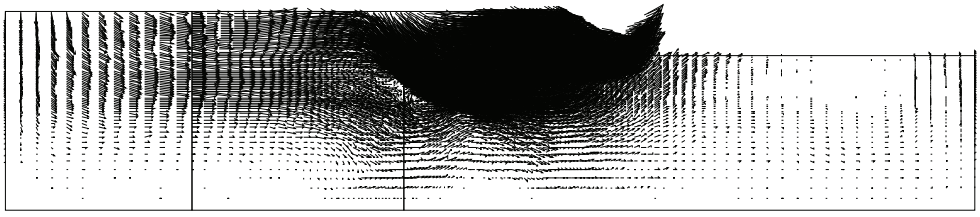

Phase 35P6

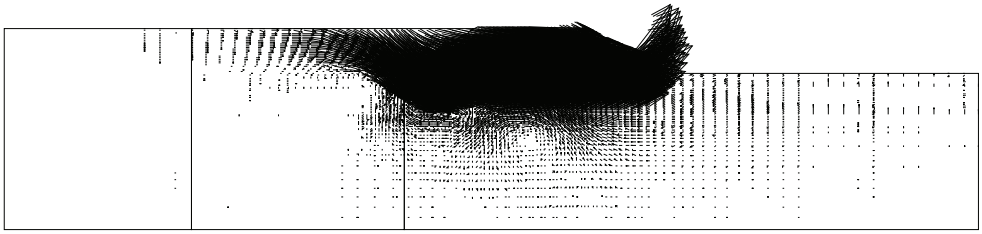

Phase 35P8

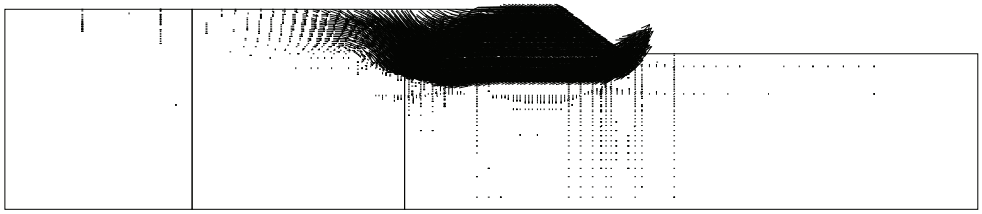

Fig. 6.31 Velocity development of Aznalcóllar dam failure

Fig. 6.32 shows the total displacement development of Aznalcóllar dam failure. The large displacement is obvious at failure stage. By comparison of Fig. 6.31, the velocity describes better the progressive failure process than total displacement.

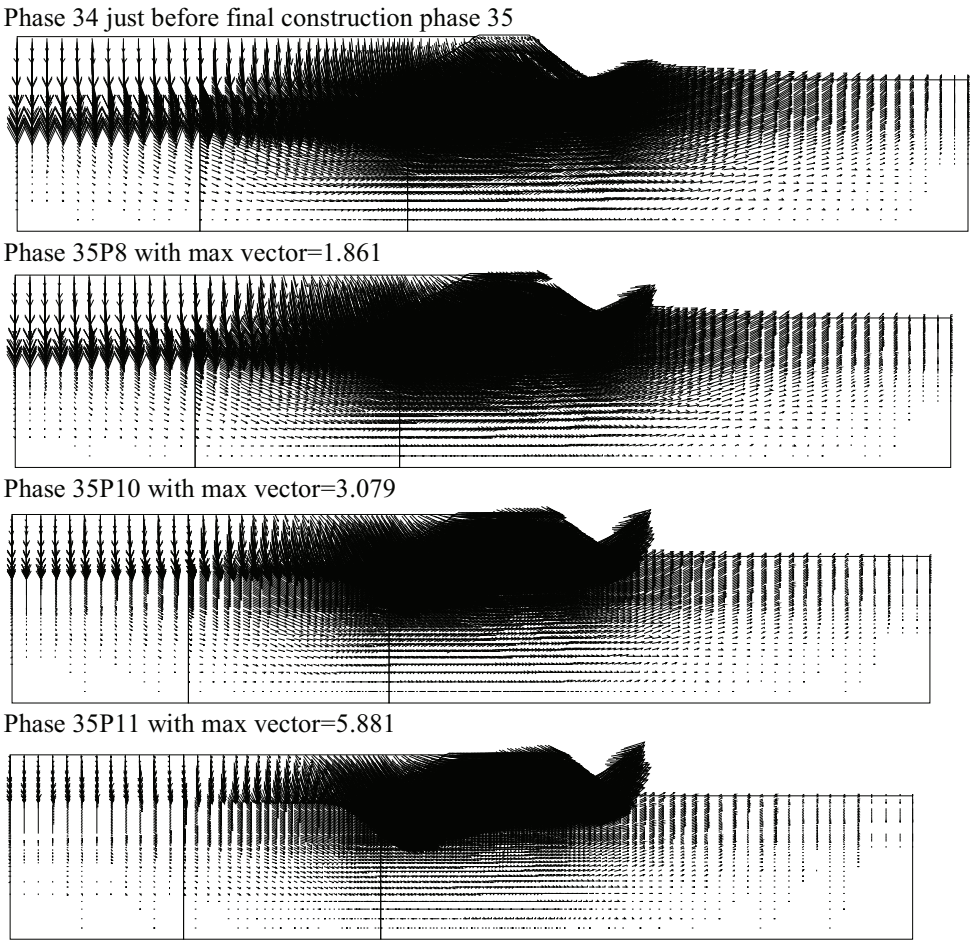

Fig. 6.32 Total displacement development of Aznalcóllar dam failure

The position of the slip surface of Aznalcóllar dam failure can be determined directly from Fig. 6.33. This figure also implies that Aznalcóllar dam failed as a rigid-body with the dam moving on the slip surface once the slip surface became continuous one. This is consistent with the viewpoint of Alonso & Gens (2006b).

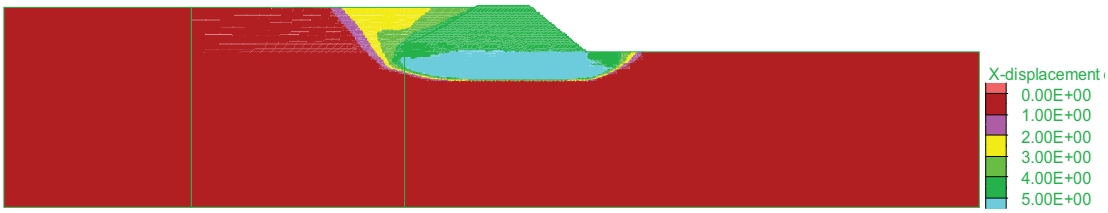

Fig. 6.33 Horizontal displacement at phase 35P11

Fig. 6.34 shows the deformed grid at final failure including the passive wedge developed at the downstream toe of dam embankment and a classic upstream active wedge. The rupture mechanism identified in terms of the mesh deformation (Fig. 6.34) is also similar to the actual failure mechanism described by Alonso & Gens (2006).

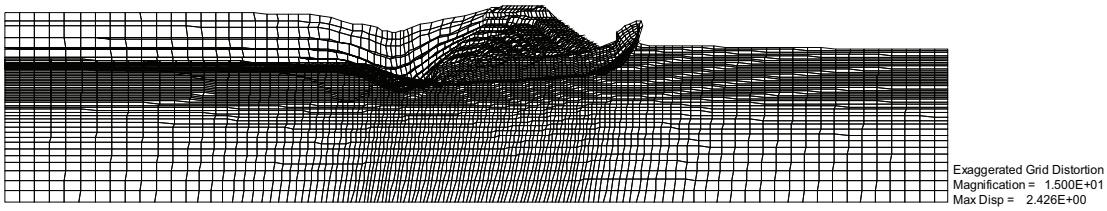

Fig. 6.34 Deformed grid with magnification=5

6.5.3.4 Development of maximum unbalanced force

The maximum unbalanced force vs. step curve shown in Fig. 6.35 clearly illustrates the process of dam construction over 11 stages as indicated by the spikes in the plot. It is interesting to discover that the maximum unbalanced force rose up to small amounts at the beginning (step=939103) of final dam construction stage, thereafter reduced to a very small value and then increased rapidly to a large value from step=1010000. The maximum value is reached approximately at step=1013000. This implies that the failure development was gradual during the initial period from step=939103 and the dam deformed slowly. Afterwards the dam failure accelerated with large deformations. This agrees with the displacement development seen in Fig. 6.32. From this point of view, the development mode of Aznalcóllar dam failure is, to some extent, similar to that of delayed progressive failure in stiff clays (see Section 5.3).

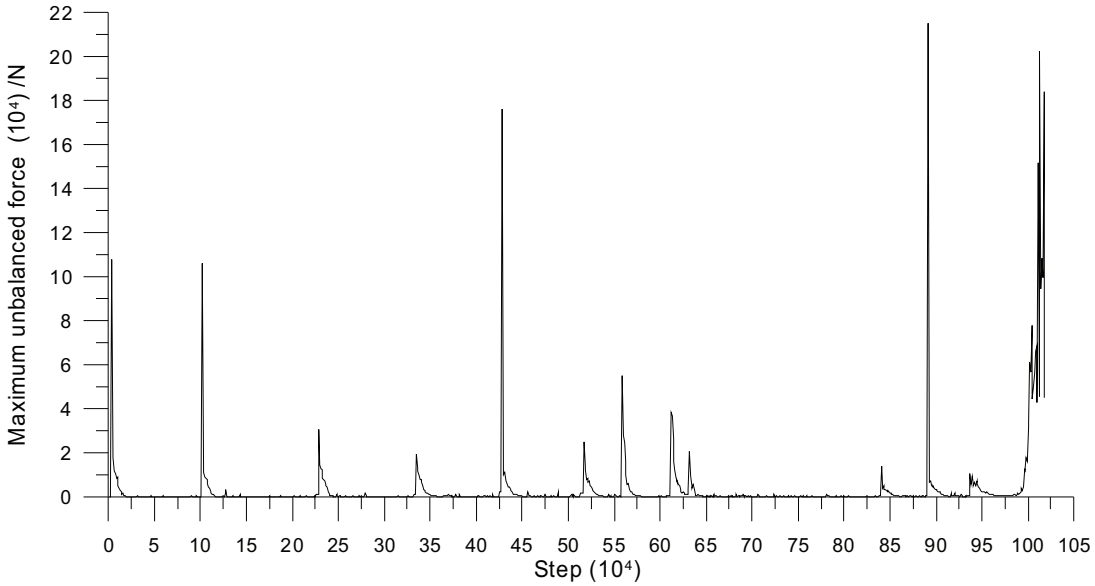

Fig. 6.35 Maximum unbalanced force vs. step till phase 35P11

6.5.3.5 Development of pore water pressure

Fig. 6.36 shows pore water pressure development for the Aznalcóllar dam case. The pore water pressure increased with dam construction. Before final construction (Phase 12-32), the pore water pressure had a similar distribution shape. But after failure began (Phase 35P1-35P11), the distribution shape changed with the development of a continuous slip surface. The distribution of pore water pressure close to the slip surface was irregular and curved.

Phase 12

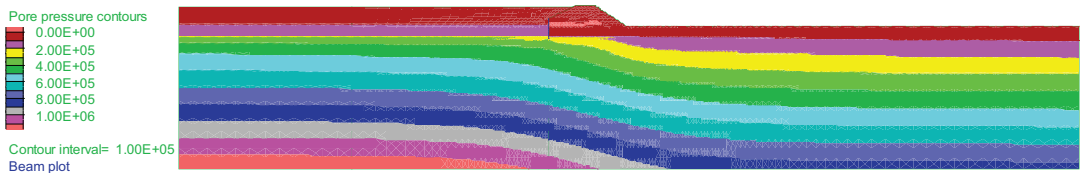

Phase 15

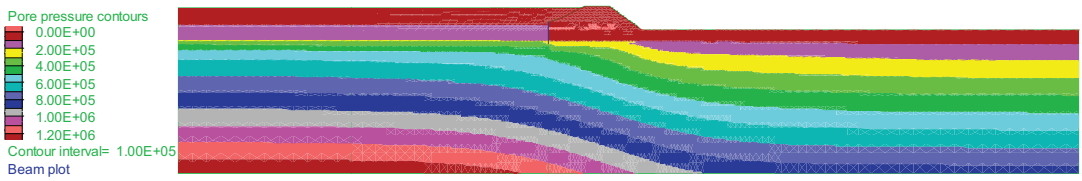

Phase 18

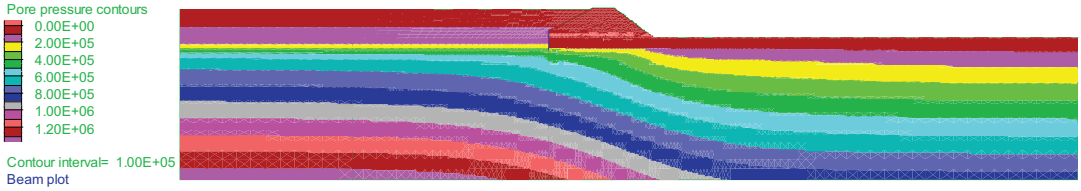

Phase 21

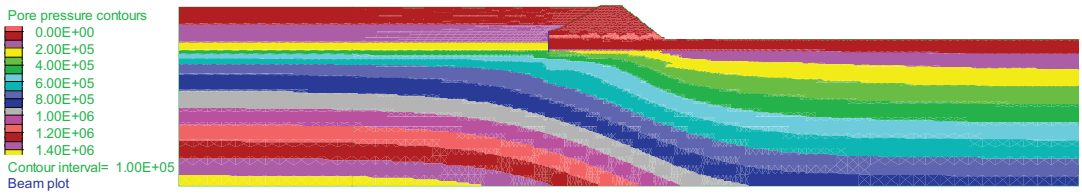

Phase 23

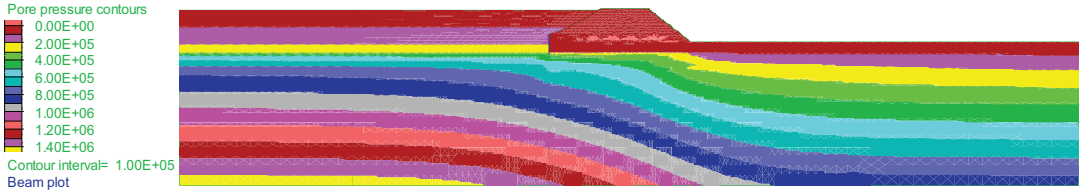

Phase 26

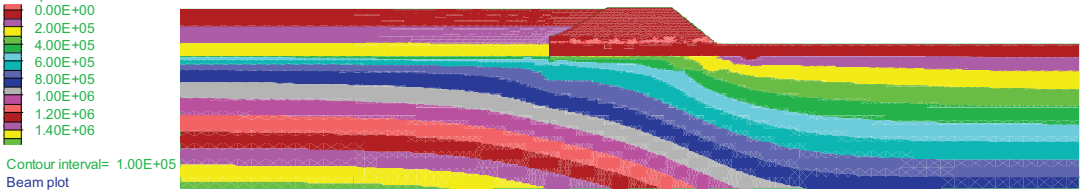

Phase 29

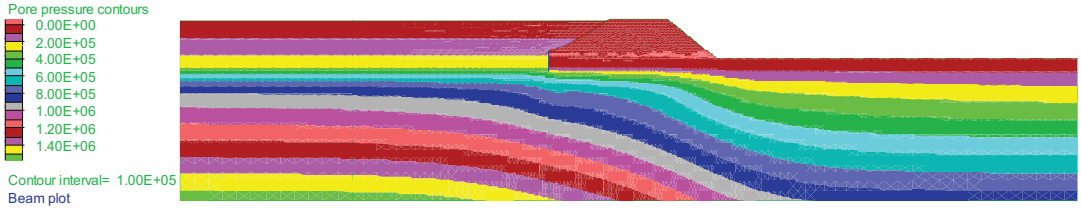

Phase 32

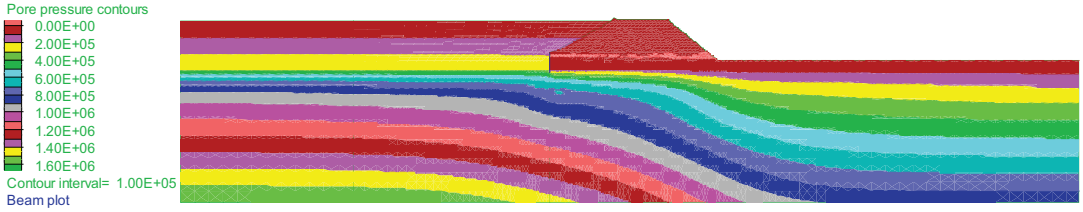

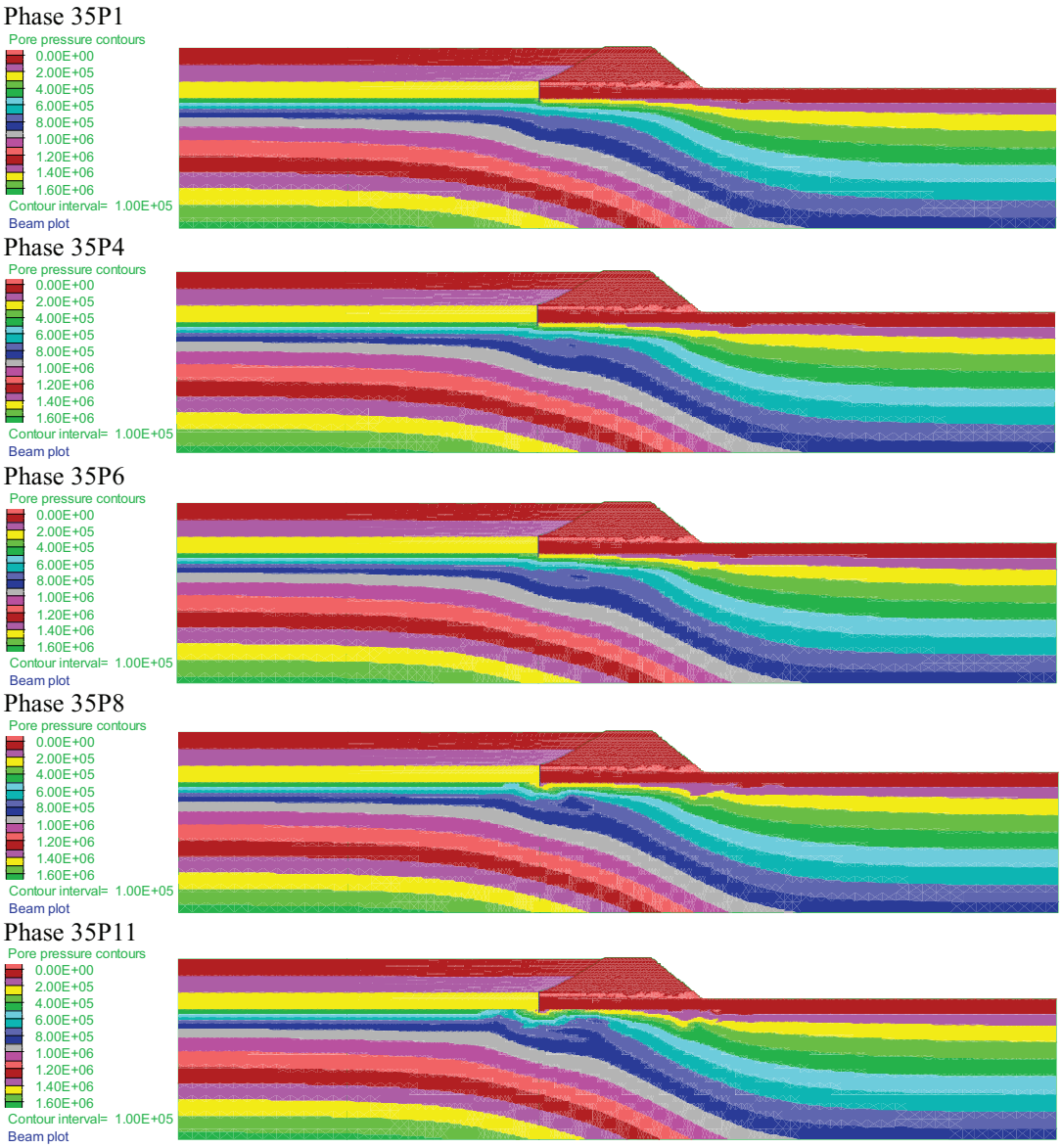

Fig. 6.36 Pore water pressure development of Aznalcóllar dam failure

6.5.3.6 Development of strength parameters in softening clays

Fig. 6.37 shows the development of accumulated plastic shear strain of Aznalcóllar dam failure in blue clay mass and weak layer for which the softening model was used.

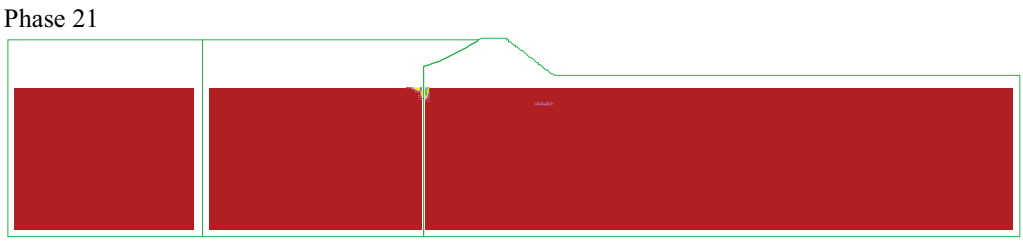

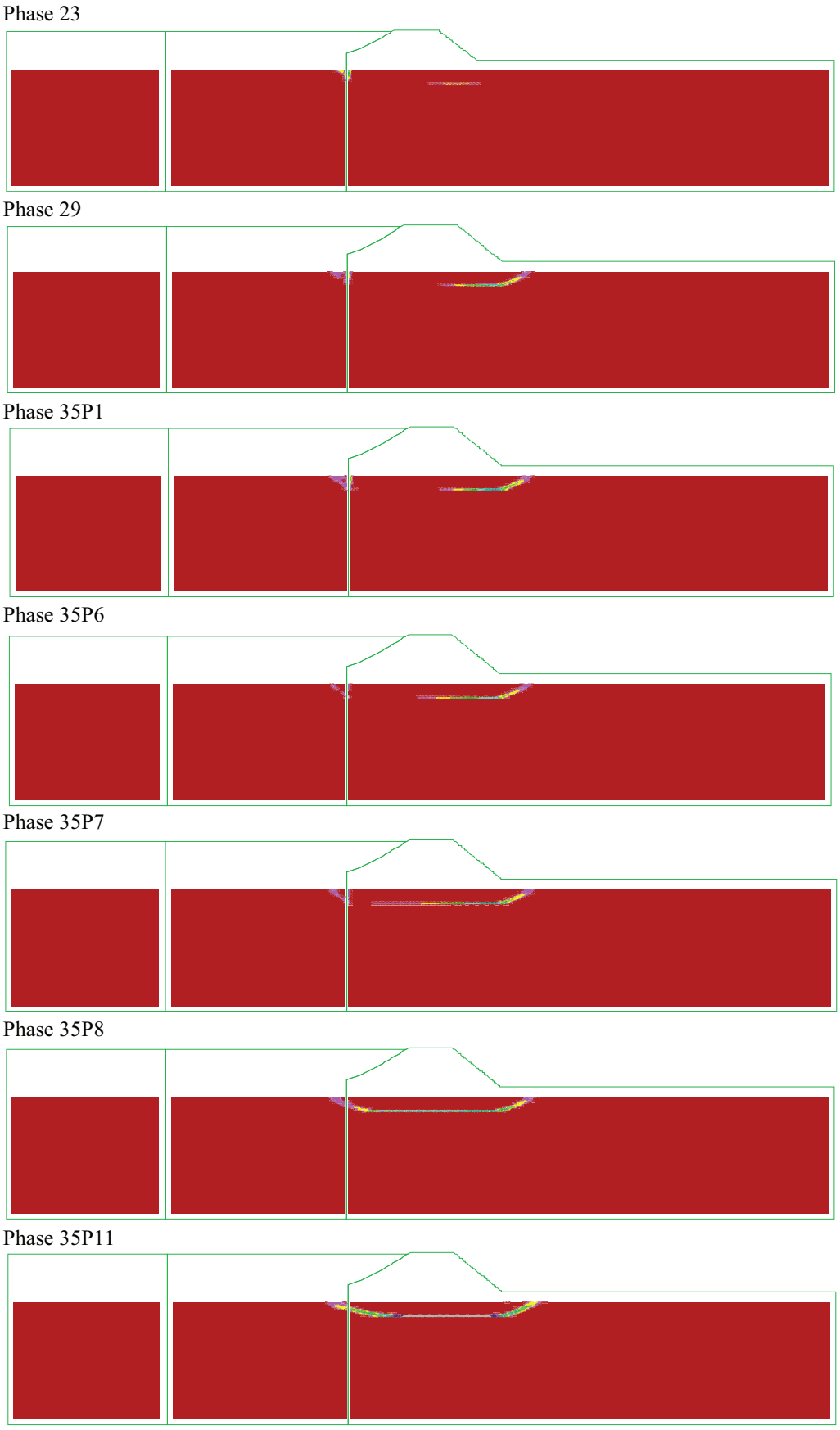

Fig. 6.37 Development of accumulated plastic shear strain of Aznalcóllar dam failure

In the model, the accumulated plastic shear strain is related to the softening of shear strength parameters and thus capable of capturing the progressive failure process. It can be seen in Fig. 6.37 that the development of slip surface in the blue clay mass and weak layer is in agreement with that observed in Fig. 6.29-Fig. 6.30.

Fig. 6.38 shows the evolution of cohesion in the Aznalcóllar dam failure. Fig. 6.39 presents the evolution of friction angle in the Aznalcóllar dam failure. From Fig. 6.38 and Fig. 6.39, it can be seen that both the cohesion softening and friction angle degradation accord with the development of accumulated plastic shear strains.

Initial cohesion

Phase 15

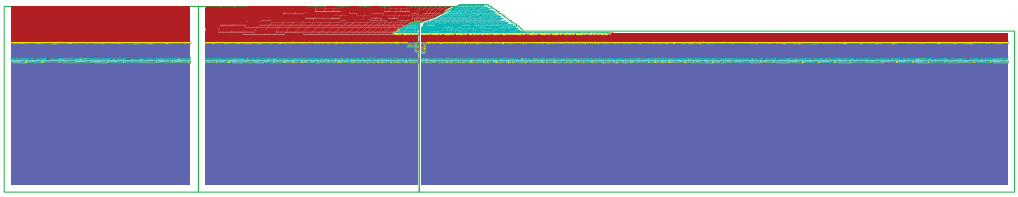

Phase 21

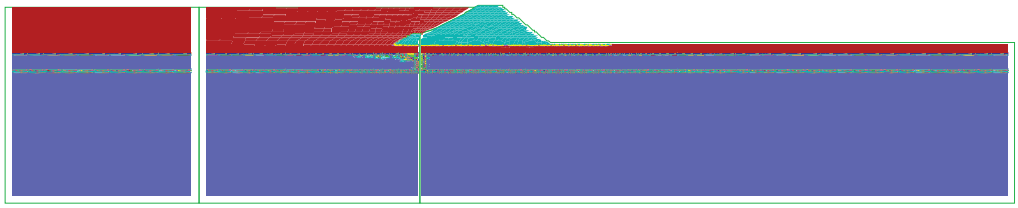

Phase 26

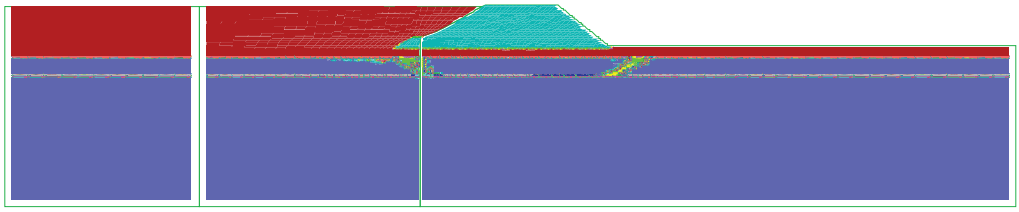

Phase 32

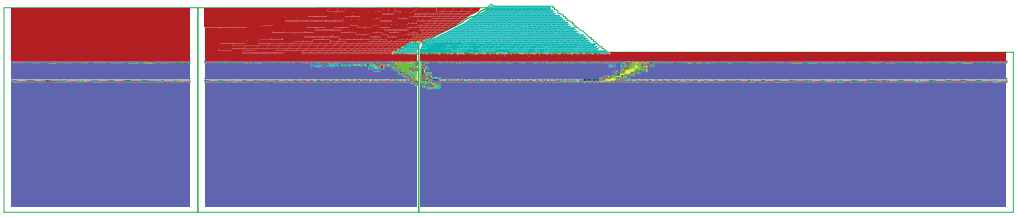

Phase 35P1

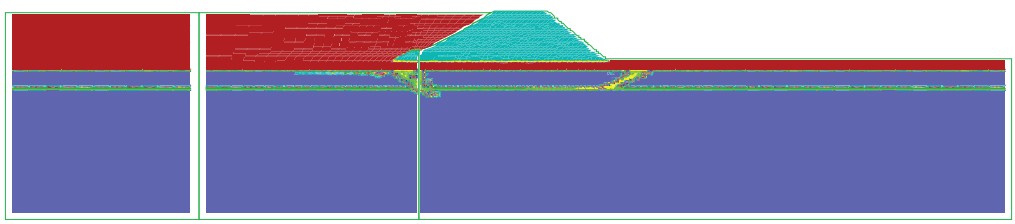

Phase 35P3

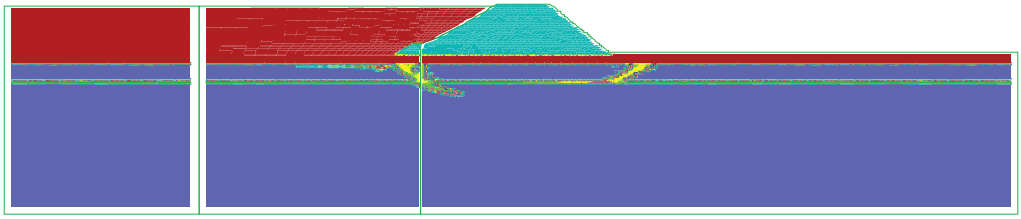

Phase 35P6

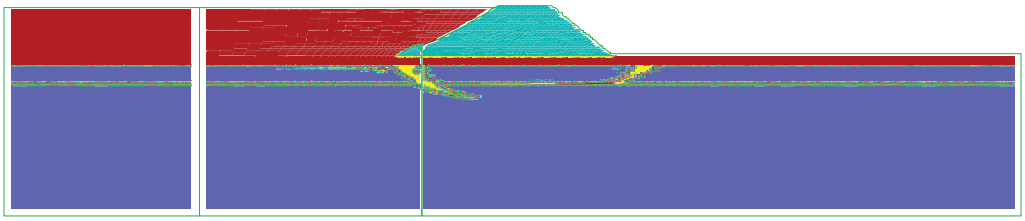

Phase 35P8

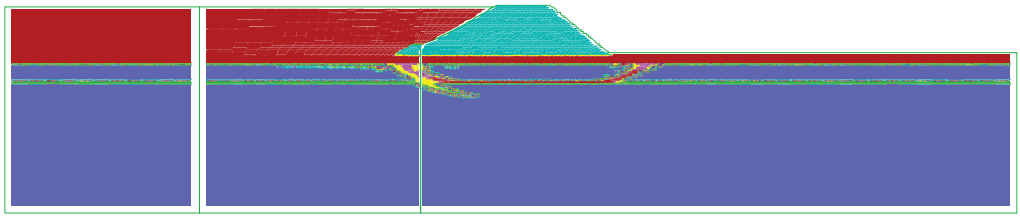

Phase 35P11

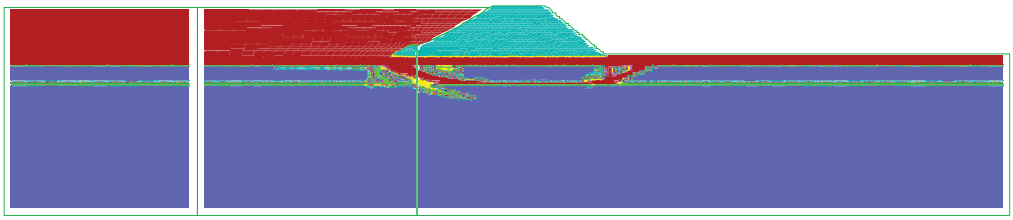

Fig. 6.38 Evolution of cohesion in Aznalcóllar dam failure (Contour interval=1.5 kPa)

Initial friction

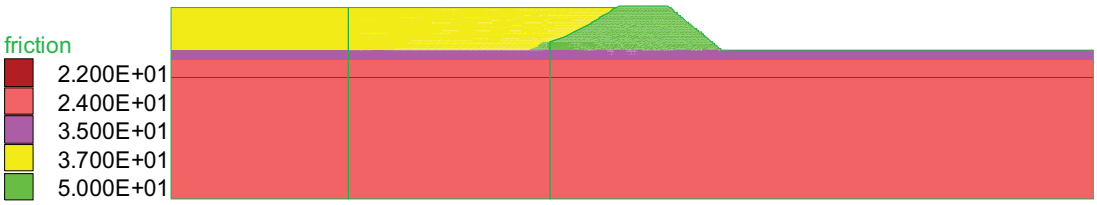

Phase 18

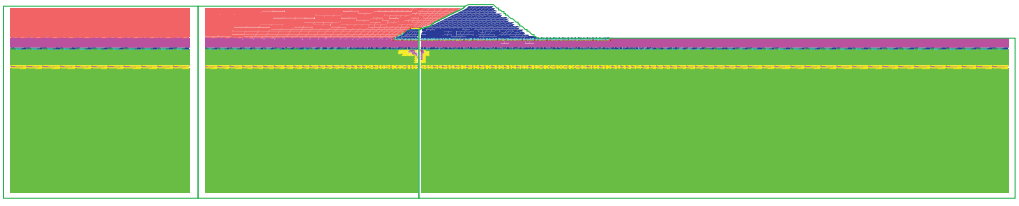

Phase 21

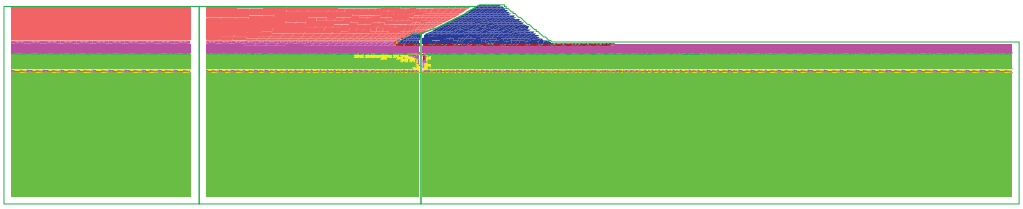

Phase 26

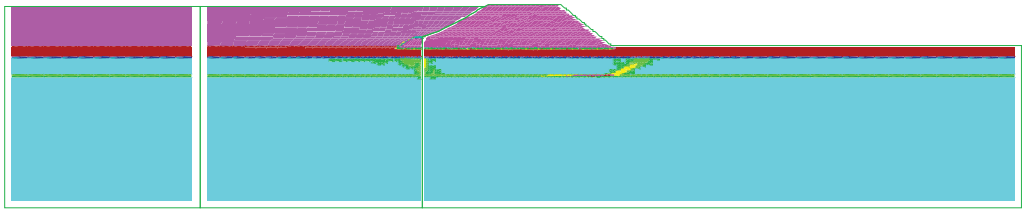

Phase 32

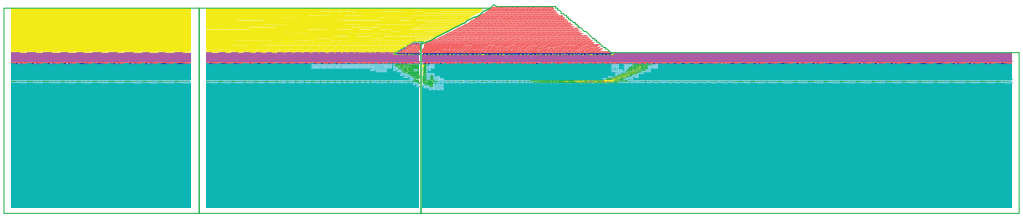

Phase 35P1

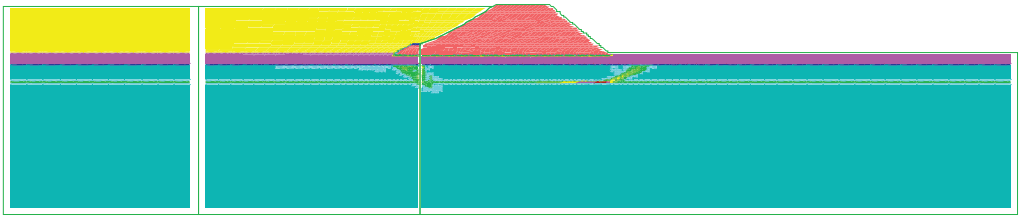

Phase 35P3

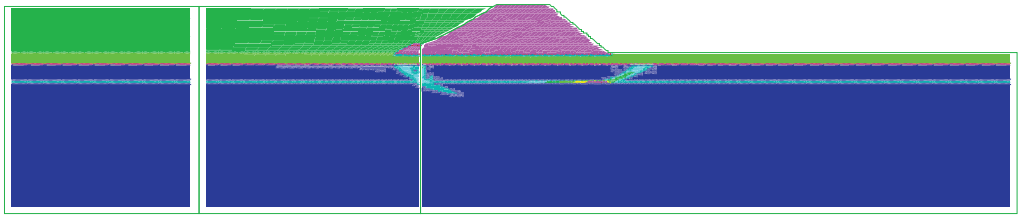

Phase 35P5

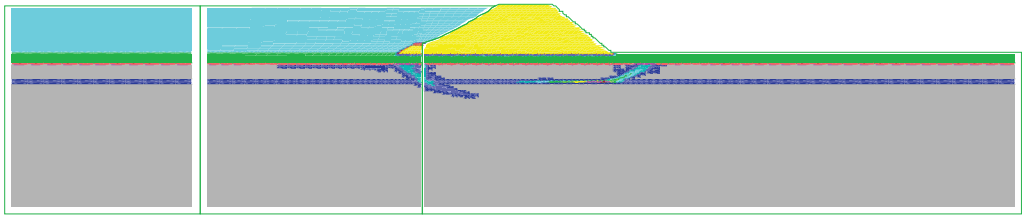

Phase 35P8

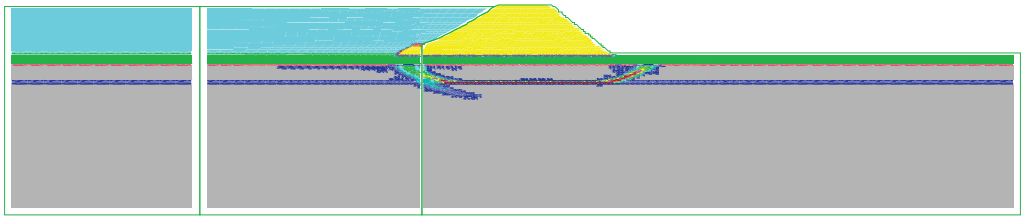

Phase 35P11

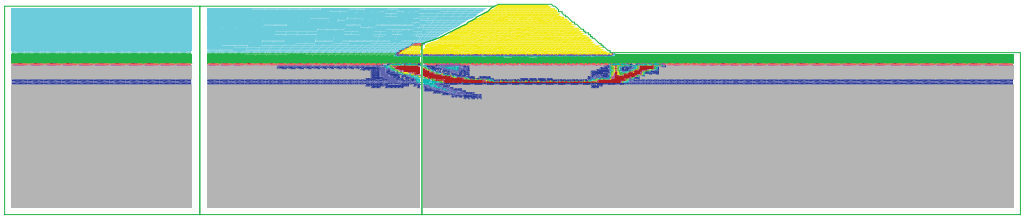

Fig. 6.39 Evolution of friction angle in Aznalcóllar dam failure (Contour interval=1.5°)

Fig. 6.38 shows the evolution of cohesion in the Aznalcóllar dam failure. Fig. 6.39 presents the evolution of friction angle in the Aznalcóllar dam failure. From Fig. 6.38 and Fig. 6.39, it can be seen that both the cohesion softening and friction angle degradation accord with the development of accumulated plastic shear strains.

6.5.3.7 Geometry of slip surface

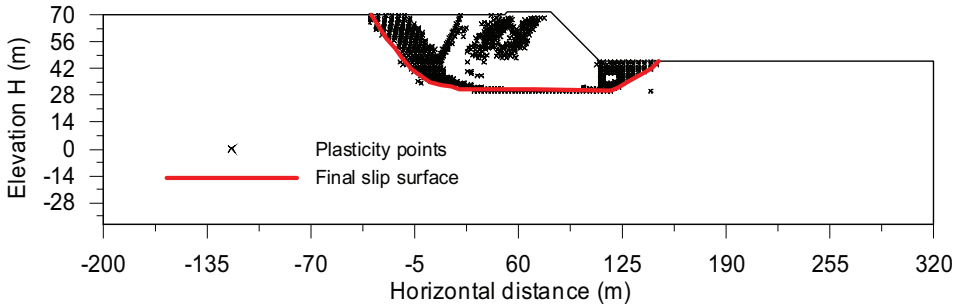

Fig. 6.40 Final slip surface predicted according to plasticity points

The position of final slip surface predicted by *FLAC* can be seen in Fig. 6.40, Fig. 6.41 and Fig. 6.42. The predicted slip surface is consistent with results of shear strain increment (Fig. 6.30), shear strain rate (Fig. 6.29), velocity (Fig. 6.31), horizontal displacement (Fig. 6.33) and mobilised strength parameters (Fig. 6.38 and Fig. 6.39). In fact, the dam failed along a shear zone (as seen in Fig. 6.40) and the slip surface is just a representative position of the sheared zone.

Fig. 6.42 also indicates that the slip surface obtained from this model is similar to those derived from previous *FEM* and *LEM* calculations. It is also similar to the failure surface calculated in Gens and Alonso (2006).

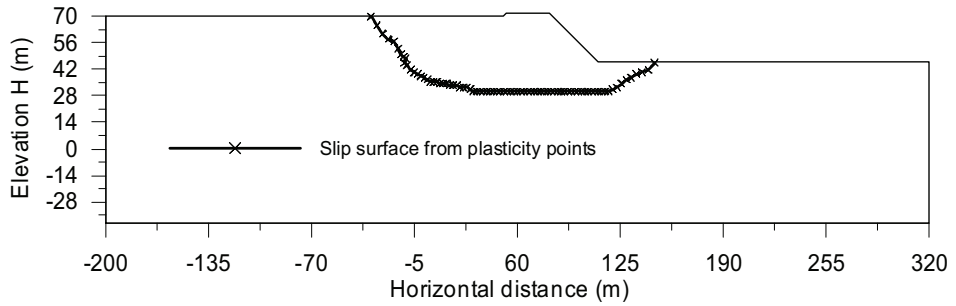

Fig. 6.41 Slip surface obtained directly from plasticity points

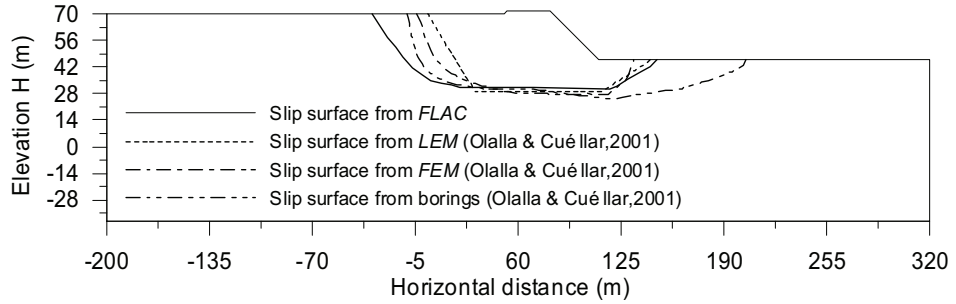

Fig. 6.42 Slip surface: comparison of *FLAC*, *FEM*, *LEM* and field borings

6.5.3.8 Post-failure evolution of representative horizontal displacements

Fig. 6.43 shows the slip surface and representative points such as F, G and H on the downstream dam embankment. It can be seen in Fig. 6.44 that the deformation of these points developed gradually first and then increased suddenly to very large values when the final slip surface formed completely. This sudden post-failure acceleration of deformation suggests that the in-situ monitoring of deformation may not be useful to anticipate the dam failure, which has also been demonstrated in the delayed collapse in stiff clays (Potts et al. 1997).

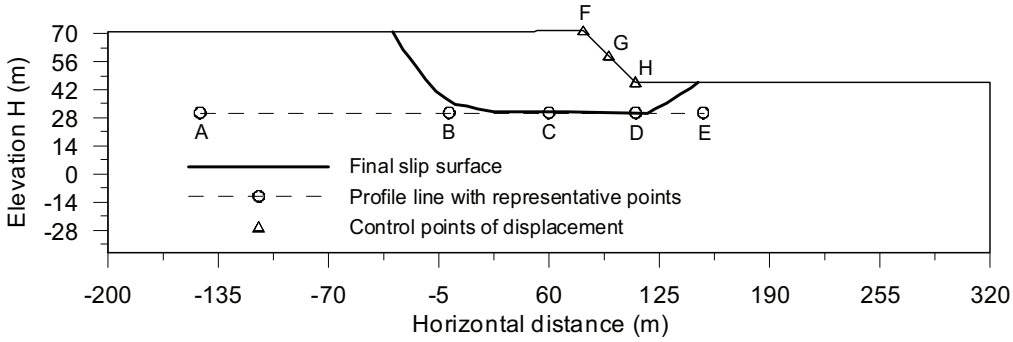

Fig. 6.43 Location of slip surface and representative points

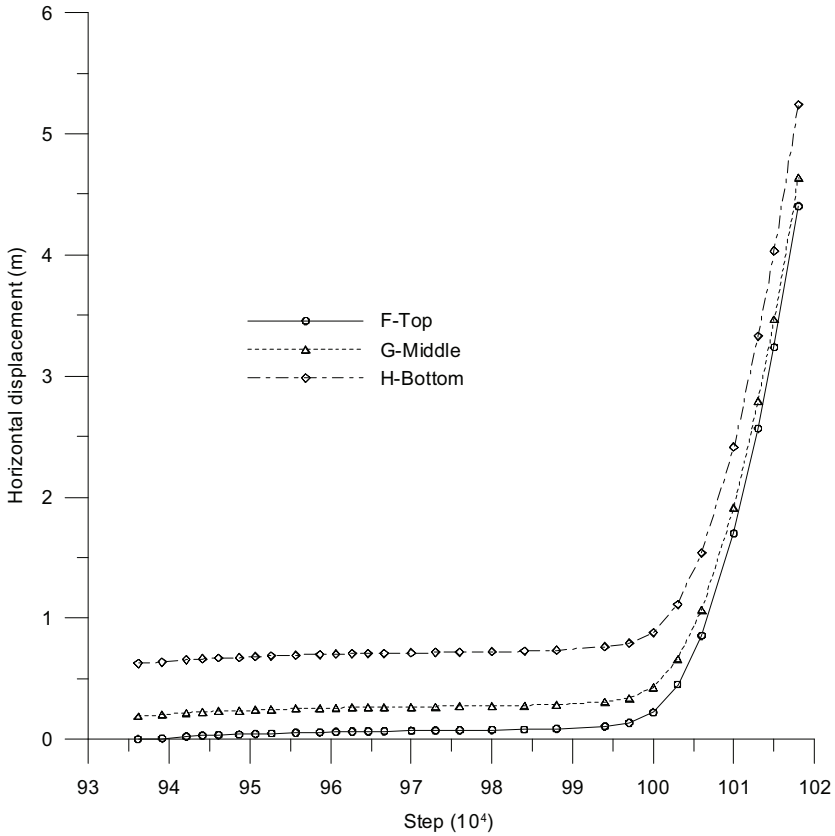

Fig. 6.44 Horizontal displacement development along downstream dam embankment

6.5.3.9 Representative model results along profile A-E

Fig. 6.43 also shows the location of a profile A-E. The five points A-E under the upstream embankment, the embankment body and the downstream embankment are the same as those examined by Gens and Alonso (2006). The development of pore pressure at points (A-E) is illustrated in Fig. 6.45 and exhibits a similar tendency as that presented by Gens and Alonso (2006). This figure also reveals the very limited dissipation of pore water pressure that took place during construction because of the very low permeability of the clay foundation. The magnitude of the pore water pressure development is mainly controlled by the weight above each point.

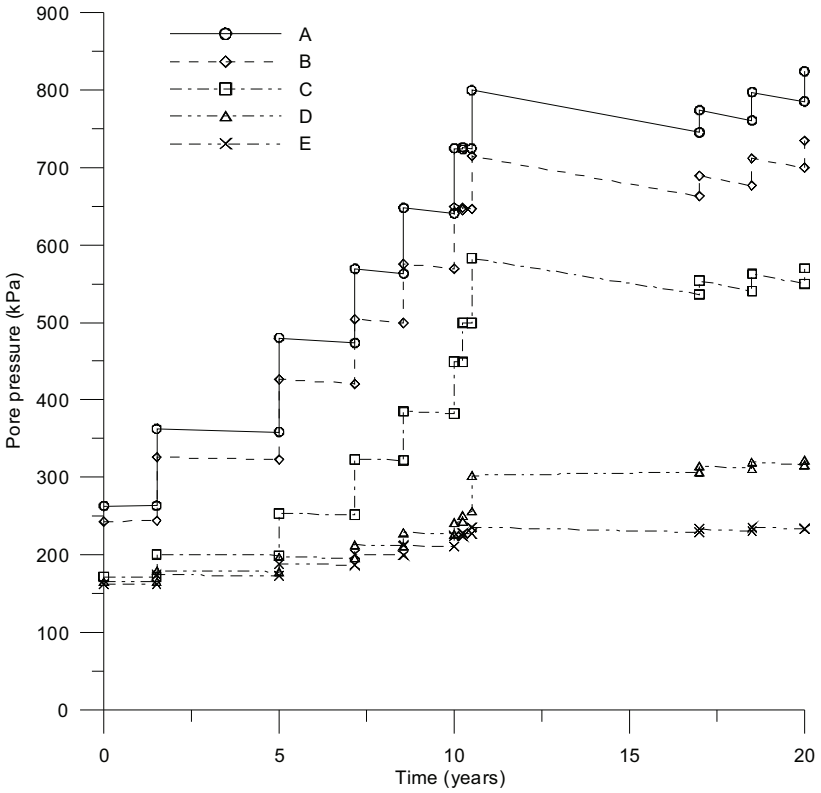

Fig. 6.45 Development of pore pressure at points (A-E) along profile ABCDE

Fig. 6.46 shows the distribution of pore pressure just at failure along profile A-E. In this figure the results calculated by *FEM* and simplified elastic-consolidation analyses are also given (Gens & Alonso 2006). The comparison indicates that the prediction with the present model agrees well with those results.

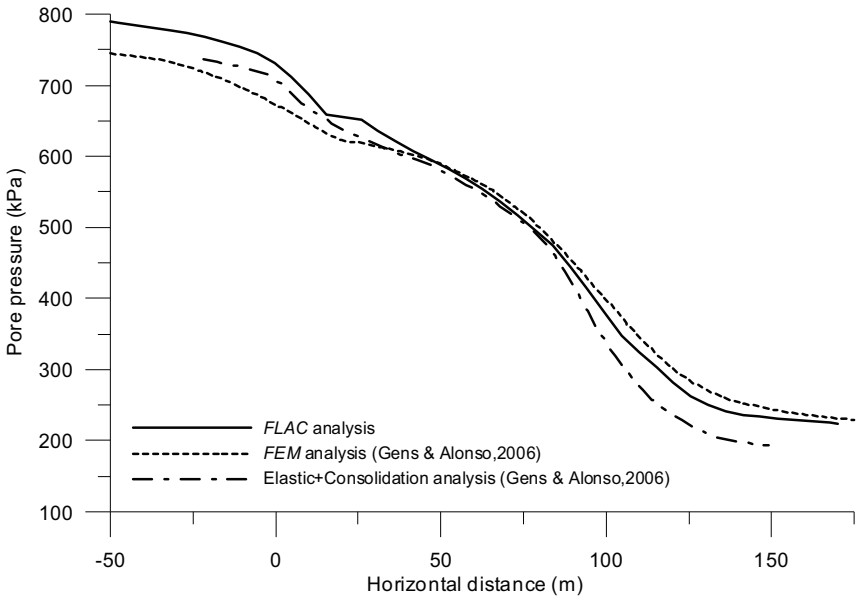

Fig. 6.46 Distribution of pore pressure just at failure along profile A-E at elevation=30.5: comparison of the present model, *FEM* and simplified elastic-consolidation analyses

Fig. 6.47 shows the evolution of post-failure of pore pressure distribution along profile A-E. It can be seen that there is an obvious change of pore pressure distribution along profile A-E at locations beneath the upstream toe and downstream toe.

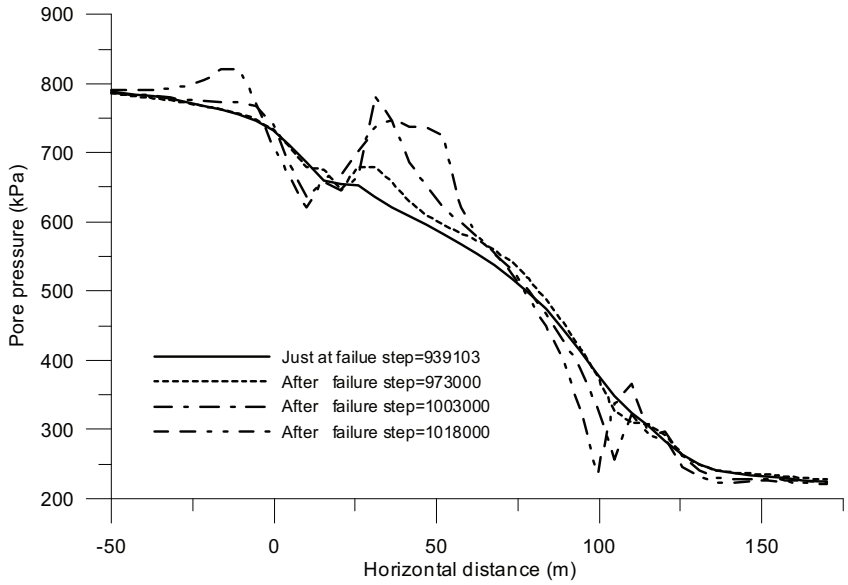

Fig. 6.47 Post-failure evolution of pore pressure distribution along profile A-E

6.5.3.10 Representative model results along slip surface

Besides the descriptive results along profile A-E, the typical behaviour along the slip surface is also necessary to demonstrate the progressive failure process. Fig. 6.48 shows the locations of representative points I-P along slip surface.

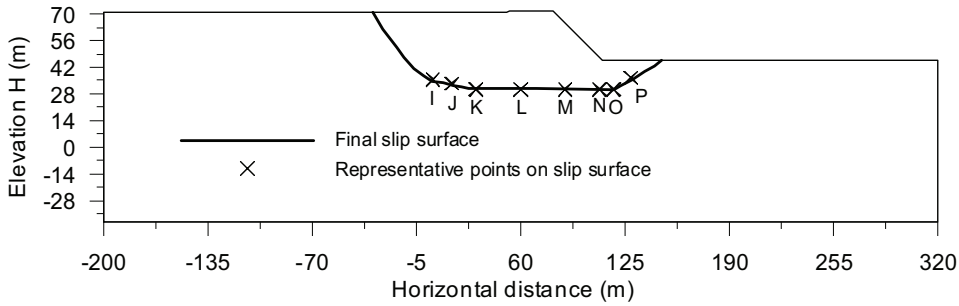

Fig. 6.48 Representative points I-P along slip surface

6.5.3.10.1 Development of deformation and pore pressure of points I-P

Fig. 6.49 presents the development of horizontal displacements of points I-P. The increase of horizontal displacement corresponds to the staged loading of dam and tailings.

Fig. 6.50 shows the development of pore water pressure of points I-P exhibiting a similar development tendency and indicates the very limited dissipation of pore water pressure as shown in Fig. 6.45 and in Gens and Alonso (2006). The magnitude of the pore water pressure development is in accordance with the added weight above the points I-P.

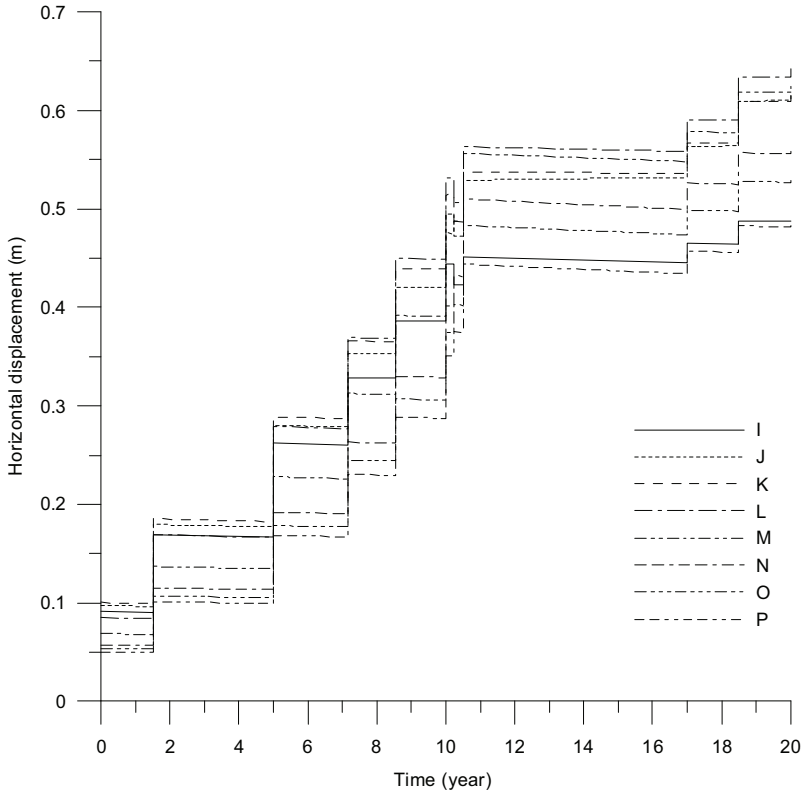

Fig. 6.49 Development of horizontal displacements of points I-P

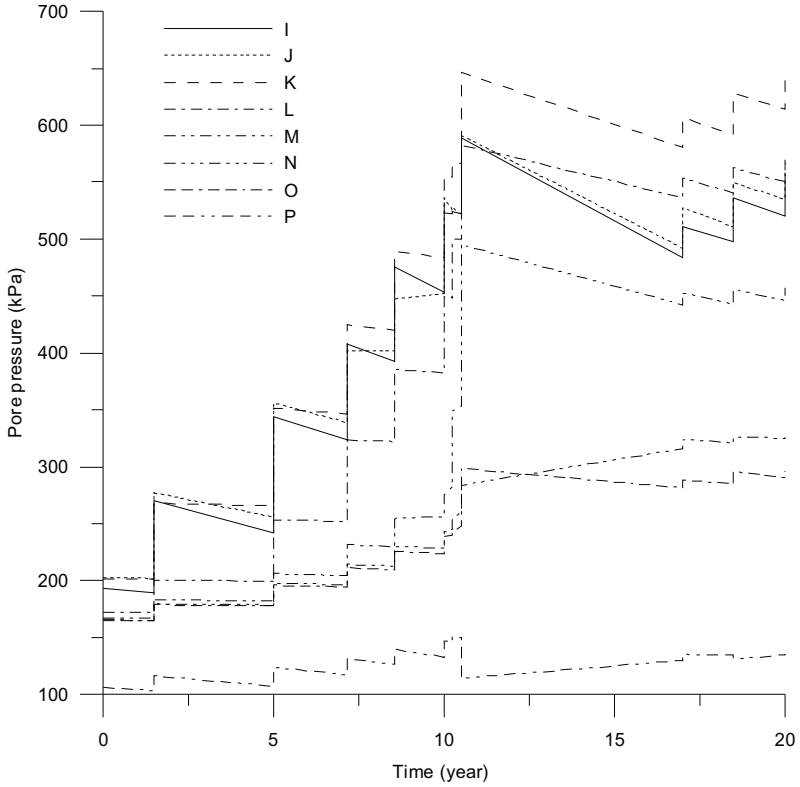

Fig. 6.50 Development of pore water pressure of points I-P

6.5.3.10.2 Indication of initial and final failure

The developments of horizontal velocity and shear strain rate of points I-P till failure (step=939103) are shown in Fig. 6.51 and Fig. 6.52. The initiation of failure is clearly demonstrated by the sudden increase of both horizontal velocity and shear strain rate.

Fig. 6.53 shows the development of shear strain increment of points I-P till final failure (step=1018000). It can be seen that the shear strain increment did not accelerate just at failure (step=939103) but increased rapidly from step=1013000. This is consistent with Fig. 6.44 and Fig. 6.35.

Fig. 6.49-Fig. 6.53 imply that the velocity and shear strain rate can capture the initiation of failure whereas the displacement and shear strain increment could be used to indicate final failure with the complete formation of slip surface. This view can also be noted in Fig. 6.29-Fig. 6.32 and Fig. 6.37-Fig. 6.39.

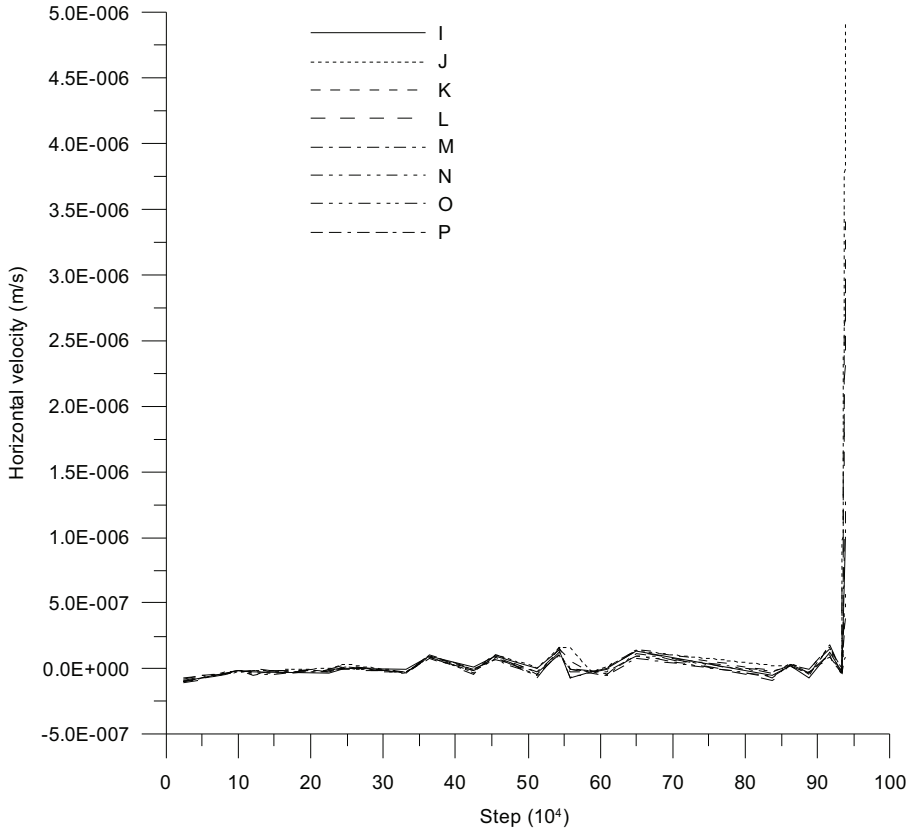

Fig. 6.51 Development of horizontal velocity of points I-P till failure (step=939103)

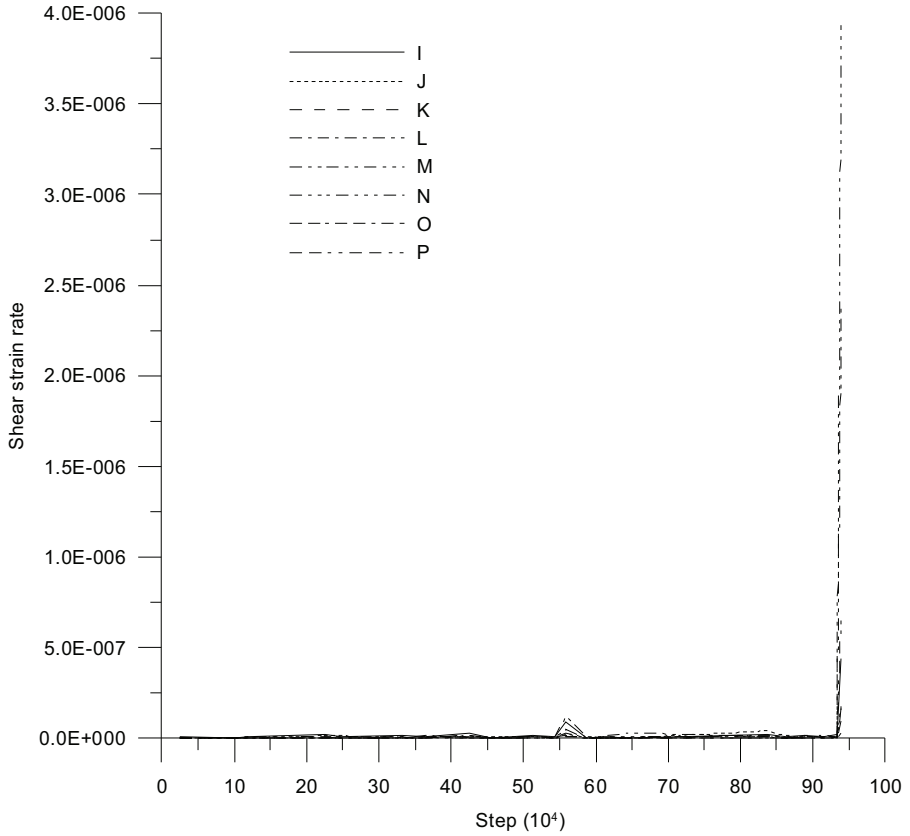

Fig. 6.52 Development of shear strain rate of points I-P till failure (step=939103)

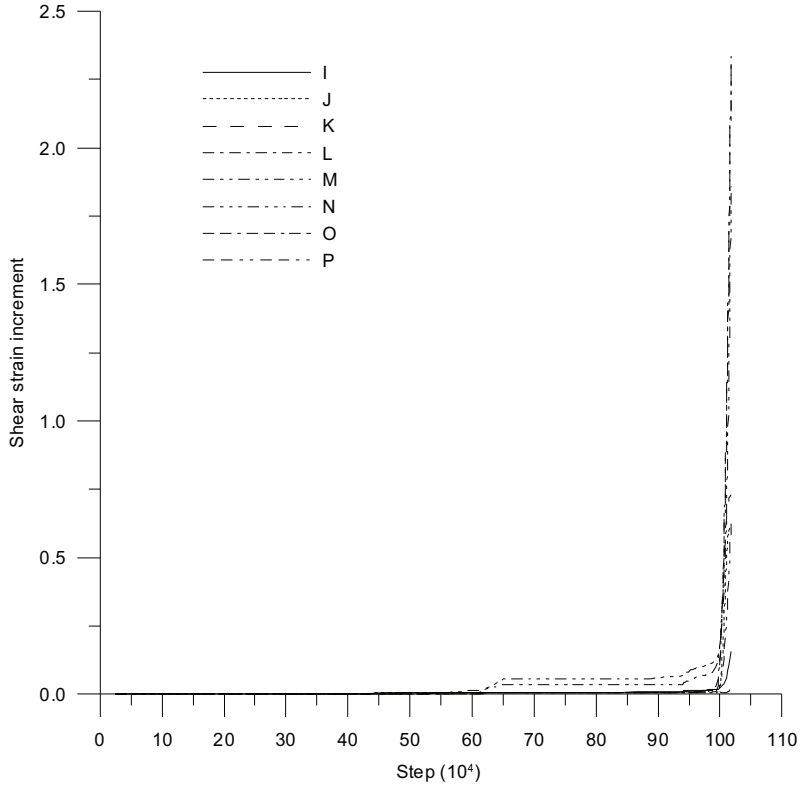

Fig. 6.53 Development of shear strain increment of points I-P till final failure

6.5.3.10.3 Stress path and variation of strength parameters at points I-P

Fig. 6.54-Fig. 6.61 show the stress paths of points I-P along slip surface. The softening model with peak, post-rupture and residual strength parameters for clay mass (Table 6.6) is operational at points I, J and P, whereas the softening model with only post-rupture and residual strength parameters for the weak clay layer (Table 6.7) is used at points K, L, M, N and O. In this case, the post-rupture strength is in fact the peak strength.

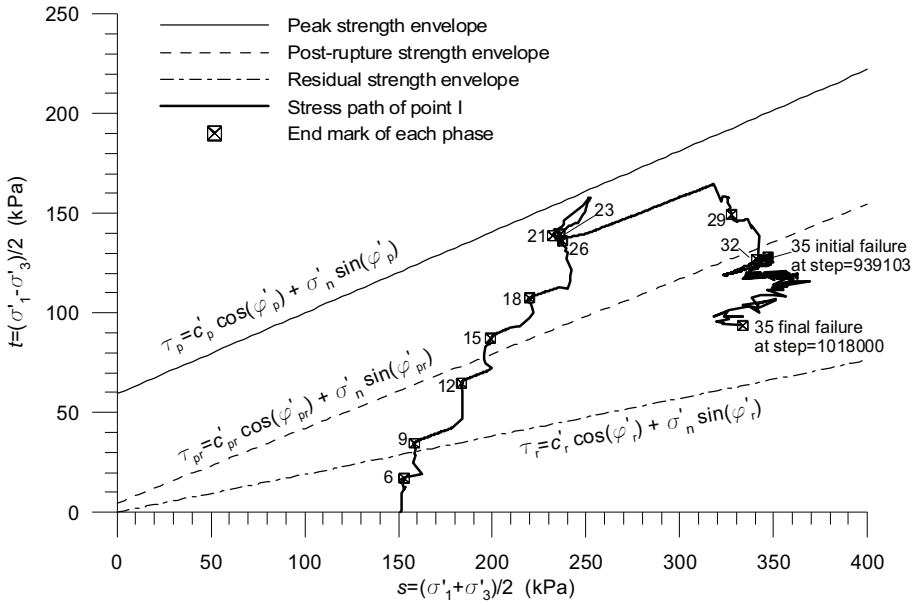

Fig. 6.54 Stress path of point I

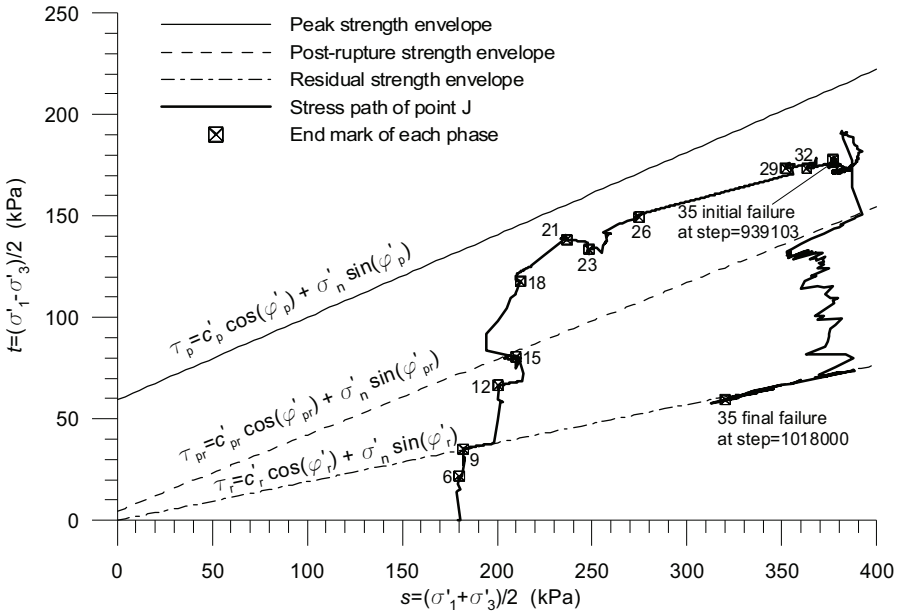

Fig. 6.55 Stress path of point J

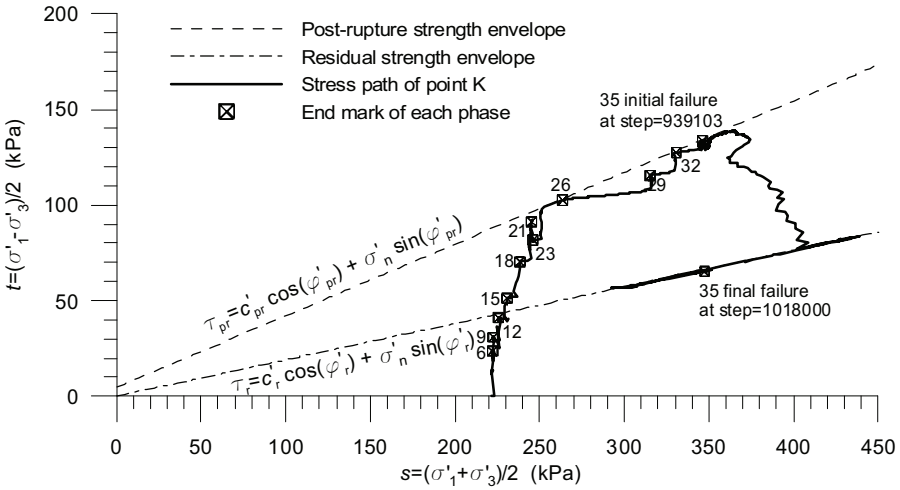

Fig. 6.56 Stress path of point K

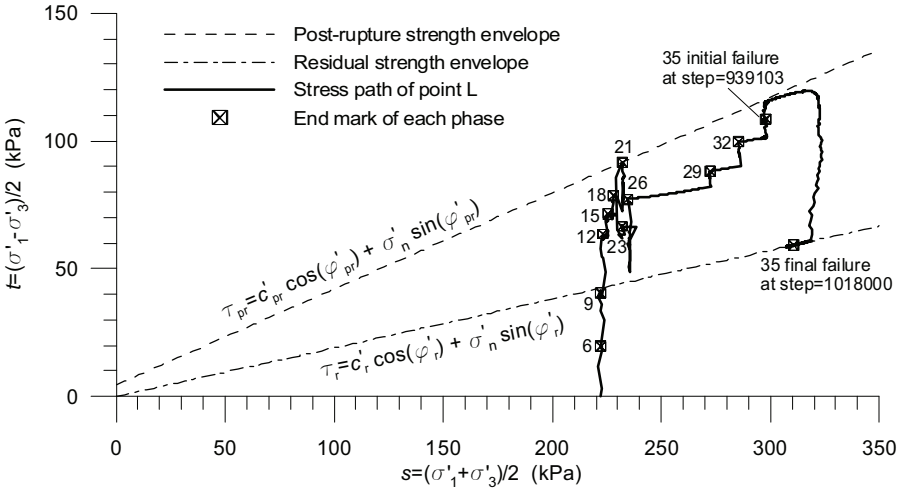

Fig. 6.57 Stress path of point L

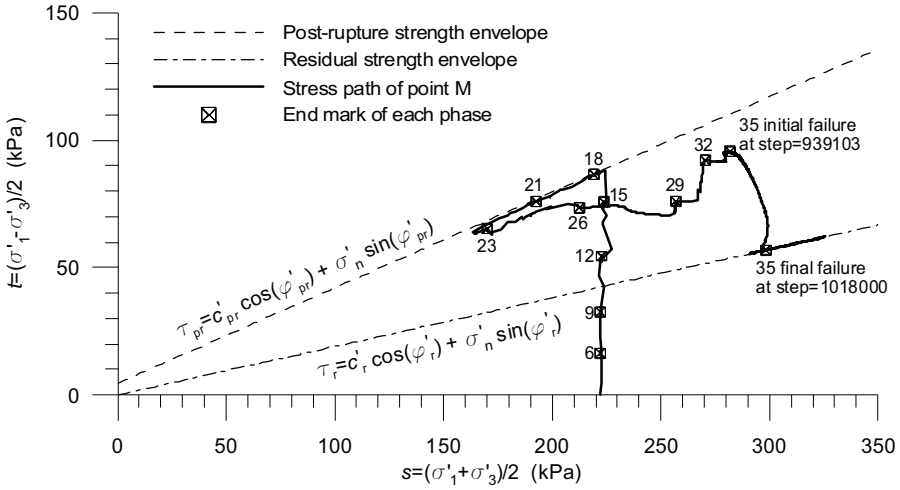

Fig. 6.58 Stress path of point M

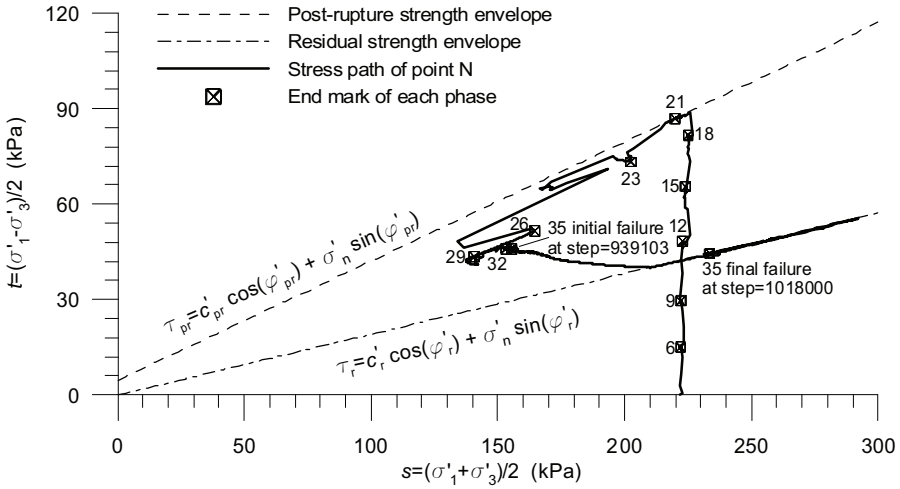

Fig. 6.59 Stress path of point N

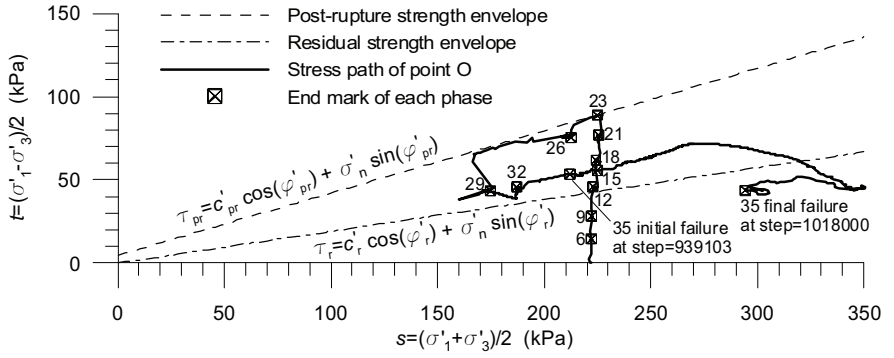

Fig. 6.60 Stress path of point O

At point I, the stress point firstly rises to nearly the peak envelope, then decreases to the post-rupture envelope at failure and afterwards reaches a stress state between the post-rupture and the residual envelopes at final failure. However, the final stress state at point P is close to the residual envelope and at point J it has arrived at residual envelope. These can also be confirmed further by observing Fig. 6.62, Fig. 6.63, Fig. 6.69, Fig. 6.70, Fig. 6.71 and Fig. 6.77.

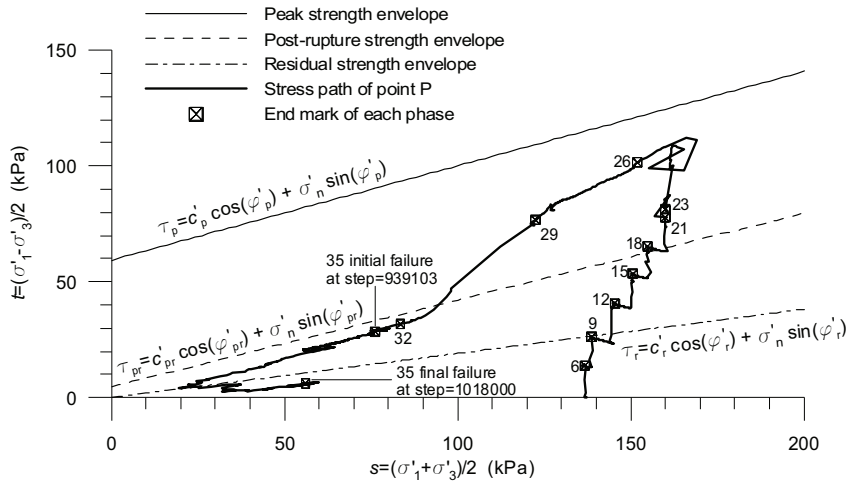

Fig. 6.61 Stress path of point P

The initial strength at points K, L, M, N and O is equal to the post-rupture strength. Fig. 6.56-Fig. 6.60 demonstrate that the stress states at points K, L, M, N and O at first get to the post-rupture envelope and afterwards lie on the residual envelope at final failure state except that the final stress point is below residual envelope at point O. This can be explained clearly in Fig. 6.64-Fig. 6.68 and Fig. 6.72-Fig. 6.76. The corresponding values of cohesion and friction angle at points K, L, M, N and O have all mobilised to residual values at final failure.

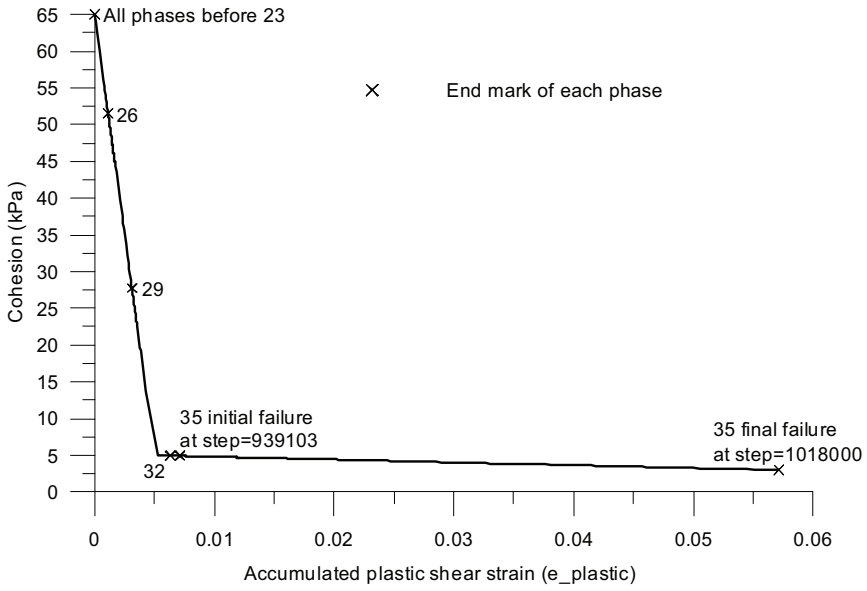

Fig. 6.62 Cohesion variation with e_plastic of point I

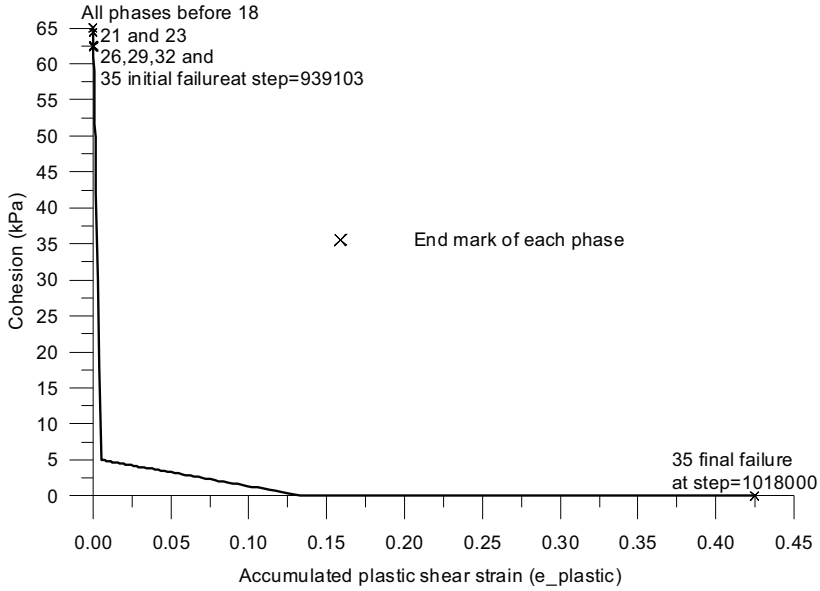

Fig. 6.63 Cohesion variation with e_plastic of point J

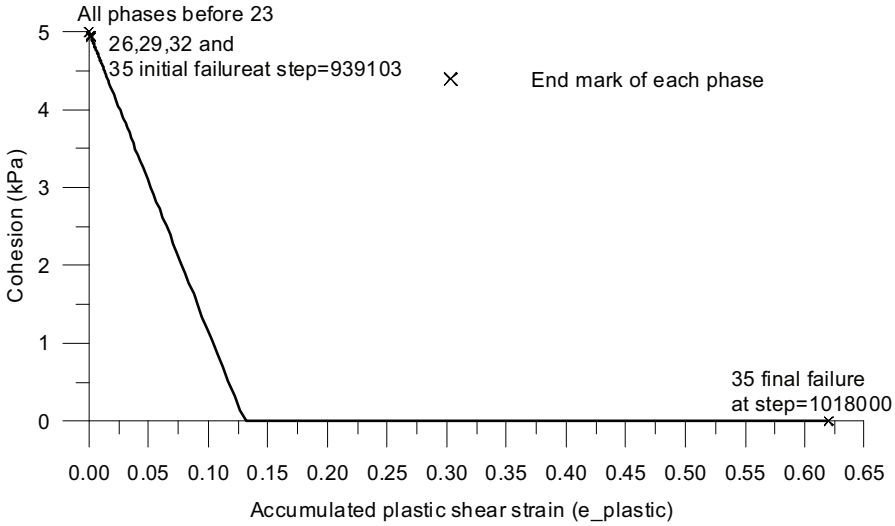

Fig. 6.64 Cohesion variation with e_plastic of point K

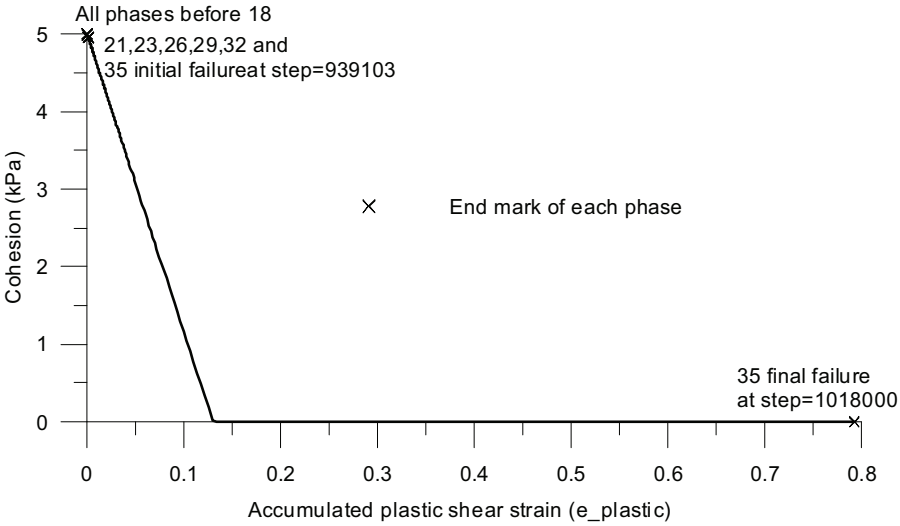

Fig. 6.65 Cohesion variation with e_plastic of point L

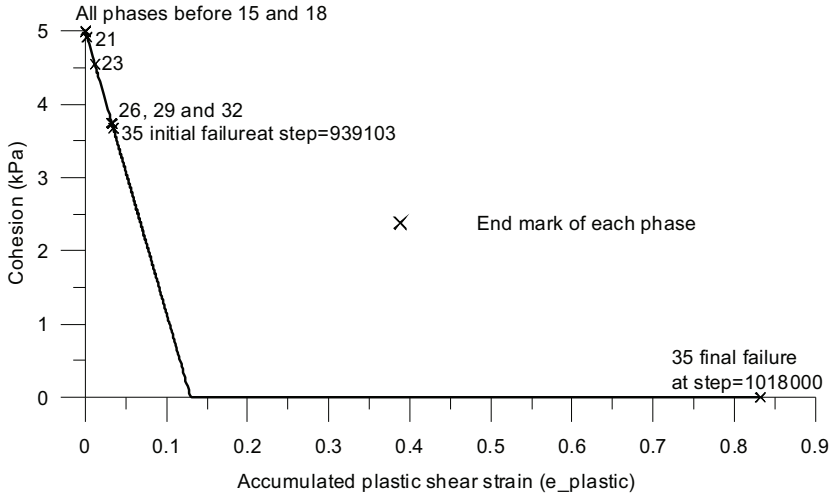

Fig. 6.66 Cohesion variation with e_plastic of point M

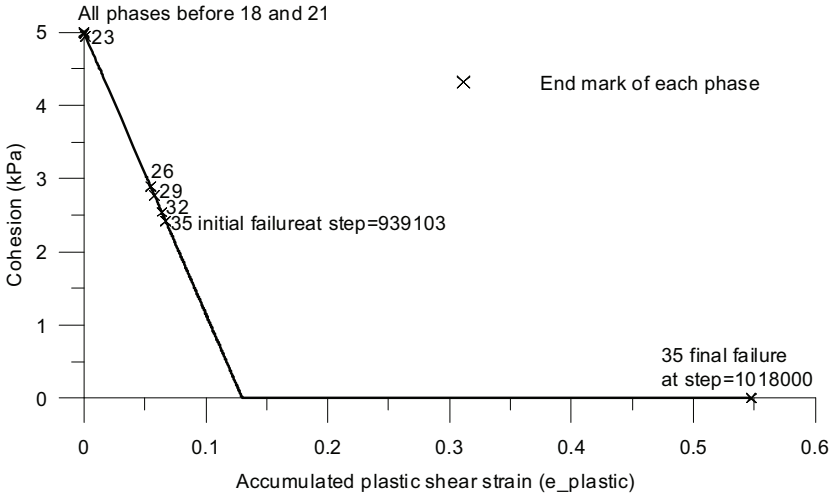

Fig. 6.67 Cohesion variation with e_plastic of point N

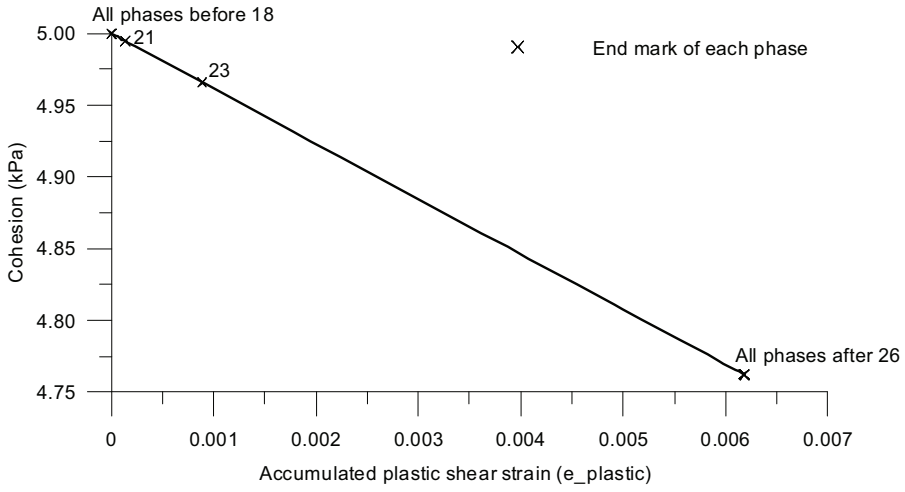

Fig. 6.68 Cohesion variation with e_plastic of point O

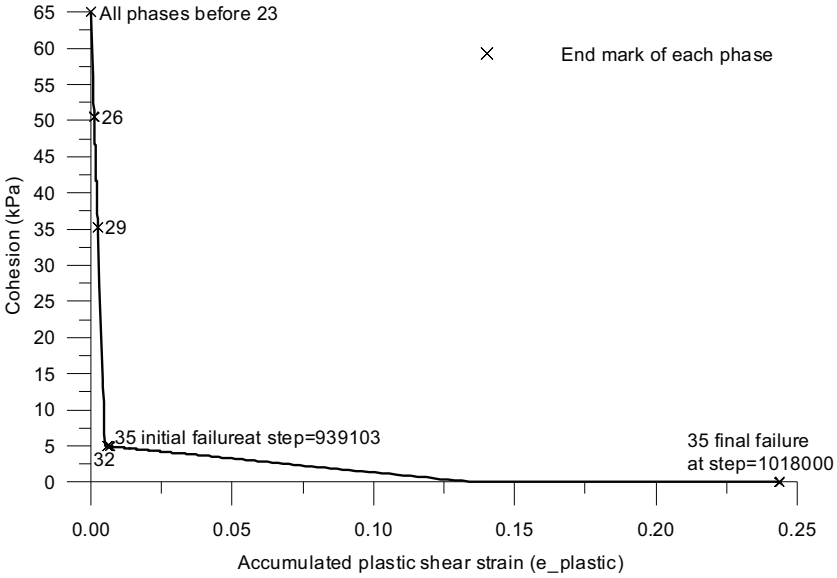

Fig. 6.69 Cohesion variation with e_plastic of point P

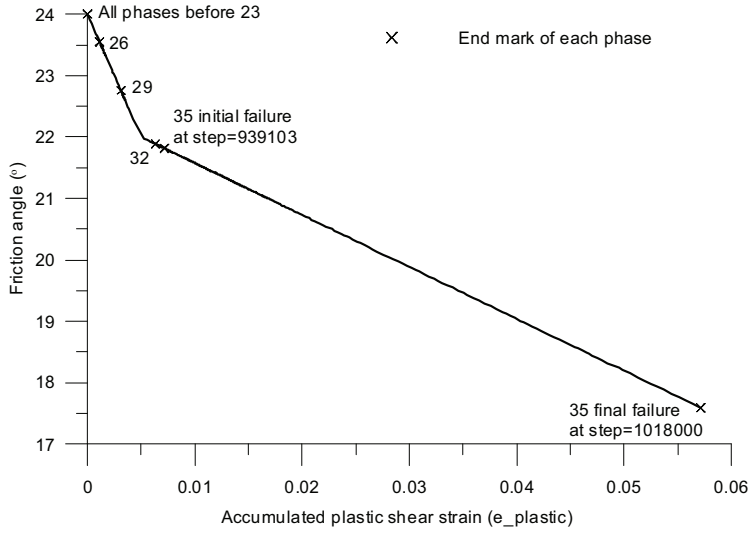

Fig. 6.70 Variation of friction angle with e_plastic of point I

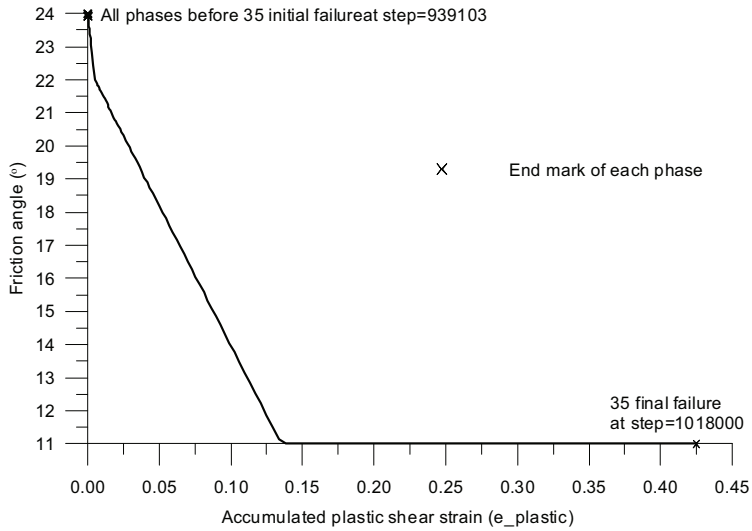

Fig. 6.71 Variation of friction angle with e_plastic of point J

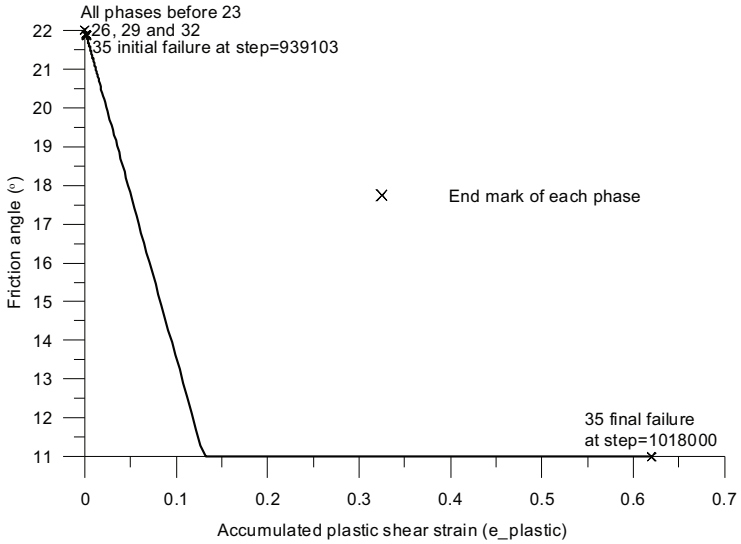

Fig. 6.72 Variation of friction angle with e_plastic of point K

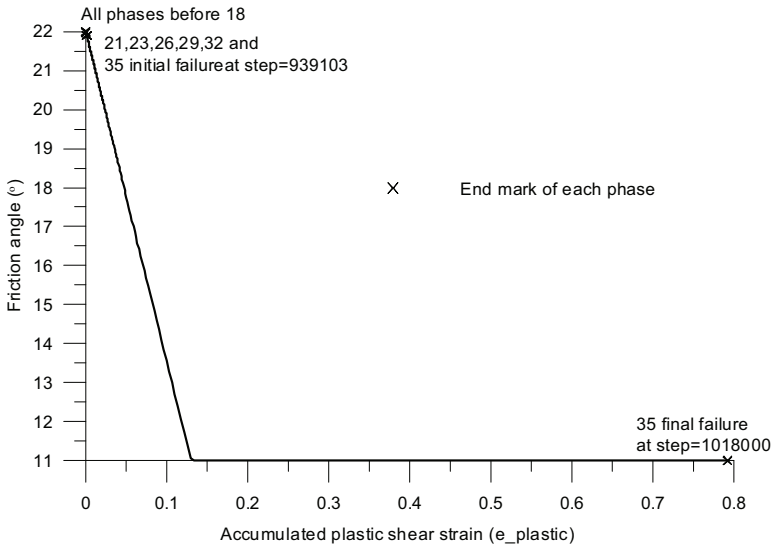

Fig. 6.73 Variation of friction angle with e_plastic of point L

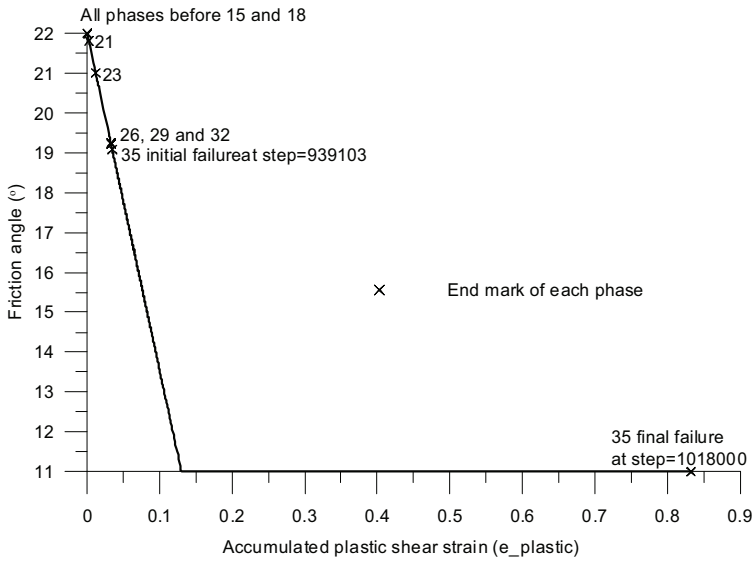

Fig. 6.74 Variation of friction angle with e_plastic of point M

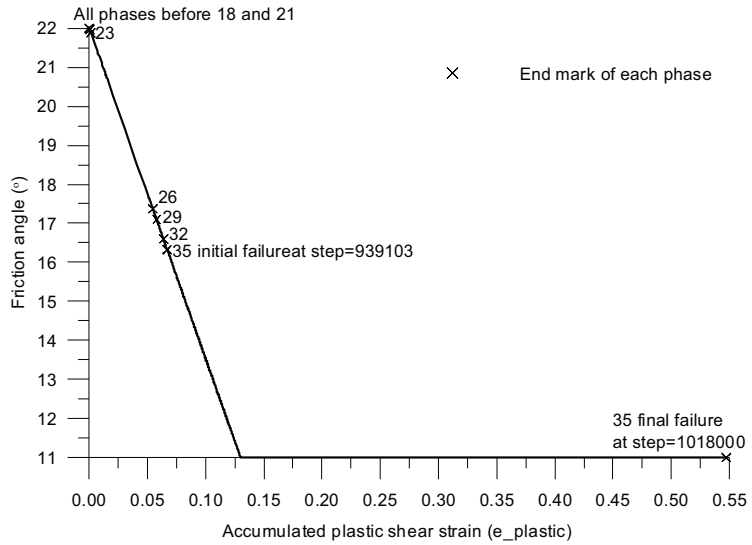

Fig. 6.75 Variation of friction angle with e_plastic of point N

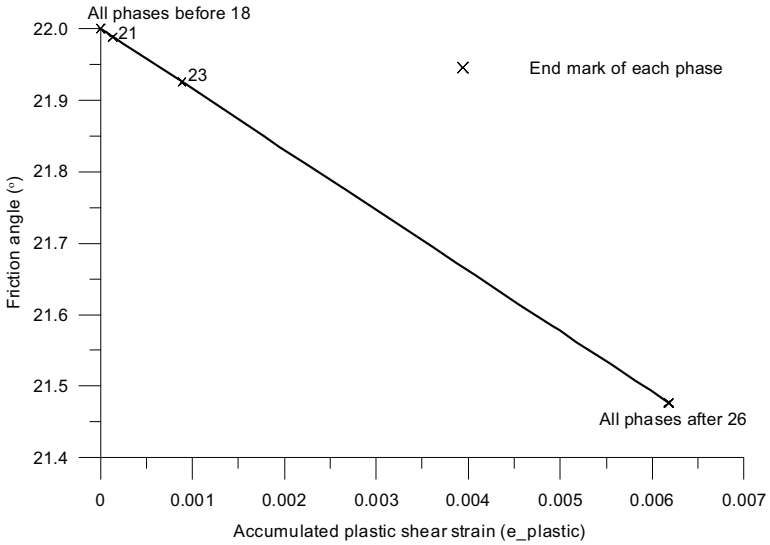

Fig. 6.76 Variation of friction angle with e_plastic of point O

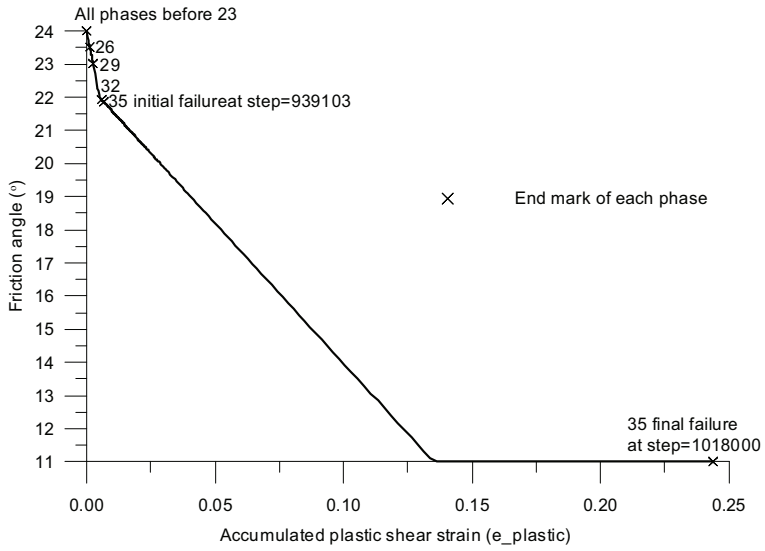

Fig. 6.77 Variation of friction angle with e_plastic of point P

6.5.3.10.4 Development of shear stress, horizontal displacement, residual factor and brittleness index with shear strain at representative points—J, L, N and P

Fig. 6.78-Fig. 6.81 show the curves of shear stress versus shear strain at points J, L, N and P. The shear stress increased firstly and then decreased till residual value. At points J and P, the decrease of shear stress exhibited a two-stage softening feature. At initial failure (step=939103), shear stress at point J was close to the peak value (Fig. 6.78) whereas at point P it arrived approximately at post-rupture value (Fig. 6.79). At points L and N, only one-stage softening of shear stress occurred although the curve at point N is wavy. It is evident that at initial failure the shear stress at point L reached almost peak value (Fig. 6.80) while the value at point P has arrived at residual value (Fig. 6.81).

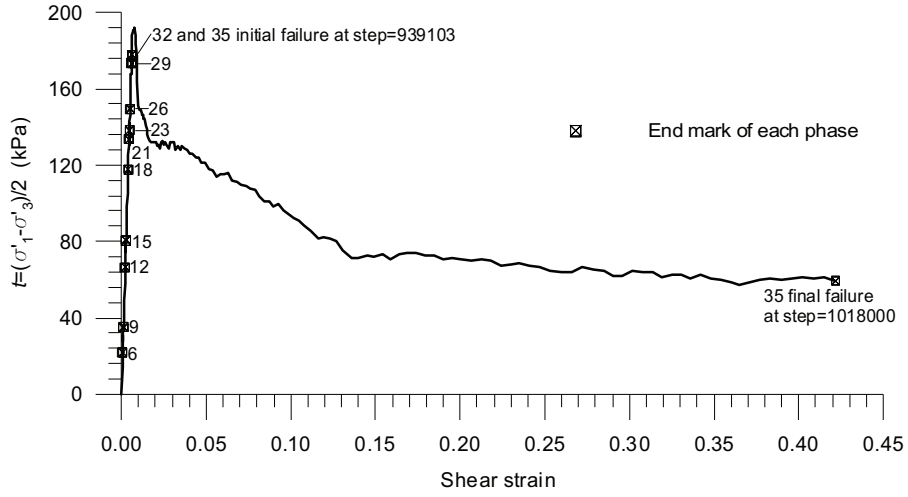

Fig. 6.78 Shear stress vs. shear strain at point J

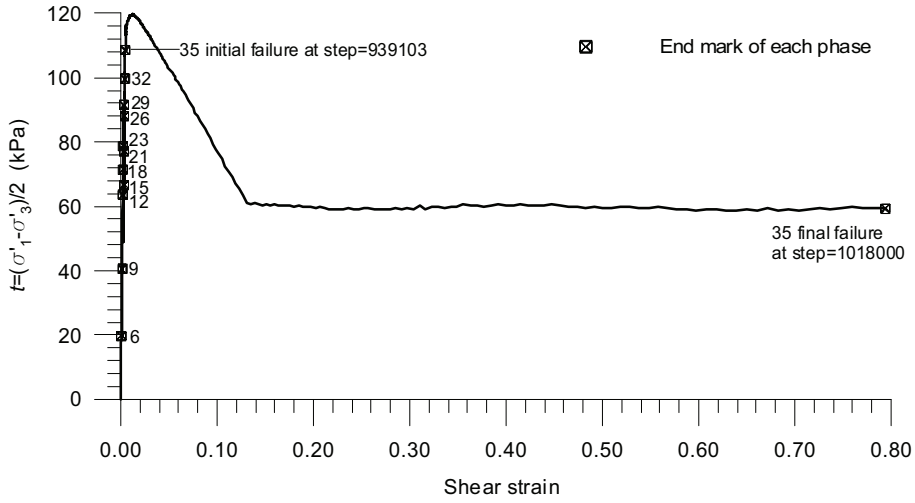

Fig. 6.79 Shear stress vs. shear strain at point L

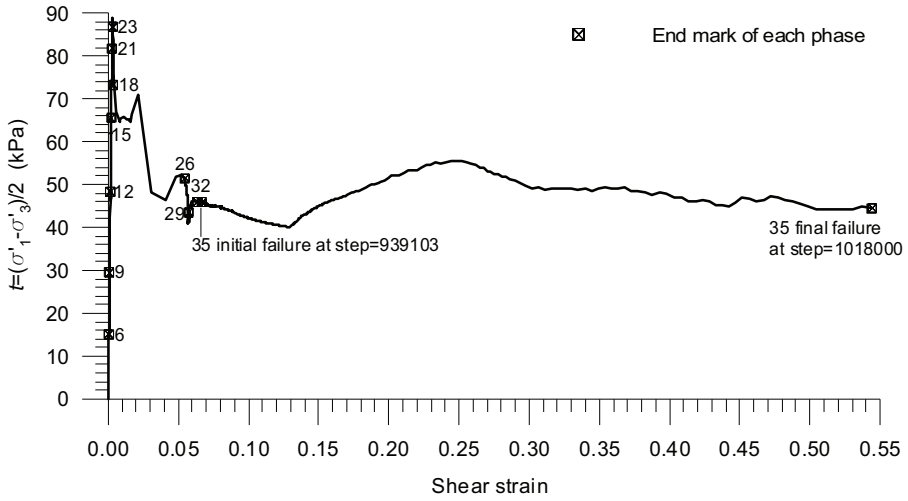

Fig. 6.80 Shear stress vs. shear strain at point N

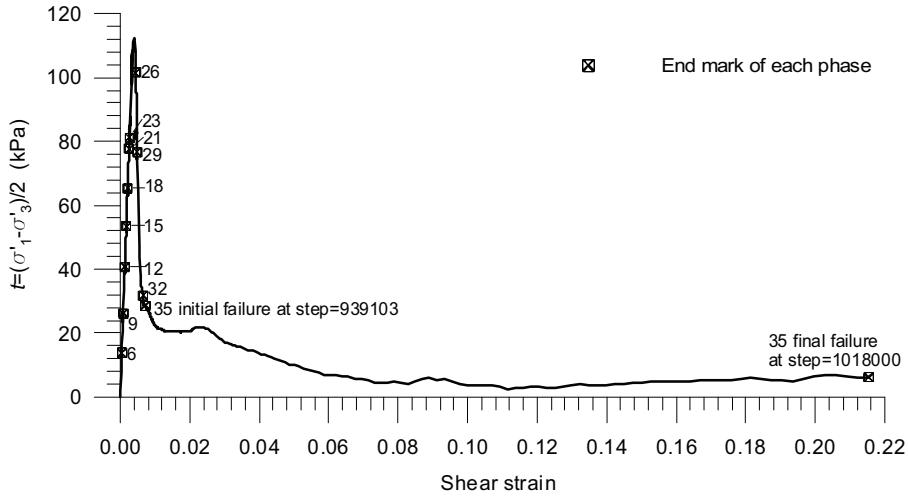

Fig. 6.81 Shear stress vs. shear strain at point P

Fig. 6.82-Fig. 6.85 show the curves of horizontal displacement versus shear strain at points J, L, N and P. As failure initiated and developed, horizontal displacement reached a constant value with shear strain at points J, L, N and P.

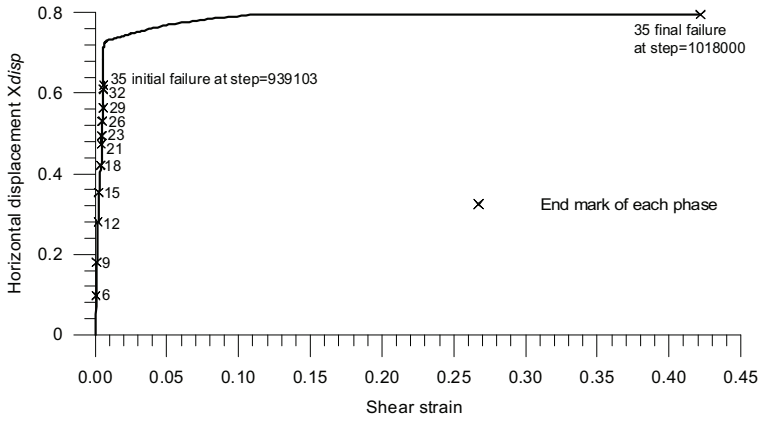

Fig. 6.82 Horizontal displacement vs. shear strain at point J

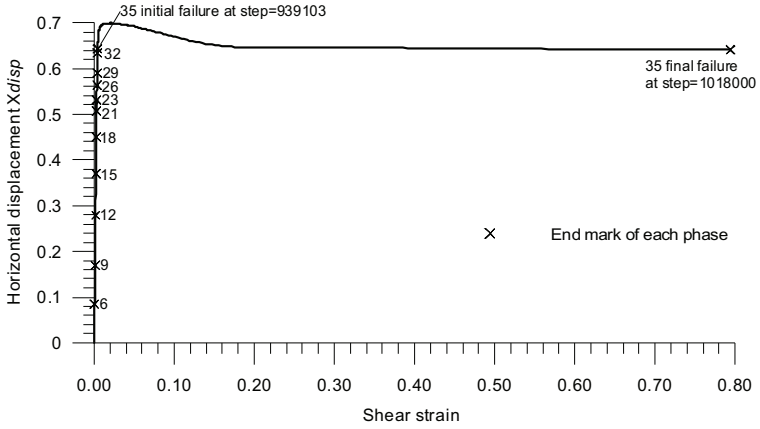

Fig. 6.83 Horizontal displacement vs. shear strain at point L

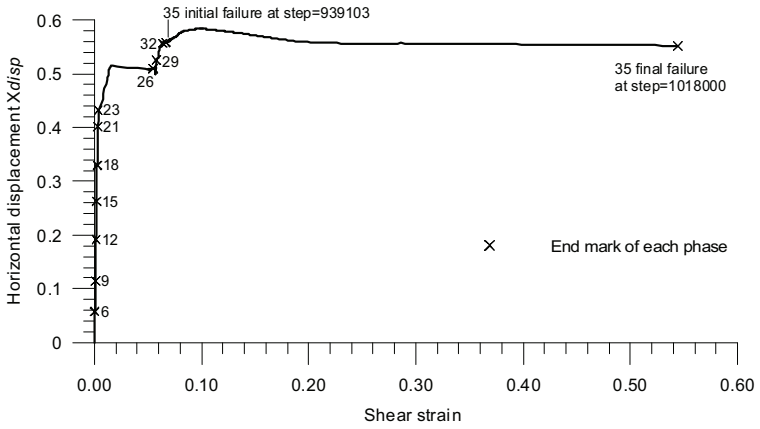

Fig. 6.84 Horizontal displacement vs. shear strain at point N

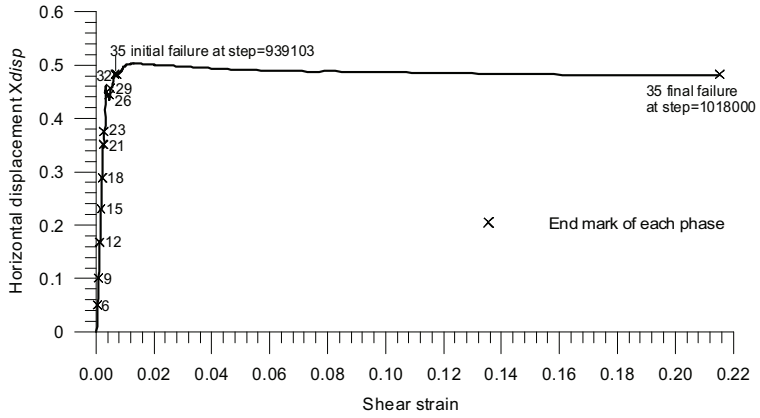

Fig. 6.85 Horizontal displacement vs. shear strain at point P

Fig. 6.86-Fig. 6.89 and Fig. 6.90-Fig. 6.93 show the evolution of both residual factor R and brittleness index IB with shear strain. These figures exhibit similar two-stage softening for points J and P and one-stage softening for points L and N. Especially for point N, the one-stage softening characteristic is much more obvious than that shown in shear stress versus shear strain curve which is wavy.

For points J and P, R initially decreased to a small minimum value and then rose up till residual state. At points L and N, R got to zero and then reached 1.0 at residual state. IB versus shear strain curves exhibit similar tendencies.

In these figures the residual factor and brittleness index is also shown by taking the shear stress equal to the value calculated with post-rupture strength parameters. For points J and P, these values correspond to the post-rupture one whereas they are zero for points L and N with the initial strength equal to the post-rupture strength.

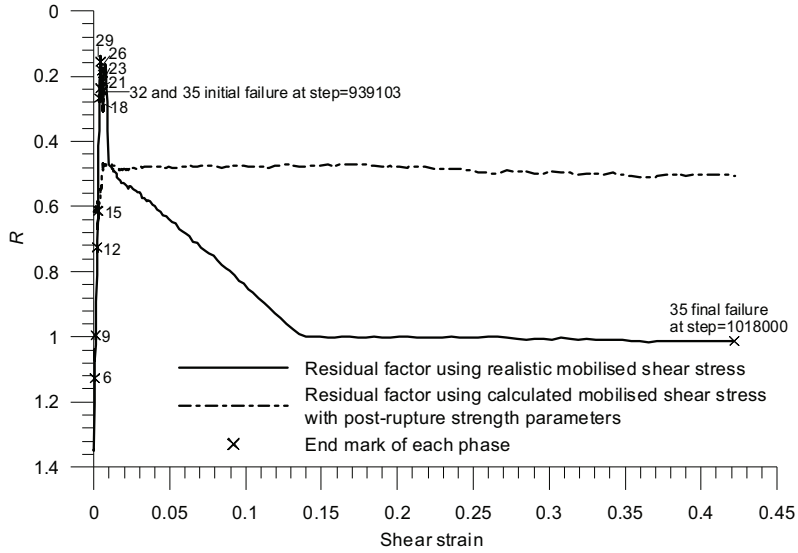

Fig. 6.86 Residual factor vs. shear strain at point J

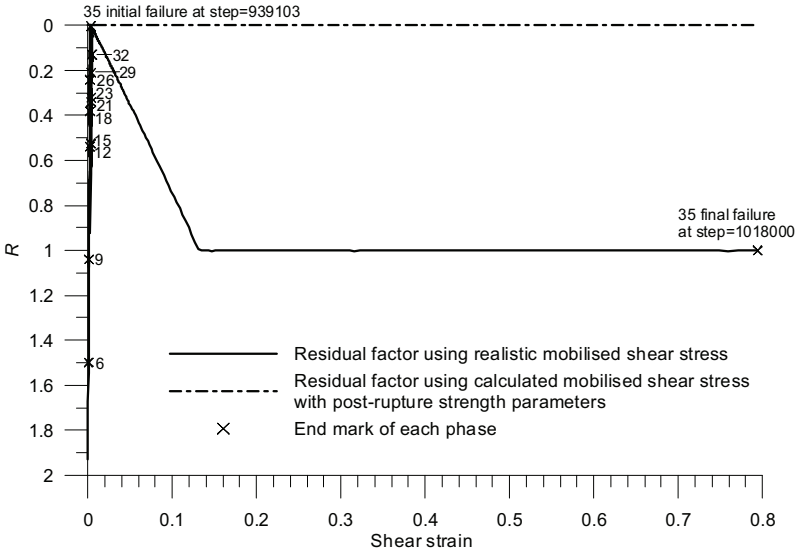

Fig. 6.87 Residual factor vs. shear strain at point L

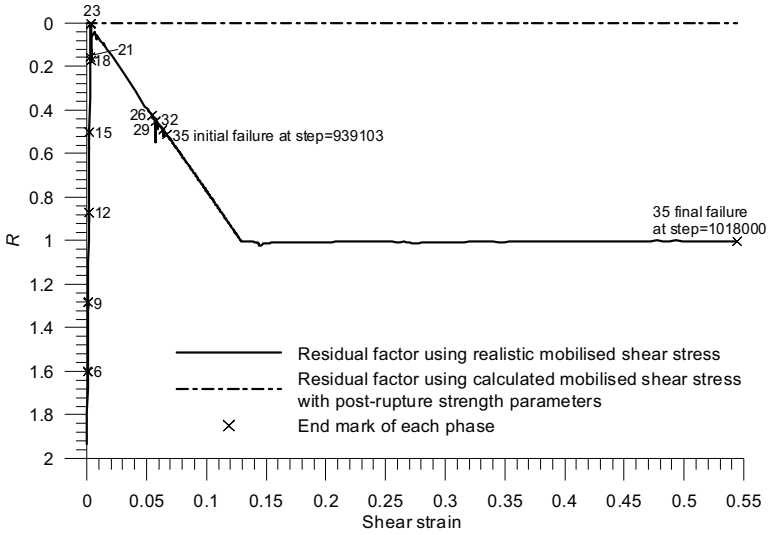

Fig. 6.88 Residual factor vs. shear strain at point N

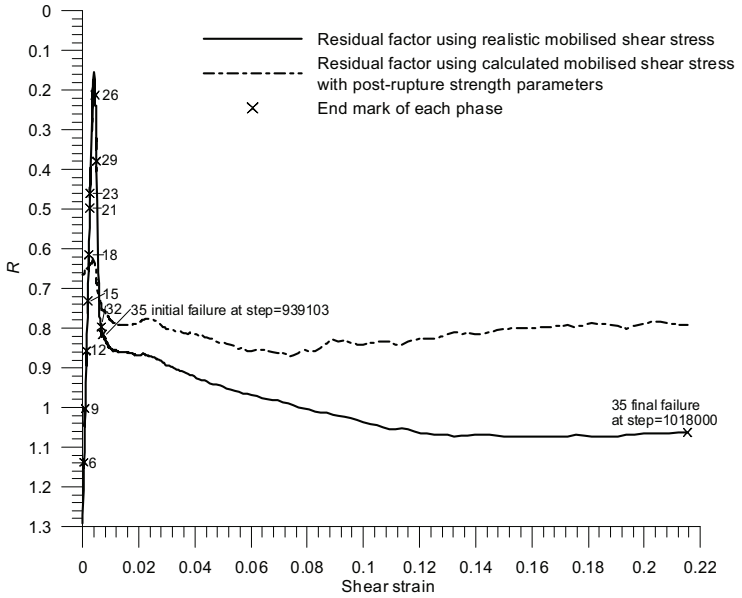

Fig. 6.89 Residual factor vs. shear strain at point P

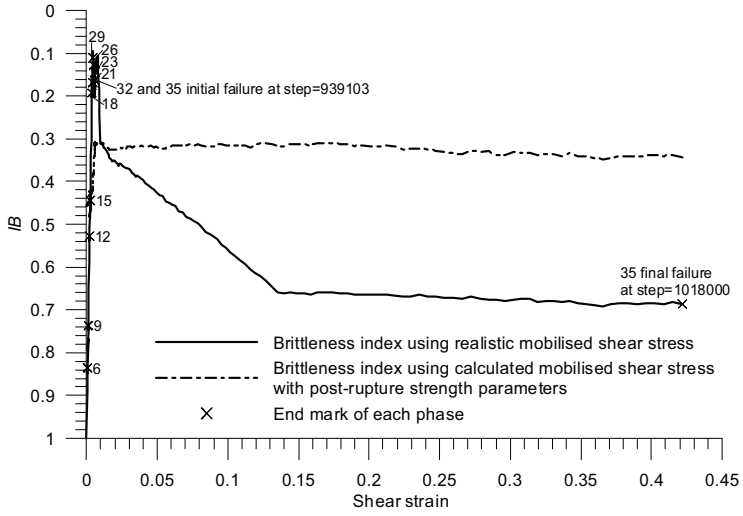

Fig. 6.90 Brittleness index vs. shear strain at point J

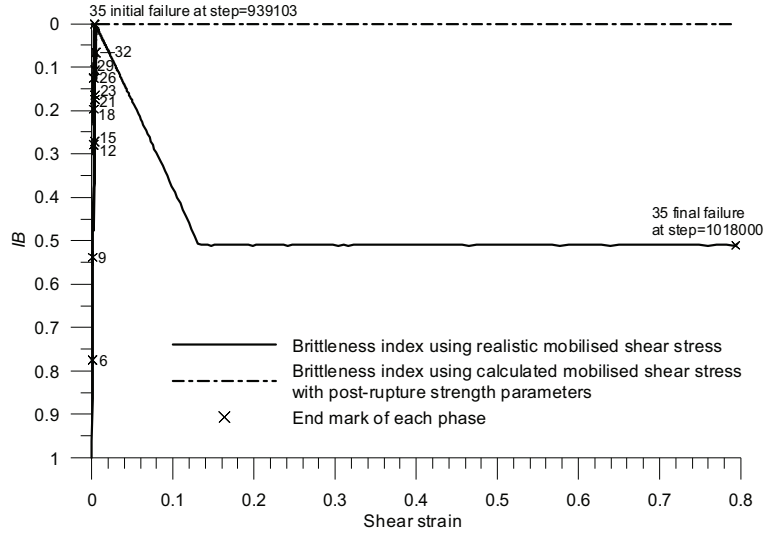

Fig. 6.91 Brittleness index vs. shear strain at point L

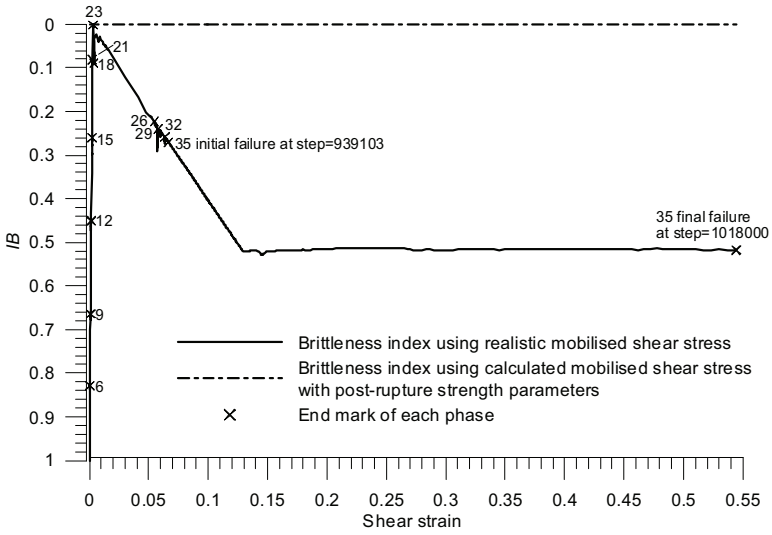

Fig. 6.92 Brittleness index vs. shear strain at point N

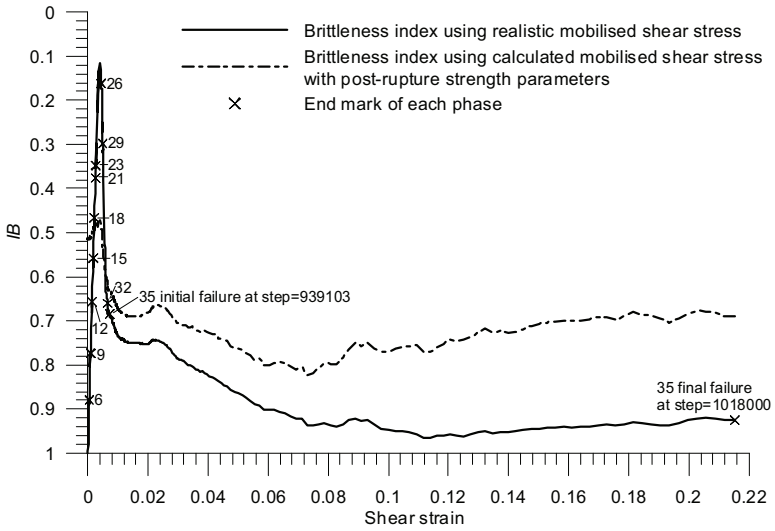

Fig. 6.93 Brittleness index vs. shear strain at point P

6.5.3.10.5 Results along slip surface (I-P) in average sense

Fig. 6.94 shows the pre-failure development of average stress ratio $\tau / \sigma_n^{'}$ along slip surface and Fig. 6.95 presents the pre-failure development of equivalent mobilised friction angle ($\phi = \arctan(\tau / \sigma_n^{'})$). Both figures exhibit an initial increasing part till phase 21 and a stable part from phase 21 to initial failure. The average stress ratio increased from 0.1075 to 0.405. The corresponding values for equivalent mobilised friction angle are about 6.1° and 22.05°.

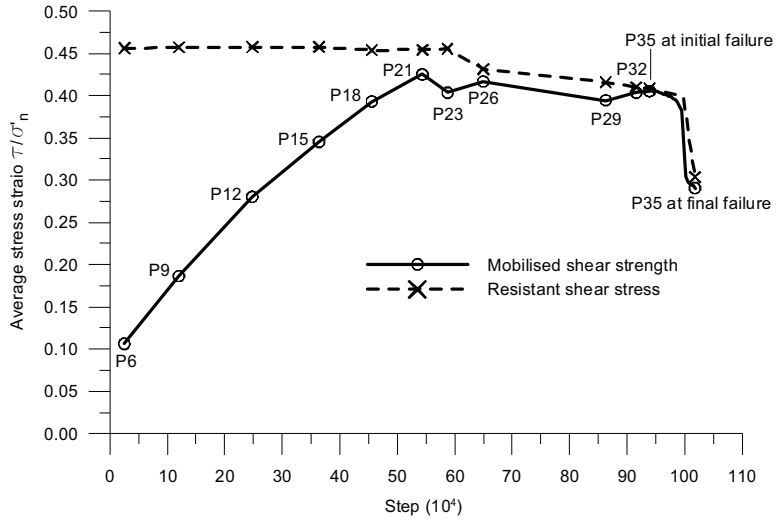

Fig. 6.94 Pre-failure development of average stress ratio along slip surface

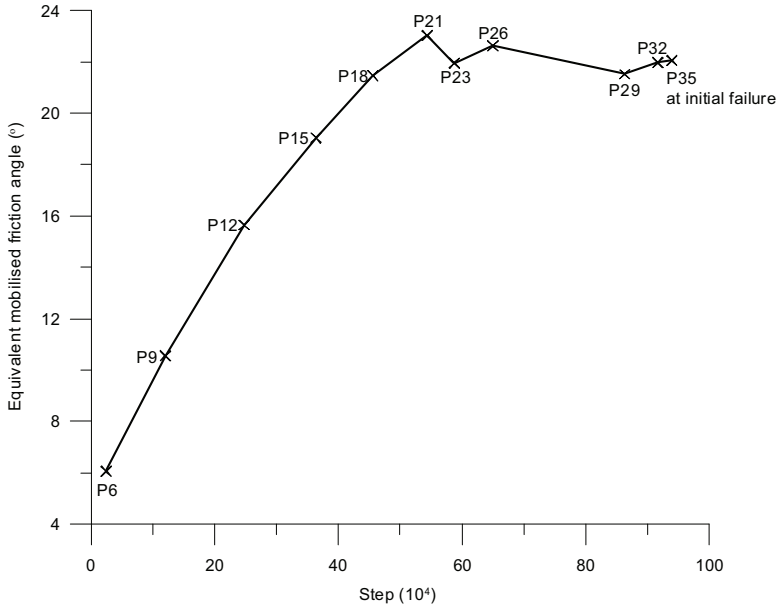

Fig. 6.95 Pre-failure development of equivalent mobilised friction angle

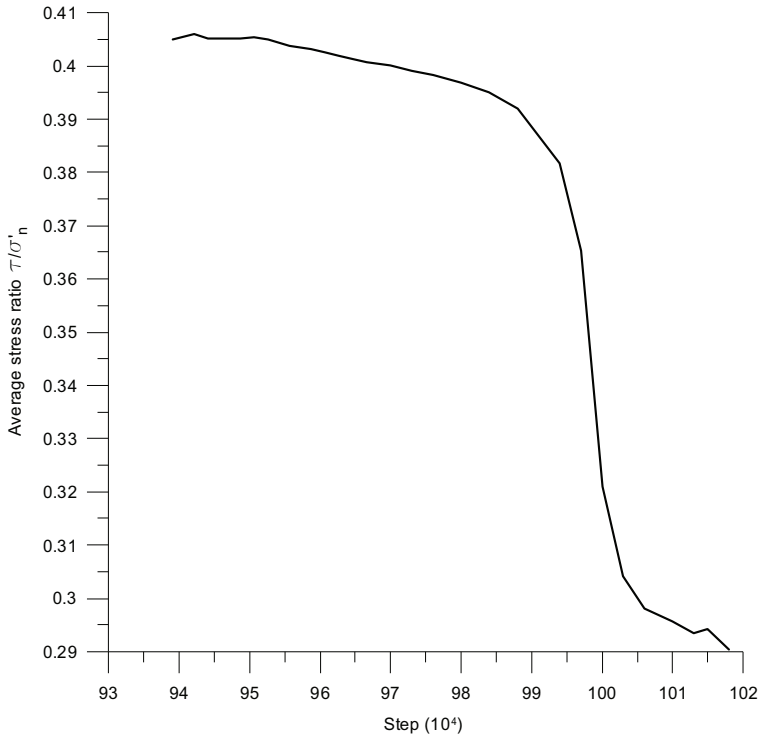

Fig. 6.96 Post-failure development of average stress ratio along slip surface

Fig. 6.96 shows the post-failure development of average stress ratio $\tau / \sigma_n^{'}$ along slip surface and Fig. 6.97 presents the post-failure development of equivalent mobilised friction angle ($\phi = \arctan(\tau / \sigma_n^{'})$). Both figures exhibit a rapid decreasing part from step=997000. The average stress ratio reduced from 0.405 at the beginning of failure (step=939103) to 0.29 at the final failure (step=1018000). The corresponding values for equivalent mobilised friction angle are about 22.05° and 16.2°.

Fig. 6.94 also presents the average mobilised shear strength along the failure surface. It is apparent that the actual resistant shear stress is higher than the mobilised shear strength until reaching phase 35 at initial failure. After that they are almost identical. Fig. 6.94-Fig. 6.97 also indicate that the average stress ratio $\tau / \sigma_n^{'}$ along slip surface and the equivalent mobilised friction angle increased before initial failure and decreased after initial failure till final failure.

Fig. 6.98 shows the pre-failure development of average residual factor defined by Eq. (1.3). The residual factor reduced from 1.15 to 0.51 at initial failure.

Fig. 6.99 shows the post-failure development of average residual factor. The residual factor at initial failure (step=939103) is about 0.51 which agrees with the value of residual factor at failure calculated by Gens and Alonso (2006).

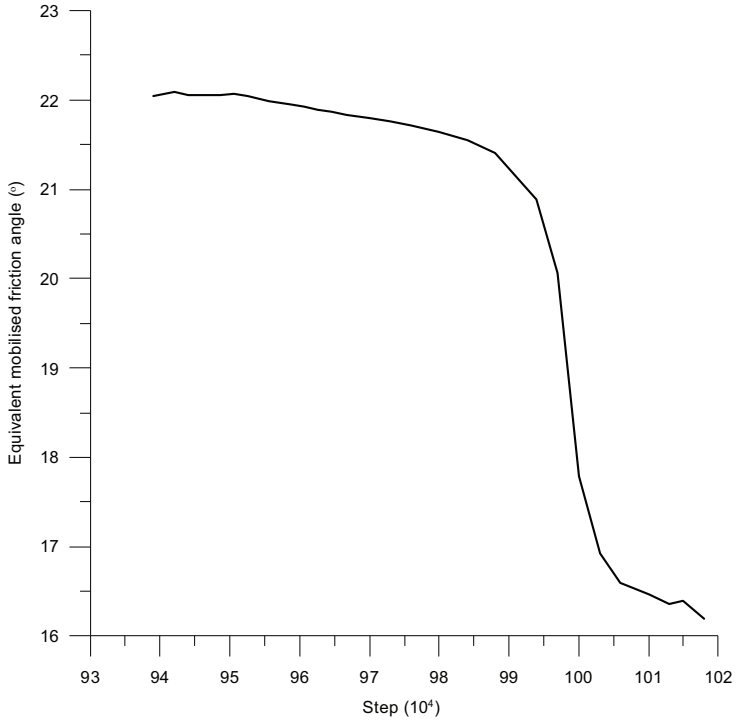

Fig. 6.97 Post-failure development of equivalent mobilised friction angle

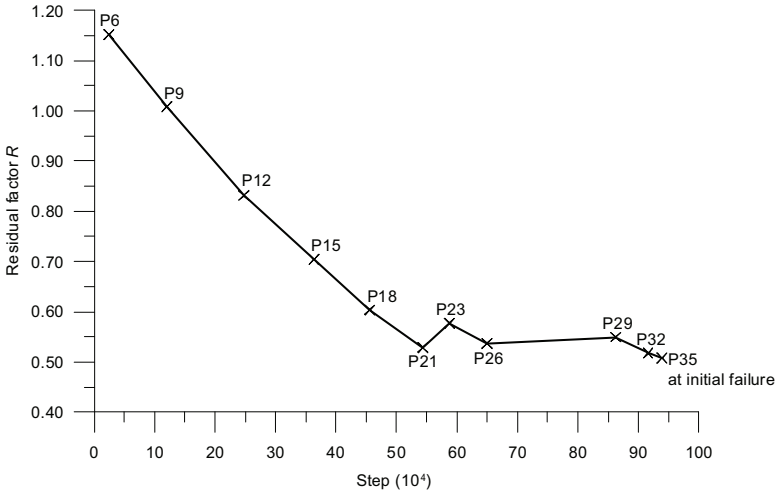

Fig. 6.98 Pre-failure development of average residual factor

Fig. 6.99 also shows the sudden change from step=997000 as indicated by Fig. 6.96 and Fig. 6.97. The residual factor augmented from 0.51 at the beginning of failure to 0.78 at the final failure (step=1018000). This implies that the shear stress is getting to the residual value according to Eq. (1.3).

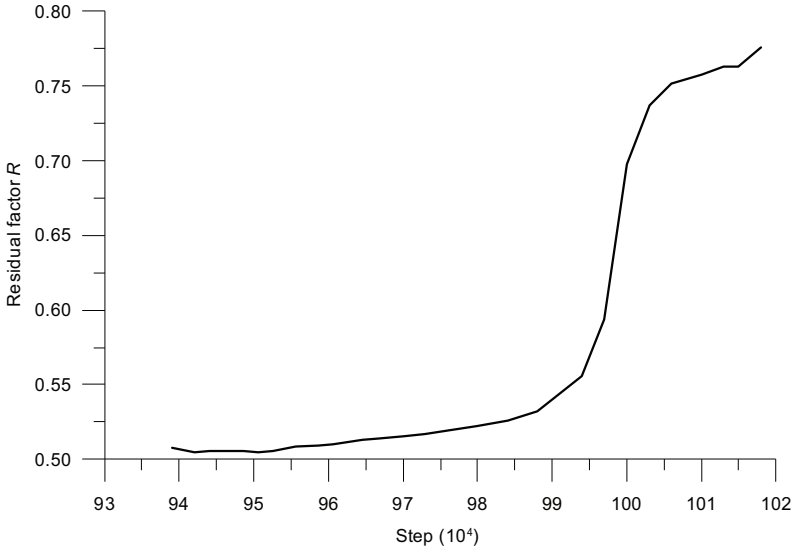

Fig. 6.99 Post-failure development of average residual factor

Fig. 6.100 shows the pre-failure development of average brittleness along slip surface which is calculated by Eq. (2.6) using average shear stresses for peak and mobilised values. This curve exhibits similar tendency as that shown in Fig. 6.98. The average brittleness decreased from 0.86 to 0.35 till initial failure. The initial value of average brittleness is close to that shown in Fig. 6.10 and Fig. 6.11.

Fig. 6.101 shows the post-failure development of average brittleness along the slip surface. This curve exhibits a similar tendency as that shown in Fig. 6.99. The average brittleness increased from 0.35 at the beginning of failure to 0.53 at final failure due to the reduction of shear stress along slip surface.

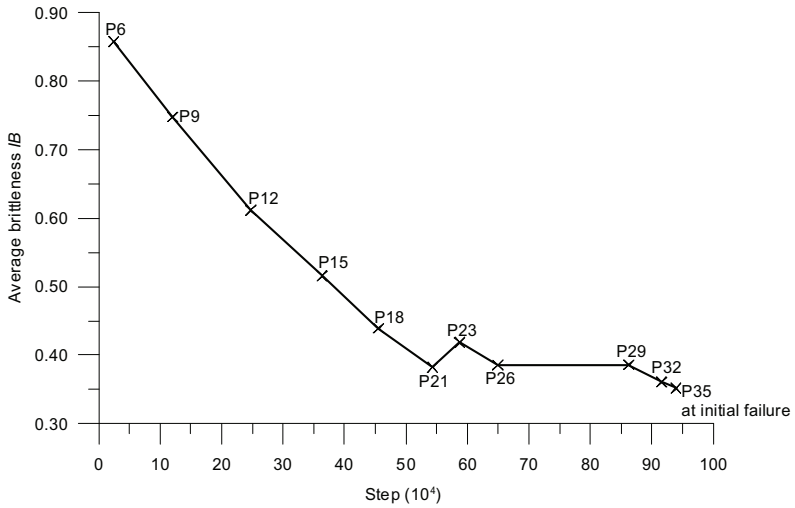

Fig. 6.100 Pre-failure development of average brittleness along slip surface

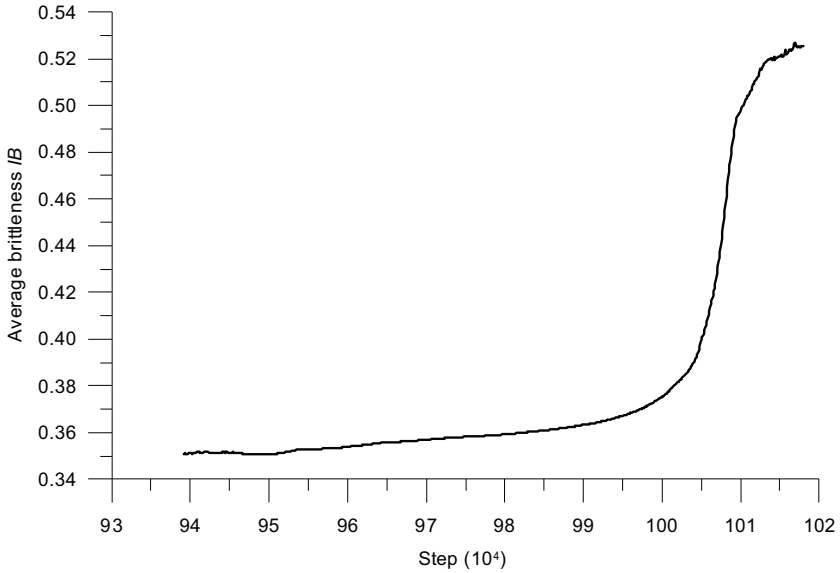

Fig. 6.101 Post-failure development of average brittleness along slip surface

Fig. 6.102 shows the pre-failure development of average pore pressure ratio along slip surface. It can be seen that the average pore pressure ratio increased firstly from 0.45 to 0.56 at phase 26 and then decreased to 0.5087 at initial failure.

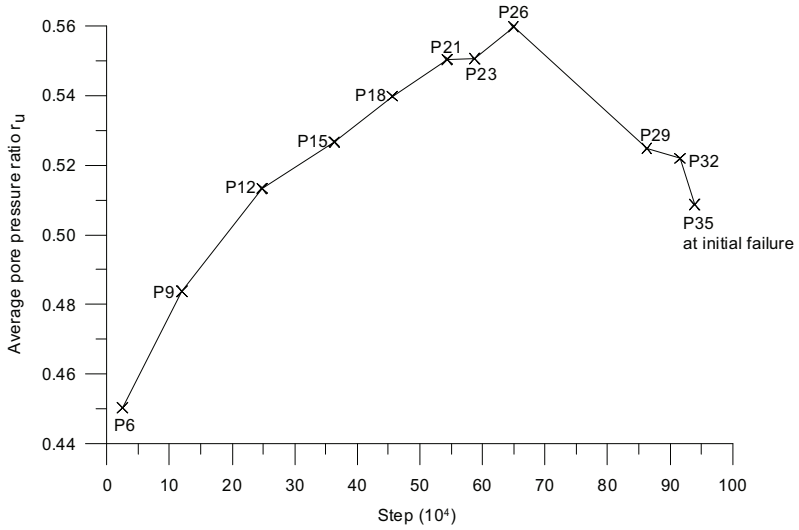

Fig. 6.102 Pre-failure development of average pore pressure ratio along slip surface

Fig. 6.103 shows both the pre-failure and post-failure development of average stress condition along the slip surface. At the same time, also shown in Fig. 6.103 are the corresponding shear strength stress envelopes at peak, post-rupture and residual states under effective normal stress $\sigma_n^{'}$.

In fact, Fig. 6.103 provides the average stress path along the slip surface. Fig. 6.103 indicates that the average shear stress augmented from the first loading phase to the initial failure and then diminished till final failure. At the beginning of failure, the stress points were very close to the post-rupture strength envelope. Afterwards, the average shear stress along the slip surface reduced nearly vertically with very little change in effective normal stress.

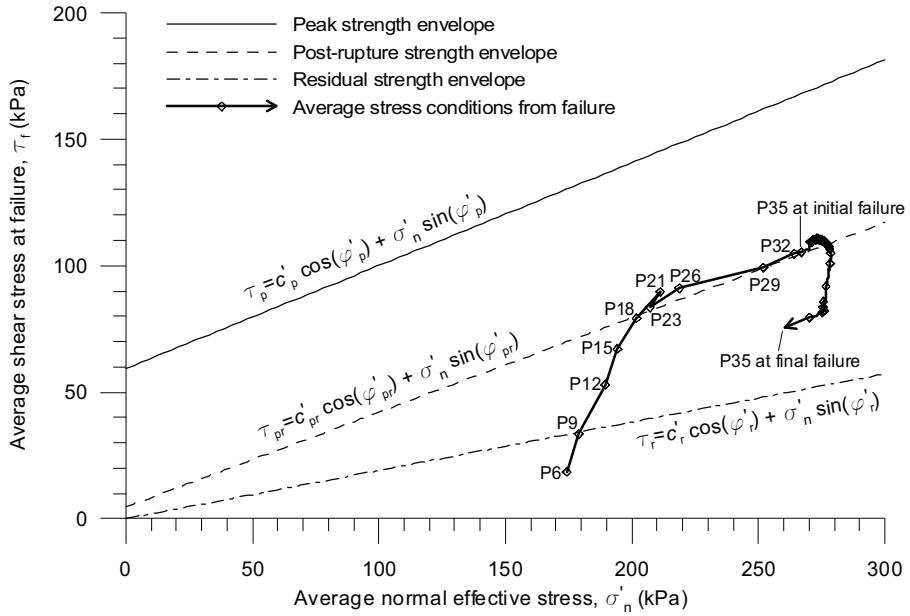

Fig. 6.103 Development of average stress condition along slip surface

Fig. 6.104 and Fig. 6.105 show the pre-failure distribution of current shear stress along the failure surface below dam embankment at phase 23 (step=587500) and phase 26 (step=649650). In these figures the peak, post-rupture, residual and current strength values calculated via Eq. (5.3) with the corresponding strength parameters are also shown. It can be seen that the value of shear stress is intermediate between peak and residual values.

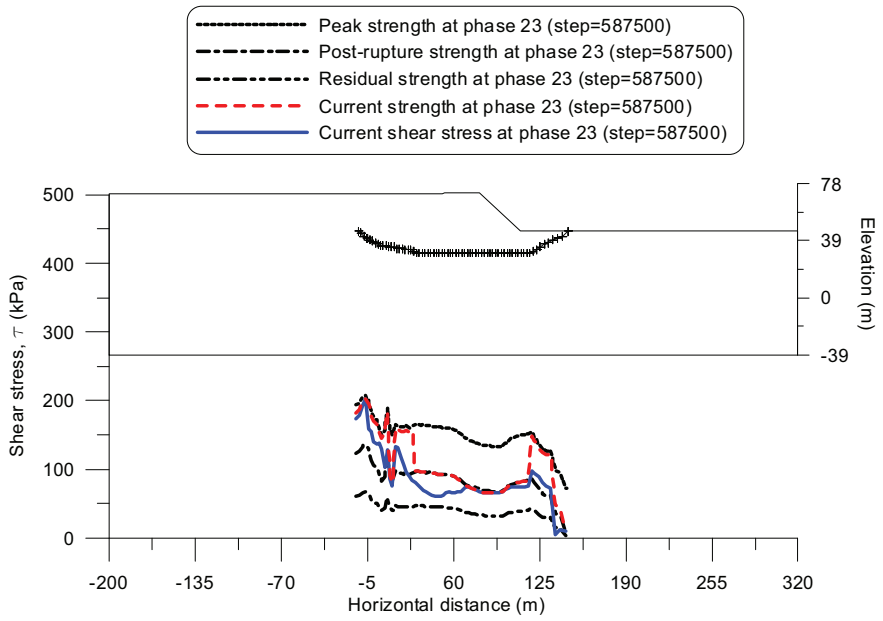

Fig. 6.104 Distribution of shear stress along failure surface at phase 23 (Step=587500)

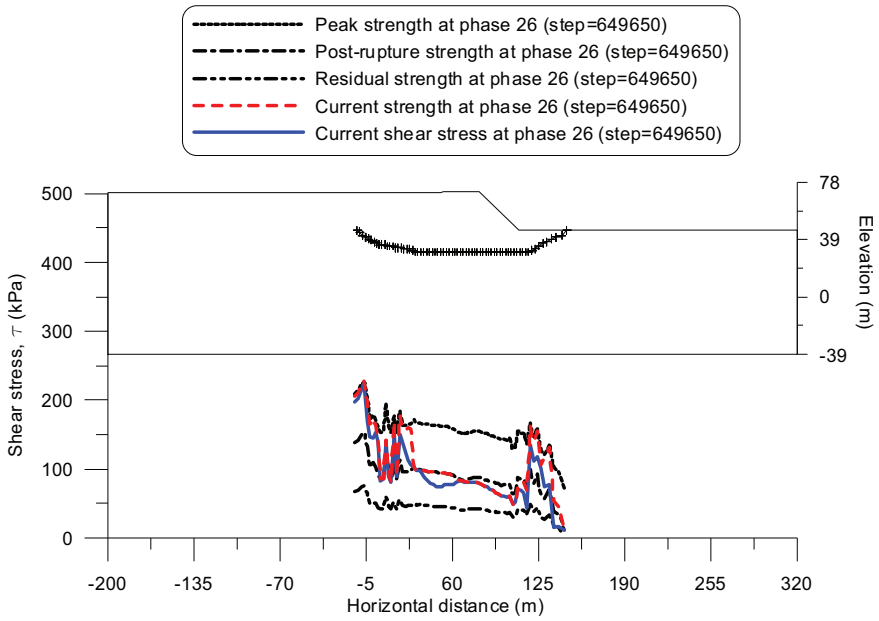

Fig. 6.105 Distribution of shear stress along failure surface at phase 26 (Step=649650)

Fig. 6.106 presents the distribution of current shear stress along failure surface below the dam embankment just at failure (step=939103). The corresponding distribution of shear strength at current, peak, post-rupture and residual states under relevant effective normal stress $\sigma_n^{'}$ are also shown in Fig. 6.106. It can be seen that the value of shear stress is intermediate between the peak and residual values and very close to the value obtained using post-rupture strength parameters.

Fig. 6.103 and Fig. 6.106 prove that the average shear strength at failure is close to the post-rupture value.

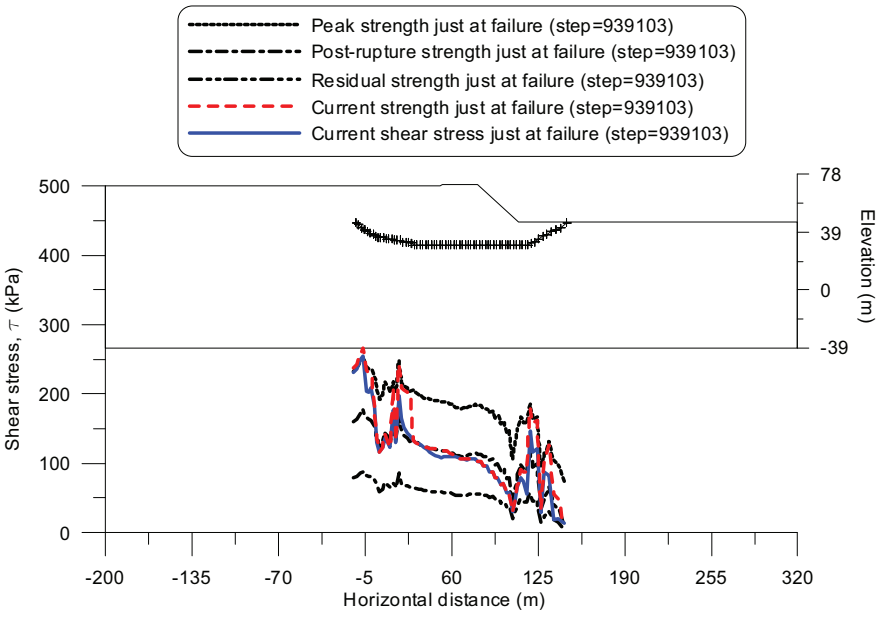

Fig. 6.106 Distribution of shear stress along failure surface at initial failure phase (step=939103)

Fig. 6.107 shows the distribution of current shear stress along failure surface at final failure (step=1018000). It is evident that the current shear stress is almost the same as

that calculated with residual strength parameters, which confirms further the mechanism of progressive failure of Aznalcóllar dam. This mechanism is also demonstrated by Fig. 6.108-Fig. 6.115 which show the cohesion and friction angle distribution along slip surface at pre-failure stage and post-failure stage. The cohesion and friction along most of the slip surface were equal or close to the relevant post-rupture values just at failure and reached the residual values at final failure.

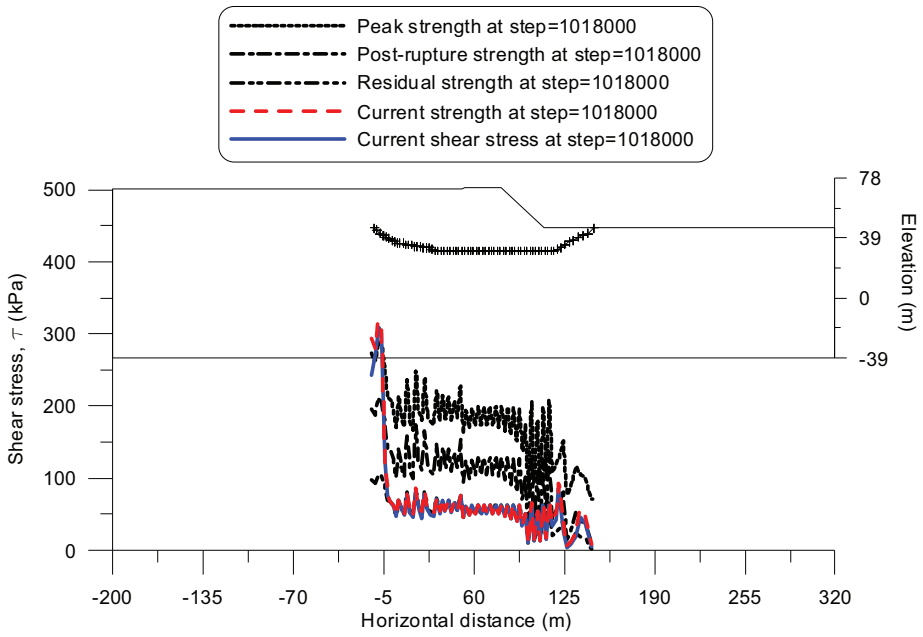

Fig. 6.107 Distribution of shear stress along failure surface at final failure phase (step=1018000)

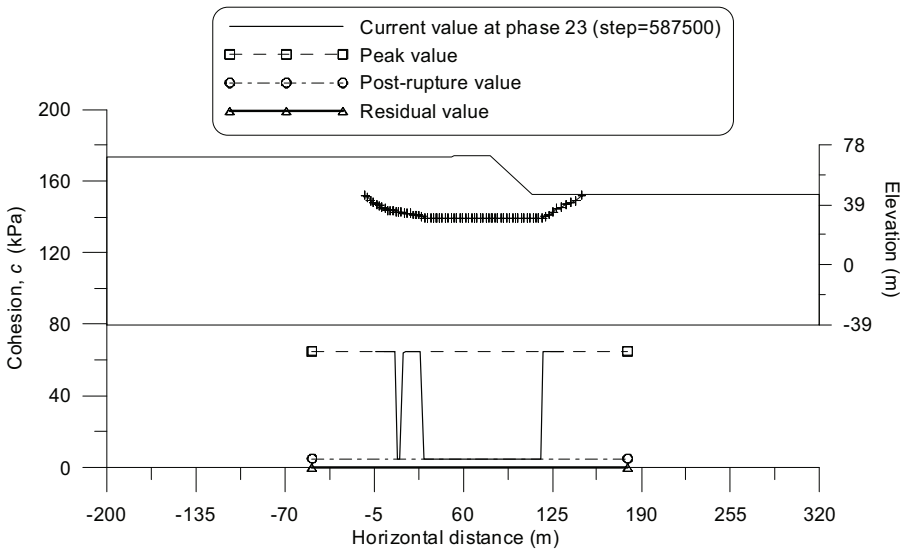

Fig. 6.108 Cohesion distribution along slip surface at phase 23 (step=587500)

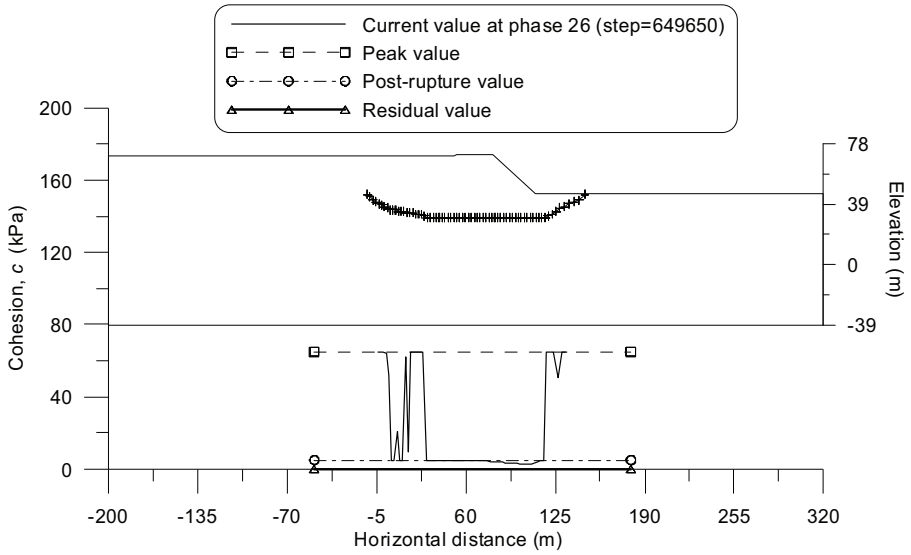

Fig. 6.109 Cohesion distribution along slip surface at phase 26 (step=649650)

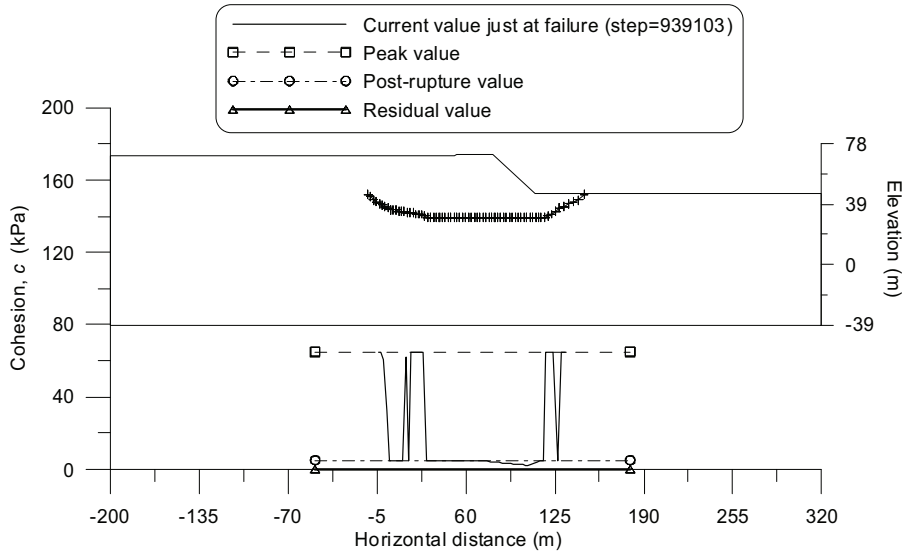

Fig. 6.110 Cohesion distribution along slip surface at initial failure phase (step=939103)

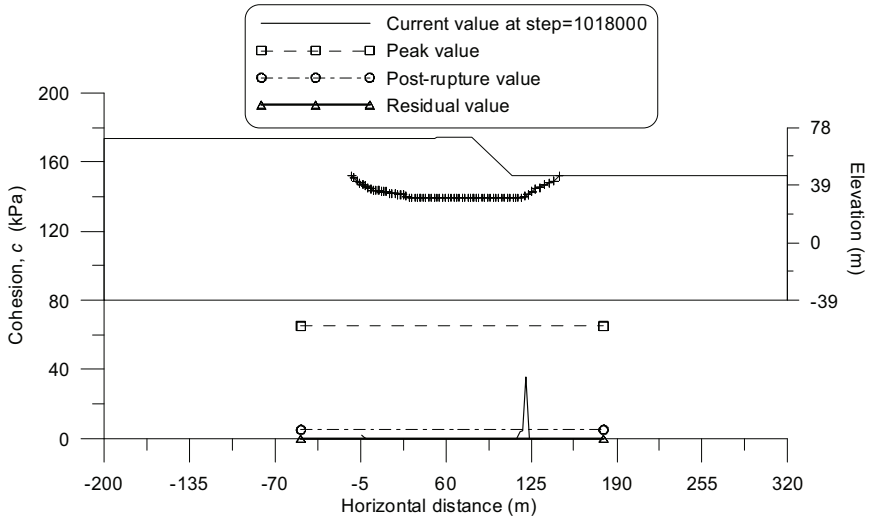

Fig. 6.111 Cohesion distribution along slip surface at final failure phase (step=1018000)

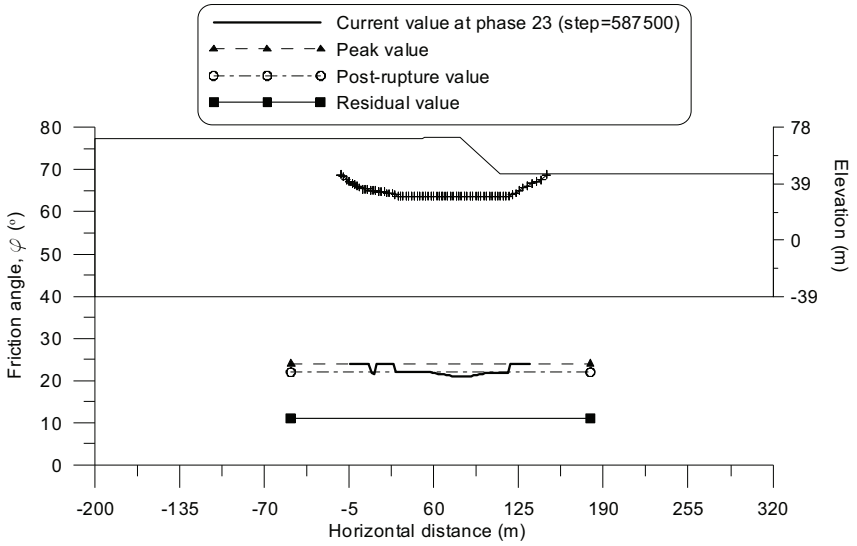

Fig. 6.112 Friction distribution along slip surface at phase 23 (step=587500)

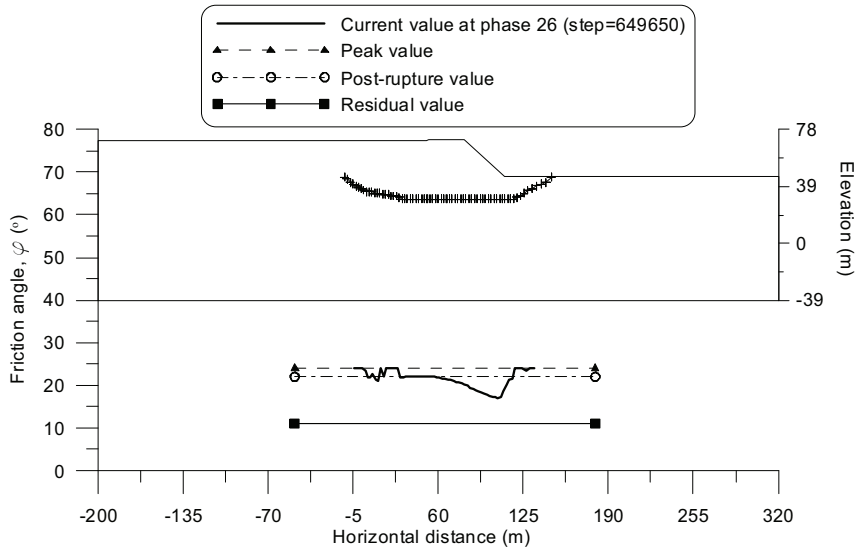

Fig. 6.113 Friction distribution along slip surface at phase 26 (step=649650)

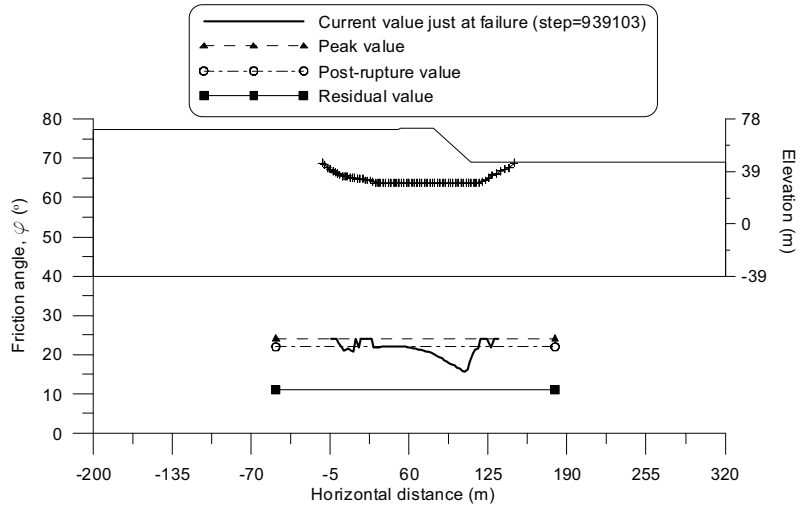

Fig. 6.114 Friction distribution along slip surface at initial failure phase (step=939103)

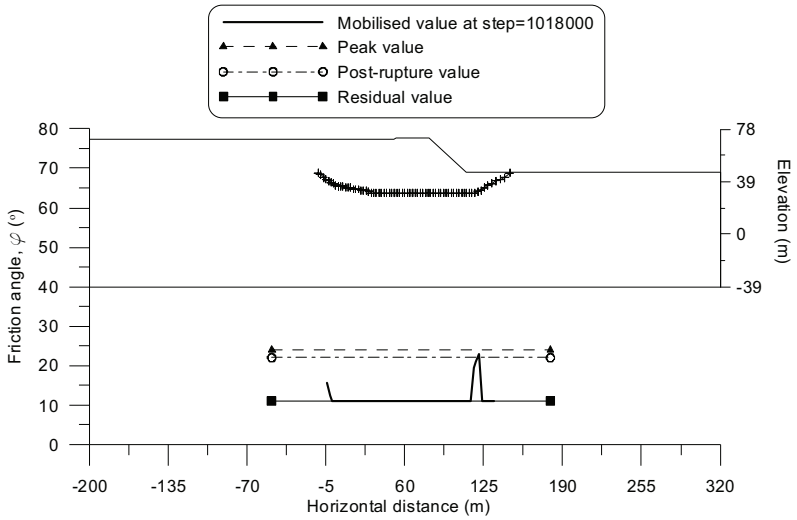

Fig. 6.115 Friction distribution along slip surface at final failure phase (step=1018000)

Fig. 6.116 shows the development of shear stress along the failure surface from phase 23 to final failure. It can be seen from Fig. 6.116 that the current shear stress increased at pre-failure stage till initial failure and then reduced during the post-failure stage till reaching the residual value.

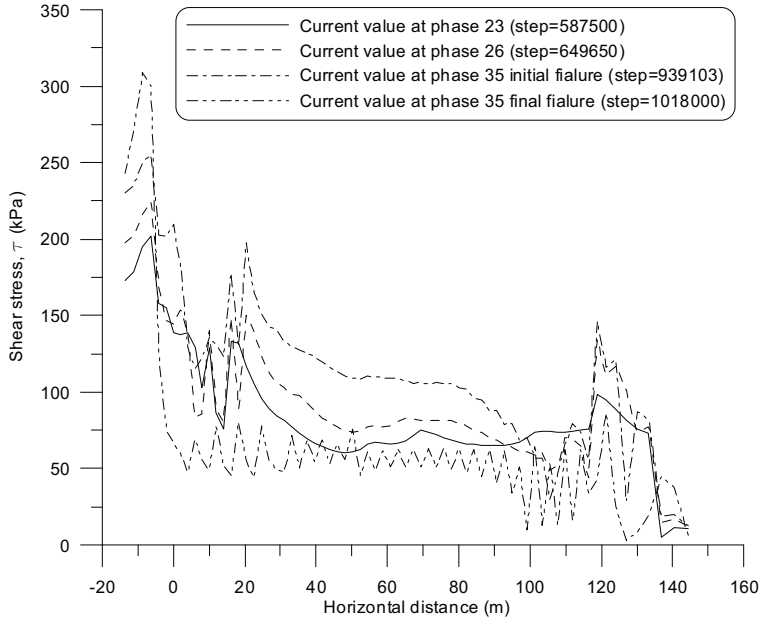

Fig. 6.116 Shear stress development along failure surface from phase 23 to final failure

6.5.3.11 Verification of position of failure surface

The Aznalcóllar dam failure occurred along the critical plane located at 10m depth below the top of blue clay stratum which has been confirmed by the simulations presented above. However, in these analyses only a weak layer at a depth approximately the same as that observed in the real failure was considered. In order to verify further the position of slip surface and shed light on the significance of location of the critical plane, a series of simulations with different settings of weak layers (seen in Fig. 6.117) are presented in this section. Table 6.9 and Table 6.10 show the model type, strength parameters and the combinations of weak layer settings. All the

modelling procedures and the model types for tailings, rockfill, red clay and alluvium are the same as those shown in Table 6.5. The strength parameters for both clay mass and weak layer in all the analyses except analysis O2 are the same as those used in analysis L. In Table 6.10, the zero elevation reference is set to be the model base and the elevation y=30.5 is the real position of failure surface.

As shown in Table 6.10, the analyses are divided into two groups—N1-N4 with a single weak layer and O1-O2-P with 5 weak layers.

Table 6.9 Model types and strength parameters

Material	Model No.	Model	γ_p	γ_{pr}	γ_r	c_p (kPa)	c_{pr} (kPa)	c_r (kPa)	ϕ_p (°)	ϕ_{pr} (°)	ϕ_r (°)	ψ (°)
Blue clay with weak layer	**1**	**SS(clay)**	**0.0**	**0.005**	**0.135**	**65**	**5**	**0**	**24**	**22**	**11**	**0**
		SS(weak)	**0.0**	**-**	**0.130**	**5**	**-**	**0**	**22**	**-**	**11**	**0**
Blue clay with weak layer	2	SS(clay)	0.0	0.001	0.1058	65	5	0	24	22	11	0
		SS(weak)	0.0	-	0.1048	5	-	0	22	-	11	0

Table 6.10 Analysis summary with different combinations of weak layer setting

Analysis No.	Model of blue clay	Number of weak layer	Elevations of weak layers	Failure condition
N1	1	1	y1=35.5	No failure
N2	1	1	y1=32.5	No failure
N3	1	1	y1=28.5	No failure
N4	1	1	y1=25.5	No failure
O1	1	5	y1=35.5 **y2=30.5** y3=25.5 y4=20.5 y5=14.6	No failure
O2	2	5	y1=35.5 **y2=30.5** y3=25.5 y4=20.5 y5=14.6	Failure at phase 35 along **y1=30.5**
P	1	5	**y1=30.5** y2=25.5 y3=20.5 y4=14.6 y5=9.4	Failure at phase 35 along **y1=30.5**

N1

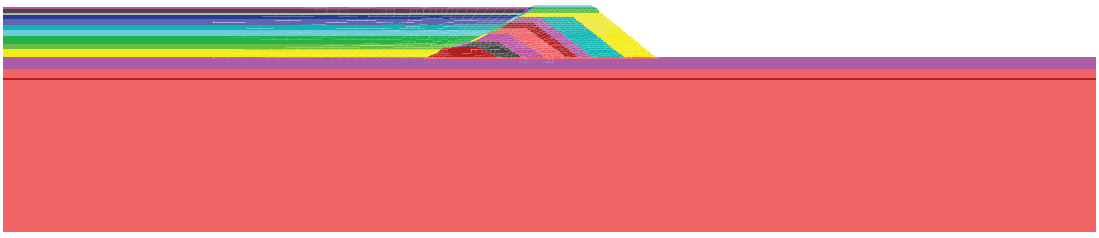

N2

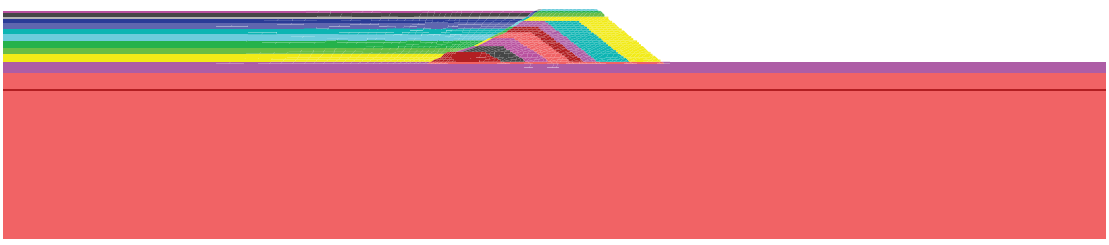

N3

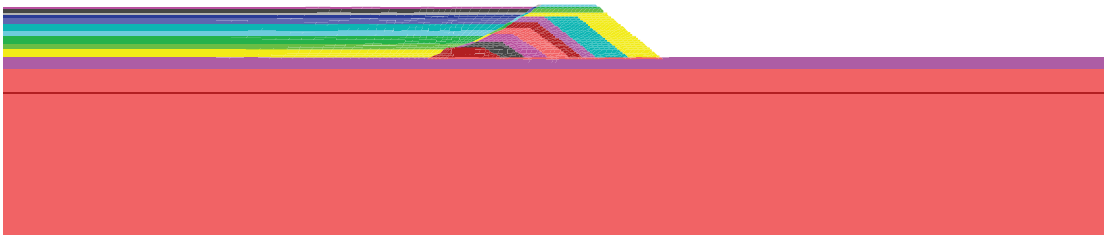

N4

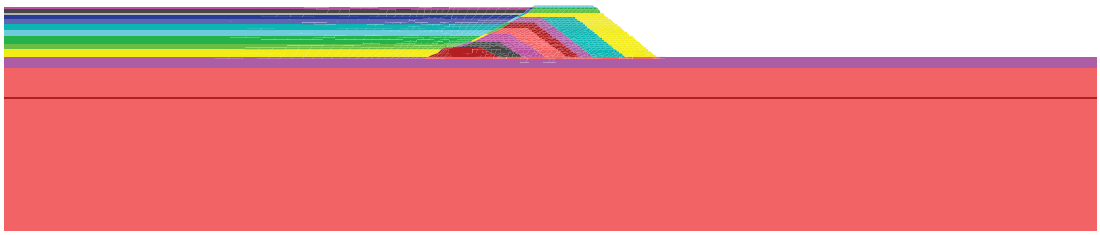

O1

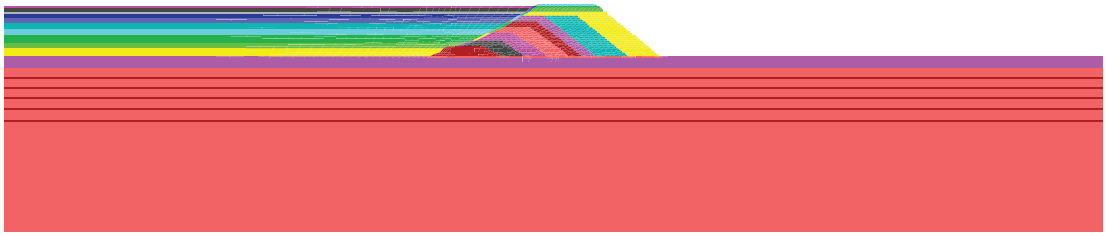

O2

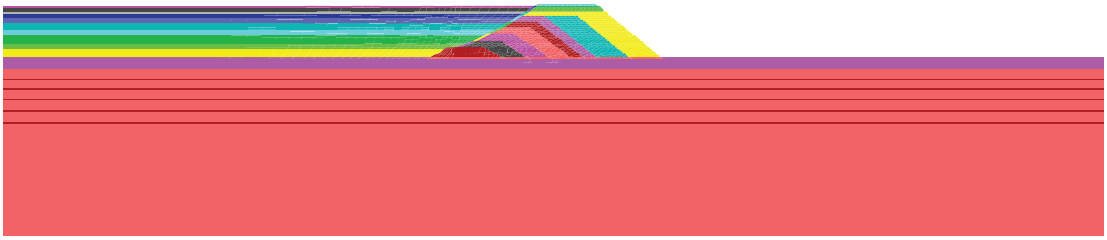

P

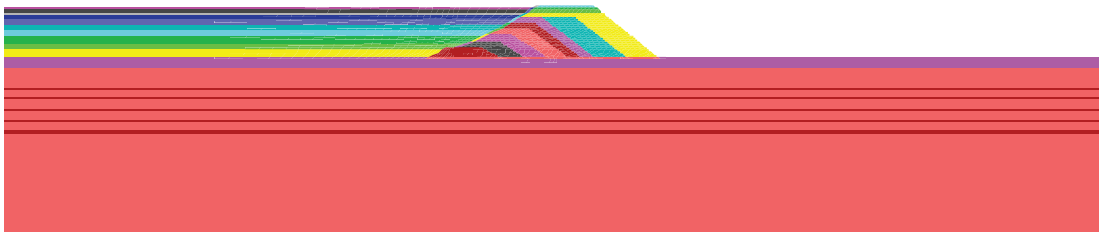

Fig. 6.117 Positions of weak layers and material groups

6.5.3.11.1 Analysis results with a single weak layer

Four analyses N1-N4 are performed with only one weak layer which is 5 m or 2 m above or below the weak layer at y=30.5 m (seen in Fig. 6.117) with the same strength parameters used in analysis L. It can be seen from Fig. 6.118-Fig. 6.119 that no failure happened in these four cases suggesting that the y=30.5 m is indeed a critical plane location.

6.5.3.11.2 Analysis results with 5 weak layers

In analyses O1 and O2, additional weak layers are set both above and below the one at y=30.5 m which is the weak layer position set in analysis L. The weak layer interval is about 5m.

In analysis O1, no failure occurred at the final phase and can be explained from Fig. 6.118-Fig. 6.119 showing the color contours of shear strain rate and accumulated plastic shear strain. In spite of this, the mobilisation along weak layer and in clay mass still occurred but did not reach the degree required to cause a general collapse. It is interesting to find that failure will not occur if a weak layer above the one at y=30.5 m is set with same strength parameters as those applied in analysis L. This is probably because the deformation or localisation concentrated only in the weak layer at y=30.5 m in analysis L whereas in analysis O1 deformation was distributed mainly in both the weak layer at y=30.5 m and the one above it, which would apparently reduce the degree of mobilisation along the weak layer at y=30.5 m. Therefore failure did not occur in this case.

Although general failure did not occur in analysis O1, the failure would happen if the softening rate of strength parameters were set to larger values. Analysis O2 was performed by setting an appropriate softening rate and failure occurred at the weak layer at y=30.5m which is the same as that in analysis L.

In analysis P, weak layers are only placed below the one at y=30.5 m which is the weak layer position set in analysis L. Weak layer intervals of 10 m, 5 m and 2 m are applied individually (seen in Fig. 6.117). In this modelling, failure occurred at the final phase along the weak layer y=30.5 m which can be observed clearly in Fig. 6.118-Fig. 6.119.

Overall, the results of analyses N1-N4, O1-O2 and P demonstrate that a plane located approximately at y=30.5m is the most likely location for the critical weak structure in the Guadalquivir blue clay mass involved in the Aznalcóllar dam failure.

N1

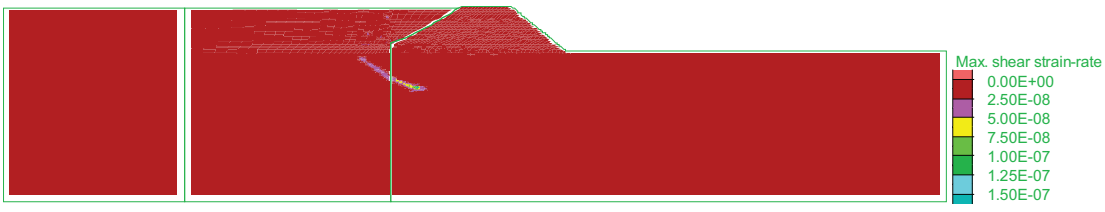

N2

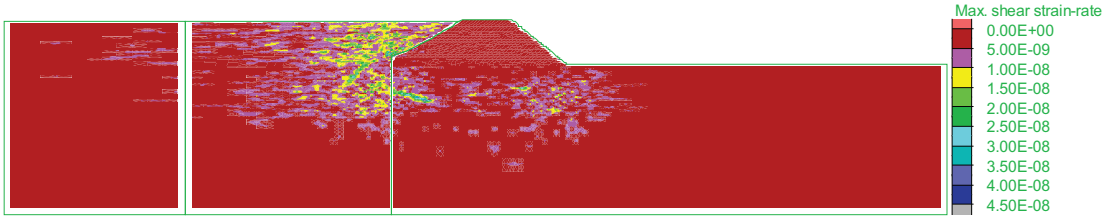

N3

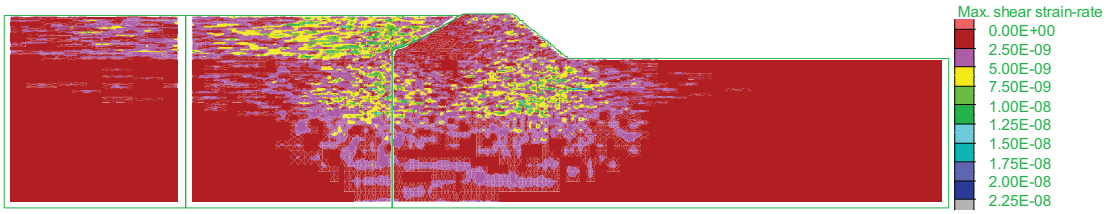

N4

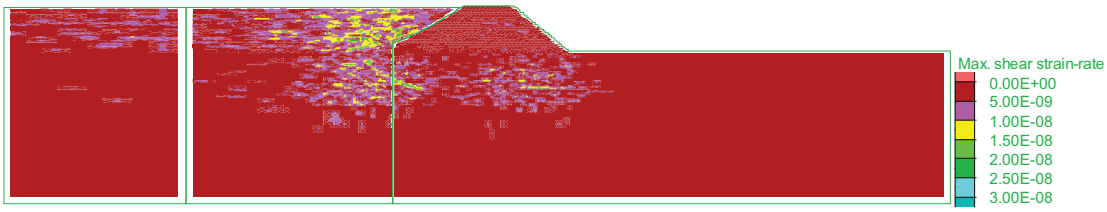

O1

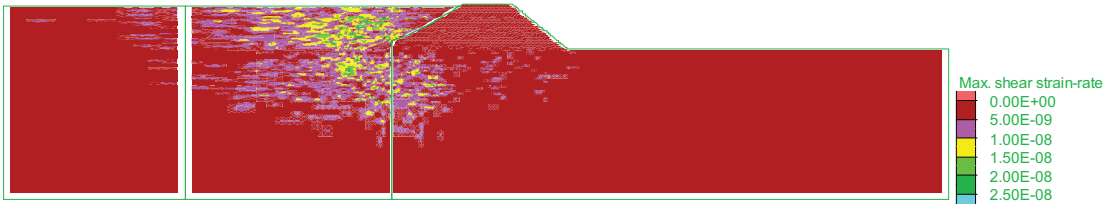

O2

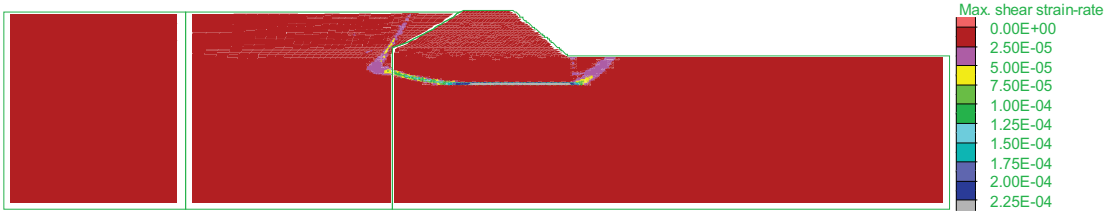

P

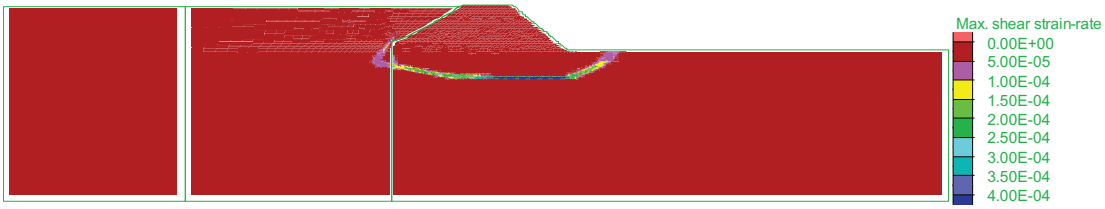

Fig. 6.118 Shear strain rate at the end of simulation

N1

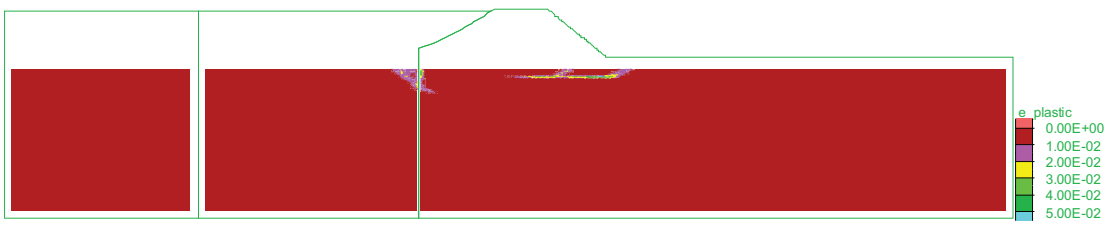

N2

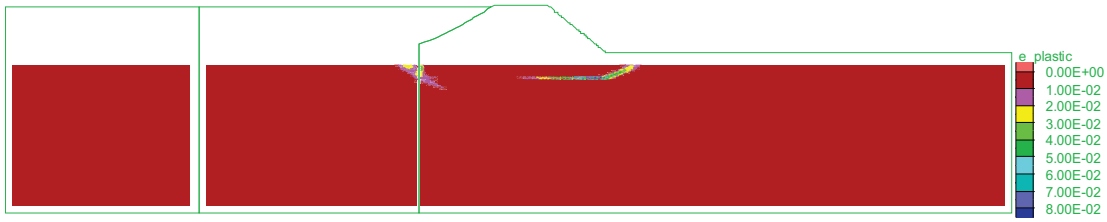

N3

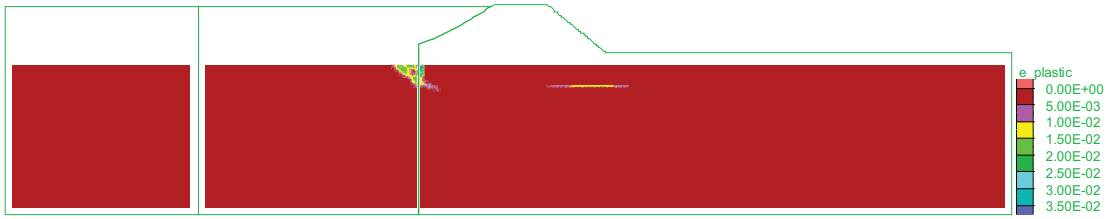

N4

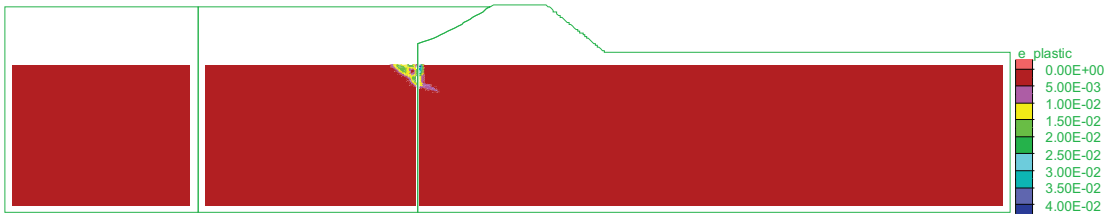

O1

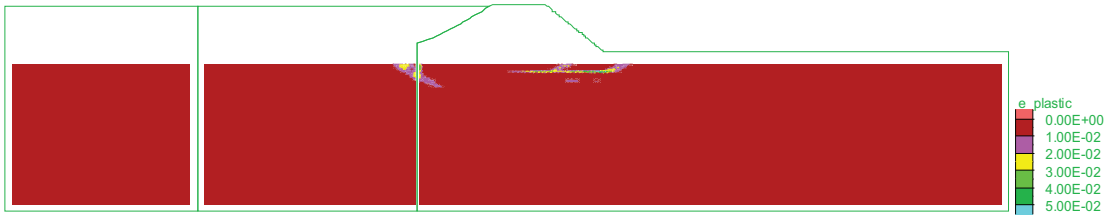

O2

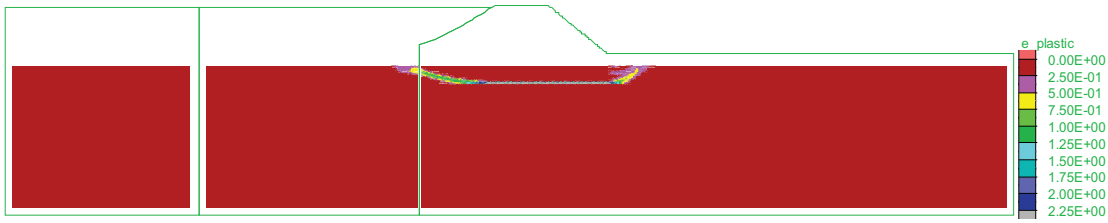

P

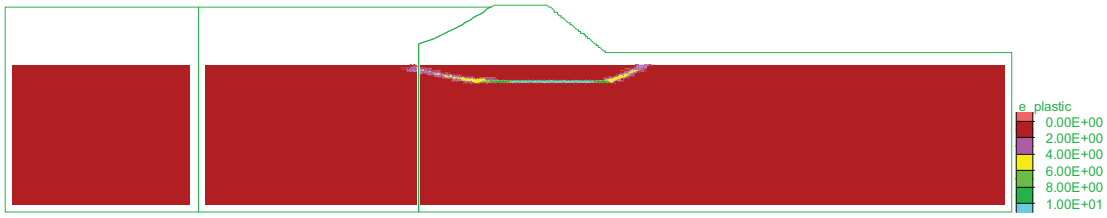

Fig. 6.119 Accumulated plastic shear strain at the end of simulation

6.5.4 Analysis with homogeneous hypothesis

In this section, a homogeneous clay mass hypothesis is proposed in analysis M. The corresponding model parameters (shown in Table 6.11) adopted in analysis M were obtained from direct shear test and the same shear displacements were applied to the elements in the numerical model. In analysis M, the clay mass was modelled with two-stage strain-softening model with the same peak, post-rupture and residual strengths but with a more rapid softening rate.

Table 6.11 Shear strength parameters and plastic shear strain limits for blue clay mass

Peak state	$c_p^{'} = 65\text{kPa},\ \phi_p^{'} = 24°,\ \gamma_p = 0$
Post-rupture state	$c_{pr}^{'} = 5\text{kPa},\ \phi_{pr}^{'} = 22°,\ \gamma_{pr} = 0.00018$
Residual state	$c_r^{'} = 0\text{kPa},\ \phi_r^{'} = 11°,\ \gamma_r = 0.0035$

The softening relationships of cohesion and friction angle with plastic shear strain for blue clay mass are plotted in Fig. 6.120 and Fig. 6.121.

The material groups of the numerical model are shown in Fig. 6.122 in which the blue clay mass is now assumed to be homogeneous.

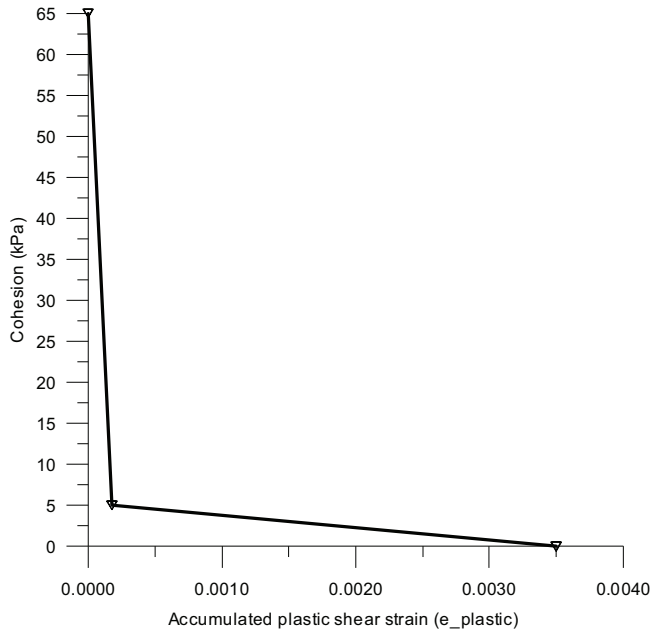

Fig. 6.120 Softening of cohesion with plastic shear strain for blue clay mass

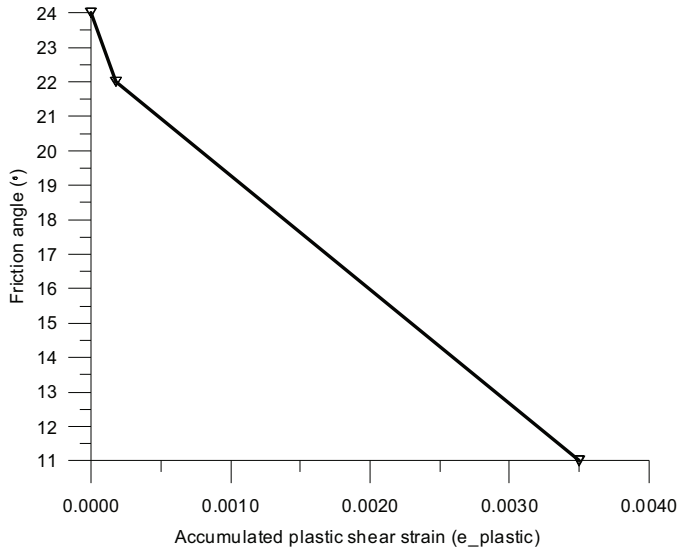

Fig. 6.121 Softening of friction angle with plastic shear strain for blue clay mass

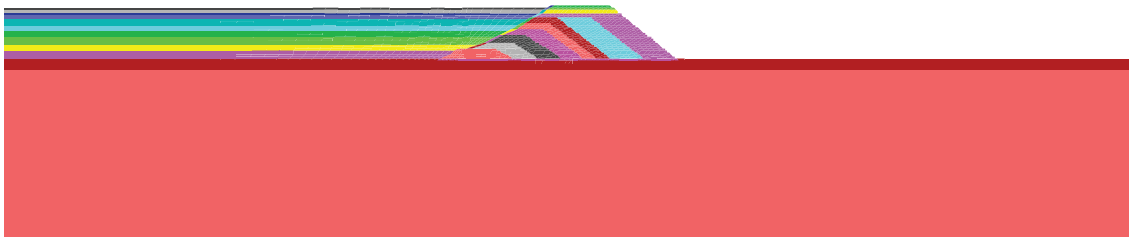

Fig. 6.122 Material groups in numerical model

In analysis M, the total step number for each modelling phase is stated in Table 6.12.

Table 6.12 Modelling step of pre-failure, initial failure and post-failure phases

Phase No.	Total step number
6	23709
9	118139
12	254553
15	389506
18	484348
21	587382
23	629502
26	689858
29	927937
32	986548
34	1010304
35P1	1013304
35P2	1016304
35P3	1018304
35P4	1020304
35P5	1026857
35P6	1032857

6.5.4.1 Development of shear strain rate and shear strain increment

As shown in Fig. 6.123, the shear strain rate development of Aznalcóllar dam failure demonstrates well the progressive failure process from the beginning of initial failure at phase 35P1. Meanwhile, shear strain increment development of Aznalcóllar dam failure (see Fig. 6.124) indicates that the shear strain concentration became gradually evident only at the final failure phases.

Phase 34 just before final construction phase 35

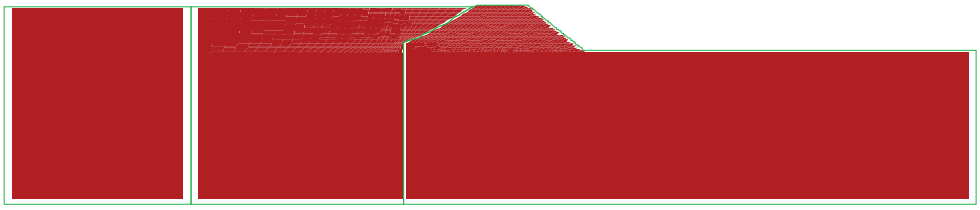

Phase 35P1

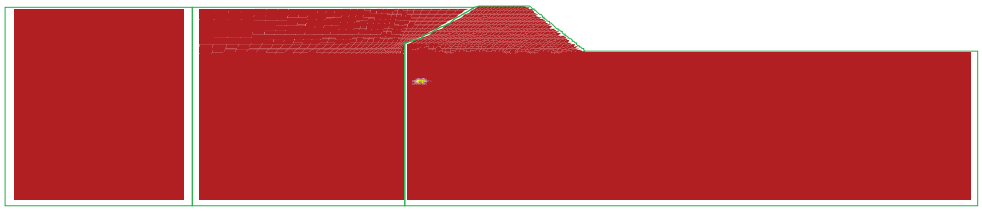

Phase 35P2

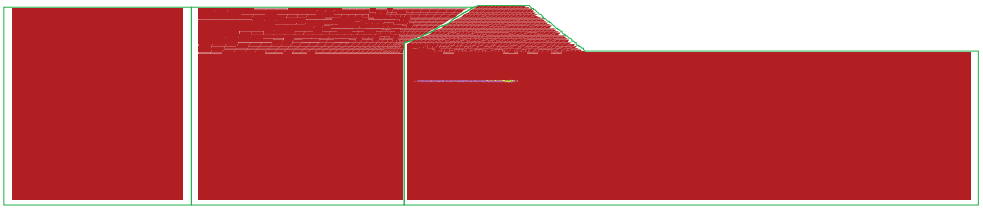

Phase 35P3

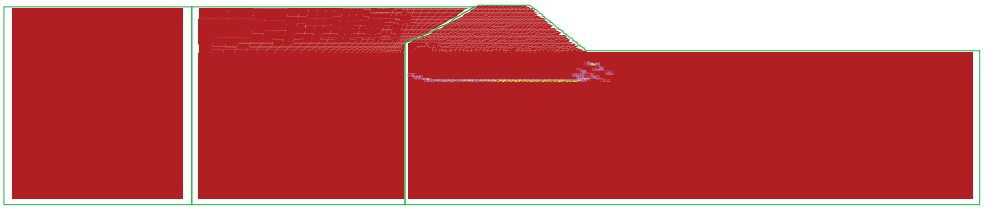

Phase 35P4

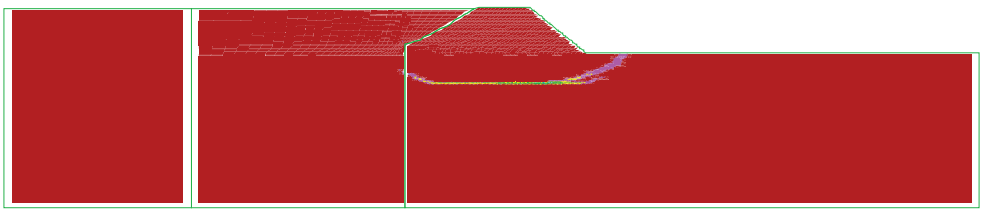

Phase 35P5

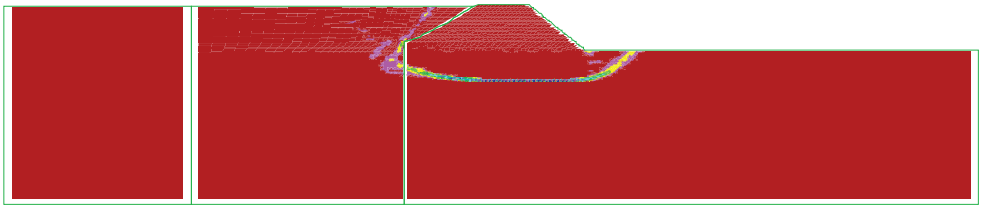

Phase 35P6

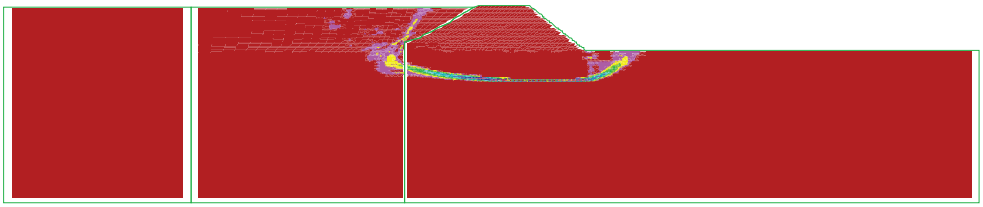

Fig. 6.123 Shear strain rate development of Aznalcóllar dam failure

Phase 35P1

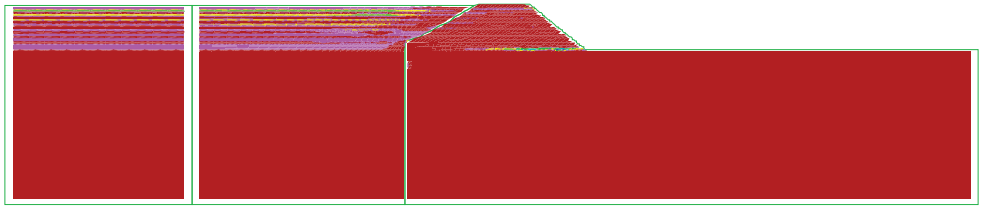

Phase 35P2

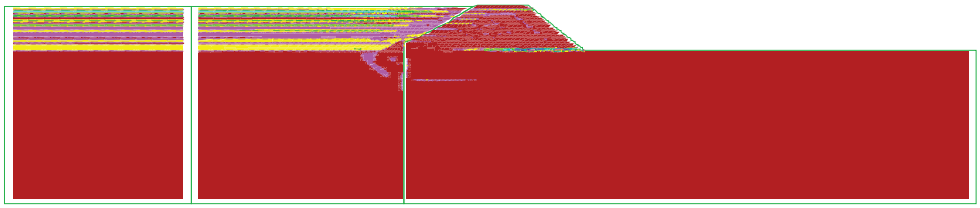

Phase 35P3

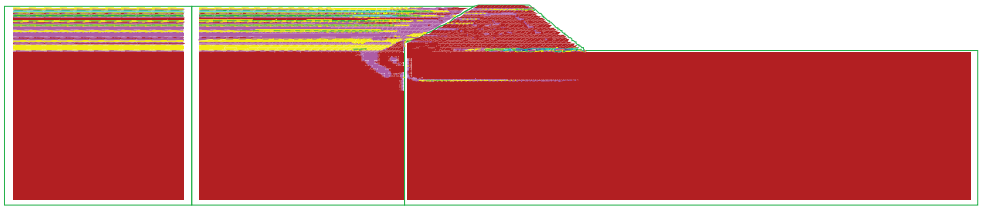

Phase 35P4

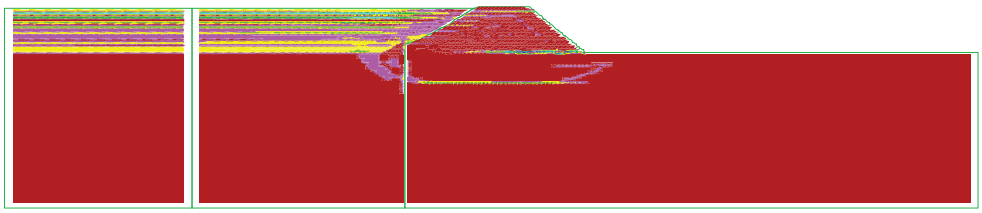

Phase 35P5

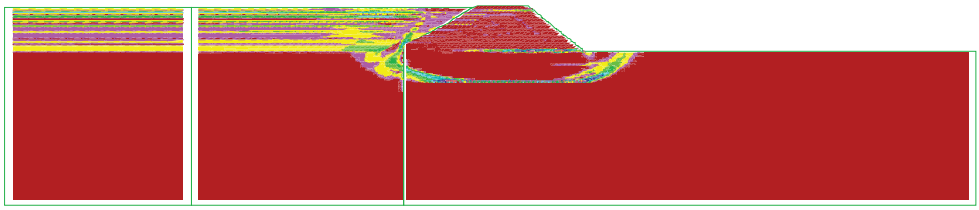

Phase 35P6

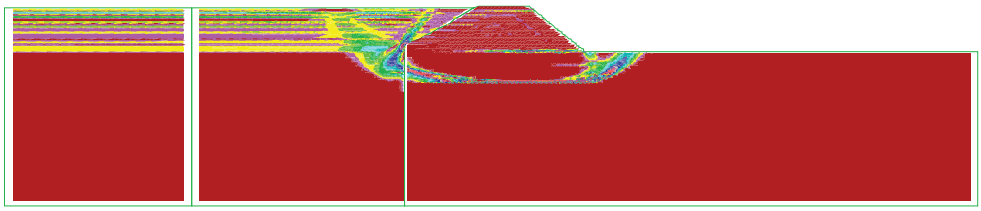

Fig. 6.124 Shear strain increment development of Aznalcóllar dam failure

6.5.4.2 Development of velocity and total displacement

The velocity development (i.e. the equivalent of displacement increment) of Aznalcóllar dam failure shown in Fig. 6.125 also illustrates the process of the formation of the continuous slip surface.

Fig. 6.126 shows the total displacement development of Aznalcóllar dam failure.

Phase 35P1

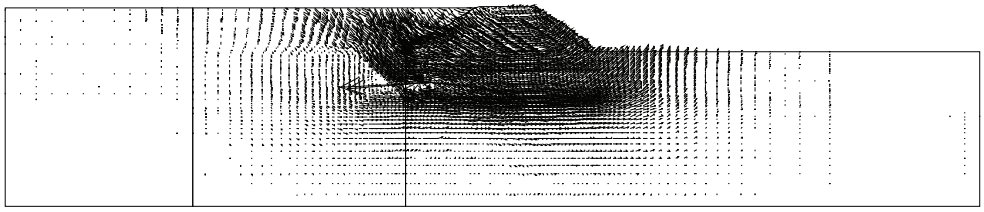

Phase 35P2

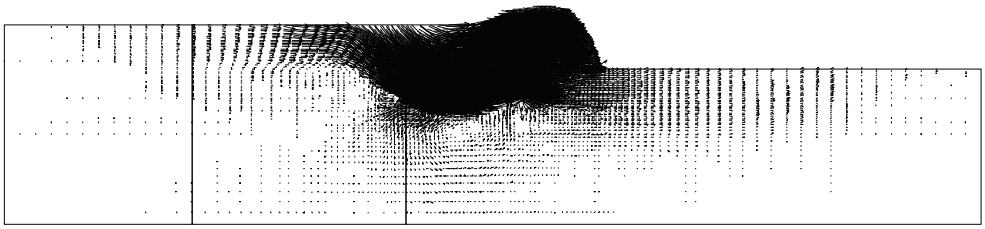

Phase 35P3

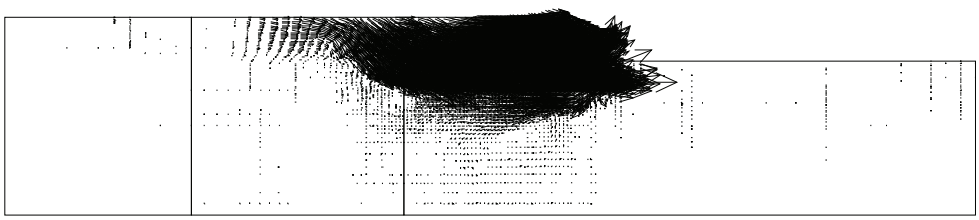

Phase 35P4

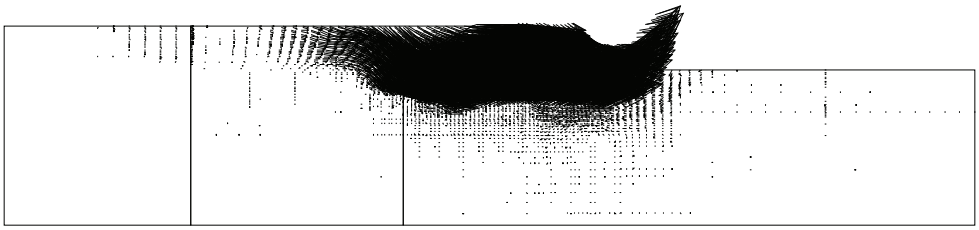

Phase 35P5

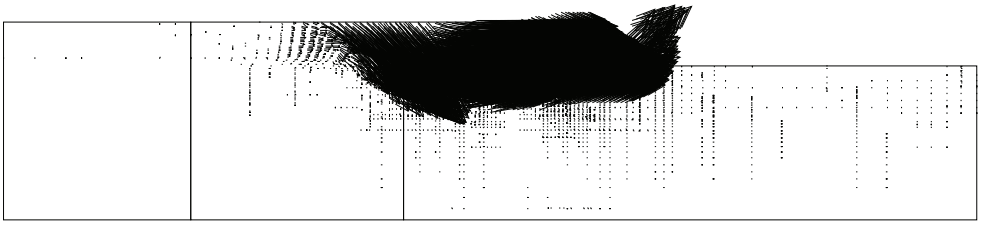

Phase 35P6

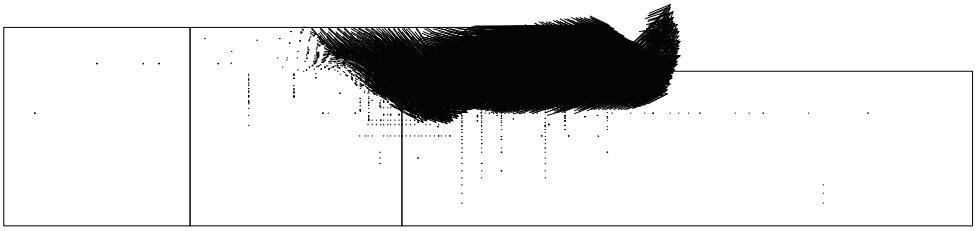

Fig. 6.125 Velocity development of Aznalcóllar dam failure

Phase 35P1

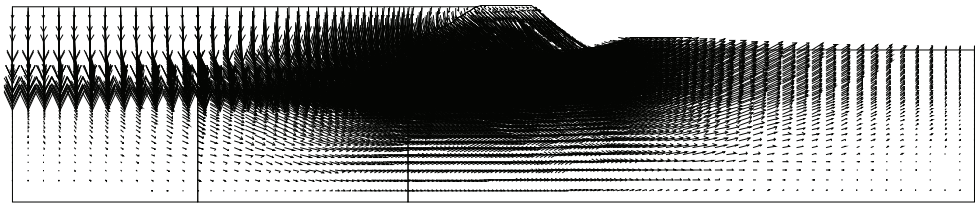

Phase 35P2

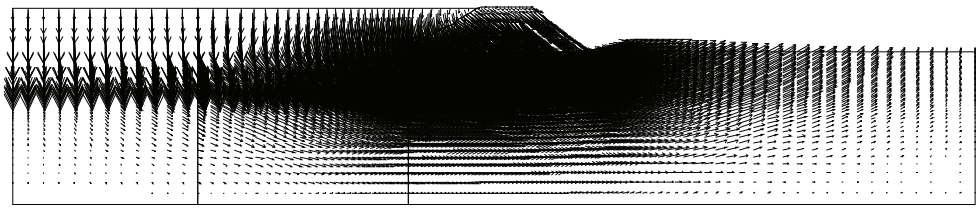

Phase 35P3

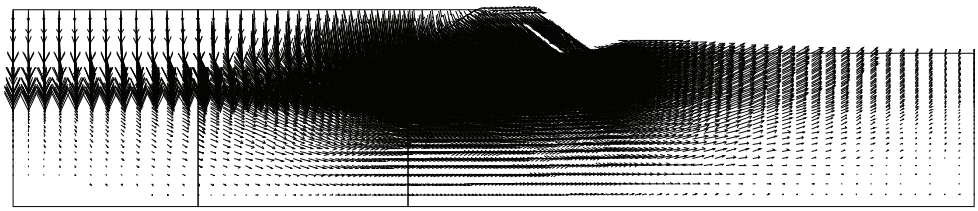

Phase 35P4

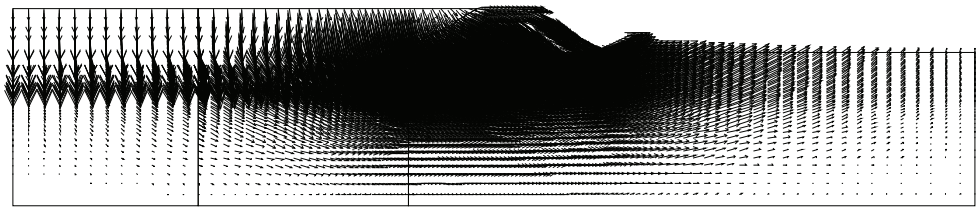

Phase 35P5

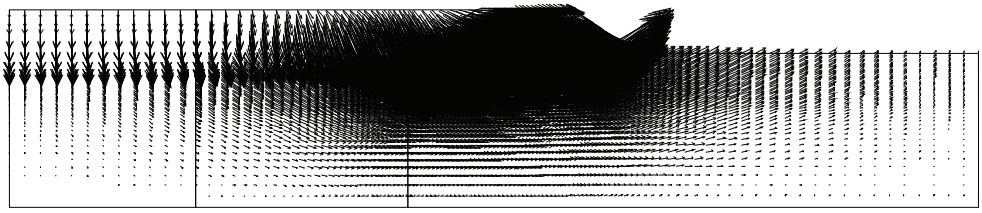

Phase 35P6

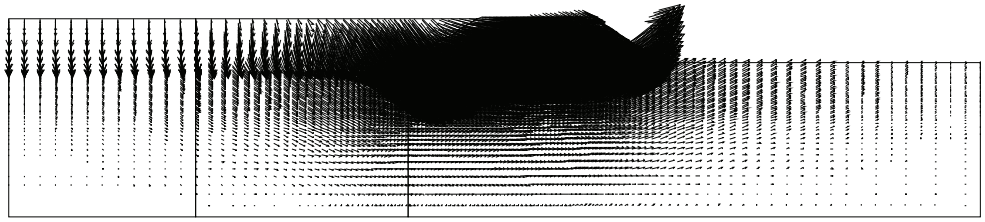

Fig. 6.126 Total displacement development of Aznalcóllar dam failure

The position of the slip surface of Aznalcóllar dam failure can be determined directly from Fig. 6.127. Fig. 6.128 shows the deformed grid at final failure including the passive wedge developed at the downstream toe of dam embankment and a classic upstream active wedge.

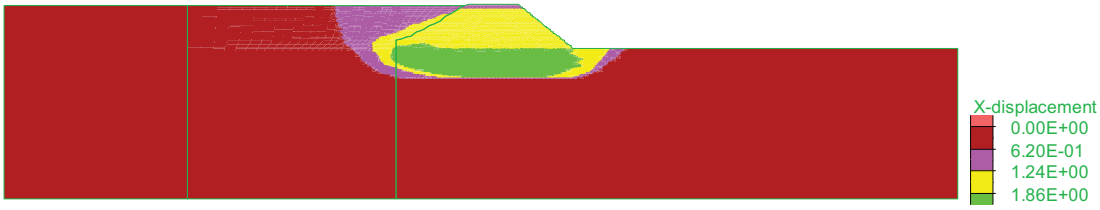

Fig. 6.127 Horizontal displacement at phase 35P6

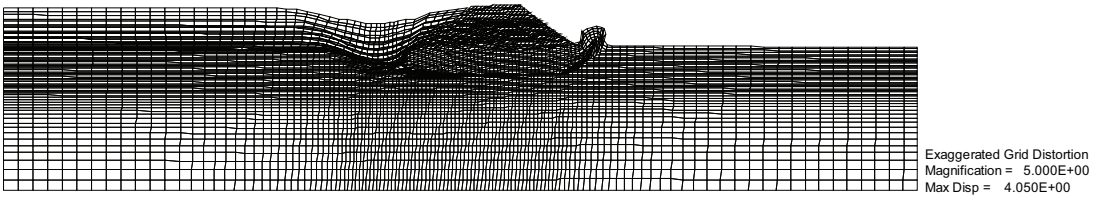

Fig. 6.128 Deformed grid with magnification=5

6.5.4.3 Development of pore water pressure

Fig. 6.129 shows the pore water pressure development for the Aznalcóllar dam case. The pore water pressure increased with dam construction. Before final construction (Phase 12-32), the pore water pressure had similar distribution mode as in previous analyses.

But after failure began (Phase 35P1-35P6), the distribution shape changed with development of a continuous slip surface. The distribution of pore water pressure close to the slip surface was irregular and curved.

Phase 12

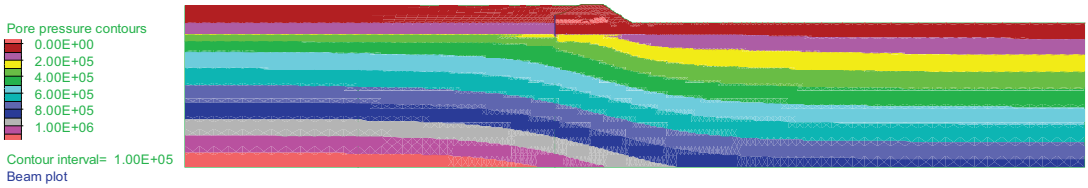

Phase 15

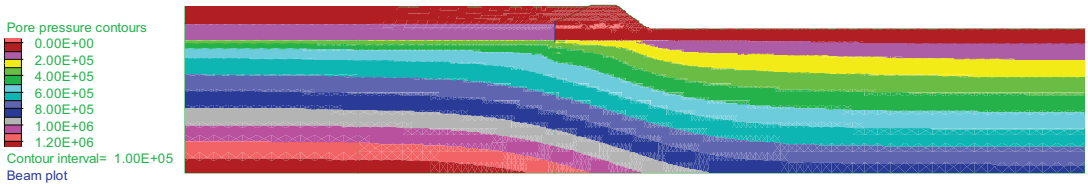

Phase 18

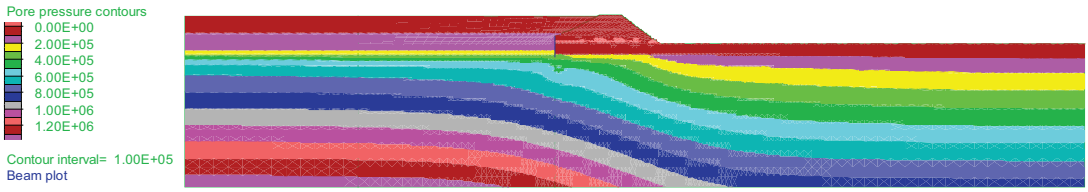

Phase 21

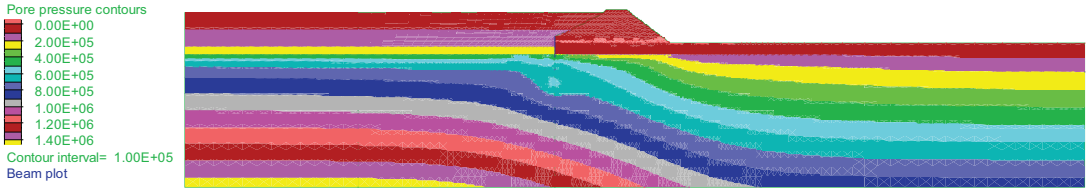

Phase 23

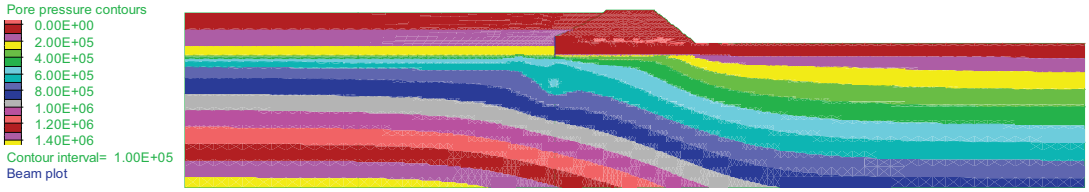

Phase 26

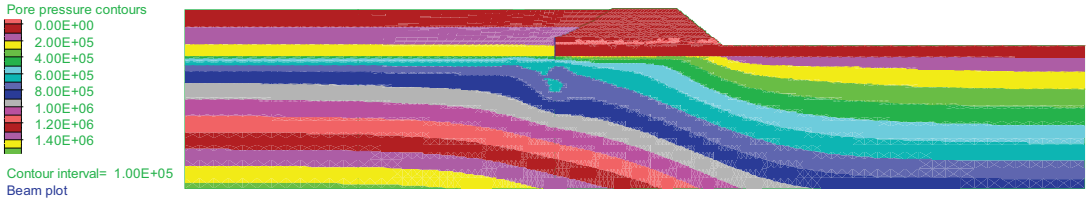

Phase 29

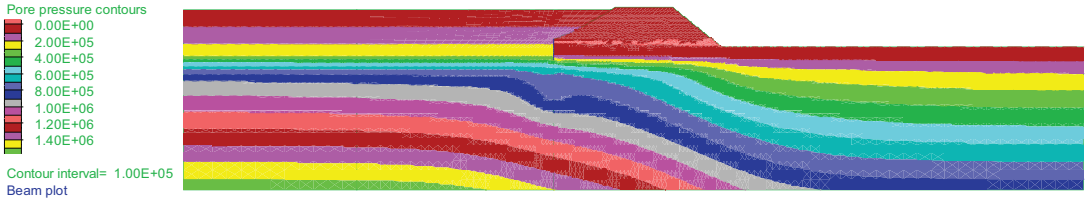

Phase 32

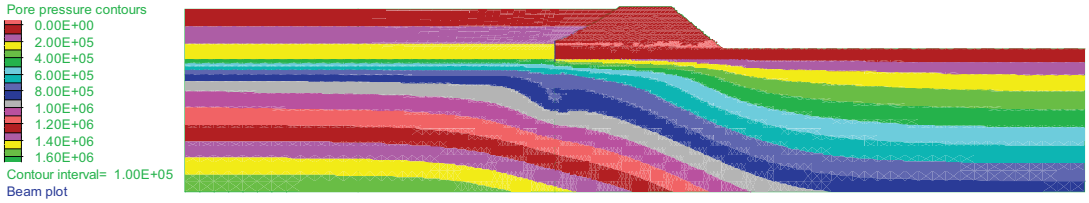

Phase 35P1

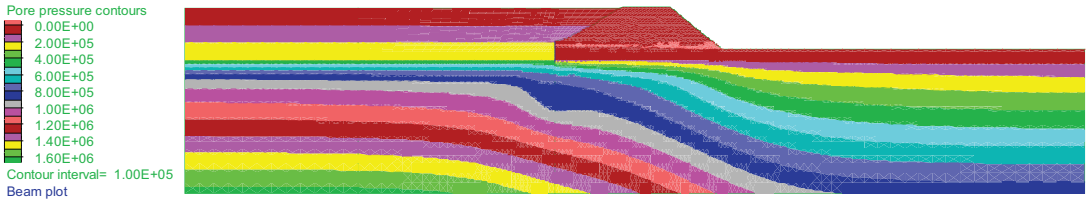

Phase 35P2

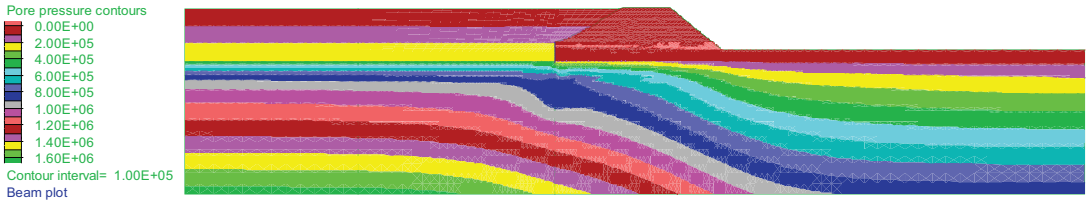

Phase 35P3

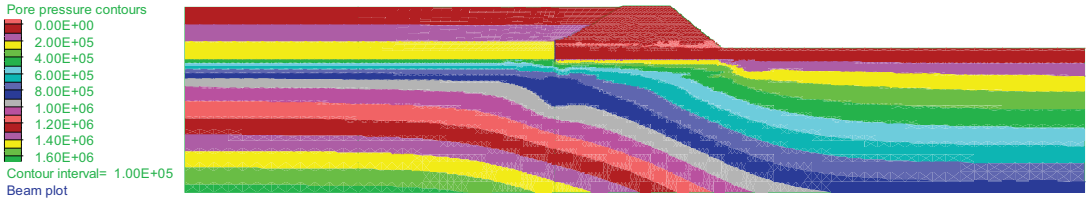

Phase 35P4

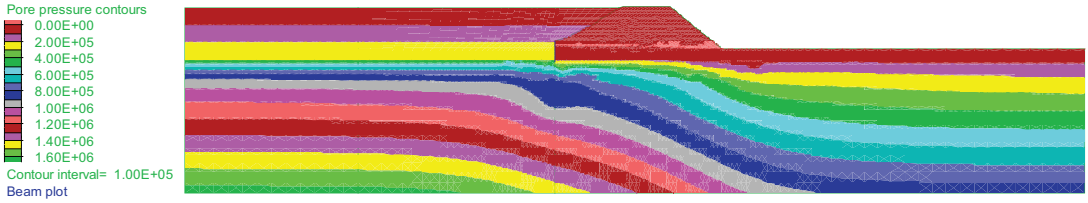

Phase 35P5

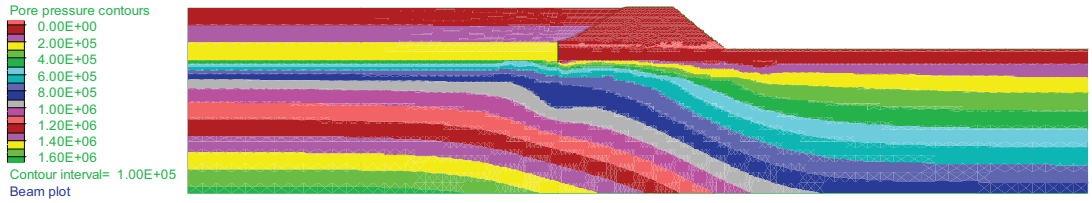

Phase 35P6

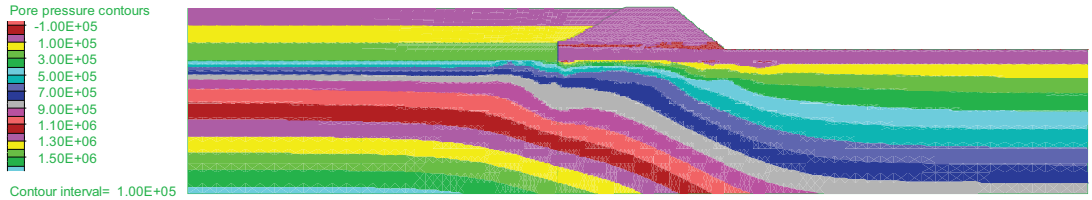

Fig. 6.129 Pore water pressure development of Aznalcóllar dam failure

6.5.4.4 Development of strength parameters in softening clays

Fig. 6.130 shows the development of accumulated plastic shear strain of Aznalcóllar dam failure in blue clay mass for which the two-stage softening model was used.

Fig. 6.131 shows the evolution of cohesion in the Aznalcóllar dam failure and Fig. 6.132 presents the evolution of friction angle in the Aznalcóllar dam failure. From Fig. 6.131 and Fig. 6.132, it can be seen that both the cohesion softening and friction angle degradation accord with the development of accumulated plastic shear strains.

Phase 34 just before final construction phase 35

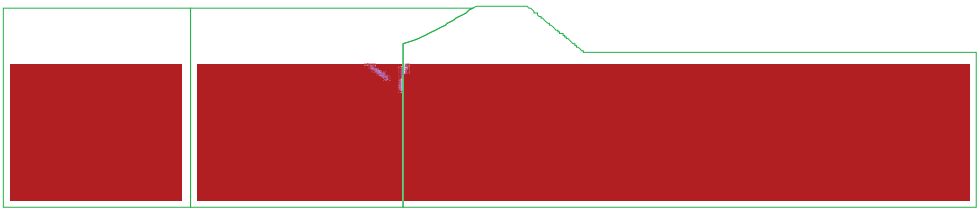

Phase 35P1

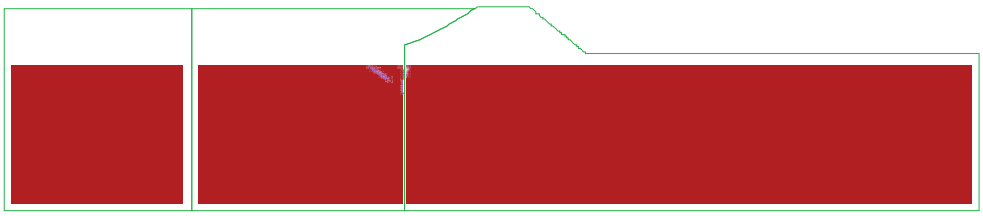

Phase 35P2

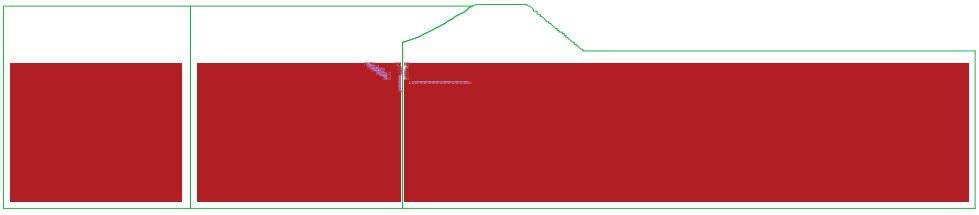

Phase 35P3

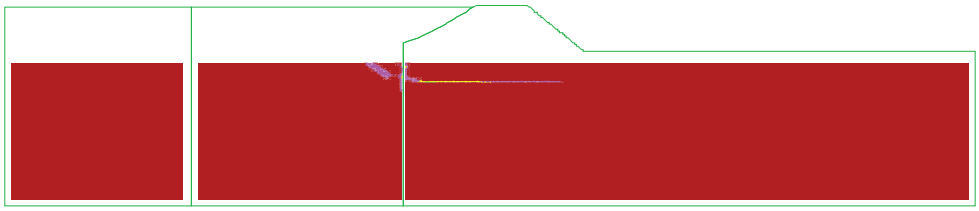

Phase 35P4

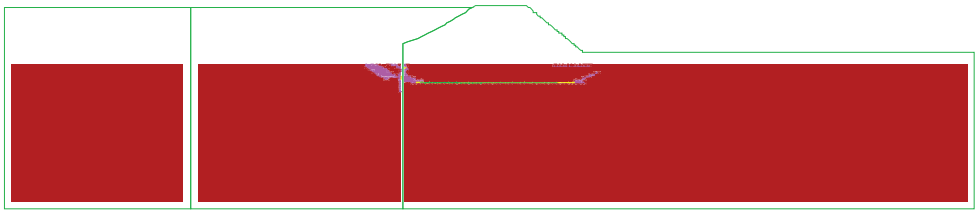

Phase 35P5

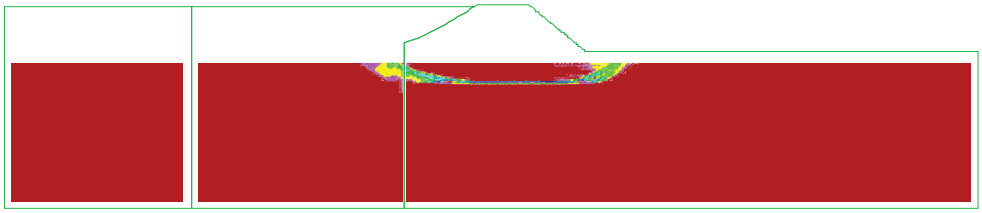

Phase 35P6

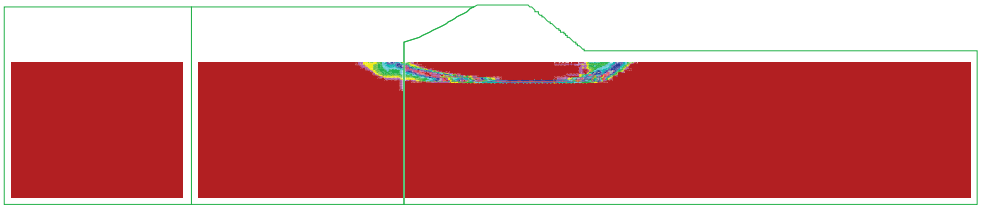

Fig. 6.130 Development of accumulated plastic shear strain of Aznalcóllar dam failure

Initial cohesion

Phase 12

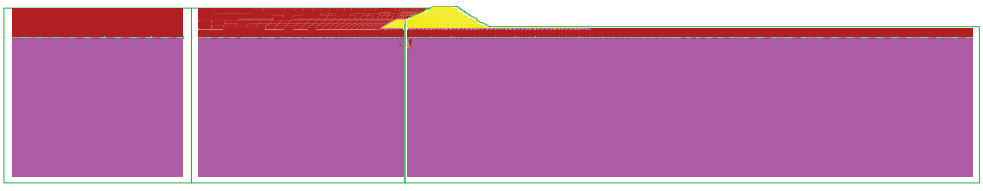

Phase 18

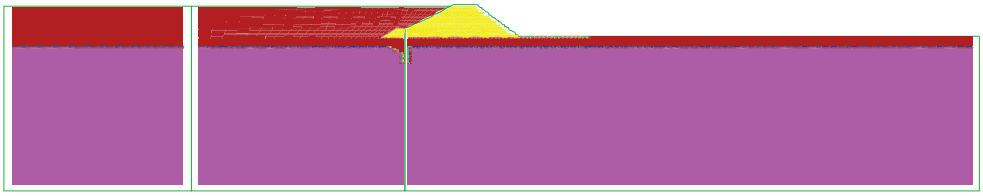

Phase 21

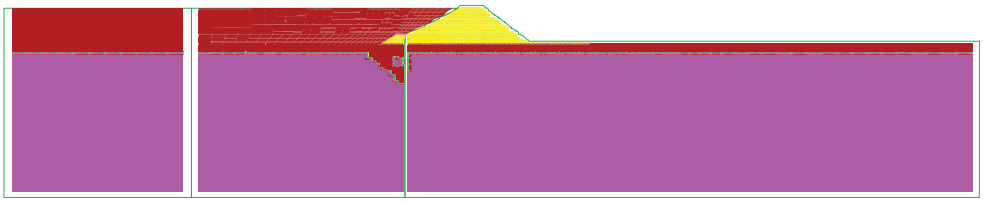

Phase 34 just before final construction phase 35

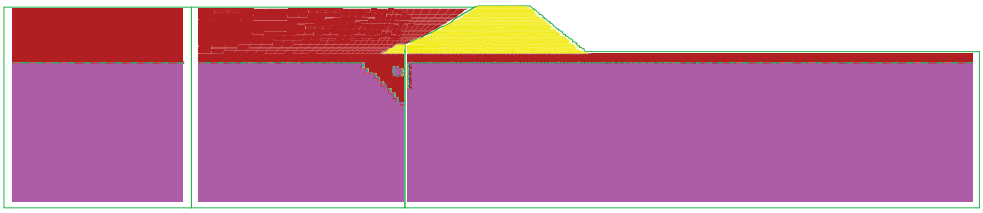

Phase 35P1

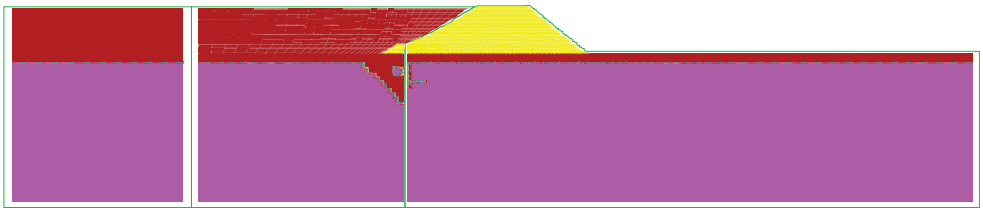

Phase 35P2

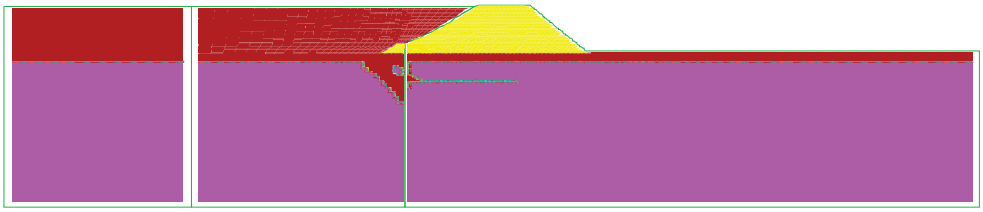

Phase 35P3

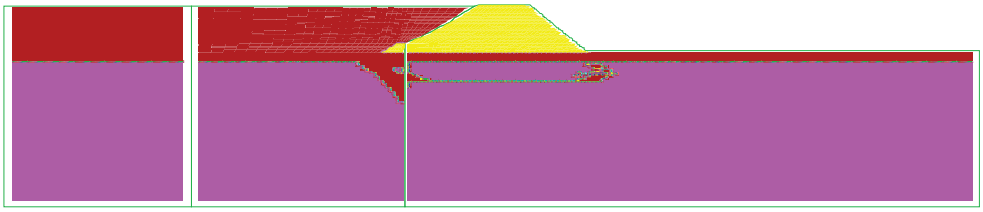

Phase 35P4

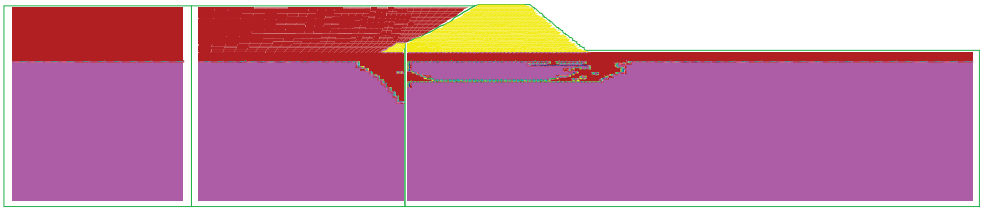

Phase 35P5

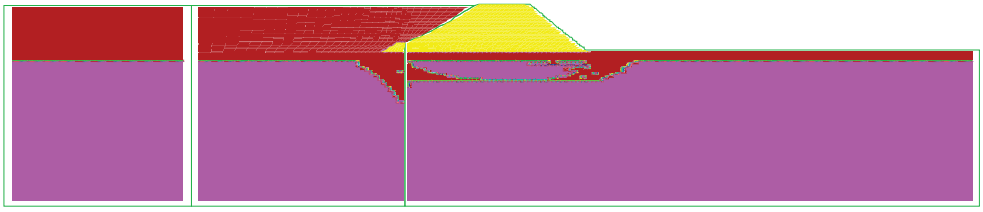

Phase 35P6

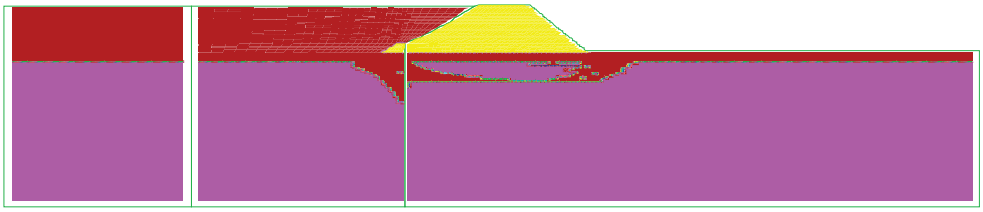

Fig. 6.131 Evolution of cohesion in Aznalcóllar dam failure (Contour interval=5 kPa)

Initial friction

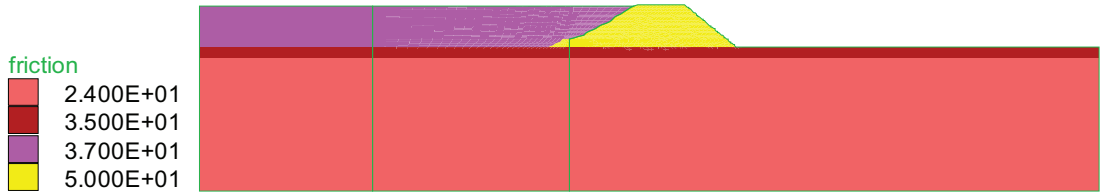

Phase 12

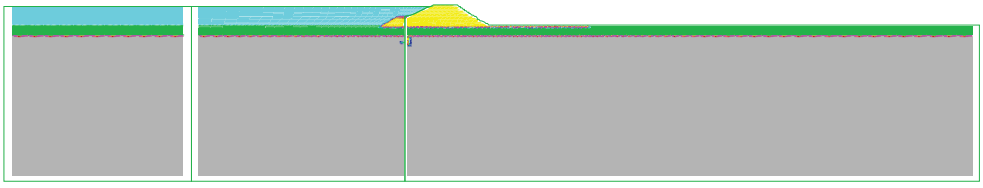

Phase 18

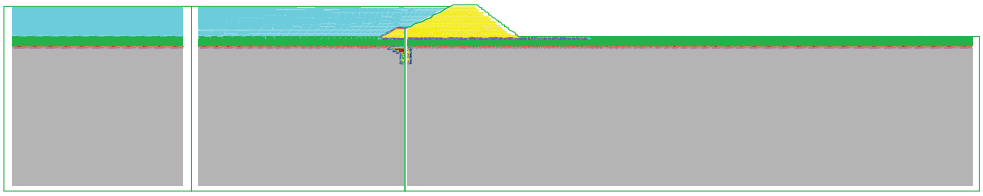

Phase 21

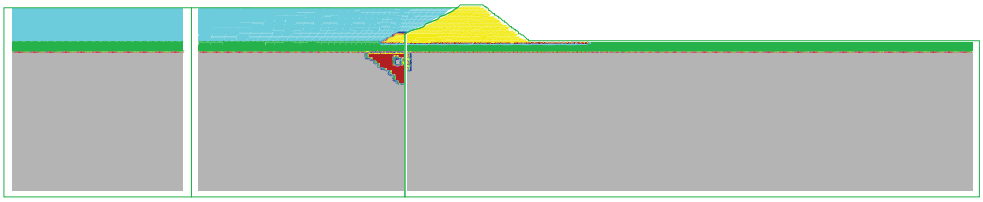

Phase 34 just before final construction phase 35

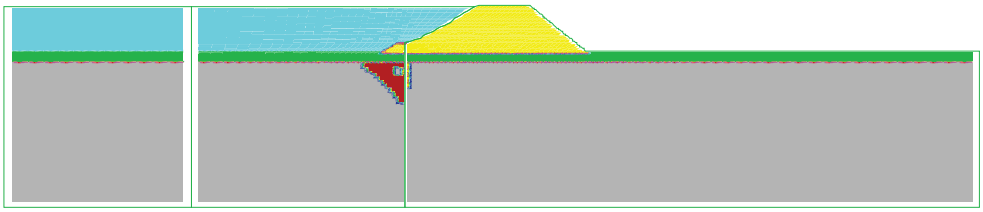

Phase 35P1

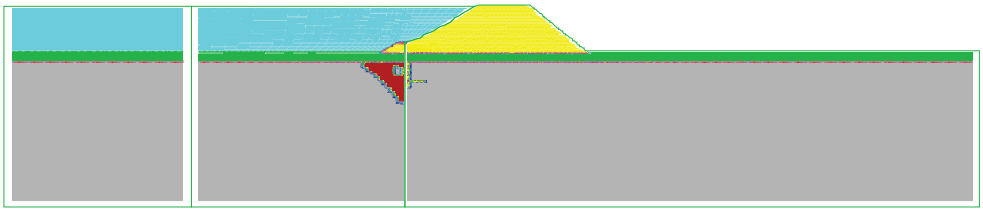

Phase 35P2

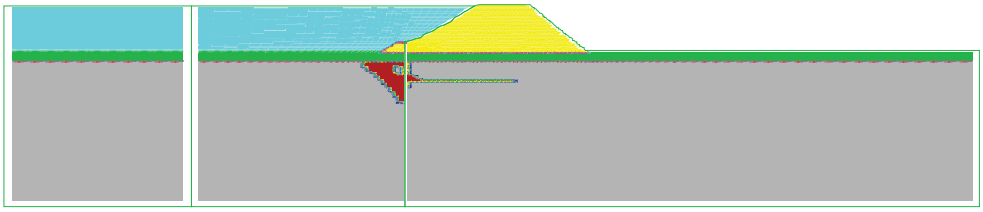

Phase 35P3

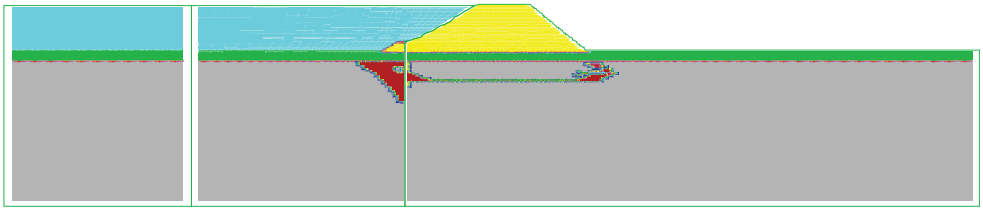

Phase 35P4

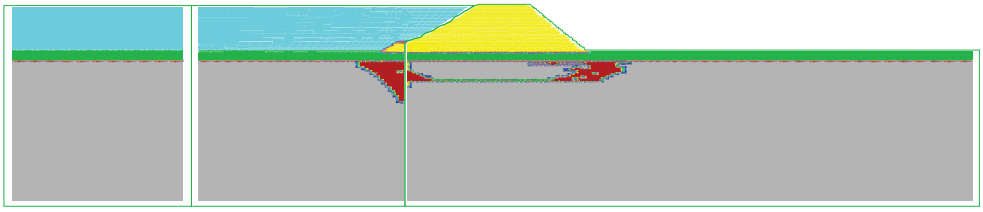

Phase 35P5

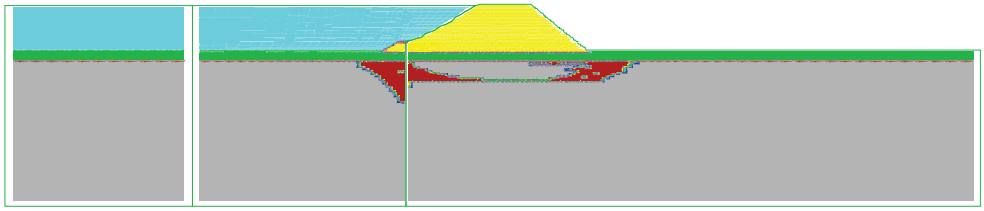

Phase 35P6

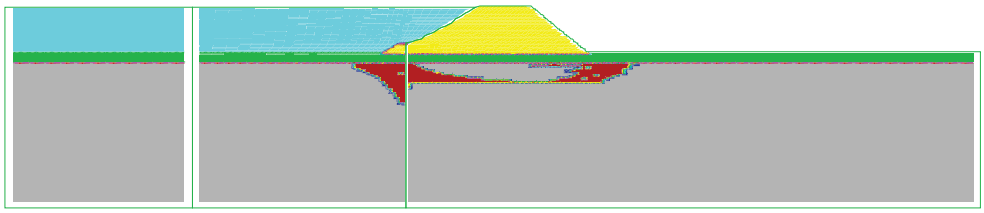

Fig. 6.132 Evolution of friction angle in Aznalcóllar dam failure (Contour interval=1.5°)

6.5.4.5 Geometry of slip surface

The representative position of final slip surface predicted by *FLAC* can be seen in Fig. 6.133, Fig. 6.134 and Fig. 6.135. The predicted slip surface is also consistent with results of shear strain increment, shear strain rate, velocity, horizontal displacement and mobilised strength parameters. Fig. 6.135 also indicates that the slip surface obtained from this model is similar to those derived from previous *FLAC* (analysis L), *FEM* and *LEM* calculations.

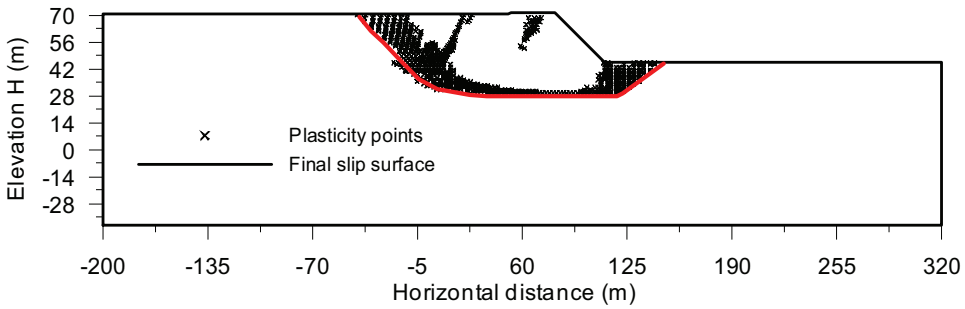

Fig. 6.133 Final slip surface predicted according to plasticity points

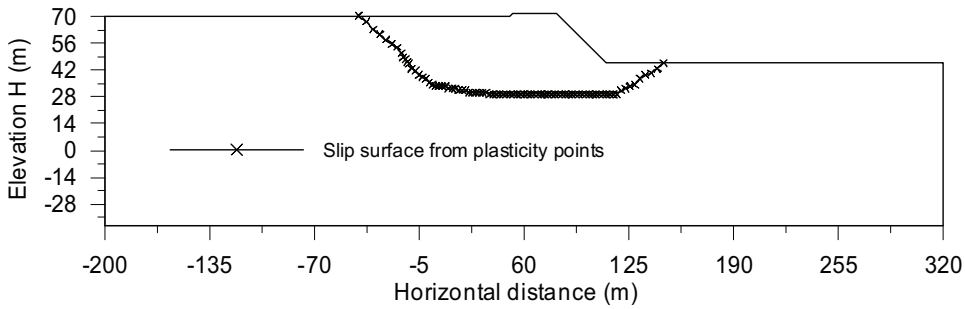

Fig. 6.134 Slip surface obtained directly from plasticity points

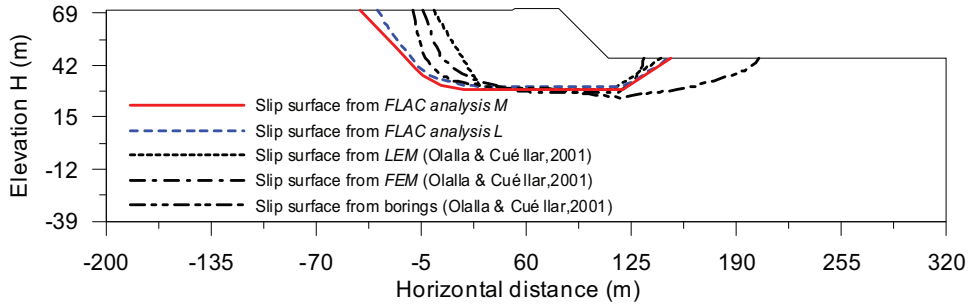

Fig. 6.135 Slip surface: comparison of *FLAC analyses L-M*, *FEM*, *LEM* and field borings

6.5.4.6 Development of representative horizontal displacements

Fig. 6.136 shows the slip surface and representative points (F, G and H) on the downstream dam embankment. As seen in Fig. 6.137, the deformation of these points developed gradually and then increased drastically to very large values when the failure initiated. This higher acceleration of deformation could be the result of quicker softening rate.

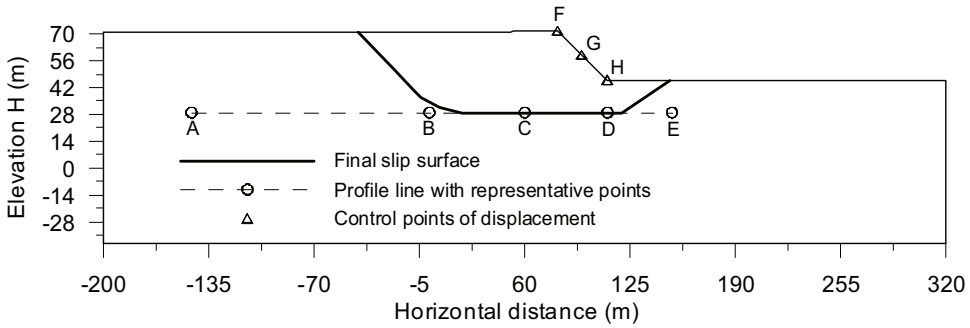

Fig. 6.136 Location of slip surface and representative points

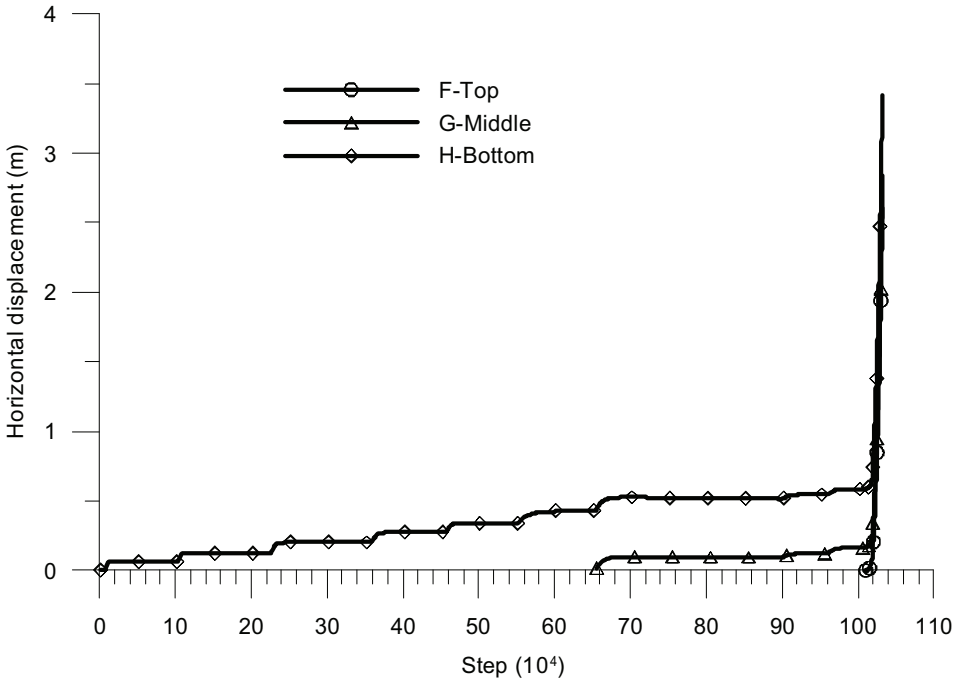

Fig. 6.137 Horizontal displacement development along downstream dam embankment

6.5.4.7 Representative results along profile A-E

Fig. 6.136 also shows the location of profile A-E. The five points A-E under the upstream embankment, the embankment and downstream embankment are 1m lower than those in previous analysis L. The development of pore pressure at points (A-E) is illustrated by Fig. 6.138 and exhibits a similar development tendency as that presented in analysis L.

Fig. 6.139 shows the distribution of pore pressure just at failure along profile A-E. Due to the lower position of profile A-E, the magnitude of the pore water pressure is a little larger than those obtained in analysis L, *FEM* and *LEM* calculations.

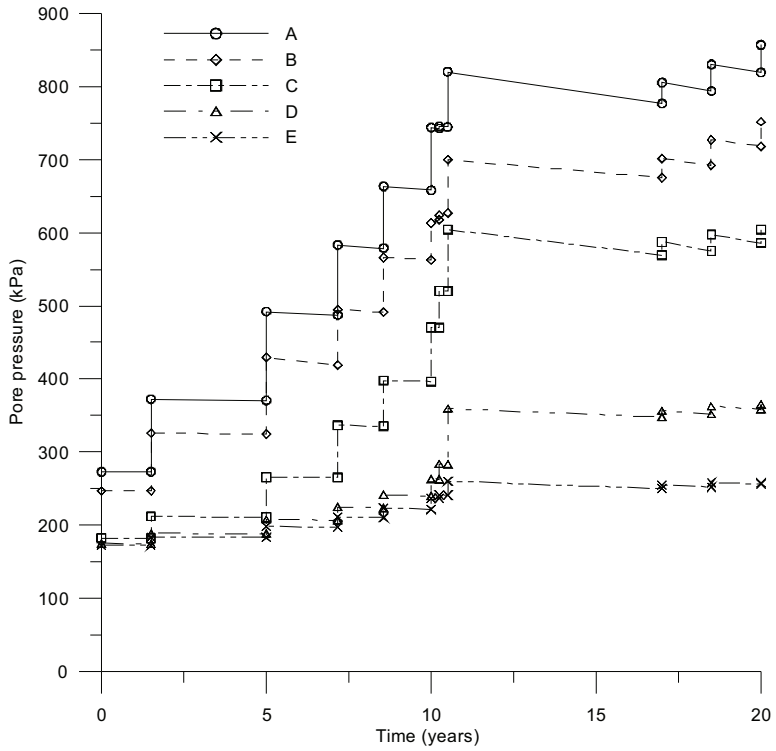

Fig. 6.138 Development of pore pressure at points (A-E) along profile ABCDE

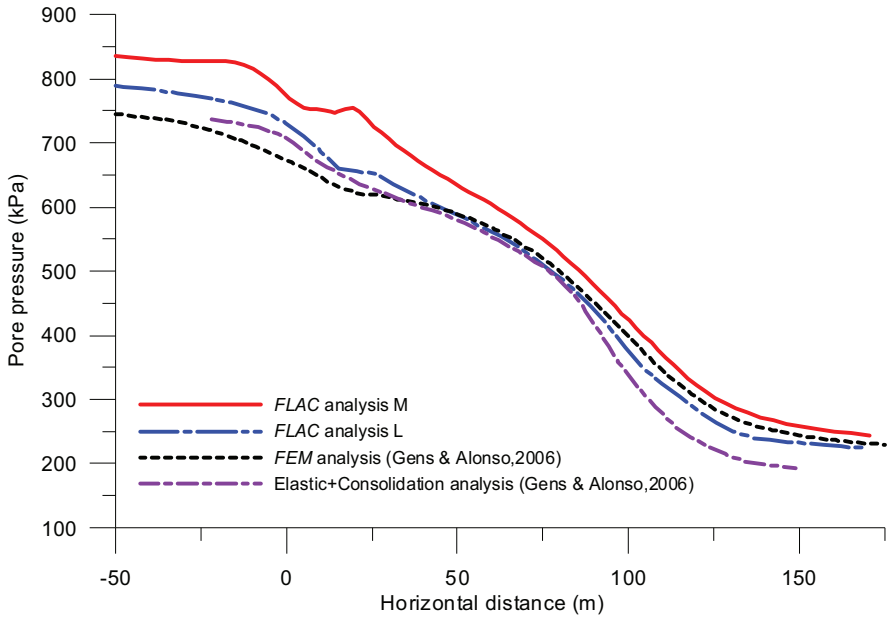

Fig. 6.139 Distribution of pore pressure just at failure along profile A-E

6.5.4.8 Representative results along slip surface

Fig. 6.140 shows the locations of representative points I-P along slip surface.

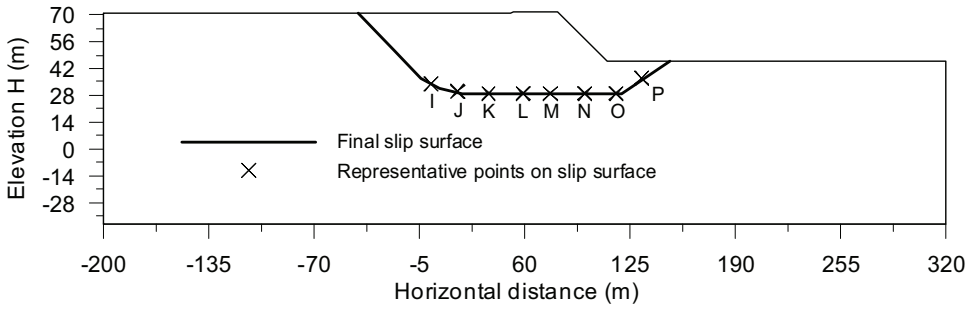

Fig. 6.140 Representative points I-P along slip surface

6.5.4.8.1 Stress path and variation of strength parameters at points I-P

Fig. 6.141-Fig. 6.148 show the stress paths of points I-P along the slip surface in which the clay mass follows the softening model with peak, post-rupture and residual strength parameters of Table 6.6.

Generally, the shear stress rises firstly, then decreases gradually before the initiation of failure and afterwards reduces drastically until reaching the residual envelope at final failure.

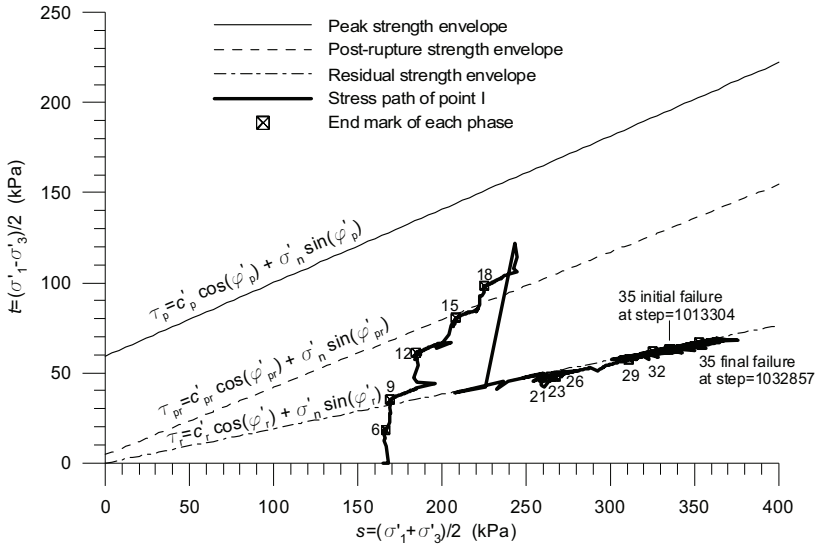

Fig. 6.141 Stress path of point I

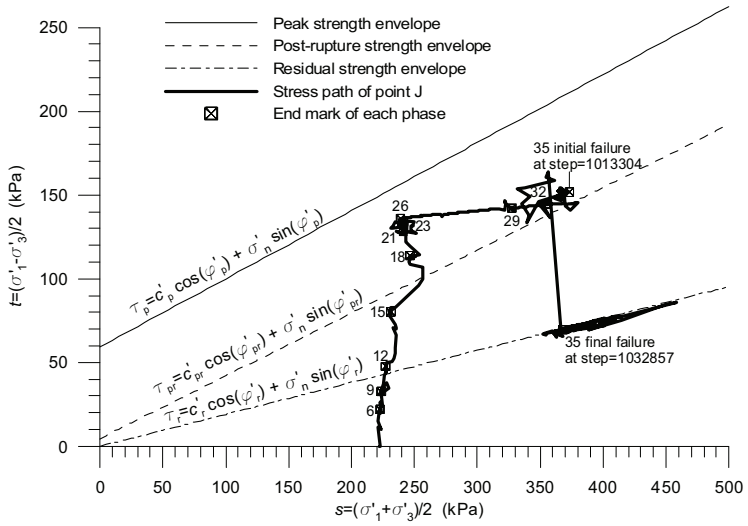

Fig. 6.142 Stress path of point J

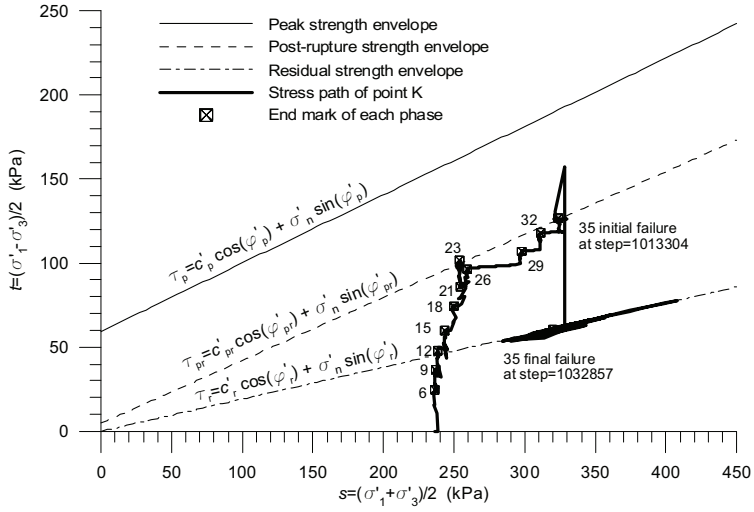

Fig. 6.143 Stress path of point K

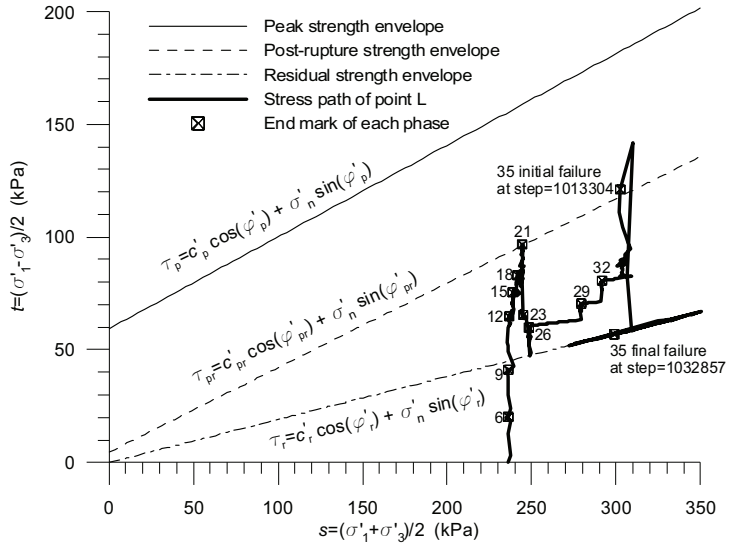

Fig. 6.144 Stress path of point L

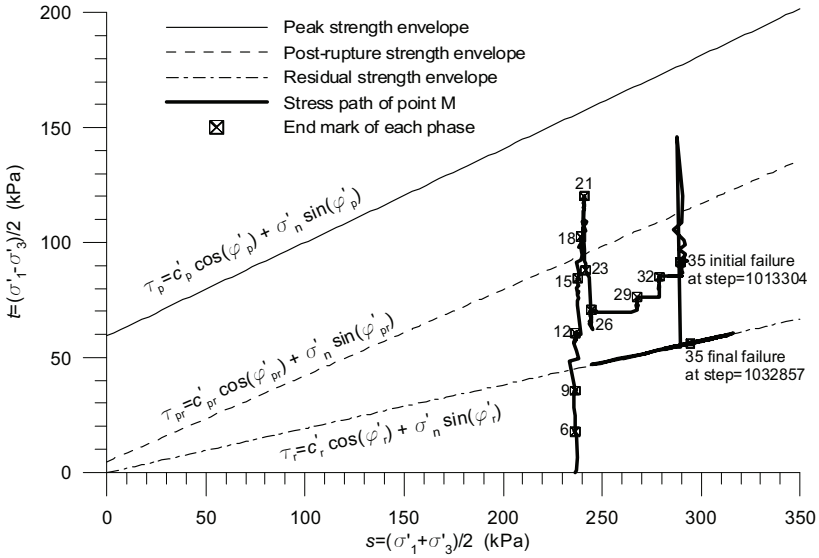

Fig. 6.145 Stress path of point M

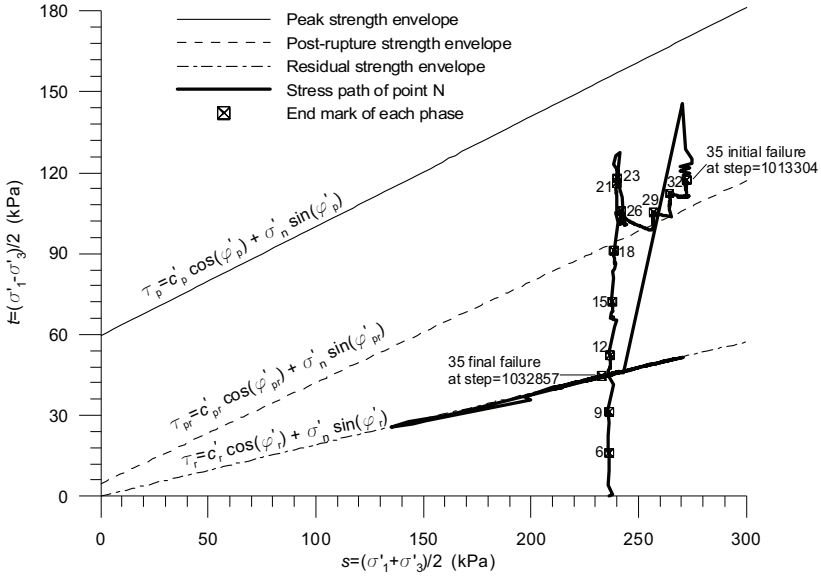

Fig. 6.146 Stress path of point N

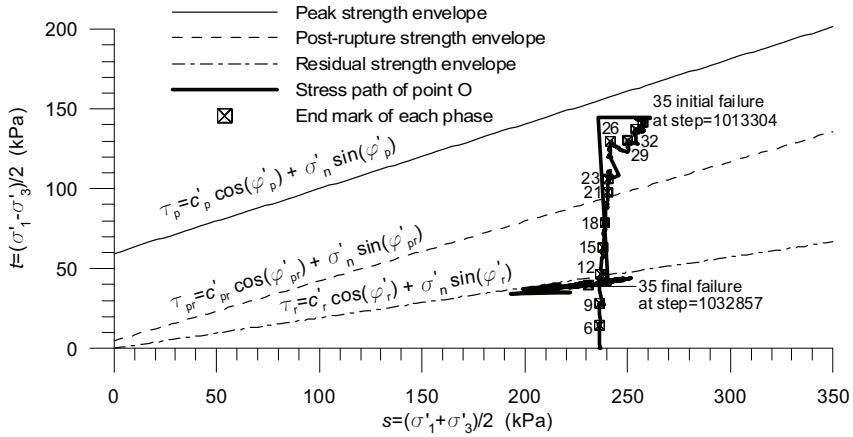

Fig. 6.147 Stress path of point O

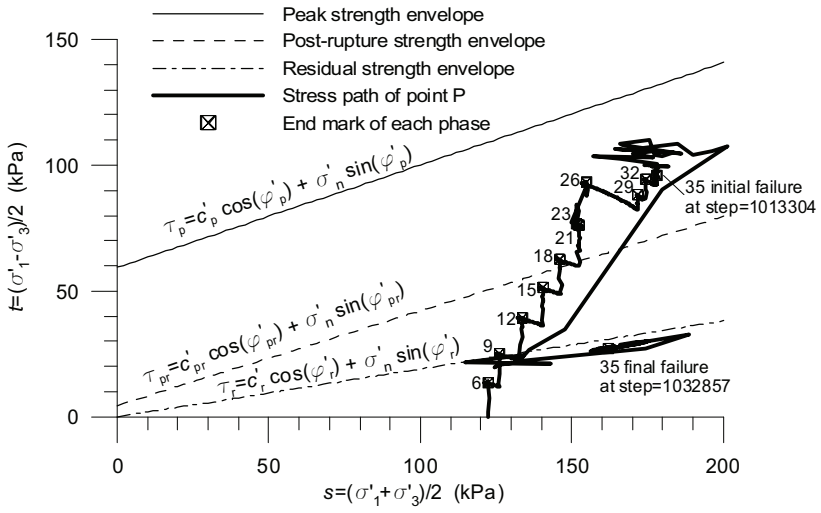

Fig. 6.148 Stress path of point P

6.5.4.8.2 *Development of shear stress with shear strain at representative points—J, L, O and P*

Fig. 6.149-Fig. 6.152 show the curves of shear stress versus shear strain at points J, L, O and P. The shear stress increased firstly and then decreased till residual value. The decrease of shear stress exhibited a two-stage softening feature. At initial failure (step=1013304), shear stress was close to the peak value.

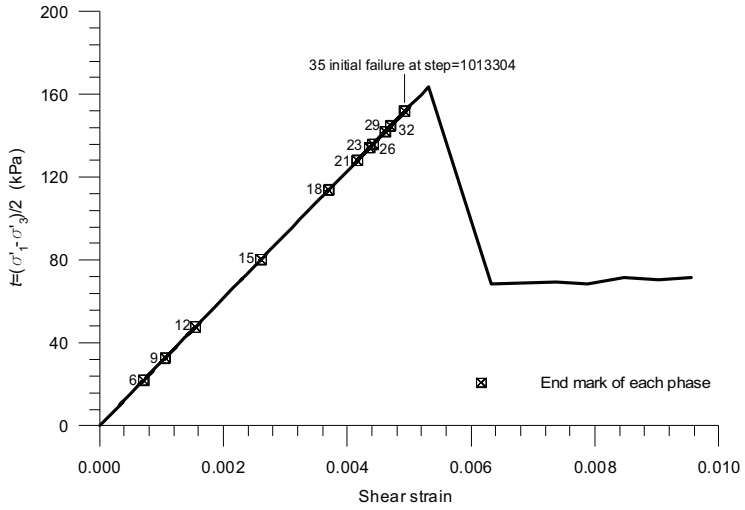

Fig. 6.149 Shear stress vs. shear strain at point J

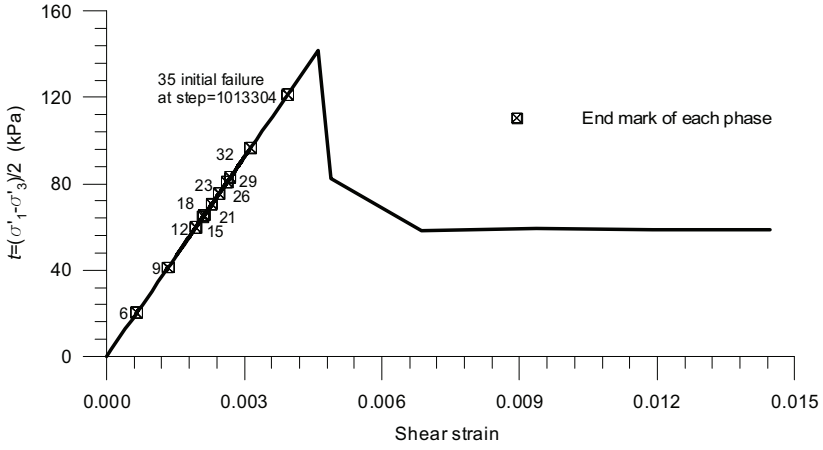

Fig. 6.150 Shear stress vs. shear strain at point L

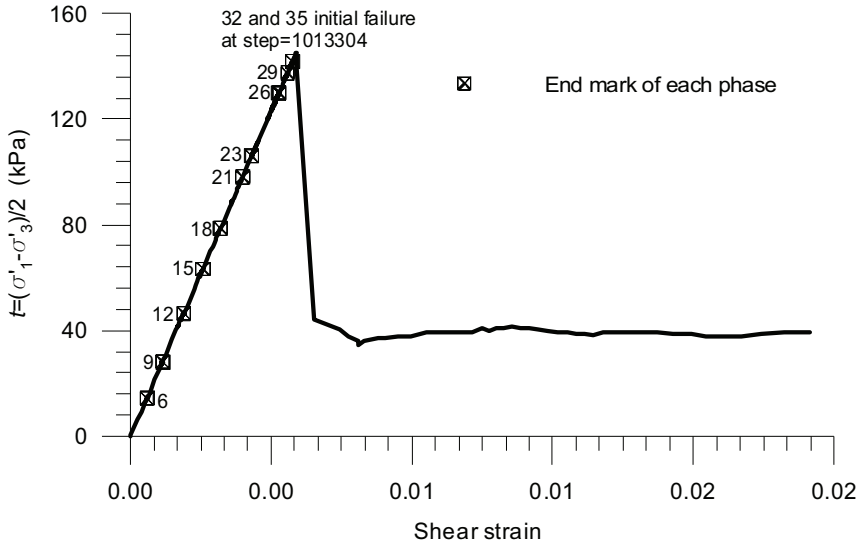

Fig. 6.151 Shear stress vs. shear strain at point O

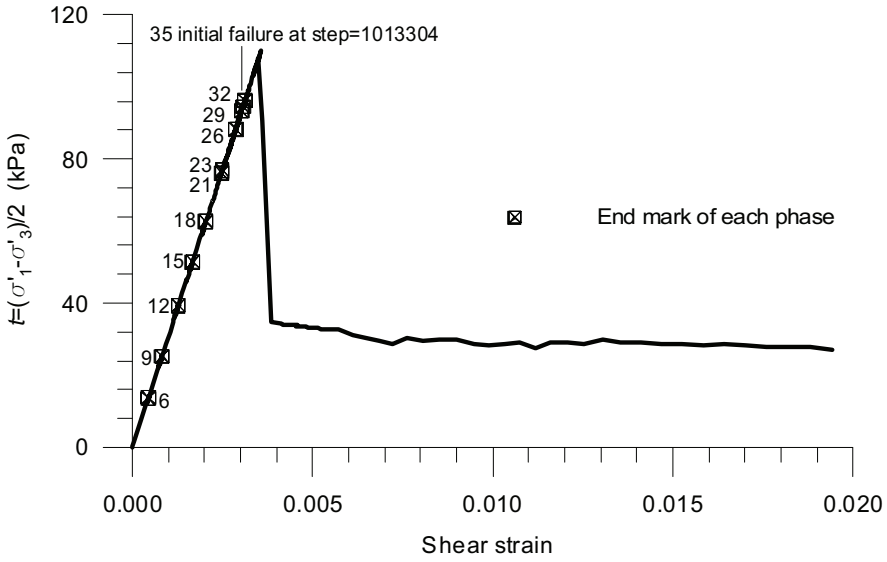

Fig. 6.152 Shear stress vs. shear strain at point P

6.5.4.8.3 Results along slip surface (I-P) in average sense

Fig. 6.153 shows the development of average stress ratio $\tau / \sigma_n^{'}$ along slip surface and Fig. 6.154 presents the development of equivalent mobilised friction angle ($\phi = \arctan(\tau / \sigma_n^{'})$). Both figures exhibit an initial increasing part till phase 21 and a stable part from phase 21 to initial failure. The average stress ratio increased from 0.10 at phase 6 to 0.39 at initial failure and to 0.28 at final failure phase. The corresponding values for equivalent mobilised friction angle are about 5.7°, 21.3° and 15.7° respectively.

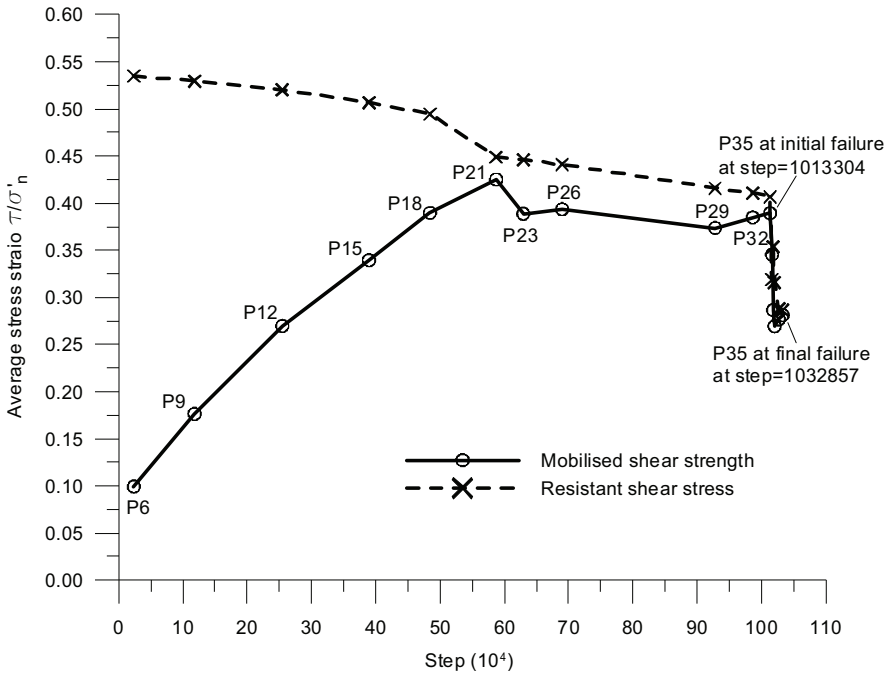

Fig. 6.153 Development of average stress ratio along slip surface

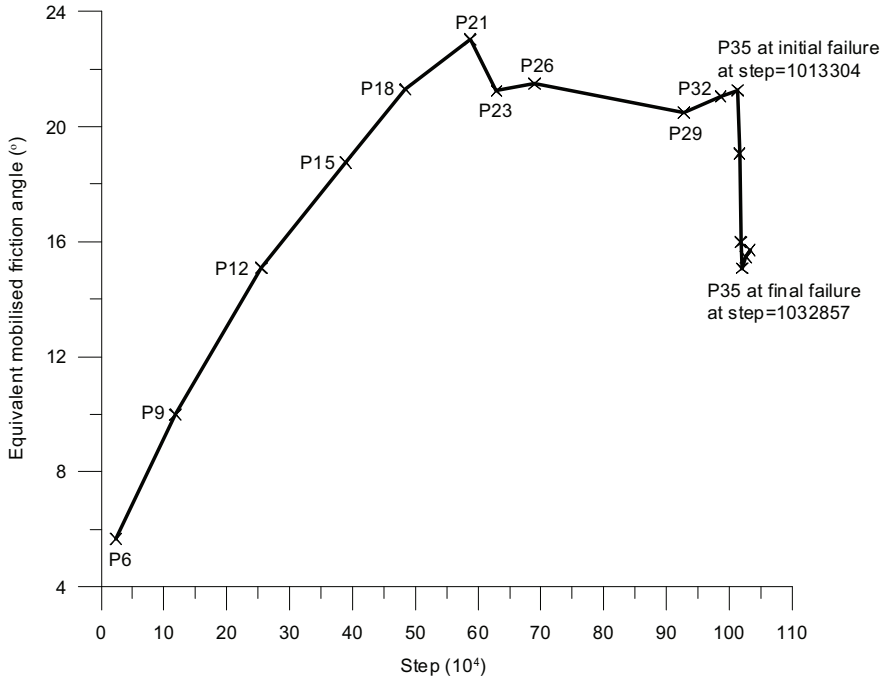

Fig. 6.154 Development of equivalent mobilised friction angle

Fig. 6.153 also presents the average mobilised shear strength along the failure surface. It is evident that the actual resistant shear stress is higher than the mobilised shear strength until reaching the phase 35P1 at initial failure. After that they are almost identical. The average stress ratio $\tau / \sigma_n^{'}$ along slip surface and the equivalent mobilised friction angle increased before initial failure and decreased after initial failure till reaching final failure.

Fig. 6.155 shows the development of average residual factor defined by Eq. (1.3). The residual factor reduced from 1.17 to 0.53 at initial failure and then increased to 0.79 at final failure.

Fig. 6.156 shows the development of average brittleness along slip surface which is calculated from Eq. (2.6) using average shear stresses for peak and mobilised values. This curve exhibits a similar tendency as that shown in Fig. 6.155. The average brittleness decreased from 0.86 to 0.37 at initial failure and then increased to 0.55 at final failure.

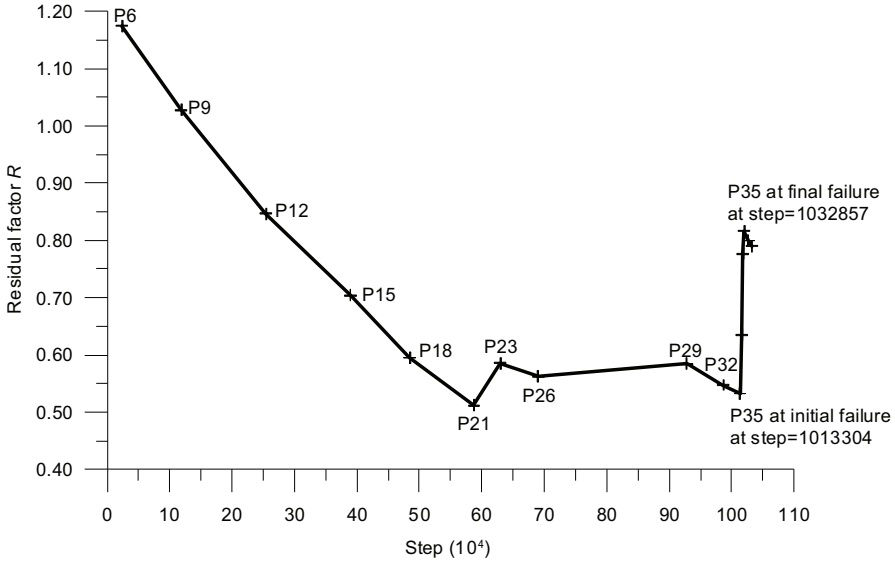

Fig. 6.155 Development of average residual factor

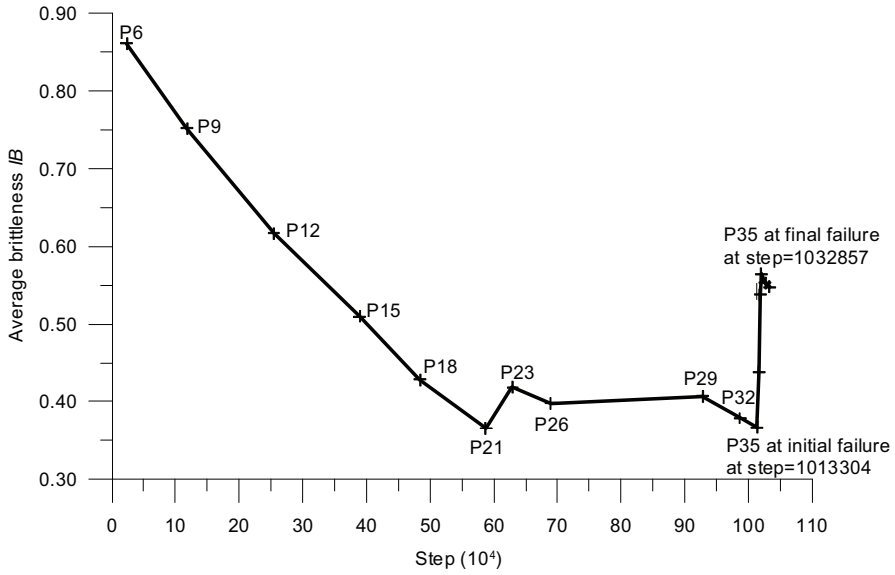

Fig. 6.156 Development of average brittleness along slip surface

Fig. 6.157 shows the development of average pore pressure ratio along slip surface. It can be seen that the average pore pressure ratio increased firstly from 0.45 to 0.59 at phase 26 and then decreased to 0.50 at final failure.

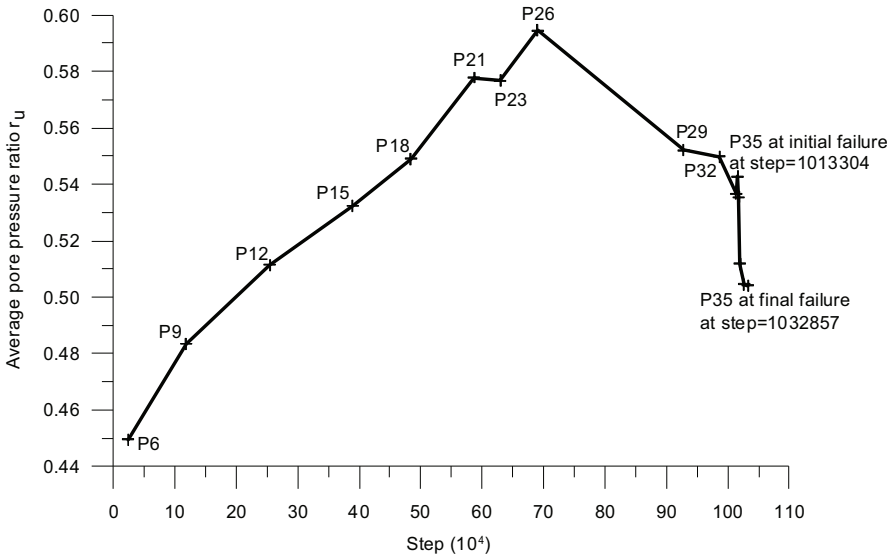

Fig. 6.157 Development of average pore pressure ratio along slip surface

Fig. 6.158 shows the development of average stress path along the slip surface. Also shown in Fig. 6.158 are the corresponding shear strength stress envelopes at peak, post-rupture and residual states under relevant effective normal stress $\sigma_n^{'}$.

Fig. 6.158 indicates that the average shear stress augmented from the first loading phase to the initial failure and then diminished till final failure. At the beginning of failure, the stress points were very close to the post-rupture strength envelope. Afterwards, the average shear stress along the slip surface reduced nearly vertically with very little change in average normal effective stress.

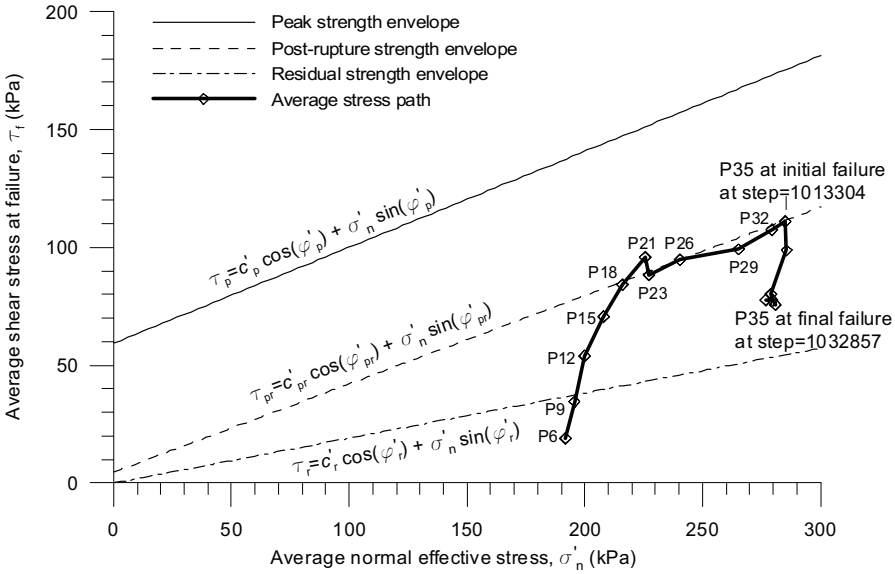

Fig. 6.158 Development of average stress path along slip surface

Fig. 6.159 and Fig. 6.160 show the pre-failure distribution of current shear stress along the failure surface below dam embankment at phase 23 (step=629502) and phase 26 (step=689858). In these figures the peak, post-rupture, residual and current strength values calculated from Eq. (5.3) with the corresponding strength parameters

are also shown. It can be seen that the value of shear stress is intermediate between peak and residual values.

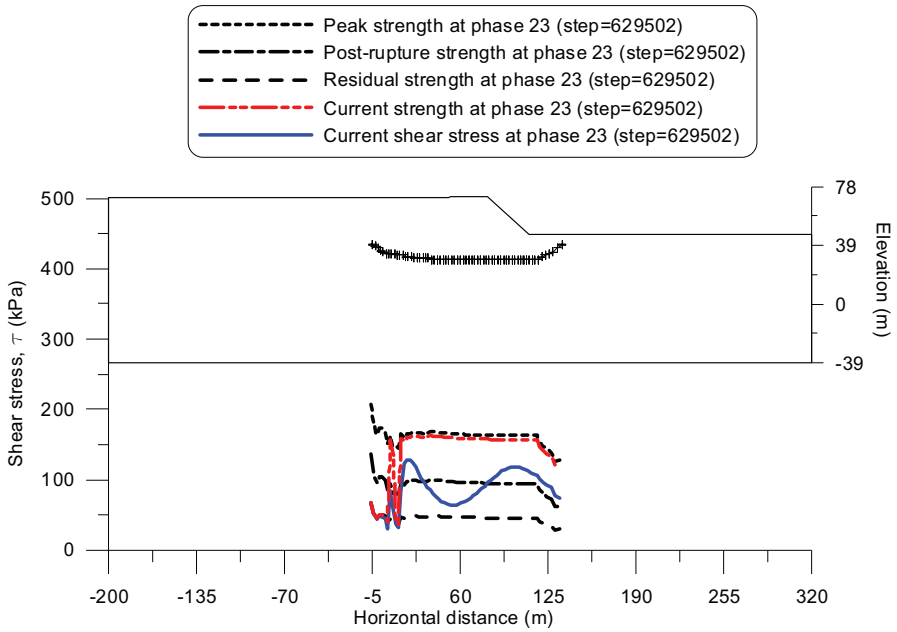

Fig. 6.159 Distribution of shear stress along failure surface at phase 23 (Step=629502)

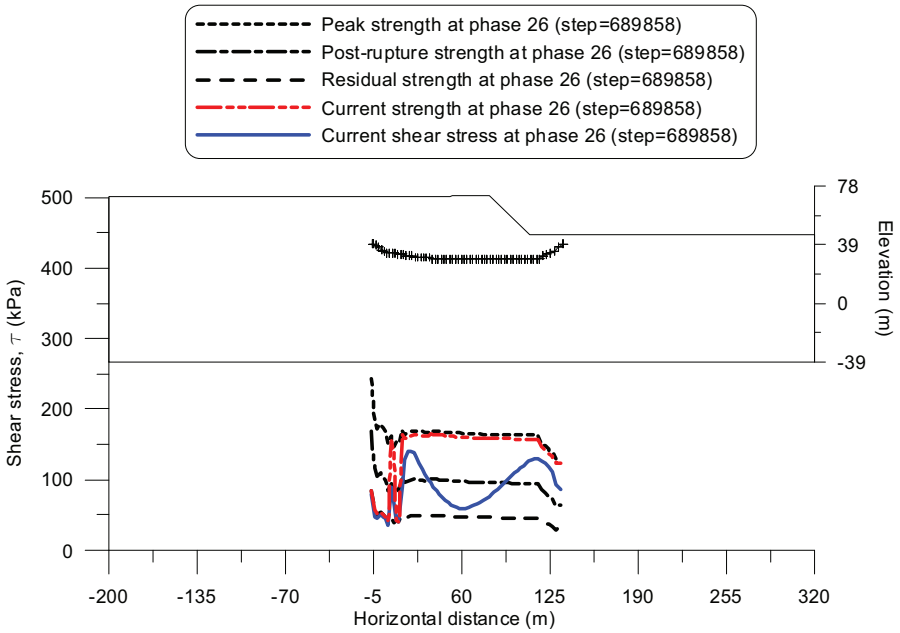

Fig. 6.160 Distribution of shear stress along failure surface at phase 26 (Step=689858)

Fig. 6.161 presents the distribution of current shear stress along failure surface below dam embankment just at failure (step=1013304). The corresponding distribution of shear strength at current, peak, post-rupture and residual states under relevant effective normal stress $\sigma_n^{'}$ are also shown in Fig. 6.161. It can be seen that the value of shear stress is intermediate between the peak and residual values.

Fig. 6.162-Fig. 6.164 show the post-failure distribution of current shear stress along the failure surface. At phase 35P2 (step=1016304) and phase 35P3 (step=1018304),

the shear stress began to reach residual envelop firstly along the upstream part of slip surface below diaphragm wall and then propagated the softening process till residual state towards the downstream part of slip surface. At final failure phase 35P6 (step=1032857), the current shear stress is almost the same as that calculated with residual strength parameters, which confirms the mechanism of progressive failure of Aznalcóllar dam.

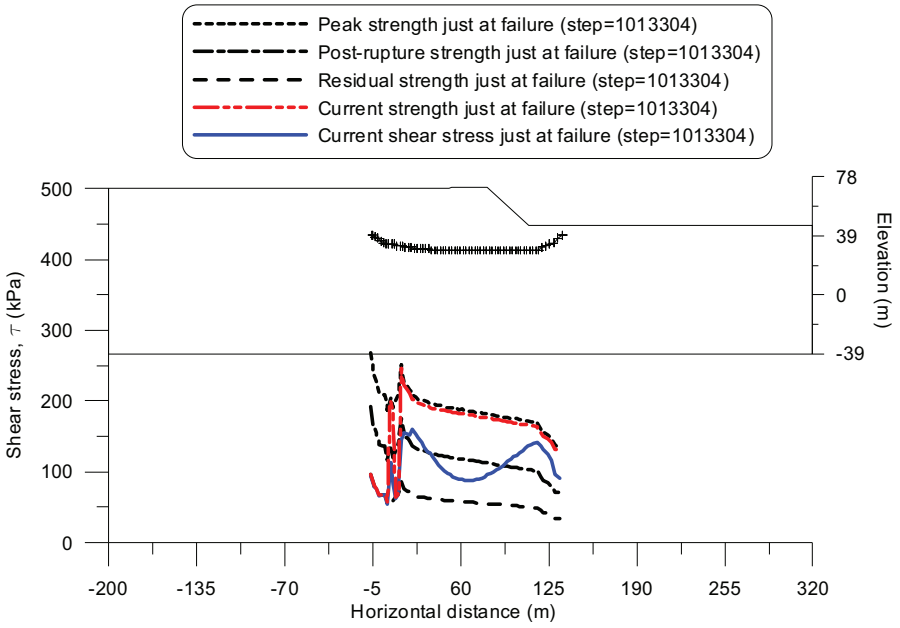

Fig. 6.161 Distribution of shear stress along failure surface at initial failure phase (step=1013304)

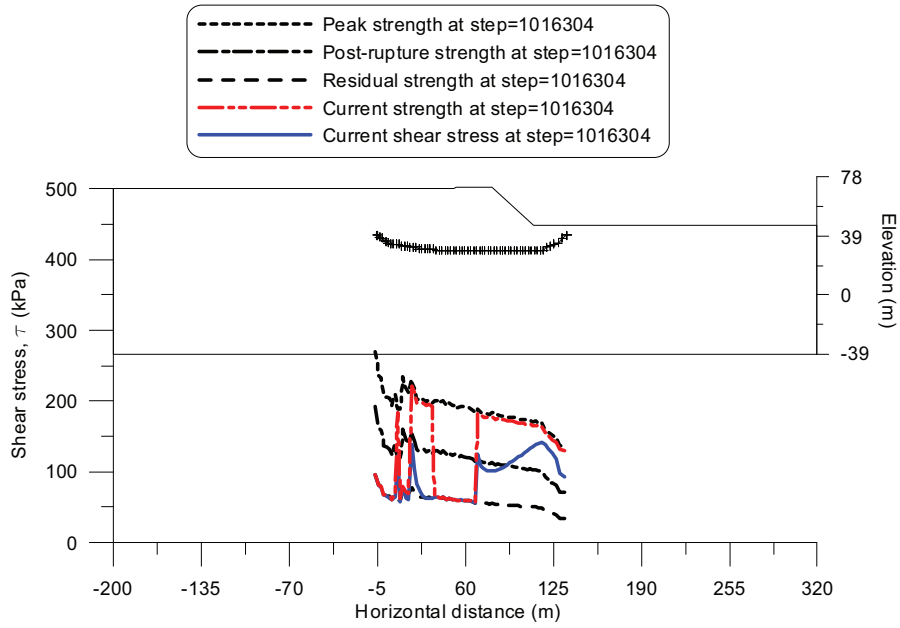

Fig. 6.162 Distribution of shear stress along failure surface at phase 35P2 (step=1016304)

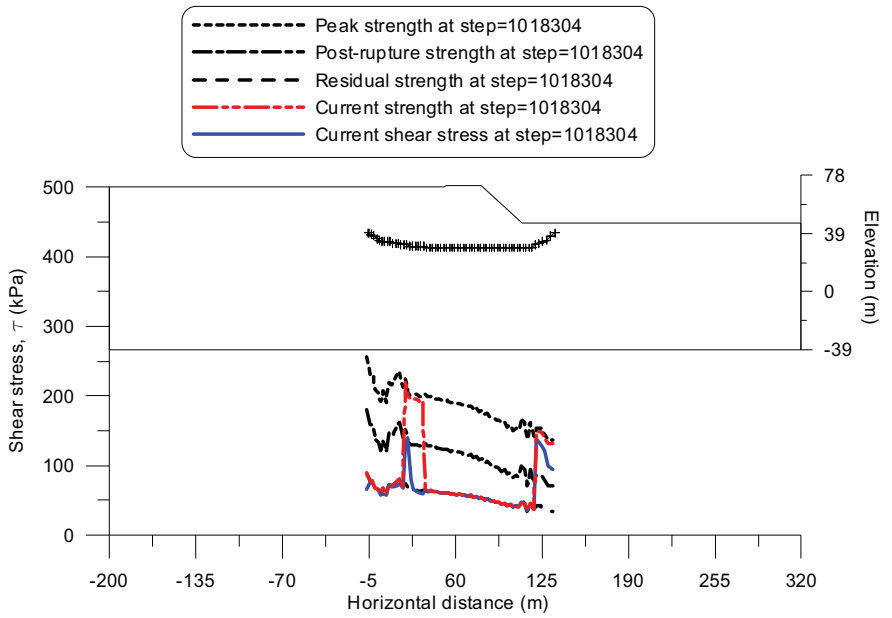

Fig. 6.163 Distribution of shear stress along failure surface at phase 35P3 (step=1018304)

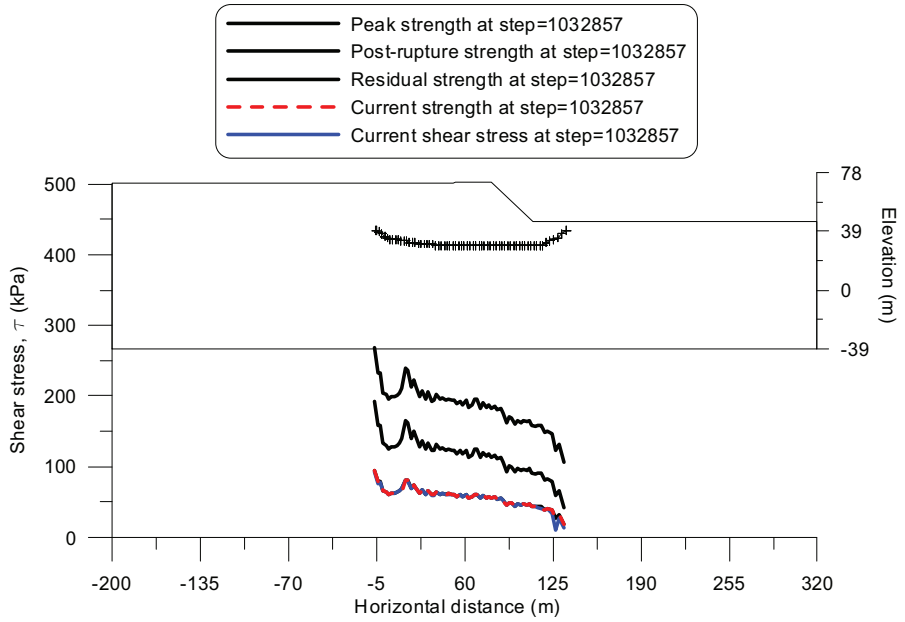

Fig. 6.164 Distribution of shear stress along failure surface at final failure phase (step=1032857)

6.5.5 Supplementary analyses

In this section, two supplementary analyses applying individually homogeneous and inhomogeneous assumptions are performed.

6.5.5.1 Supplementary analysis with homogeneous assumption

In this section, analysis R is presented by applying the softening rates shown in Table 6.13 to homogeneous blue clay.

In analysis R, the dam did not fail till the final construction stage (seen in Fig. 6.165 and Fig. 6.166). This demonstrates that with the slower softening rate dam failure can not be induced.

Table 6.13 Shear strength parameters and plastic shear strain limits for blue clay mass

Peak state	$c_p^{'} = 65\text{kPa},\ \phi_p^{'} = 24°,\ \gamma_p = 0$
Post-rupture state	$c_{pr}^{'} = 5\text{kPa},\ \phi_{pr}^{'} = 22°,\ \gamma_{pr} = 0.005$
Residual state	$c_r^{'} = 0\text{kPa},\ \phi_r^{'} = 11°,\ \gamma_r = 0.135$

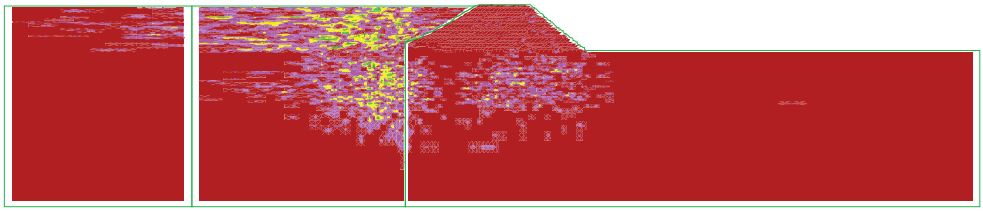

Fig. 6.165 Shear strain rate at final phase in supplementary analysis R

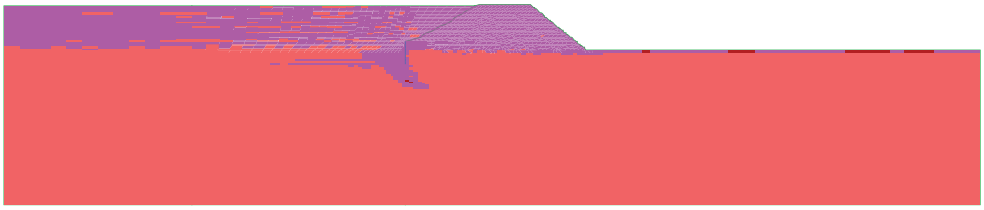

Fig. 6.166 Plastic zones final phase in supplementary analysis R

6.5.5.2 Supplementary analysis with inhomogeneous assumption

In this section, inhomogeneous hypothesis is proposed in analysis S. The corresponding model parameters for blue clay mass and weak layer are shown in Table 6.14 and Table 6.15.

In analysis S, the dam failed at phase 21 (seen in Fig. 6.167 and Fig. 6.168) with failure surface located at y=29 m. This indicates that the more rapid softening rate will cause an earlier dam failure.

Table 6.14 Shear strength parameters and plastic shear strain limits for blue clay mass

Peak state	$c_p^{'} = 65\text{kPa},\ \phi_p^{'} = 24°,\ \gamma_p = 0$
Post-rupture state	$c_{pr}^{'} = 5\text{kPa},\ \phi_{pr}^{'} = 22°,\ \gamma_{pr} = 0.00018$
Residual state	$c_r^{'} = 0\text{kPa},\ \phi_r^{'} = 11°,\ \gamma_r = 0.00350$

Table 6.15 Shear strength parameters and plastic shear strain limits for weak layer

Initial strength	$c_p^{'} = 5\text{kPa},\ \phi_p^{'} = 22°,\ \gamma_p = 0$
Final residual state	$c_r^{'} = 0\text{kPa},\ \phi_r^{'} = 11°,\ \gamma_r = 0.00332$

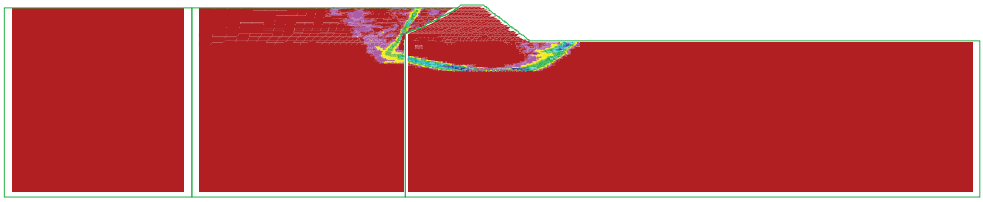

Fig. 6.167 Shear strain rate at final phase in supplementary analysis S

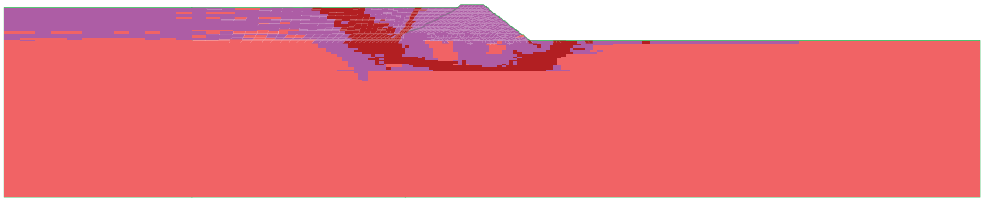

Fig. 6.168 Plastic zones final phase in supplementary analysis S

6.6 Summary

In this chapter, the Aznalcóllar dam failure has been simulated using the two-stage softening model incorporating the post-rupture strength concept under both inhomogeneous and homogeneous hypotheses with different softening rates.

All the simulation results demonstrate:

(1) Analyses under both inhomogeneous and homogeneous hypotheses reproduced well the Aznalcóllar dam failure. The mechanism of Aznalcóllar dam failure is deemed to be progressive failure mainly due to the softening of Guadalquivir blue clay. In analysis with the inhomogeneous hypothesis, the critical failure plane may be assumed to be at post-rupture strength. In the analysis with homogeneous hypothesis, however, failure only happened with a much quicker softening rate than that adopted in analysis with the inhomogeneous hypothesis.

(2) The slip surface can be deduced directly from shear strain rate, shear strain increment, displacement and velocity plots. The slip surfaces predicted in analyses under both inhomogeneous and homogeneous hypotheses are similar with only 1m difference of slip surface depth. In addition, the results of simulations with several weak layers confirmed further the location of the critical surface.

(3) The failure initiated just after the construction of the final dam layer and can be captured clearly through plots of development curves of velocity and shear strain rate. Afterwards, the dam moved gradually till the sudden occurrence of post-failure acceleration of displacement and shear strain increment when the final slip surface formed completely. The pattern of development of displacements suggests that the monitoring of displacements and/or deformations may not be useful in this case.

(4) The whole failure process can be explained directly by the development of shear strain rate, shear strain increment, displacement, velocity and strength parameters.

In analysis with inhomogeneous assumption, yield points started to form at phase 15 near the upstream of the diaphragm wall and then progressed along the weak layer starting from both the downstream part beneath the dam toe and the upstream part close to the toe of diaphragm wall. Afterwards failure extended upward till the downstream ground surface (Phase 26-Phase 34). At phase 34 some yield points existed but no general failure occurred. At phase 35P1 general failure occurred. Failure extended subsequently along the weak layer progressively until the downstream failure part along the horizontal weak layer connected with the upstream failure part. Eventually failure developed upwards till reaching the upstream tailings surface and the final continuous failure surface came into being with an acceleration of large deformations.

In the analysis with homogeneous assumption, yield points began to concentrate in upstream zones below and behind diaphragm wall. At phase 35P1, failure initiated firstly close to the diaphragm wall and then extended horizontally toward the downstream part of dam. Afterwards failure developed upwards till reaching the upstream tailings surface and thus formed the continuous failure surface.

(5) There is very limited dissipation of pore water pressure and small extent of consolidation due to the low permeability of the clay. This is demonstrated by the development of pore pressure along profile A-E on the slip surface. The magnitude of the pore water pressure development agrees with the added dam and tailings weight above the points analysed. The distribution of pore water pressure at failure is consistent with the results of the numerical analyses performed previously and with the simplified elastic-consolidation analyses.

(6) In the analyses under both inhomogeneous and homogeneous hypotheses, the post-failure development of average stress ratio along slip surface reduced from 0.405/0.39 at the beginning of failure to 0.29/0.28 at the final failure with corresponding values of equivalent mobilised friction angle to be 22.05°/21.3° (almost the same as post-rupture value) and 16.2°/15.7° (half way between post-rupture and residual values). The corresponding residual factor R at initial failure is about 0.51/0.53 which is very close to that calculated by Gens and Alonso (2006). It then increased to 0.78/0.79 at the final failure implying that the shear stress is half way between peak and residual values. Naturally, the brittle nature of clay could underlie the progressive failure process with reduction of available strength during the construction of the dam. The average brittleness increased from 0.35/0.37 at the beginning of failure to 0.53/0.55 at final failure due to the reduction of shear stress along slip surface. At the same time, the brittleness of the clay and the low residual friction angle indicate that, once the failure has initiated, there is a potential for an accelerated motion due to the progressive loss of clay strength. This acceleration is confirmed by the rapid increase in average stress ratio, residual factor and average brittleness and characterizes the final failure.

(7) The average stress path along the slip surface shows that, at the beginning of failure, stress points lay close to the post-rupture strength envelope. Afterwards the average shear stress along the slip surface reduced with very little change in effective normal stress.

(8) The distribution of shear stress along the failure surface was intermediate between the peak and residual values. Whereas at final failure the shear stress is almost the same as residual value, which confirms further the mechanism of progressive failure of Aznalcóllar dam. The stress paths and variations of strength parameters with plastic shear strain at points I-P along the slip surface illustrate also the progressive failure mechanism. All these results indicate that at final failure stage of the analysis most of the slip surface is at residual state, especially on the horizontal part.

(9) Furthermore, it should be noted that the Aznalcóllar dam failure is sensitive to the softening rate denoted by γ_{pr} and γ_r. Larger rates will induce earlier failure and no failure will occur with slow softening rate. Only an appropriate value of softening rate can cause failure at the final phase under both inhomogeneous and homogeneous hypotheses.

Chapter 7. Analytical solution to cylindrical cavity expansion in stiff clays with the two-stage softening model

7.1 Introduction

Over the last 50 years, cavity expansion theory has been widely used in the field of geotechnical engineering such as in the bearing capacity of deep foundations (Vesic, 1977; Randolph et al., 1979), installation of driven piles (Randolph et al., 1994; White, 2004), stress distribution around tunnels (Li et al., 2004), interpretations of pressuremeter tests (Monnet, 2006) and cone penetration tests (Battaglio et al., 1981; Ramesh & John, 1986; Mayne, 1991; Salgado et al., 1997; Chang et al., 1998).

The classical elastoplastic cylindrical cavity expansion theory (Vesic, 1972) has provided a series of applications in theoretical analysis and engineering practice. However, as stated by (Wang & Xiong, 1999; Zheng et al., 2004), it has some disadvantages:

(1) The applied perfect elastoplastic model can not reproduce well the complex stress-strain relation of actual soils.

(2) The plastic volumetric strain is considered to be known. But in engineering practice, it must be determined according to its relationship with stress components.

(3) Volumetric strain is assumed to be positive and can not consider volume dilation in plastic regions induced by shear.

Meanwhile, soils such as stiff clays, dense sand and even rock, exhibit brittle properties and strain-softening characteristics. Solutions of cylindrical cavity expansion including strain softening have already been studied. Brown et al. (1983) developed a stepwise sequence of calculations for brittle-plastic rocks and Carter & Yeung (1985) presented a numerical solution for strain-weakening materials.

Jiang & Shen (1995,1996a, 1996b, 1996c) introduced a stress-dropping strain-softening model, implying an immediate stress reduction from peak value to residual strength, into cylindrical cavity expansion theory and provided the corresponding explicit solutions to stress, strain and displacement fields. This method has been used to analyse the bearing capacity of a foundation with strain-softening behaviour. In addition, Jiang & Shen (1997) also developed a one-stage linear softening model based on conventional triaxial compression tests and presented the corresponding calculation procedure. This model has been adopted by Zheng J.J. et al. (2004) to deduce an analytical solution to cylindrical cavity expansion and applied by Li et al. (2004) to the analysis of cavity of surrounding rocks.

Carter & Yeung (1985), Cividini & Gioda (1992), Potts et al. (1987, 1990 and 1997), Dounias et al (1988, 1996) and Troncone (2005) used a generalised non-linear strain-softening and strain-hardening soil model based on Mohr-Coulomb yield criterion. This is an elastoplastic model in which softening behaviour is accounted for by allowing the angle of shearing resistance, ϕ', and the apparent cohesion intercept, c', to vary from the initial peak value to the residual flow phase with the deviatoric plastic strain invariant, ε_D^P. For the cylindrical cavity expansion, the deviatoric plastic strain is replaced by radial strain. However, such models assume one-stage linear softening for strength parameters c' and ϕ' and unable to distinguish the two-stage softening feature and post-rupture strength point of stiff clays.

This chapter mainly aims to develop a simplified quadralinear elastic—strain-softening—residual-plastic model for stiff overconsolidated clays comprising two-stage linear softening based on the results of laboratory tests. The Mohr-Coulomb yield criterion is used for the initial, intermediate post-rupture and final plastic flow stage. Simplified yield functions for the two-stage strain-softening phases are constructed on the basis of experimental stress-strain curves. Meanwhile, the relevant flow rules are defined according to the major principal strain versus minor principal strain relationship. By integrating the equilibrium equation, boundary conditions and establishing continuities of stress, strain and displacements, the analytical solutions to the limit pressure, the stress, strain, and displacement fields for the expansion of a cylindrical cavity are presented. Afterwards, some examples are calculated and a parametric study is performed.

7.2 Governing equations and simplified quadralinear model

Adopting a similar method as used by Wang & Xiong (1999) and Zheng et al. (2004), the stress-strain curve (Fig. 2.21) for stiff overconsolidated clays can be simplified into a quadralinear curve as shown in Fig. 7.1. Under the surrounding pressure σ_3, the soil responds as a linearly elastic material before peak strength. After the peak value, the strength decreases linearly and rapidly from peak value to post-rupture strength and then reaches residual strength at a relatively slower rate (Fig. 7.1).

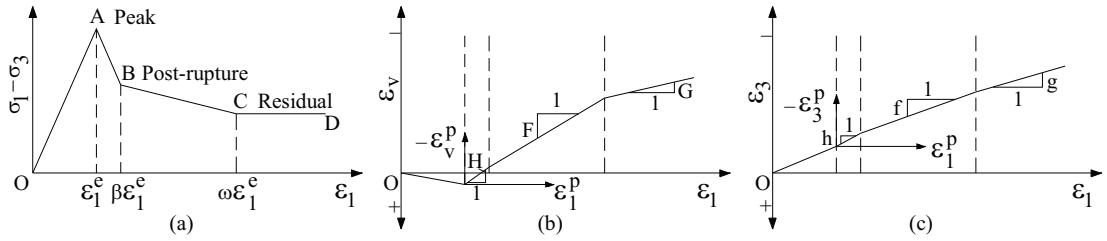

Fig. 7.1 Simplified model from test curves

The curves of $\varepsilon_v - \varepsilon_1$ and $\varepsilon_3 - \varepsilon_1$ are also simulated by a quadralinear model. ε_v, ε_1 and ε_3 are respectively the bulk strain, the major principal strain and the minor principal strain. And ε_v^p, ε_1^p and ε_3^p denote the corresponding plastic strains after peak strength. Compressive strains are considered positive. For the calibration of the simplified quadralinear model from test curves, the values of the parameters

$\beta, \omega, H, F, G, h, f, g$ can be obtained through the slope of the corresponding straight lines (Fig. 7.1). Among these parameters, h, f, g are non-negative proportionality coefficients. They may be equal to, smaller than or greater than 1.0 and represent, respectively, incompressibility, shear dilation and shear contraction.

In cylindrical cavity expansion, the radial stress σ_r corresponds to the major principal stress σ_1 and the circumferential stress σ_θ corresponds to the minor principal stress σ_3. The same rule holds for strains.

As assumed by Carter & Yeung (1985), the cavity expansion occurs in a medium of infinite extent. Initially, at time $t = 0$, the cavity has a radius R_i, which is usually very small compared with the ultimate radius R_u, and internal pressure p_0. Everywhere in the surrounding material the radial and circumferential stress components are compressive and have magnitude p_0.

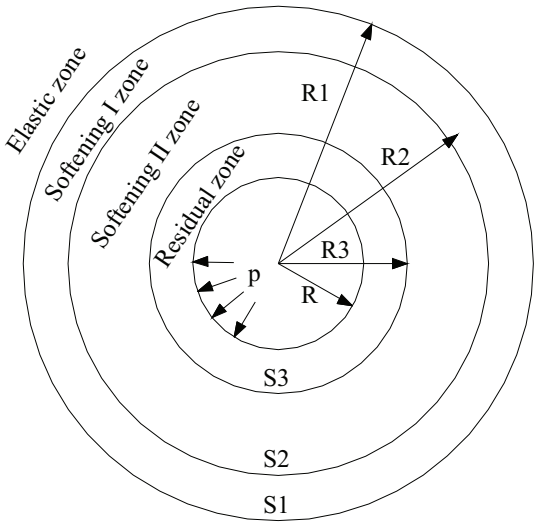

Fig. 7.2 Sketch of cylindrical cavity expansion

In accordance with the quadralinear model, the surrounding region of the cylindrical cavity expansion under internal pressure p in an infinite soil can be divided in four zones as shown in Fig. 7.2. When the value of p is smaller than the elastic limit, the soil around the cavity is in the elastic state and when p increases to a certain value causing the soil to yield, strain-softening stage I initiates. The interface between elastic zone and softening I zone is denoted by $S1$ whose radius is R_1. With the increase of p, the strain-softening zone enlarges gradually. Up to some certain value, the surrounding soil reaches the post-rupture strength and strain-softening stage II starts. Thus interface $S2$ and radius R_2 are defined similarly. When p reaches a limit pressure p_u, the surrounding soil enters the residual phase. Finally, these four zones extend outward further with R_3 as the radius of the residual zone, and $S3$ the corresponding interface.

Here, the cylindrical cavity expansion is an axisymmetric problem and the equation of equilibrium is

$$\frac{d\sigma_r}{dr}+\frac{\sigma_r-\sigma_\theta}{r}=0 \tag{7.1}$$

which is an ordinary differential equation that can be solved analytically.

Two boundary conditions for the expanding cavity are

$$\text{At } r=R,\ \sigma_r=p \tag{7.2}$$

$$\text{At } r=\infty,\ \sigma_r=p_0 \tag{7.3}$$

p_0 is the initial stress.

The definitions of strains are

$$\varepsilon_r=-\frac{du(r)}{dr} \tag{7.4}$$

$$\varepsilon_\theta=-\frac{u(r)}{r} \tag{7.5}$$

where r is the radial coordinate and u is the radial displacement (assumed small compared with r).

At the linear elastic stage, in accordance with Hooke's law, the stress-strain relationship can be expressed as:

$$\varepsilon_r=\frac{1-\nu^2}{E}\left(\sigma_r-\frac{\nu}{1-\nu}\sigma_\theta\right) \tag{7.6}$$

$$\varepsilon_\theta=\frac{1-\nu^2}{E}\left(\sigma_\theta-\frac{\nu}{1-\nu}\sigma_r\right) \tag{7.7}$$

E is the Young's modulus and ν is Poisson's ratio.

And by virtue of elastoplastic theory, strain can be divided into elastic and plastic parts as shown in

$$\varepsilon_r=\varepsilon_r^e+\varepsilon_r^p \tag{7.8}$$

$$\varepsilon_\theta=\varepsilon_\theta^e+\varepsilon_\theta^p \tag{7.9}$$

where ε_r^e, ε_r^p, ε_θ^e and ε_θ^p are the radial elastic and plastic strains, and the circumferential elastic and plastic strains, respectively.

In Fig. 7.1a, it can be seen that after peak value the value of $(\sigma_1-\sigma_3)$ decreases linearly with the radial strain. Therefore the yield functions of the soil for the two-stage softening can be respectively formulated as:

$$\sigma_r-\sigma_\theta=(\sigma_r-\sigma_\theta)\big|_{r=R_1}-\lambda_1\varepsilon_r^p \tag{7.10}$$

$$\sigma_r-\sigma_\theta=(\sigma_r-\sigma_\theta)\big|_{r=R_2}-\lambda_2\varepsilon_r^p \tag{7.11}$$

where λ_1,λ_2 denote undetermined parameters describing strain softening and R_1,R_2 are radii of cavity. It is evident that the soil in the strain-softening phases does not

obey Mohr-Coulomb yield criterion, but satisfies the rules expressed in Eq. (7.10) and Eq. (7.11).

In addition, the stresses, strains and displacements must be continuous at interfaces of $S1, S2, S3$. Therefore, at point A, point B and residual phase, Mohr-Coulomb criterion is assumed as the yield function which is equivalent to the aforementioned yield functions and can be written as:

$$\sigma_r = \frac{1+\sin\phi}{1-\sin\phi}\sigma_\theta + \frac{2c\cos\phi}{1-\sin\phi} = k_1\sigma_\theta + k_2 \tag{7.12}$$

where c, ϕ are the corresponding cohesion and the frictional angle respectively, and

$$k_1 = \frac{1+\sin\phi}{1-\sin\phi} \tag{7.13}$$

$$k_2 = \frac{2c\cos\phi}{1-\sin\phi} \tag{7.14}$$

For peak, post-rupture and residual phases, they can be symbolised as $c_p, \phi_p, c_{pr}, \phi_{pr}, c_r, \phi_r$ and $k_{1p}, k_{2p}, k_{1pr}, k_{2pr}, k_{1r}, k_{2r}$.

At the initial peak yield point, the soil should conform to Eq. (7.12), while serving as the starting point for Eq. (7.10). At the post-rupture point, the soil should also be consistent with Eq. (7.12), which must be assumed as the end point for Eq. (7.10) and the starting point for Eq. (7.11). Just as it reaches the residual phase, the soil complies also with Eq. (7.12), which is also the ending point for Eq. (7.11). In this way, the yield functions of the soil are continuous from the initial yield point to the residual phase.

At the same time, the flow rules for the two-stage softening and residual phase can be constructed from Fig. 7.1(c). The plastic strains ε_3^p and ε_1^p satisfy the following equations corresponding to different phases

$$\varepsilon_3^p = -h\varepsilon_1^p \tag{7.15}$$

$$\varepsilon_3^p = -f\varepsilon_1^p \tag{7.16}$$

$$\varepsilon_3^p = -g\varepsilon_1^p \tag{7.17}$$

which could be used to describe the shear dilation and determine the plastic volumetric strain.

As assumed by Carter & Yeung (1985) and studied by Georgiannou & Burland (2001) and Alonso & Gens (2006a), the basic elastic parameters, peak, post-rupture and residual strength parameters and strain-related parameters can be obtained from laboratory tests such as triaxial tests and shear tests.

7.3 Analytical solutions

7.3.1 Stress, strain and displacement fields in elastic zone ($r \geq R_1$)

By means of the elasticity theory, the solutions to the stress, strain and displacement fields in the elastic zone are given by Yu (2000) as

$$\sigma_r = p_0(1-\frac{R_1^2}{r^2})+\sigma_{R1}\frac{R_1^2}{r^2} \tag{7.18}$$

$$\sigma_\theta = p_0(1+\frac{R_1^2}{r^2})-\sigma_{R1}\frac{R_1^2}{r^2} \tag{7.19}$$

$$u(r) = \frac{(1+\nu)(\sigma_{R1}-p_0)R_1^2}{Er} = B\frac{R_1^2}{r} \tag{7.20}$$

$$\varepsilon_r = \frac{(1+\nu)(\sigma_{R1}-p_0)R_1^2}{Er^2} = B\frac{R_1^2}{r^2} \tag{7.21}$$

$$\varepsilon_\theta = -\frac{(1+\nu)(\sigma_{R1}-p_0)R_1^2}{Er^2} = -B\frac{R_1^2}{r^2} \tag{7.22}$$

Substituting Eq. (7.18) and Eq. (7.19) into Eq. (7.12), we have

$$\sigma_{R1} = \sigma_r\big|_{r=R_1} = \frac{2k_{1p}p_0+k_{2p}}{1+k_{1p}} = (1+\sin\phi_p)p_0 + c_p\cos\phi_p \tag{7.23}$$

$$\sigma_\theta\big|_{r=R_1} = (1-\sin\phi_p)p_0 - c_p\cos\phi_p \tag{7.24}$$

Strains and displacement at $r = R_1$ can be obtained as shown in

$$\varepsilon_r\big|_{r=R_1} = \frac{(1+\nu)(\sigma_{R1}-p_0)}{E} = B \tag{7.25}$$

$$\varepsilon_\theta\big|_{r=R_1} = -\frac{(1+\nu)(\sigma_{R1}-p_0)}{E} = -B \tag{7.26}$$

$$u\big|_{r=R_1} = \frac{(1+\nu)(\sigma_{R1}-p_0)R_1}{E} = BR_1 \tag{7.27}$$

7.3.2 Stress, strain and displacement fields in softening I zone ($R_2 \leq r \leq R_1$)

In this zone, strains can be expressed by

$$\varepsilon_r = \varepsilon_r\big|_{r=R_1} + \varepsilon_r^p \tag{7.28}$$

$$\varepsilon_\theta = \varepsilon_\theta\big|_{r=R_1} + \varepsilon_\theta^p \tag{7.29}$$

From Eq. (7.28) and Eq. (7.29), we obtain

$$\varepsilon_r^p = \varepsilon_r - \varepsilon_r\big|_{r=R_1} \tag{7.30}$$

$$\varepsilon_\theta^p = \varepsilon_\theta - \varepsilon_\theta\big|_{r=R_1} \tag{7.31}$$

By combining Eqs. (7.15), (7.4), (7.5), (7.25) and (7.26) with Eq. (7.30) and Eq. (7.31), the compatibility equation of the displacement can be derived as

$$h\frac{du(r)}{dr} + \frac{u(r)}{r} + B(h-1) = 0 \tag{7.32}$$

With the boundary condition Eq. (7.27), Eq. (7.32) can be solved to obtain the expression of displacement as

$$u(r) = -\frac{h-1}{h+1}Br + \frac{2hBR_1}{h+1}\left(\frac{R_1}{r}\right)^{\frac{1}{h}} \tag{7.33}$$

Substitution of Eq. (7.33) into Eq. (7.4) and Eq. (7.5) gives

$$\varepsilon_r = \frac{h-1}{h+1}B + \frac{2B}{h+1}\left(\frac{R_1}{r}\right)^{\frac{h+1}{h}} \tag{7.34}$$

$$\varepsilon_\theta = \frac{h-1}{h+1}B - \frac{2hB}{h+1}\left(\frac{R_1}{r}\right)^{\frac{h+1}{h}} \tag{7.35}$$

Substitution of Eq. (7.34) and Eq. (7.35) into Eq. (7.30) and Eq. (7.31) yields

$$\varepsilon_r^p = -\frac{2}{h+1}B + \frac{2B}{h+1}\left(\frac{R_1}{r}\right)^{\frac{h+1}{h}} \tag{7.36}$$

$$\varepsilon_\theta^p = \frac{2h}{h+1}B - \frac{2hB}{h+1}\left(\frac{R_1}{r}\right)^{\frac{h+1}{h}} \tag{7.37}$$

Using the continuity condition of strain at $r = R_2$

$$\varepsilon_r\big|_{r=R_2} = \beta\,\varepsilon_r\big|_{r=R_1} = \beta B \tag{7.38}$$

we can obtain the ratio of R_2 to R_1

$$C = \frac{R_2}{R_1} = \left[\frac{2}{(1+h)\beta - h + 1}\right]^{\frac{h}{h+1}} \tag{7.39}$$

Furthermore, substitution of Eqs. (7.23), (7.24) and (7.36) into Eq. (7.10) leads to

$$\sigma_r - \sigma_\theta = 2\sin\phi_p p_0 + 2c_p\cos\phi_p - \lambda_1\left(-\frac{2}{h+1}B + \frac{2B}{h+1}\left(\frac{R_1}{r}\right)^{\frac{h+1}{h}}\right) \tag{7.40}$$

Solving Eq. (7.1) with Eq. (7.40) and boundary conditions Eq. (7.23) gives the solutions of stresses

$$\sigma_r = \frac{2hB\lambda_1}{(h+1)^2}\left[1-(\frac{R_1}{r})^{\frac{h+1}{h}}\right]+(2c_p\cos\phi_p+\frac{2B\lambda_1}{h+1})\ln(\frac{R_1}{r})+c_p\cos\phi_p + \left(1+\sin\phi_p+2\sin\phi_p\ln(\frac{R_1}{r})\right)p_0 \tag{7.41}$$

$$\sigma_\theta = \frac{2B\lambda_1}{(h+1)^2}\left[-1+(\frac{R_1}{r})^{\frac{h+1}{h}}\right]+(2c_p\cos\phi_p+\frac{2B\lambda_1}{h+1})\ln(\frac{R_1}{r})-c_p\cos\phi_p + \left(1-\sin\phi_p+2\sin\phi_p\ln(\frac{R_1}{r})\right)p_0 \tag{7.42}$$

At post-rupture state ($r=R_2$), σ_r and σ_θ must satisfy the yield function Eq. (7.12). In this way, the parameter λ_1 can be determined as

$$\lambda_1 = \frac{k_{2pr}-(1+k_{1pr})c_p\cos\phi_p-\frac{2c_p\cos\phi_p h(1-k_{1pr})}{h+1}\ln\frac{(1+h)\beta-h+1}{2}}{\frac{B(h+k_{1pr})(1-\beta)}{h+1}+\frac{2Bh(1-k_{1pr})}{(h+1)^2}\ln\frac{(1+h)\beta-h+1}{2}} + \frac{\left(\frac{2h\sin\phi_p(k_{1pr}-1)}{h+1}\ln\frac{(1+h)\beta-h+1}{2}+k_{1pr}-1-\left(1+k_{1pr}\right)\sin\phi_p\right)p_0}{\frac{B(h+k_{1pr})(1-\beta)}{h+1}+\frac{2Bh(1-k_{1pr})}{(h+1)^2}\ln\frac{(1+h)\beta-h+1}{2}} \tag{7.43}$$

7.3.3 Stress, strain and displacement fields in softening II zone ($R_3 \le r \le R_2$)

In this zone, strains can be expressed as

$$\varepsilon_r = \varepsilon_r\big|_{r=R_2} + \varepsilon_r^p \tag{7.44}$$

$$\varepsilon_\theta = \varepsilon_\theta\big|_{r=R_2} + \varepsilon_\theta^p \tag{7.45}$$

From Eq. (7.44) and Eq. (7.45), we obtain

$$\varepsilon_r^p = \varepsilon_r - \varepsilon_r\big|_{r=R_2} \tag{7.46}$$

$$\varepsilon_\theta^p = \varepsilon_\theta - \varepsilon_\theta\big|_{r=R_2} \tag{7.47}$$

By combining Eqs. (7.16), (7.4), (7.5), (7.34) and (7.35)(with $r=R_2$) with Eq. (7.46) and Eq. (7.47), the compatibility equation of the displacement can be deduced as

$$f\frac{du(r)}{dr}+\frac{u(r)}{r}+B\left[(f-h)\beta+h-1\right]=0 \tag{7.48}$$

With the boundary condition

$$u(r)\big|_{r=R_2} = \left(1-h+h\beta\right)BR_2 \tag{7.49}$$

Eq. (7.48) can be solved to determine the expression of displacement as

$$u(r) = -\frac{(f-h)\beta + h - 1}{f+1} Br + \frac{(1+h)\beta - h + 1}{f+1} BR_2 f \left(\frac{R_2}{r}\right)^{\frac{1}{f}} \tag{7.50}$$

Substitution of Eq. (7.50) into Eq. (7.4) and Eq. (7.5) gives

$$\varepsilon_r = \frac{(f-h)\beta + h - 1}{f+1} B + \frac{(1+h)\beta - h + 1}{f+1} B \left(\frac{R_2}{r}\right)^{\frac{f+1}{f}} \tag{7.51}$$

$$\varepsilon_\theta = \frac{(f-h)\beta + h - 1}{f+1} B - \frac{(1+h)\beta - h + 1}{f+1} Bf \left(\frac{R_2}{r}\right)^{\frac{f+1}{f}} \tag{7.52}$$

So, using Eq. (7.51) and Eq. (7.46) gives

$$\varepsilon_r^p = \frac{(1+h)\beta - h + 1}{f+1} B \left[\left(\frac{R_2}{r}\right)^{\frac{f+1}{f}} - 1 \right] \tag{7.53}$$

Using the continuity condition of strain

$$\varepsilon_r\big|_{r=R_3} = \omega \varepsilon_r\big|_{r=R_1} = \omega B \tag{7.54}$$

we can obtain the ratio of R_3 to R_2

$$D = \frac{R_3}{R_2} = \left[\frac{(1+h)\beta - h + 1}{(1+f)\omega - (f-h)\beta - h + 1} \right]^{\frac{f}{f+1}} = \left[E\right]^{\frac{f+1}{f}} \tag{7.55}$$

where

$$E = \frac{(1+f)\omega - (f-h)\beta - h + 1}{(1+h)\beta - h + 1} \tag{7.56}$$

Replacing r by R_2 into Eq. (7.41) and Eq. (7.42) produces

$$\begin{aligned} \sigma_{R_2} = \sigma_r\big|_{r=R_2} = {} & \frac{2h}{(h+1)^2}\left[(h+1)c_p \cos\phi_p + B\lambda_1\right] \ln\left(\frac{(1+h)\beta - h + 1}{2}\right) + c_p \cos\phi_p \\ & + \frac{hB\lambda_1}{h+1}(1-\beta) + \left[1 + \sin\phi_p + \frac{2h\sin\phi_p}{h+1} \ln\left(\frac{(1+h)\beta - h + 1}{2}\right)\right] p_0 \end{aligned} \tag{7.57}$$

$$\begin{aligned} \sigma_\theta\big|_{r=R_2} = {} & \frac{2h}{(h+1)^2}\left[(h+1)c_p \cos\phi_p + B\lambda_1\right] \ln\left(\frac{(1+h)\beta - h + 1}{2}\right) - c_p \cos\phi_p \\ & - \frac{B\lambda_1}{h+1}(1-\beta) + \left[1 - \sin\phi_p + \frac{2h\sin\phi_p}{h+1} \ln\left(\frac{(1+h)\beta - h + 1}{2}\right)\right] p_0 \end{aligned} \tag{7.58}$$

From Eq. (7.57) and Eq. (7.58), we can get

$$(\sigma_r - \sigma_\theta)\big|_{r=R_2} = 2c_p \cos\phi_p + (1-\beta)B\lambda_1 + 2\sin\phi_p p_0 \tag{7.59}$$

Substitution of Eq. (7.53) and Eq. (7.59) into Eq.(7.11) leads to

$$\sigma_r-\sigma_\theta=2c_p\cos\phi_p+(1-\beta)B\lambda_1+2\sin\phi_p p_0-\lambda_2\frac{(1+h)\beta-h+1}{f+1}B\left[\left(\frac{R_2}{r}\right)^{\frac{f+1}{f}}-1\right]$$
$$=M-\lambda_2 N\left[\left(\frac{R_2}{r}\right)^{\frac{f+1}{f}}-1\right] \tag{7.60}$$

where

$$M=2c_p\cos\phi_p+(1-\beta)B\lambda_1+2\sin\phi_p p_0 \tag{7.61}$$

$$N=\frac{(1+h)\beta-h+1}{f+1}B \tag{7.62}$$

Solving Eq. (7.1) with Eq. (7.60) and boundary conditions Eq. (7.57) gives the solutions of stresses

$$\sigma_r=\frac{f(M+\lambda_2 N)\ln\left(\left(\frac{R_2}{r}\right)^{\frac{f+1}{f}}\right)-f\lambda_2 N\left(\frac{R_2}{r}\right)^{\frac{f+1}{f}}+(\lambda_2 N+\sigma_{R_2})f+\sigma_{R_2}}{1+f} \tag{7.63}$$

$$\sigma_\theta=\frac{f(M+\lambda_2 N)\ln\left(\left(\frac{R_2}{r}\right)^{\frac{f+1}{f}}\right)+\lambda_2 N\left(\frac{R_2}{r}\right)^{\frac{f+1}{f}}+(\sigma_{R_2}-M)f-M-\lambda_2 N+\sigma_{R_2}}{1+f} \tag{7.64}$$

At residual -rupture state ($r=R_3$), σ_r and σ_θ must satisfy the yield function Eq. (7.12) and the parameter λ_2 can be determined as

$$\lambda_2=\frac{(1-k_{1r})Mf\ln(E)+(1+f)\left[(M-\sigma_{R_2})k_{1r}+\sigma_{R_2}-k_{2r}\right]}{N\left[(k_{1r}-1)f\ln(E)+(E-1)(k_{1r}+f)\right]} \tag{7.65}$$

7.3.4 Stress, strain and displacement fields in residual flow zone ($R_u\le r\le R_3$)

The strain in residual flow zone can be expressed by

$$\varepsilon_r=\varepsilon_r\big|_{r=R_3}+\varepsilon_r^p \tag{7.66}$$

$$\varepsilon_\theta=\varepsilon_\theta\big|_{r=R_3}+\varepsilon_\theta^p \tag{7.67}$$

From Eq. (7.66) and Eq. (7.67), we obtain

$$\varepsilon_r^p=\varepsilon_r-\varepsilon_r\big|_{r=R_3} \tag{7.68}$$

$$\varepsilon_\theta^p=\varepsilon_\theta-\varepsilon_\theta\big|_{r=R_3} \tag{7.69}$$

By combining Eqs. (7.17), (7.4), (7.5), (7.51) and (7.52) (with $r=R_3$) with Eq. (7.68) and Eq. (7.69), the compatibility equation of the displacement can be deduced as

$$g\frac{du(r)}{dr}+\frac{u(r)}{r}+B\left[(f-h)\beta+h-1+(g-f)\omega\right]=0 \tag{7.70}$$

With the boundary condition

$$u(r)\big|_{r=R_3}=\left[1-h+(h-f)\beta+f\omega\right]BR_3 \tag{7.71}$$

Eq. (7.70) can be solved to obtain the expression of displacements as

$$u(r)=-\frac{(g-f)\omega+(f-h)\beta+h-1}{g+1}Br+\frac{(1+f)\omega+(h-f)\beta-h+1}{g+1}BR_3g\left(\frac{R_3}{r}\right)^{\frac{1}{g}} \tag{7.72}$$

Substitution of Eq. (7.72) into Eq. (7.4) and Eq. (7.5) gives

$$\varepsilon_r=\frac{(g-f)\omega+(f-h)\beta+h-1}{g+1}B+\frac{(1+f)\omega+(h-f)\beta-h+1}{g+1}B\left(\frac{R_3}{r}\right)^{\frac{g+1}{g}} \tag{7.73}$$

$$\varepsilon_\theta=\frac{(g-f)\omega+(f-h)\beta+h-1}{g+1}B-\frac{(1+f)\omega+(h-f)\beta-h+1}{g+1}Bg\left(\frac{R_3}{r}\right)^{\frac{g+1}{g}} \tag{7.74}$$

The boundary condition under the ultimate expansion pressure p_u is

$$\sigma_{\mathrm{r}}\big|_{r=R_u}=p_u \tag{7.75}$$

Combining both Eq. (7.12) and Eq. (7.1) with boundary condition Eq. (7.75) yields the solutions to the stress field in the residual flow zone as

$$\sigma_r=\left(p_u+c_r\cot\phi_r\right)\left(\frac{R_u}{r}\right)^{\frac{2\sin\phi_r}{1+\sin\phi_r}}-c_r\cot\phi_r \tag{7.76}$$

$$\sigma_\theta=\frac{1-\sin\phi_r}{1+\sin\phi_r}\left(p_u+c_r\cot\phi_r\right)\left(\frac{R_u}{r}\right)^{\frac{2\sin\phi_r}{1+\sin\phi_r}}-c_r\cot\phi_r \tag{7.77}$$

7.3.5 Calculation of radii for different zones and the ultimate internal pressure

As demonstrated by Jiang & Shen (1995,1996a, 1996b, 1997), Wang & Xiong (1999) and Zheng et al. (2004), after the expansion of the cylindrical cavity, the volume change of the cylindrical cavity is assumed to be equal to the sum of the volume change of the soil in the elastic zone, the two strain-softening zones and the residual flow zone. In view of this bulk equilibrium condition, it is easily obtained from the following expression

$$\pi R_u^2-\pi R_i^2=\pi R_1^2-\pi\left(R_1-u_{R_1}\right)^2+\Delta_1+\Delta_2+\Delta_3 \tag{7.78}$$

where R_i and R_u are the initial and ultimate radii of the cylindrical cavity, u_{R_1} the radial displacement at $r=R_1$, and Δ_1, Δ_2 and Δ_3 are the bulk changes of the soil in the strain softening I zone and II zone, and the residual flow zone, respectively.

In addition, as a case of plain strain ($\varepsilon_z = 0$), the volume of cavity expansion is hereby given by

$$\varepsilon_v = \varepsilon_r + \varepsilon_\theta \tag{7.79}$$

Therefore, Δ_1, Δ_2 and Δ_3 can be expressed as

$$\Delta_1 = 2\pi \int_{R_2}^{R_1} \varepsilon_v r dr = 2\pi \int_{R_2}^{R_1} (\varepsilon_r + \varepsilon_\theta) r dr = \pi R_1^2 I \tag{7.80}$$

$$\Delta_2 = 2\pi \int_{R_3}^{R_2} \varepsilon_v r dr = 2\pi \int_{R_3}^{R_2} (\varepsilon_r + \varepsilon_\theta) r dr = \pi R_2^2 \left[J\left(1 - D^2\right) - K\left(1 - D^{\frac{f-1}{f}}\right) \right] \tag{7.81}$$

$$\Delta_3 = 2\pi \int_{R_u}^{R_3} \varepsilon_v r dr = 2\pi \int_{R_u}^{R_3} (\varepsilon_r + \varepsilon_\theta) r dr = \pi R_3^2 \left\{ X\left[1 - \left(\frac{R_u}{R_3}\right)^2\right] - Y\left[1 - \left(\frac{R_u}{R_3}\right)^{\frac{g-1}{g}}\right] \right\} \tag{7.82}$$

where

$$I = \frac{2B\left[(h-1)\left(1-C^2\right) - 2h\left(1 - C^{\frac{h-1}{h}}\right)\right]}{h+1} \tag{7.83}$$

$$J = \frac{2B\left[(f-h)\beta + h - 1\right]}{1+f} \tag{7.84}$$

$$K = \frac{2Bf\left[(1+h)\beta - h + 1\right]}{1+f} \tag{7.85}$$

$$X = \frac{2B\left[(g-f)\omega + (f-h)\beta + h - 1\right]}{1+g} \tag{7.86}$$

$$Y = \frac{2Bg\left[(1+f)\omega + (h-f)\beta - h + 1\right]}{1+g} \tag{7.87}$$

Substituting Eqs. (7.80), (7.81) and (7.82) into Eq. (7.78) and ignoring the term πR_i^2 and the higher order terms of u_{R_1} produces the following equation

$$(1+X)\left(\frac{R_u}{R_3}\right)^2 - Y\left(\frac{R_u}{R_3}\right)^{\frac{g-1}{g}} = \frac{I + 2B}{(C \cdot D)^2} + \frac{J - K}{D^2} + KD^{\frac{f+1}{f}} + X - Y - J \tag{7.88}$$

Solving the above equation, the radius R_3 can be obtained and hence the radii R_2 and R_1 can also be computed through Eq. (7.55) and Eq. (7.39).

Finally, applying the continuity condition of the radial stress at $r = R_3$ and using Eq. (7.76) and Eq. (7.63) with $r = R_3$, we can obtain the solution of the ultimate expansion pressure p_u as

$$p_u = \frac{\left\{ f\left(M + \lambda_2 N\right)\ln(E) + f\left(1-E\right)\lambda_2 N + \left(1+f\right)\sigma_{R_2} + c_r \cot\phi_r \left(1+f\right)\right\}}{\left(1+f\right)\left(\frac{R_u}{R_3}\right)^{\frac{2\sin\phi_r}{1+\sin\phi_r}}} - c_r \cot\phi_r \tag{7.89}$$

7.3.6 Remarks

Eq. (7.89) is valid only if the surrounding clay reaches the residual flow stage. There are three critical stresses—σ_{R1}, σ_{R2} and σ_{R3}, which can be calculated by Eqs. (7.23), (7.57) and (7.63). By virtue of these three stresses, the internal pressure p controls the utmost stage that the surrounding clay can reach.

7.4 Computational examples

Based on the aforementioned formulae, a Maple program is designed to calculate the analytical solutions of the cylindrical cavity expansion.

7.4.1 Verification of maple program with trilinear model

By setting $c_{pr} = c_r$, $\phi_{pr} = \phi_r$, $\beta = \omega$, $\lambda_2 = 0$ and $f = g$, $R_2 = R_3$, the quadralinear model with two-stage linear softening degenerates into the trilinear model with one-stage linear softening. In order to verify the new program, the same parameter values used by Zheng et al. (2004) are applied here, which are given as

$$E = 1.0\times10^4\,\text{kPa},\ \nu = 0.3,\ c_p = 40\text{kPa},\ \phi_p = 30°,\ c_{pr} = c_r = 32\text{kPa},\ \phi_{pr} = \phi_r = 26°$$
$$\beta = \omega = 2.0,\ h = f = g = 1.0,\ p_0 = 0\text{kPa},\ R_u = 0.3\text{m}$$

The results are listed in Table 7.1 and are the same as those obtained by Zheng et al. (2004). Here $h = f = g = 1.0$ means that the plastic volume change is 0, which is consistent with the assumption for the analytical solution to the cavity expansion given by Vesic (1972).

Table 7.1 Computational results

R_u (m)	p_u (kPa)	R_3 (m)	R_2 (m)	R_1 (m)
0.30	360.76	2.24	2.24	3.16
u_{R_3} (mm)	$\varepsilon_r\big\|_{r=R_3}$	$\varepsilon_\theta\big\|_{r=R_3}$	$\sigma_r\big\|_{r=R_3}$ (kPa)	$\sigma_\theta\big\|_{r=R_3}$ (kPa)
20.1	9.0×10^{-3}	-9.0×10^{-3}	59.74	-16.66

u_{R_2} (mm)	$\varepsilon_r\|_{r=R_2}$	$\varepsilon_\theta\|_{r=R_2}$	$\sigma_r\|_{r=R_2}$ (kPa)	$\sigma_\theta\|_{r=R_2}$ (kPa)
20.1	9.0×10^{-3}	-9.0×10^{-3}	59.74	-16.66
u_{R_1} (mm)	$\varepsilon_r\|_{r=R_1}$	$\varepsilon_\theta\|_{r=R_1}$	$\sigma_r\|_{r=R_1}$ (kPa)	$\sigma_\theta\|_{r=R_1}$ (kPa)
14.2	4.5×10^{-3}	-4.5×10^{-3}	34.64	-34.64

7.4.2 Examples with quadralinear model and parametric study

7.4.2.1 Effect of shear dilation h, f and g

The effect of shear dilatation is taken into account by the values of the parameters h, f and g. The basic model parameters of Example 1 are

$$E=1.0\times10^4\text{kPa},\ \nu=0.2,\ c_p=25\text{kPa},\ \phi_p=26°,\ c_{pr}=5\text{kPa},\ \phi_{pr}=23°$$
$$c_r=0\text{kPa},\ \phi_r=14°,\ \beta=1.2,\ \omega=5.0,\ h=f=g=1.0,\ p_0=0\text{kPa},\ R_u=0.3\text{m}$$

where c, ϕ values are drawn from unweathered Gault Clay values (Cooper et al., 1998).

On the basis of Example 1, changing only shear dilation parameters h, f and g but keeping the others unchanged yields produce Example 2-6 as listed in Table 7.2.

Table 7.2 Data of shear dilation parameters h, f and g

Example 1	$h=1.0,\ f=1.0,\ g=1.0$	Example 4	$h=3.0,\ f=2.0,\ g=1.0$
Example 2	$h=2.0,\ f=1.5,\ g=1.0$	Example 5	$h=2.5,\ f=2.0,\ g=1.0$
Example 3	$h=2.5,\ f=1.5,\ g=1.0$	Example 6	$h=3.0,\ f=2.5,\ g=1.0$

Table 7.3 Results of ultimate pressure p_u and radii (R_3, R_2, R_1)

	R_u (m)	p_u (kPa)	R_3 (m)	R_2 (m)	R_1 (m)
$h=1.0,\ f=1.0,\ g=1.0$	0.3	82.56	1.29	3.73	4.09
$h=2.0,\ f=1.5,\ g=1.0$	0.3	93.32	1.66	4.17	4.96
$h=2.5,\ f=1.5,\ g=1.0$	0.3	96.58	1.65	4.08	5.05
$h=3.0,\ f=2.0,\ g=1.0$	0.3	106.85	1.52	4.50	5.79
$h=2.5,\ f=2.0,\ g=1.0$	0.3	103.57	1.53	4.61	5.71
$h=3.0,\ f=2.5,\ g=1.0$	0.3	112.94	1.43	4.98	6.41

Table 7.4 Results for displacement, strain and stress at R_3

	u_{R_3} (mm)	$\varepsilon_r\big\vert_{r=R_3}$	$\varepsilon_\theta\big\vert_{r=R_3}$	$\sigma_r\big\vert_{r=R_3}$ (kPa)	$\sigma_\theta\big\vert_{r=R_3}$ (kPa)
$h=1.0,\ f=1.0,\ g=1.0$	34.8	27.0×10^{-3}	-27.0×10^{-3}	46.74	28.53
$h=2.0,\ f=1.5,\ g=1.0$	31.7	13.5×10^{-3}	-19.1×10^{-3}	47.96	29.28
$h=2.5,\ f=1.5,\ g=1.0$	32.0	13.5×10^{-3}	-19.4×10^{-3}	49.72	30.35
$h=3.0,\ f=2.0,\ g=1.0$	37.8	13.5×10^{-3}	-24.8×10^{-3}	56.72	34.62
$h=2.5,\ f=2.0,\ g=1.0$	37.5	13.5×10^{-3}	-24.5×10^{-3}	54.90	33.51
$h=3.0,\ f=2.5,\ g=1.0$	42.7	13.5×10^{-3}	-29.9×10^{-3}	61.50	37.54

Table 7.5 Results for displacement, strain and stress at R_2

	u_{R_2} (mm)	$\varepsilon_r\big\vert_{r=R_2}$	$\varepsilon_\theta\big\vert_{r=R_2}$	$\sigma_r\big\vert_{r=R_2}$ (kPa)	$\sigma_\theta\big\vert_{r=R_2}$ (kPa)
$h=1.0,\ f=1.0,\ g=1.0$	12.1	3.2×10^{-3}	-3.2×10^{-3}	25.51	4.56
$h=2.0,\ f=1.5,\ g=1.0$	15.7	3.2×10^{-3}	-3.8×10^{-3}	28.46	5.85
$h=2.5,\ f=1.5,\ g=1.0$	16.5	3.2×10^{-3}	-4.0×10^{-3}	29.91	6.49
$h=3.0,\ f=2.0,\ g=1.0$	19.4	3.2×10^{-3}	-4.3×10^{-3}	31.34	7.11
$h=2.5,\ f=2.0,\ g=1.0$	18.6	3.2×10^{-3}	-4.0×10^{-3}	29.91	6.49
$h=3.0,\ f=2.5,\ g=1.0$	21.5	3.2×10^{-3}	-4.3×10^{-3}	31.34	7.11

Table 7.6 Results for displacement, strain and stress at R_1

	u_{R_1} (mm)	$\varepsilon_r\big\vert_{r=R_1}$	$\varepsilon_\theta\big\vert_{r=R_1}$	$\sigma_r\big\vert_{r=R_1}$ (kPa)	$\sigma_\theta\big\vert_{r=R_1}$ (kPa)
$h=1.0,\ f=1.0,\ g=1.0$	11.0	2.7×10^{-3}	-2.7×10^{-3}	22.47	-22.47
$h=2.0,\ f=1.5,\ g=1.0$	13.4	2.7×10^{-3}	-2.7×10^{-3}	22.47	-22.47
$h=2.5,\ f=1.5,\ g=1.0$	13.6	2.7×10^{-3}	-2.7×10^{-3}	22.47	-22.47
$h=3.0,\ f=2.0,\ g=1.0$	15.6	2.7×10^{-3}	-2.7×10^{-3}	22.47	-22.47
$h=2.5,\ f=2.0,\ g=1.0$	15.4	2.7×10^{-3}	-2.7×10^{-3}	22.47	-22.47

$h=3.0,\ f=2.5,\ g=1.0$	17.3	2.7×10^{-3}	-2.7×10^{-3}	22.47	-22.47

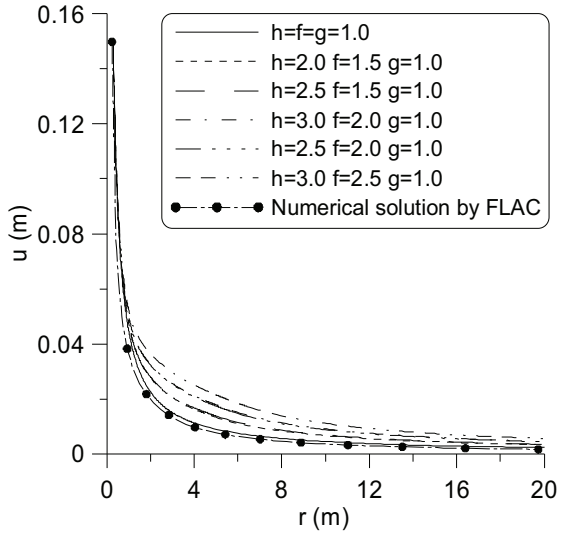

Fig. 7.3 Displacement distribution

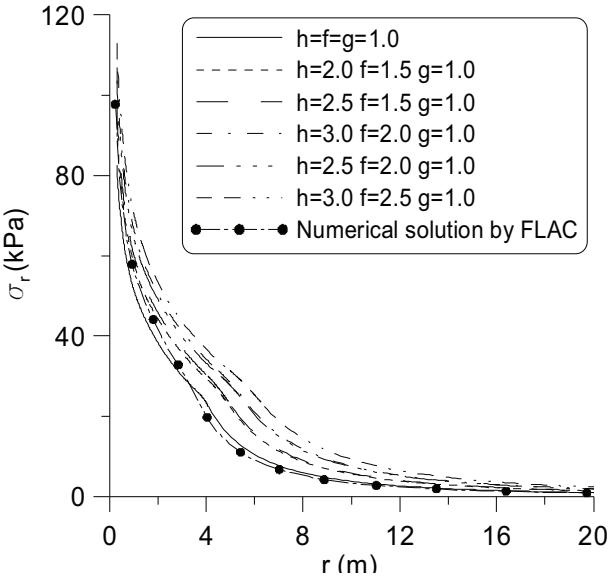

Fig. 7.4 Radial stress distribution

The computed results are shown in Table 7.3-Table 7.6, Fig. 7.3 and Fig. 7.4. According to Table 7.3, the ultimate pressure and the maximum plastic radius R_1 increase with the higher shear dilation and this is consistent with the result of Carter & Yeung (1985). The same tendency results for the displacement, strain and stress at R_3, R_2, whereas the strain and stress at R_1 remain constant.

From Fig. 7.3 and Fig. 7.4, we can see the increase of displacement and radial stress with shear dilation. It is also interesting to find from Example 2-5 that the variation for displacement and stress is very small if only h is changed but f and g remain constant.

7.4.2.2 Effect of β

Based on Example 2, only β is changed while the other parameters kept constant, as shown in Table 7.7.

Table 7.7 Data of softening parameter β

Example 2	$\beta=1.2$	Example 8	$\beta=1.4$	Example 10	$\beta=2.0$
Example 7	$\beta=1.3$	Example 9	$\beta=1.5$		

The computed results are shown in Table 7.8, Fig. 7.5 and Fig. 7.6. According to Table 7.8, the ultimate pressure and the maximum plastic radius R_1 increase with β and this is again consistent with the result of Carter & Yeung (1985). However, R_2 decreases with β and there is little reduction of R_3.

From Fig. 7.5 and Fig. 7.6, we can find that there is little influence of β on the displacement and the increase in radial stress with β occurs mainly in plastic region.

Table 7.8 Results of ultimate pressure p_u and radii (R_3, R_2, R_1)

	R_u (m)	p_u (kPa)	R_3 (m)	R_2 (m)	R_1 (m)
$\beta=1.2$	0.3	93.32	1.66	4.17	4.96
$\beta=1.3$	0.3	98.09	1.65	3.90	5.00
$\beta=1.4$	0.3	102.39	1.65	3.68	5.04
$\beta=1.5$	0.3	106.31	1.65	3.49	5.07
$\beta=2.0$	0.3	121.66	1.63	2.82	5.20

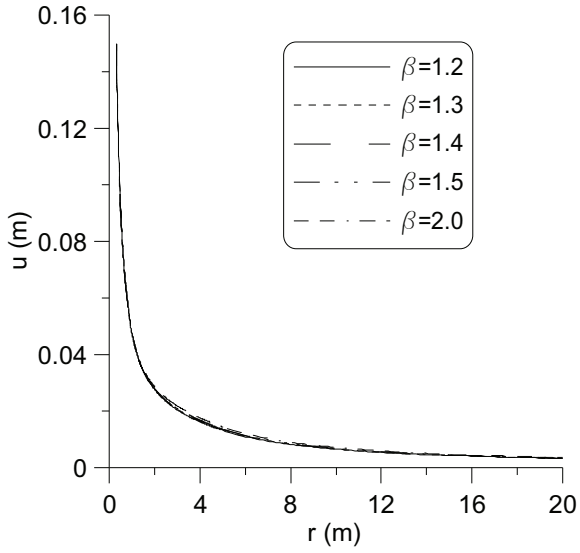

Fig. 7.5 Displacement distribution

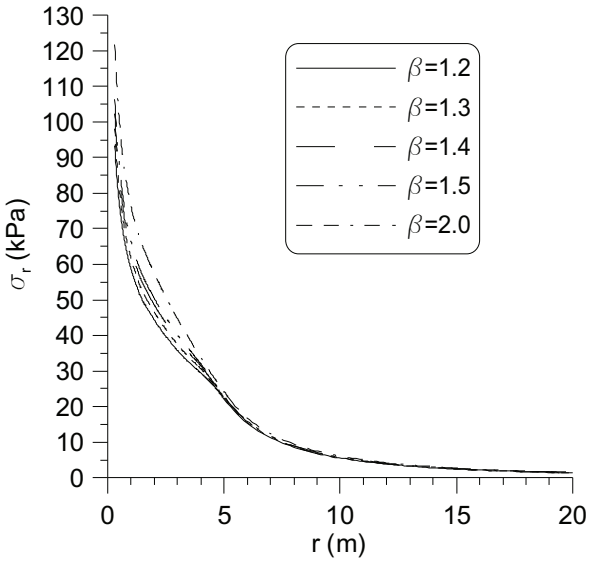

Fig. 7.6 Radial stress distribution

7.4.2.3 Effect of ω

Based on Example 2, only ω is changed while the other parameters kept constant, as shown in Table 7.9.

Table 7.9 Data of softening parameter ω

Example 11	$\omega = 4.0$	Example 12	$\omega = 6.0$	Example 14	$\omega = 10.0$
Example 2	$\omega = 5.0$	Example 13	$\omega = 8.0$		

Table 7.10 Results of ultimate pressure p_u and radii (R_3, R_2, R_1)

	R_u (m)	p_u (kPa)	R_3 (m)	R_2 (m)	R_1 (m)
$\omega = 4.0$	0.3	90.73	1.86	4.07	4.85
$\omega = 5.0$	0.3	93.32	1.66	4.17	4.96
$\omega = 6.0$	0.3	95.29	1.51	4.24	5.05
$\omega = 8.0$	0.3	98.14	1.30	4.36	5.20
$\omega = 10.0$	0.3	100.08	1.16	4.46	5.31

The computed results are shown in Table 7.10, Fig. 7.7 and Fig. 7.8. According to Table 7.10, the ultimate pressure and the maximum plastic radius R_1 and R_2 increase with ω whereas R_3 decreases with ω. This agrees with the results of Carter & Yeung (1985).

From Fig. 7.7 and Fig. 7.8, we can see that the displacement and radial stress increase with ω but the magnitude of enhancement is much lower than that caused by β.

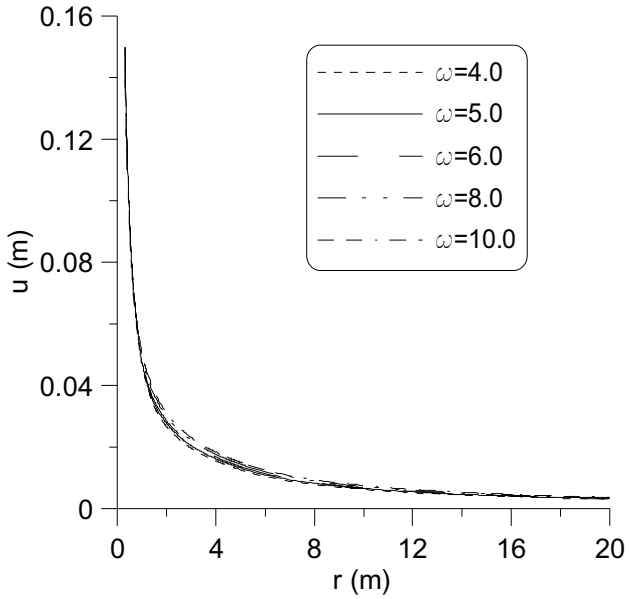

Fig. 7.7 Displacement distribution

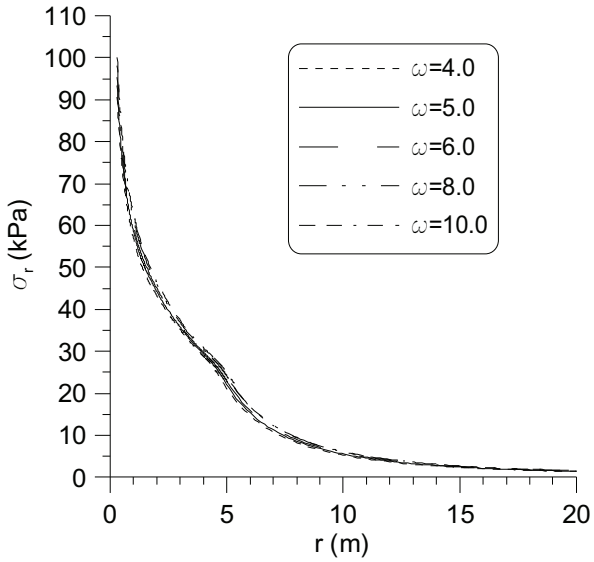

Fig. 7.8 Radial stress distribution

7.4.2.4 Effect of initial stress p_0

In the study above, the initial stress p_0 is 0kPa. Here we change the initial stress p_0 and keep other parameters constant. The parameter data is shown in Table 7.11.

Table 7.11 Data of initial stress p_0

Example 2	$p_0 = 50.0\text{kPa}$	Example 16	$p_0 = 100.0\text{kPa}$	Example 18	$p_0 = 500.0\text{kPa}$
Example 15	$p_0 = 50.0\text{kPa}$	Example 17	$p_0 = 200.0\text{kPa}$		

The computed results are shown in Table 7.12**Error! Not a valid bookmark self-reference.**, Fig. 7.9 and Fig. 7.10. According to Table 7.12, the ultimate pressure

increases to a great extent with p_0 whereas the maximum plastic radius R_1, R_2 and R_3 naturally decrease with p_0.

Table 7.12 Results of ultimate pressure p_u and radii (R_3, R_2, R_1)

	R_u (m)	p_u (kPa)	R_3 (m)	R_2 (m)	R_1 (m)
$p_0 = 0.0$kPa	0.3	93.32	1.66	4.17	4.96
$p_0 = 50.0$kPa	0.3	289.15	1.18	2.96	3.52
$p_0 = 100.0$kPa	0.3	458.82	0.96	2.41	2.87
$p_0 = 200.0$kPa	0.3	761.27	0.74	1.86	2.22
$p_0 = 500.0$kPa	0.3	1534.94	0.49	1.23	1.47

From Fig. 7.9 and Fig. 7.10, we can see that both the displacement and radial stress increase with p_0 but the influence on radial stress is much more apparent than that on displacement.

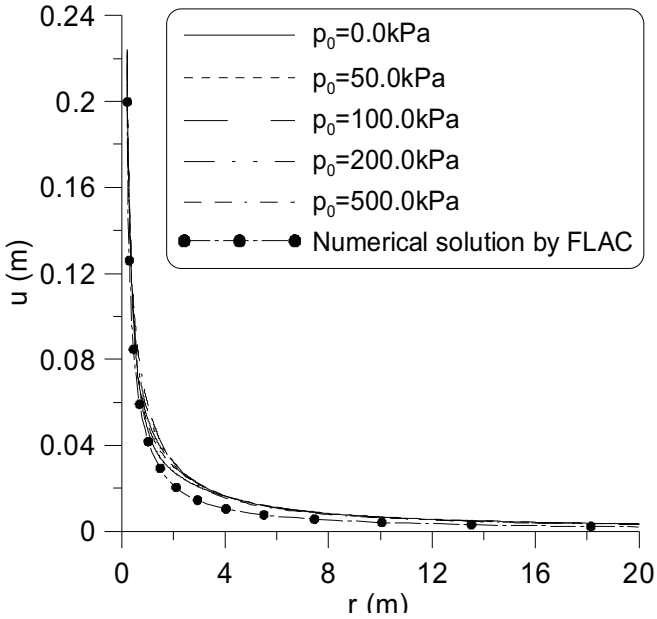

Fig. 7.9 Displacement distribution

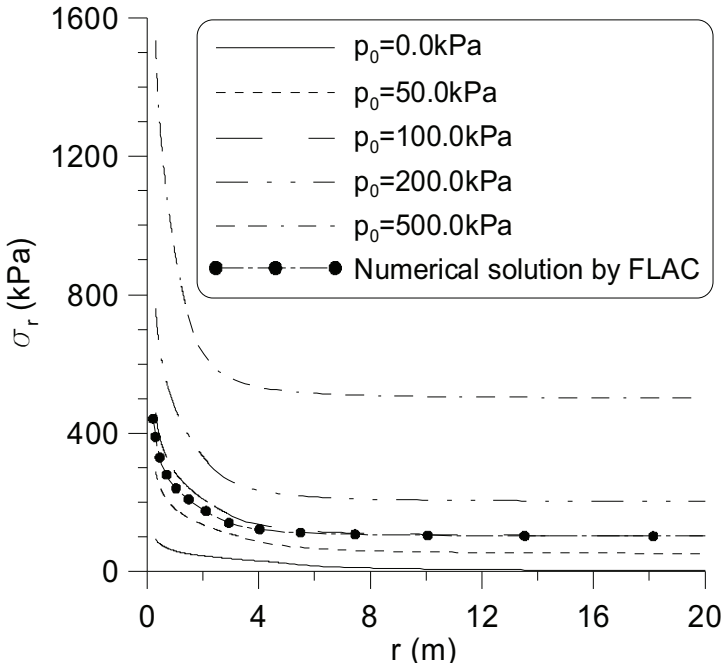

Fig. 7.10 Radial stress distribution

7.4.2.5 Effect of E and ν

To study the effect of E and ν, the four examples listed in Table 7.13 are calculated. The computed results are shown in Table 7.14, Fig. 7.11 and Fig. 7.12.

According to Table 7.14, the ultimate pressure and radii R_1, R_2 and R_3 decrease slightly with the enhancement of Poisson's ratio and increase dramatically with Young's modulus.

Table 7.13 Data of E and ν

Example 2	$E=1.0e4,\ \nu=0.2$	Example 20	$E=5.0e4,\ \nu=0.2$
Example 19	$E=1.0e4,\ \nu=0.3$	Example 21	$E=5.0e4,\ \nu=0.3$

Table 7.14 Results of ultimate pressure p_u and radii (R_3, R_2, R_1)

	R_u (m)	p_u (kPa)	R_3 (m)	R_2 (m)	R_1 (m)
$E=1.0e4,\ \nu=0.2$	0.3	93.32	1.66	4.17	4.96
$E=1.0e4,\ \nu=0.3$	0.3	91.86	1.59	4.00	4.77
$E=5.0e4,\ \nu=0.2$	0.3	127.79	3.71	9.34	11.12
$E=5.0e4,\ \nu=0.3$	0.3	125.81	3.57	8.97	10.69

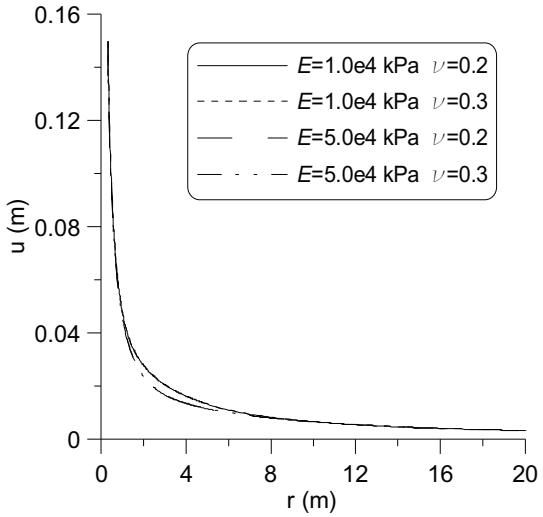

Fig. 7.11 Displacement distribution

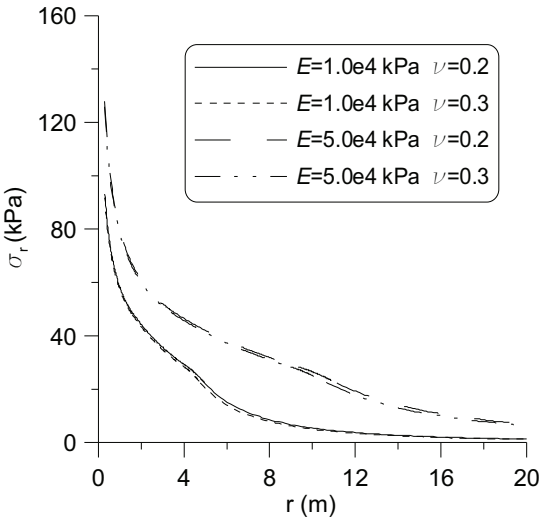

Fig. 7.12 Radial stress distribution

From Fig. 7.11 and Fig. 7.12, we can see that both the displacement reduction with Young's modulus and the radial stress increase with Young's modulus. But the influence of Poisson's ratio on displacement and stress is small.

7.4.2.6 Effect of post-rupture strength parameters c_{pr} and ϕ_{pr}

By only changing the c_{pr} and ϕ_{pr} values, we can perform the examples shown in Table 7.15.

Table 7.15 Data of E and ν

Example 2	$c_{pr}=5\text{kPa},\ \phi_{pr}=23°$	Example 24	$c_{pr}=5\text{kPa},\ \phi_{pr}=20°$
Example 22	$c_{pr}=10\text{kPa},\ \phi_{pr}=23°$	Example 25	$c_{pr}=2\text{kPa},\ \phi_{pr}=20°$
Example 23	$c_{pr}=2\text{kPa},\ \phi_{pr}=23°$		

Table 7.16 Results of ultimate pressure p_u and radii (R_3, R_2, R_1)

	R_u (m)	p_u (kPa)	R_3 (m)	R_2 (m)	R_1 (m)
$c_{pr}=5\text{kPa}$, $\phi_{pr}=23°$	0.3	93.32	1.66	4.17	4.96
$c_{pr}=10\text{kPa}$, $\phi_{pr}=23°$	0.3	103.61	1.66	4.17	4.96
$c_{pr}=2\text{kPa}$, $\phi_{pr}=23°$	0.3	87.14	1.66	4.17	4.96
$c_{pr}=5\text{kPa}$, $\phi_{pr}=20°$	0.3	91.61	1.66	4.17	4.96
$c_{pr}=2\text{kPa}$, $\phi_{pr}=20°$	0.3	85.10	1.66	4.17	4.96

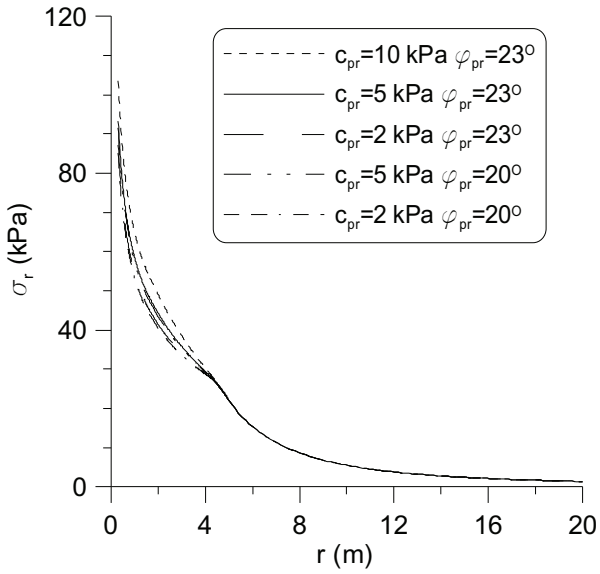

Fig. 7.13 Radial stress distribution

The computed results are shown in Table 7.16 and Fig. 7.13.

According to Table 7.16, the ultimate pressure decreases with the reduction of post-rupture strength parameters c_{pr} and ϕ_{pr}. But the radii R_1, R_2 and R_3 are uninfluenced and remain constant.

From Fig. 7.13, we can see that radial stresses decrease with c_{pr} and ϕ_{pr}.

7.4.3 Numerical simulation of cavity expansion

Some numerical simulations of cavity expansion using two-stage softening model are performed for comparison with analytical solutions. The strain-hardening/softening model is chosen in *FLAC* and has been described in Section 3.6.2.

The problem is modelled using an axisymmetric configuration and plane-strain boundary conditions, as indicated in Fig. 7.14. The *FLAC* model is of finite extent, but the length, L, is chosen to be very large as compared to a_0.

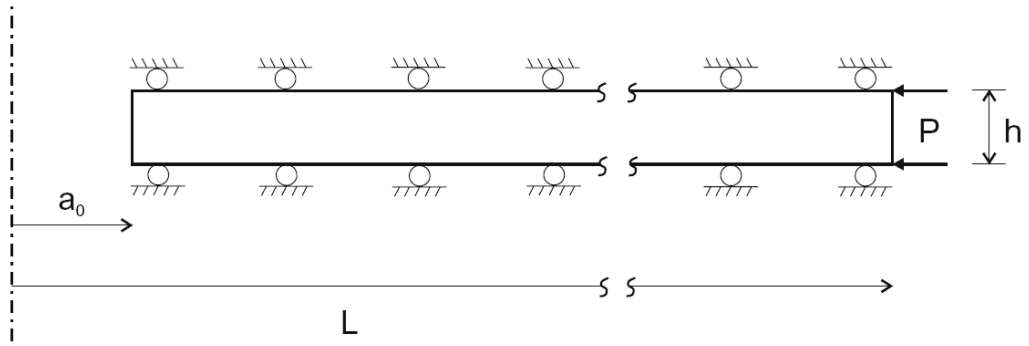

Fig. 7.14 Model geometry

Here both a_0 and h is taken as 0.01 and L 50. The grid is composed of a single layer of 50 zones of constant height and variable zone width, graded by a factor of 1.1. All the model information is given in Table 7.17. The basic model parameters are the same as those used in Section 7.4.2.1. Instead of using Young's modulus and Poisson's ratio, bulk and shear moduli are adopted. Dilation angle is supposed to vary in the same way as the frictional angle and associated flow rule is assumed. Initial stress is considered as 0kPa and initial x-velocity is 1.0e-6 m/s. For cavity expansion, the large deformation setting is appropriate. In total, 200000 steps are computed.

Table 7.17 Model and parameter configuration

```
; --- model geometry ---
g 50 1
gen 0.01 0 0.01 0.01 50 0.01 50 0 rat 1.05 1
; --- model properties ---
model ss
pro bu 5.556e6 sh 4.167e6 co 2.5e4 fric 26 dil 26 ten 51257 den 2000
pro ftab=1 ctab=2 dtab=3
table 1 0,26 3.24e-3,23 13.5e-3,14
table 2 0,2.5e4 3.24e-3,5e3 13.5e-3,0
table 3 0,26 3.24e-3,23 13.5e-3,14
; --- boundary conditions ---
fix y
ini sxx 0 syy 0 szz 0
apply press 0 i 51
fix x i 1
ini xv 1.0e-6 i 1
; model settings ---
set large
```

…

step 200000

…

As shown in Fig. 7.3, the displacement distribution line after 200000 steps is very similar to those from the analytical procedure though it lies a little lower with conservative results. The same tendency is found for the radial stress distribution as indicated in Fig. 7.4.

In addition, the typical expansion curve is plotted in Fig. 7.15, from which we can see that the ultimate pressure p_u is about 106 kPa. The calculated ultimate pressure is quite close to that obtained in Section 7.4.2.1. r and r_0 are respectively the current cavity radius and the initial cavity radius.

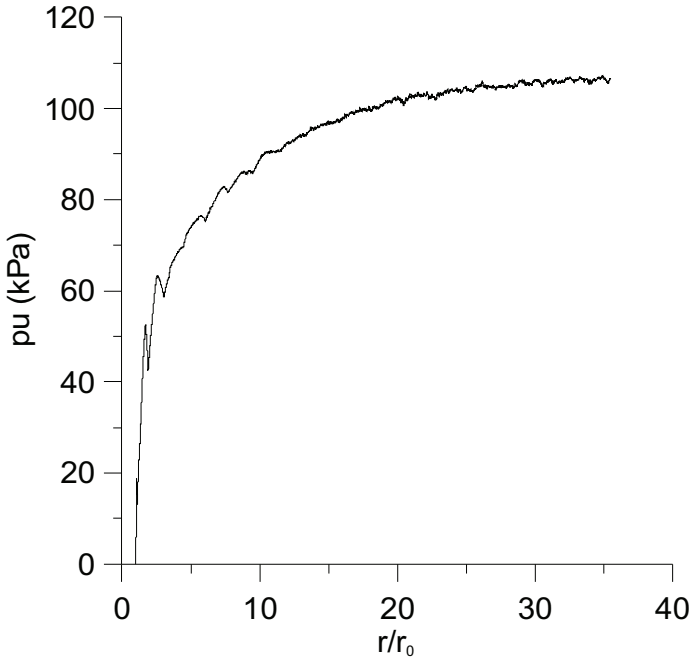

Fig. 7.15 Expansion curve with zero initial stress

The stress path for two-stage softening case in $q-p$ space is shown in Fig. 7.16. This stress path line $\overline{\text{ABCDEF}}$ can be explained in a similar manner as that stated by Carter & Yeung (1985). The initial condition is represented by point A and during the early expansion the material behaves elastically and deformation occurs at a constant value of p (defined in Eq. (I.3)). At point B the material first yields until reaching point C with its peak strength parameters ϕ_p, c_p. After C an obvious rapid reduction in q (defined in Eq. (I.6)) occurs and afterwards q decreases slowly until point E. After point E, the critical residual state is reached and q changes linearly with p. The line $\overline{\text{EF}}$ passes the origin point (0,0).

Similarly, a second simulation is conducted with almost the same parameters (Table 7.17) as in the first simulation apart from the fact that the initial stress is assumed to be 100 kPa.

As shown in Fig. 7.9, the displacement distribution line after 200000 steps is quite similar to that obtained from the analytical procedure though it lies a little lower with conservative results. The same tendency is found for the radial stress distribution as indicated in Fig. 7.10.

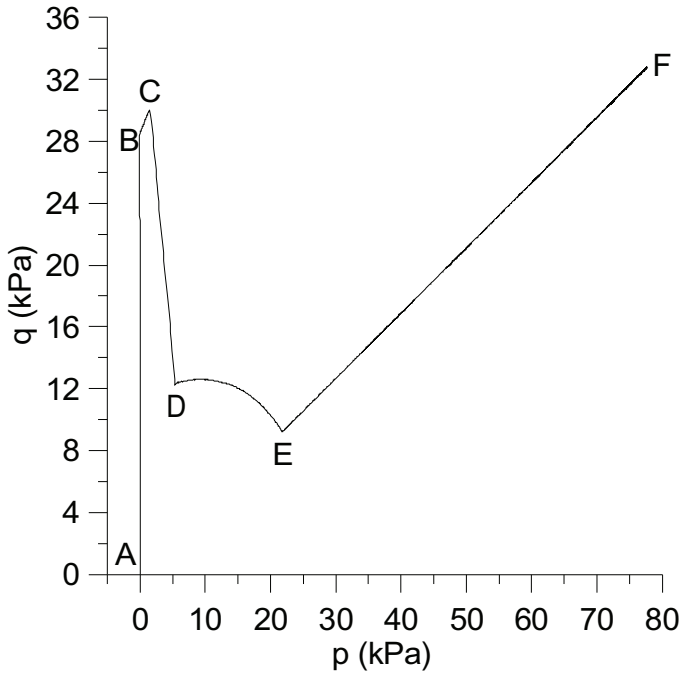

Fig. 7.16 $q-p$ **stress path curve with zero initial stress**

In addition, the typical expansion curve is plotted in Fig. 7.17, from which we can see that the ultimate pressure is about 446 kPa. The calculated ultimate pressure is quite close to the value obtained in Section 7.4.2.4 which is 458.82 kPa.

The corresponding stress path is represented in $q-p$ space as shown in Fig. 7.18. This stress path line $\overline{\text{ABCDEF}}$ can be explained similarly to the previous case. From Fig. 7.18, it can be seen that the two-stage softening feature in $q-p$ curve becomes less apparent when increasing the confining pressure. This is reasonable because the strength of clay increases with the confining pressure and there is less difference in strength during the two-stage softening process.

In summary, the numerical solutions in cavity expansion problem are similar to those calculated by the analytical method. In turn, this confirms the validity of the analytical procedure.

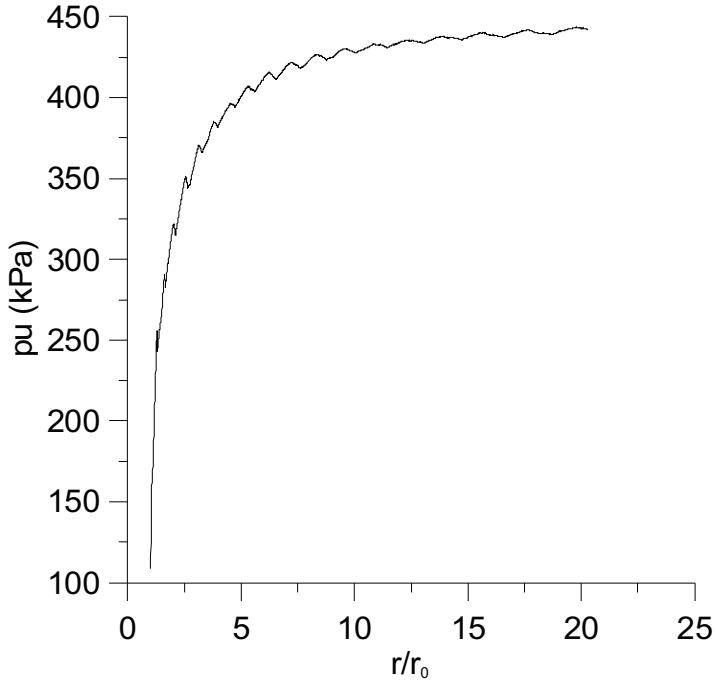

Fig. 7.17 Expansion curve with 100 kPa initial stress

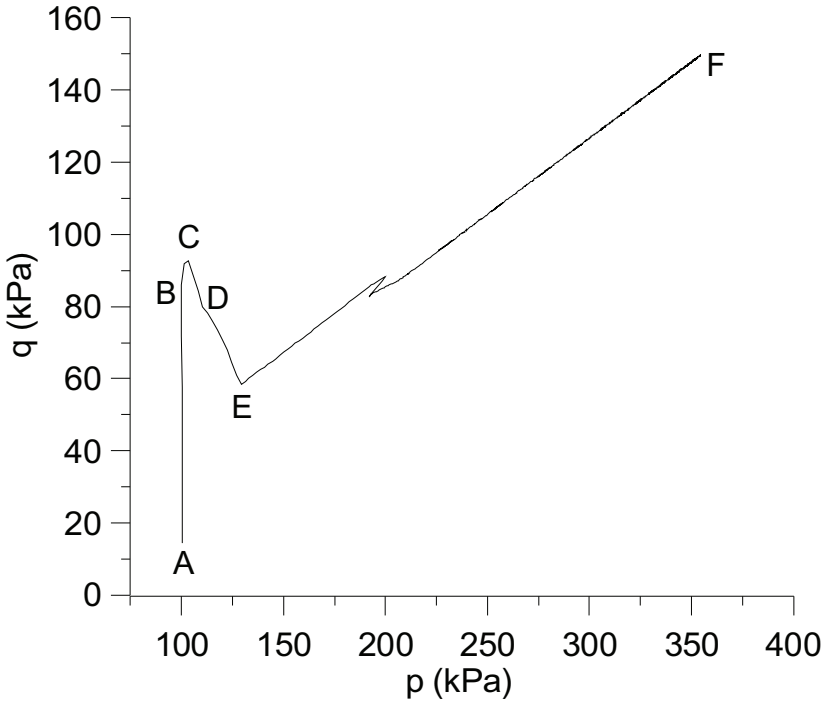

Fig. 7.18 $q-p$ stress path curve with 100 kPa initial stress

7.5 Summary

By introducing the post-rupture strength for stiff overconsolidated clays, a simplified elastoplastic model comprising two-stage linear softening is proposed to simulate the corresponding stress-strain softening curve. Subsequently, all the analytical solutions

for limit pressure, stress, strain, and displacement fields for the expansion of cylindrical cavity have been derived in a simple way. This method is particularly appropriate for stiff overconsolidated clays and overcome the defects in the classical theory of the expansion of elastoplastic cylindrical cavity.

The computational examples indicate that the quadralinear softening model can degenerate to the original trilinear model and give the same results as those published previously.

This model is quite flexible to perform a parametric study. It shows that all the parameters including shear dilation (h, f and g),initial stress p_0 , softening mode (β and ω), post-rupture strength parameters (c_{pr} and ϕ_{pr}) and elastic constants (E and ν) can influence the ultimate pressure p_u , transition radii (R_3, R_2, R_1), and the displacement, strain and stress fields. This formulation provides a simple method for theoretical studies.

In addition, the similarity between numerical solution and analytical one inversely verifies the correctness of the analytical solution to cavity expansion in stiff clays using two-stage softening characteristics.

The concept of post-rupture strength and the method presented in this chapter may also be applicable to other cases using different yield criterions such as the Tresca yield criterion (Liang & Chen, 2004). With a similar procedure, the corresponding analytical solutions can be worked out.

Chapter 8. Conclusions

According to all the aforementioned demonstration of two-stage softening of stiff clays involving post-rupture strength, the following conclusions can be drawn:

1. Laboratory, field and numerical results verify the existence and robustness of post-rupture strength for stiff overconsolidated clays. The post-rupture strength envelope for the slip surfaces formed during the failure of initially intact stiff clay is well defined, repeatable, not sensitive to stress history or softening due to dilation and distortion, and not influenced by the rotation of the principal stresses but dependent on the stress level.
2. Analysis of collected data demonstrates that the post-peak strain-softening characteristic of stiff clays can be divided into two stages. The microstructure studies indicate that the first softening stage is induced by the loss of interbonding between particles, i.e. the cohesive component of strength at relatively small displacement and hence termed as cementation loss; while the second is due to the gradual realignment, i.e. reorientation of clay particles at large displacements and can be called as gradual frictional resistance loss.
3. Although post-rupture is different from so called critical-state strength (i.e. fully softened strength), the critical-state strength can still be considered as a good reference for post-rupture strength. The main difference between these two strengths lies on that the cohesion of critical-state strength is zero and is a special case of post-rupture strength which involves small cohesion (normally between 0 and 10 kPa) due to rapid reduction of cohesion after peak with relatively small displacement.
4. The modified two-stage softening model based on the generalised non-linear strain softening/hardening model through improving original Mohr-Coulomb model is established and formulated. This model is implemented into *FLAC* in a easy way based on built-in strain softening/hardening model and can be used to simulate the two-stage post-peak softening feature of stiff overconsolidated clays, especially the post-rupture strength.
5. The triaxial tests and direct shear box test are reproduced via two-stage strain-softening model. All the numerical results demonstrate the capability and efficiency of the modified softening model to model the two-stage strain-softening behaviour of stiff clays.
6. A series of analyses of delayed progressive failure of cut slopes in stiff clays similar to those conducted by Potts et al. (1997) have been performed using both one-stage and two-stage softening models. The results obtained state:

(a) The numerical results reproduce well the progressive failure process, position of failure surface and failure time.

(b) Parametric analyses such as K_0 effect, surface suction effect, slope geometry effect, influence of post-rupture strength parameters and critical stable cutting height are also carried out to demonstrate the general influence of post-rupture strength while taking bulk peak strength as the initial peak strength in two-stage softening model.

(c) The local FOS and average FOS can be used to evaluate the slope stability in stiff clays with softening behaviour.

(d) In cases using bulk peak strength as initial peak strength in two-stage softening model, the critical stable cutting height using post-rupture strength parameters is 0.5 meter lower than that using only one-stage softening parameters whereas the collapse time with two-stage softening model is longer than that with one-stage softening model.

(e) In consideration of the whole formation process of highly fissured clay, the intact peak strength might be reckoned as the initial original peak strength ($c_p^{'}=20$kPa, $\phi_p^{'}=20°$) and the bulk peak strength could be reasonably assumed as the so-called relevant post-rupture strength ($c_{pr}^{'}=7$kPa, $\phi_{pr}^{'}=20°$) accounting for the fissures in clay. The residual strength is chosen as $c_r^{'}=2$kPa, $\phi_r^{'}=13°$.

(f) The results in analyses applying intact peak strength elucidate that:

- The softening rate of strength parameters has remarkable influence on the collapse time and plays the main role of controlling collapse time.
- The collapse time with two-stage softening model applying intact peak strength is shorter than that with one-stage softening model due to the notable cohesion difference between peak and post-rupture strengths.
- The critical stable height with two-stage softening model applying intact peak strength is lower than that with one-stage softening model adopting bulk peak strength.

(g) The slope stability with the adoption of two-stage softening model is reduced compared with that using one-stage softening model due to the quicker cohesion reduction with deviatoric plastic strain in the first softening stage of two-stage softening model. Post-rupture strength is of significance to account for the quicker cohesion degradation at the first stage in two-stage softening model.

7. The results of numerical simulations of Aznalcóllar dam failure via two-stage softening model incorporating the post-rupture strength concept under both inhomogeneous and homogeneous hypotheses with different softening rates respectively demonstrate:

(a) The mechanism of Aznalcóllar dam failure is deemed to be progressive failure mainly due to the softening of Guadalquivir blue clay, which can be elucidated by the whole failure process in both analyses.

(b) The slip surfaces predicted in analyses under both inhomogeneous and homogeneous hypotheses are similar to the real case.

(c) The failure initiated just after the construction of final dam layer and then developed gradually till the sudden post-failure acceleration of displacement when the final slip surface formed completely.

(d) There is very limited dissipation of pore water pressure and small extent of consolidation due to the low permeability. This is proved by the development of pore pressure along profile A-E and slip surface. The magnitude of the pore water pressure development agrees with the added dam and tailings weight above the analysed point.

(e) The average stress path along the slip surface shows that, at the beginning of failure, stress points lay closely to the post-rupture strength envelope. Afterwards the average shear stress along the slip surface reduced nearly vertically with very little change in effective normal stress.

(f) The distribution of shear stress along failure surface was intermediate between the peak and residual values. Whereas at final failure the shear stress is almost the same as residual value, which confirms further the mechanism of progressive failure of Aznalcóllar dam.

(g) The Aznalcóllar dam failure is sensitive to the softening rate denoted by γ_{pr} and γ_r. Larger rates will induce earlier failure and no failure will occur with slow softening rate. Only an appropriate value of softening rate can cause failure at final phase under both inhomogeneous and homogeneous hypotheses.

8. The extension of the post-rupture strength concept to analytical solutions to cylindrical cavity expansion in stiff overconsolidated clay illuminates the generalisation of post-rupture strength concept and the relevant two-stage softening model in geotechnical engineering problems. The relevant analytical and numerical modelling results elucidate:

(a) By introducing the post-rupture strength for stiff overconsolidated clays and on the basis of the trilinear model, a simplified elastoplastic model comprising two-stage linear softening is proposed to simulate the corresponding stress-strain-softening curve. All the analytical solutions to limit pressure, the stress, strain, and displacement fields for the expansion of cylindrical cavity have been derived in a simple way. This method can cope especially with stiff overconsolidated clays and overcome the defects in the classical theory about the expansion of elastoplastic cylindrical cavity.

(b) This model is quite flexible to make parametric study. The computational examples indicate that the quadralinear softening model can degenerate to the original trilinear model and gives the same results as those published.

(c) The similarity between numerical solution and analytical one inversely verifies the reasonableness of the analytical solution to cavity expansion in stiff clays with two-stage softening characteristics.

(d) This analysis illuminates the possibility of generalisation of post-rupture strength concept and the relevant two-stage softening model in geotechnical engineering problems.

9. Future work may be resumed and is listed in the following:

(a) Though this thesis presents the general information of post-rupture strength, the relevant experimental study such as more detailed examination of strength degradation of stiff clays via advanced microscopic devices and laboratory tests should be carried out so as to develop a feasible method to associate directly the mobilised softening strength parameters with plastic shear strain or displacement for stiff clays. A good example is the biaxial compressive unconfined tests on Beaucaire marl conducted at the *Laboratoire 3S* of the Université Fourier of Grenoble with the method of *False Relief Stereo-photogrammetry* (Allodi A. et al., 2003; Castelli, M., Allodi, A., Scavia C., 2009). Meanwhile, in their study, a computer code BEMCOM with Slip-Weakening-Model (SWM) based on the BEM technique of the Displacement Discontinuity Method was utilised to simulate the relevant experimental results. Of importance, in this simulation, one-stage softening model was assumed for Beaucaire marl. Analogously the corresponding with experimental test can be designed to capture the two-stage softening process of stiff clays such as Guadalquivir blue clay and numerical modelling with BEMCOM via two-stage softening scheme may be performed.

(b) Particle flow code PFC might also be used to investigate the failure mechanism with two-stage softening behaviour of stiff clays.

(c) It will be of significance to apply the automeshing technique to simulate large deformation in the progressive failure cases presented in this thesis.

(d) The two-stage softening model can also be implemented into finite element code such as ICFEP and comparisons might be made between FEM and FDM.

(e) Nonlocal elasto-viscoplastic model (Troncone, 2005) might also be combined with the two-stage softening model to minimize the mesh size influence.

(f) Schuller and Schweiger (2002) formulated a constitutive model within the framework of Multilaminate Models, which takes into account of both frictional and cohesive softening behaviour with the development of plastic shear involving shear banding, to analyse the practical problem of a tunnel construction according to the principles of the NATM (New Austrian Tunnelling Method). Again the two-softening model might be incorporated into this model to make similar analysis in tunnelling problems such as tunnelling swelling in stiff clays.

(g) The author believes that the study on stiff clays in micro-meso-macro scales and the development of corresponding multi-scale constitutive model combining continuum and discontinuum methods, conventional soil mechanics, fracture mechanics, and damage mechanics will lead the research trend in next decades.

References

(1) Al-Tabbaa, A. (1987). *Permeability and stress-strain response of speswhite kaolin*. PhD thesis, University of Cambridge, Cambridge, UK.

(2) Al-Tabbaa, A. and Wood, D.M. (1989). An experimental based "bubble" model for clay. *International Conference on Numerical Models in Geomechanics*, A. Pietruszczak and G.N. Pande (eds.), Balkema, pp. 91-99.

(3) Allodi, A., Castelli M., Marello S., Scavia C. (2003). Shear band propagation in soft rocks: numerical simulation of experimental results. *ISRM 2003–Technology roadmap for rock mechanics*, South African Institute of Mining and Metallurgy.

(4) Alonso, E., Alejano, L. R., Varas, F., Fdez-Manín, G. and Carranza-Torres, C. (2003). Ground response curves for rock masses exhibiting strain-softening behaviour. *International Journal for Numerical and Analytical Methods in Geomechanics*, Volume 27, Issue 13, 1153-1185.

(5) Alonso, E. E. & Gens, A. (2006a). Aznalcóllar dam failure. Part 1: Field observations and material properties. *Géotechnique*, Vol. 56, No. 3, pp. 165-183.

(6) Alonso, E. E. & Gens, A. (2006b). Aznalcóllar dam failure. Part 3: Dynamics of the motion. *Géotechnique*, Vol. 56, No. 3, pp. 203-210.

(7) Anagnostopoulos, A. G., Kalteziotis, N., Tsiambaos, G. K. & Kavvadas, M. (1991). Geotechnical properties of the Corinth canal marls. *J. Geotech. Geol. Engng*. 9, 1-26.

(8) Atkinson, J. H. & Richardson, D. (1987). The effect of local drainage in shear zones on the undrained strength of overconsolidated clay. *Géotechnique*, 37, No. 3, 393-403.

(9) Atkinson, J. H. (2000). Non-linear soil stiffness in routine design. *Géotechnique.* Vol.50, No. 5, 487–508.

(10) Atkinson, J.H., Richardson, D. and Stallebrass, S.E. (1990). Effect of recent stress history on the stiffness of overconsolidated soil. *Géotechnique.* Vol. 40, No. 4, pp. 531-540.

(11) Badr, S., Ozbay, U., Kieffer, S. & Salamon, M. (2003). Three-dimensional strain softening modelling of deep longwall coal mine layouts. *FLAC and Numerical Modelling in Geomechanics–Proceedings of the Third International FLAC Symposium*, Sudbury, Ontario, pp. 233-239.

(12) Barla, G. and Barla, M. (2001). Numerical simulation of squeezing behavior in tunnels. *FLAC and Numerical Modelling in Geomechanics–Proceedings of the Second International FLAC Symposium*, Lyon, France, pp. 323-328.

(13) Battaglio, M., Jamiolkowski, M., Lancellotta, R. & Maniscalco, R. (1981). Piezometer probe test in cohesive deposits. *In Cone penetration testing and experience* (eds G. M. Norris and R. D. Holtz), pp. 264-302. New York: ASCE.

(14) Baudet, B.A. (2001). *Modelling effects of structure in soft natural clays*. PhD thesis, City University, London, UK.

(15) Baudet, B. and Stallebrass, S. (2004). A constitutive model for structured clays. *Géotechnique*, 54, No. 4, 269–278.

(16) Berchenko, J. (1998). Thermal loading of a saturated rock mass: field experiment and modelling using thermoporoelastic singular solutions. Ph.D. Thesis, University of Minnesota.

(17) Binnie, M. A., Clark, J. F. F. & Skempton, A. W. (1967). The effect of discontinuities in clay bedrock on the design of dams in the Mangla'project. *Trans. 9th Int. Congr. Large Dams, Istanbul* 1, 165-183.

(18) Bishop, A. W. (1955). The use of the slip circle in the stability analysis of slopes. *Géotechnique*, 5, No. 1, 7-17.

(19) Bishop, A. W. (1967). Progressive failure with special reference to the mechanism causing it. *Proc. Geotech. Conf., Oslo* 2, 142-150.

(20) Bishop, A. W. (1971). The influence of progressive failure on the choice of the method of stability analysis. *Géotechnique*, 21, No.2, 168–172.

(21) Bishop, A. W. (1973). The influence of an undrained change in stress on the pore pressure in porous media of low compressibility. *Géotechnique*, 23, No.3, 435–442.

(22) Bishop, A. W. & Bjerrum, L. (1960). The relevance of the triaxial test to the solution of stability problems. *Proceedings of the ASCE research conference on shear strength of cohesive soils, Boulder*. pp. 437-501.

(23) Bishop, A. W., Green, G. E., Garga, V. K., Andresen, A., and Brown, J. D. (1971). A new ring shear apparatus and its application to the measurement of residual strength. *Géotechnique*, 21, No.4, 273–328.

(24) Bishop, A. W., Webb, D. L. & Lewin, P. I. (1965). Undisturbed samples of London Clay from the Ashford Common shaft: strength-effective stress relationship. *Géotechnique*, 15, No.1, 1-31.

(25) Bjerrum. L. (1967). Progressive failure in slopes of overconsolidated plastic clay and clay shales. *Jnl Soil Mech. Fdns Div. Am.Soc.Civ.Engrs*. 93, SM5, 3-49.

(26) Blondeau, F. & Josseaume, H. (1976). Mesure de la résistance au cisaillement résiduelle en laboratoire. Bulletin de Liaison des Laboratoires des Ponts et Chaussées. *Stabilité de talus* 1, versants naturels, numéro spécial II, 90-106.

(27) Bolton, M. D. & Whittle, R. W. (1999). A non-linear elastic/perfectly plastic analysis for plane strain undrained expansion tests. *Géotechnique*, Vol. 49, No. 1, 133-141.

(28) Borowicka, H. (1965). The influence of the colloidal content on the shear strength of clay. *Proc. 6th Int. Conf: Soil Mech., Montreal* 1, 175-178.

(29) Brand, E. W. (1982). Analysis and design in residual soils. Proceedings of the ASCE special conference on engineering and construction in tropical and residual soils, Hawaii, pp. 463-482.

(30) Bromhead, E. N., Cooper, M. R. & Petley, D. J. (1998). The Selborne cutting slope stability experiment (CD-ROM-The Selborne data collection CD).

(31) Brooker, E. W., and Peck, R. B. (1993). Rational design treatment of slides in overconsolidated clays and clay shales. *Can. Geotech. J.*, 30, 526–544.

(32) Brown, E. T. , Bray, J. W., Ladanyi, B. & Hoek. E. (1983). Ground response curves for rock tunnels. *J. Geotech. Engng.*, ASCE 109, No. 1, 15–39.

(33) Brummeq, R.K., Andrieux, P.P. and O'Connor, C.P. (2003). Stability analyses of undermined sill mats for base metal mining. *FLAC and Numerical Modelling in Geomechanics–Proceedings of the Third International FLAC Symposium*, Sudbury, Ontario, pp. 189-196.

(34) Bu, S. (2001). Seismic evaluation of concrete gravity dams using *FLAC*. *FLAC* and Numerical Modelling in Geomechanics–Proceedings of the Second International *FLAC* Symposium, Lyon, France, pp. 39-42.

(35) Bucher, F. (1975). *Die Restscherfestigkeit natürlicher Böden, ihre Einfluussgrössen und Beziehungen als Ergebnis experimenteller Untersuchungen*. Report NO. 103. Zürich: Institutes für Grundbau und Bodenmechanik Eidgenössische Technische Hochschule.

(36) Burland, J. B. (1989). The ninth Bjerrum Memorial Lecture: 'Small is beautiful'-the stiffness of soils at small strains. *Can. Geotech. J.* 26,499-516.

(37) Burland, J. B. (1990). On the compressibility and shear strength of natural clays. *Géotechnique*, 40, No. 3, 329-378.

(38) Burland, J. B., Longworth, T. I., and Moore, J. F. (1977). A study of ground movement and progressive failure caused by a deep excavation in Oxford clay. *Géotechnique*, 27, No.4, 557–591.

(39) Burland, J. B., Longworth, T. I., and Moore, J. F. A. (1978). A study of ground movement and progressive failure caused by a deep excavation in Oxford clay. *Géotechnique*, 28, No.3, 357–358.

(40) Burland, J. B., Rampello, S., Georgiannou, V. N. & Calabresi, G. (1996). A laboratory study of the strength of four stiff clays. *Géotechnique* 46, No. 3, 491-514.

(41) Burland, J. B. & Symes, M. (1982). A simple axial displacement gauge for use in the triaxial apparatus. *Géotechnique*, 32, No. 1, 62-65.

(42) Calabresi, G. (1980). The effect of sample size on strength parameters for intact and fissured stiff clays. *Proceedings of Euromech colloquium No.* 134. Copenhagen: Technical University of Denmark.

(43) Calabresi, G. and Manfredini, G. (1973). Shear strength characteristics of the jointed clay of S.Barbara. *Géotechnique* 23, No. 2, 233-244.

(44) Calabresi, G. and Rampello, S. and Viggiani, G. (1990). ´I1 comportamento meccanica delle argille consistenti´, Atti III Ciclo di Conferenze di Meccanica

ed Ingegneria delle Rocce, Department of Structural Engineering, Politecnico di Torino, Italy.

(45) Callisto, L., Gajo A. and Muir Wood, D. (2002). Simulation of triaxial and true triaxial tests on natural and reconstituted Pisa clay. *Géotechnique*, Vol. 52, No. 9, pp. 649-666.

(46) Cancelli, A. (1981). Evaluation of slopes in overconsolidated clays. *Proc., 10th Int. Conf. on Soil Mechanics and Foundation Engineering*, A. A. Balkma, Rotterdam, 3, 377–380.

(47) Cao, L. F., Na, Y. M., Win, B. M. & Choa, V. (1998). Analysis of cone pressuremeter test in clay. *Proc. 13th Southeast Geotech. Conf.*, Taiwan, 23-28.

(48) Carter, J. P. & Yeung, S. K. (1985). Analysis of cylindrical cavity expansion in strain-weakening material. *Comput. Geotech.*, Vol. 1, No. 3 , 161–180.

(49) Castelli, M., Allodi, A., Scavia C. (2009). A numerical method for the study of shear band propagation in soft rocks. *Int. J. Num. Methods and Anal. Methods in Geomech.*, 33, 1561-1587.

(50) Chan, D. H. (1986). *Finite element analysis of strain softening material*. Ph.D thesis, Department of Civil Engineering, The University of Alberta, Edmonton.

(51) Chan, D. H. & Morgenstem, N. R. (1987).Analysis of progressive deformation of the Edmonton Convention Centre. *Can. Geotech. J*. 24, 430-440.

(52) Chan, D. H. & Morgenstem, N. R. (1989). *Bearing capacity of strain softening soil*. De Mello volume, 59-68. Editora Edgard Blucher Ltda.

(53) Chandler, R. J. (1966). The measurement of residual strength in triaxial compression. *Géotechnique* 16, No. 3, 181-186.

(54) Chandler, R. J. (1972). Lias clay: weathering processes and their effect on shear strength. *Géotechnique*, 22, No.3, 403–431.

(55) Chandler, R. J. (1974). Lias clay: the long term stability of cutting slopes. *Géotechnique*, 24, No.1, 21–38.

(56) Chandler, R. J. (1977). Back analysis techniques for slope stabilization works: a case record. *Géotechnique*, 27, No.4, 479–495.

(57) Chandler, R. J. (1984a). Recent European experience of landslides in over-consolidated clays and soft rocks. State-of-the-art report. *Proc. 4th Int. Symp. Landslides*, *Toronto* 1, 61-81.

(58) Chandler, R. J. (1984b). Delayed failure and observed strengths of first-time slides in stiff clays. *Proc. 4th Int. Symp. Landslides*, *Toronto*, 2, 19–25.

(59) Chandler, R. J. (1998). Tectonic shear zones in the London Clay Formation. *Géotechnique*, 48, No.2, 257–270.

(60) Chandler, R. J. (2000). Clay sediments in depositional basins: the geotechnical cycle. *Q. J. Engng Geol. Hydrogeol*. 33, 7-39.

(61) Chandler, R. J., and Apted, J. P. (1988). The effect of weathering on the strength of London Clay. *Q. J. Eng. Geol*., 21, 59–68.

(62) Chandler, R. J., and Skempton, A. W. (1974). The design of permanent cutting slopes in stiff fissured clays. *Géotechnique*, 24, No.4, 457–466.

(63) Chang, M. F., Choa, V., Cao, L. F. & Arulrajah A. (1998). Evaluating the state of consolidation of clay at a reclaimed site. *Proc. First Int. Symp. Geotech. Site Characterization*, Atlanta, 1403-1408.

(64) Chen, Z. (1990). *Analysis of progressive failure of the Carsington Dam*. Ph.D thesis, Department of Civil Engineering, The University of Alberta, Edmonton.

(65) Chen, Z., Morgenstern, N. R. & Chan, D. H. (1992). Progressive failure of the Carsington Dam: a numerical study. *Can. Geotech. J.* 29, Dec., 971-988.

(66) Cividini, A. and Gioda, G. (1992). Finite element analysis of direct shear tests of stiff clays. *Int. J. Numer. Anal. Meth.Geomech*., 16, 869-886.

(67) Collins, B. & Znidarcic, D. (1997). Triggering mechanisms of rainfall induced debris flows. *Proc. 2nd Int. Pan-American Symp. Landslides, Rio de Janeiro* 1, 277-286.

(68) Collins, B. & Znidarcic, D. (1998). Slope stability issues of rainfall induced landslides. *Proc. 11th Danube-European Conf. Soil Mech. Geotech. Engng, Porec, Croatia*, 791-798.

(69) Collotta, T., Beretta, P., D'Angelantonio, M., Cianciosi, O. & Di Napoli, M. (1999). Stabilization of deep landslides in overconsolidated clays: 3D back-analyses of centrifuge model. *FLAC and Numerical Modelling in Geomechanics–Proceedings of the First International FLAC Symposium*, Minneapolis, Minnesota, pp. 79-85.

(70) Cotecchia, F. & Chandler, R. J. (1997). The influence of structure on the pre-failure behaviour of a natural clay. *Géotechnique* 47, No. 3, 523-544.

(71) Cotecchia, F. & Chandler, R. J. (1998). One-dimensional compression of a natural clay: Structural changes and mechanical effects. *Proc. 2nd Symp. Geotech. Hard Soils-Soft Rocks, Napoli* 2, 103-114.

(72) Cooper, M. R. (1996). The progressive development of a failure surface in overconsolidated clay at Selborne, U.K. *Proc. 7th Int. Symp. on Landslides, Trondheim*, Vol. 2, pp. 683-688.

(73) Cooper, M. R., Bromhead, E. N., Petley, D. J., and Grant, D. I. (1998). The Selborne cutting stability experiment. *Géotechnique*, 48, No.1, 83–101.

(74) Cunningham, M. R., Ridley, A. M., Dineen, K. & Burland, J. J. (2003). The mechanical behaviour of a reconstituted unsaturated silty clay. *Géotechnique*, 53, No.2, 183–194.

(75) D'Elia, B., Esu, F., Tommasi, P. & Utzeri, L. (1999). *FLAC* modelling of the deformation and failure mechanism of a high cut in clay shales. *FLAC and Numerical Modelling in Geomechanics–Proceedings of the First International FLAC Symposium*, Minneapolis, Minnesota, pp. 47-54.

(76) D'Elia, B., Picarelli, L., Leroueil, S. & Vaunat, J. (1998). Geotechnical characterization of slope movements in structurally complex clay soils and stiff jointed clays. *Italian Geotech. J.* No. 32, No. 3, 5-32.

(77) Dafalias, Y.F. and Herrmann (1980). A bounding surface soil plasticity model. *International Symposium on Soils under Cyclic and Transient loading*, Swansea, Vol. 1, pp. 335-345.

(78) Dafalias, Y.F. and Herrmann (1982). Bounding surface formulation of soil plasticity. *Soil Mechanics-Transient and Cyclic Loads*, G.N. Pande and O.C. Zienkiewicz (eds.). John Wiley and Sons Ltd.

(79) Dafalias, Y.F. and Popov, E.P. (1975). A model of nonlinearly hardening materials for complex loadings. *Acta Mechanica*, Vol. 21, pp. 173-192.

(80) Dafalias, Y.F. and Popov, E.P. (1976). Plastic internal variables formalism of cyclic plasticity. *Journal of Applied Mechanics, ASME*, Vol. 98, pp. 645-650.

(81) Davachi, M.M., Sinclair, B.J., Hartmaier, H.H. and Baggott, B.L. (1991). Determination of the Oldman River Dam foundation shear strength. *Can. Geotech. J.*, 28, 698–707.

(82) De Beer, E. E. (1969). Experimental data concerning clay slopes. *Proc. 7th Int. Conf. Soil Mech. Found. Engng, Mexico City* 2, 517-525.

(83) De Borst, R. (1988). Bifurcations in finite element models with a non associated flow law, *Int. J. Numer. Anal. Meth. Geomech.*, 12, 99-116.

(84) DeLory, F. A. (1957). *Long term stability in slopes in overconsolidated clays*. PhD thesis, Univ. of London, London.

(85) Desai, C. S. (1974). A consistent finite element technique for strain-softening behaviour, in J. Oden et al. (eds), *Proc. Int. Conf. Computational Meth. in Nonlin. Mech.*, Austin, TX.

(86) Desai, C. S. & Siriwardane, H. J. (1984). *Constitutive laws for engineering materials with emphasis on geological materials*. Prentice-Hall, Inc., Englewood Cliffs, New Jersey.

(87) Desai, C. S., Somasundaram, S. and Frantziskonis, G. (1986). A hierarchical approach for constitutive modelling of geologic materials, *Int. J. Numer. Anal. Meth. Geomech.*, 10, 225-257.

(88) Deschamps, R. J. & Leonards, G. A. (1992). A study of slope stability analysis. *ASCE Specialty Conf. Stability and Performance of Slopes and Embankments II, San Francisco* 1, 267-291.

(89) Di Maio, C. (1996a). The influence of pore fluid composition on the residual shear strength of some natural clayey soils. *Proc. 7th Int. Symp. Landslides, Trondheim* 2, 1189-1194, Balkema, Rotterdam.

(90) Di Maio, C. (1996b). Exposure of bentonite to salt solution: osmotic and mechanical effects. *Géotechnique*, 46, No. 4, 695-707.

(91) di Prisco, C. & Imposimato, S. (2003). Non local numerical analyses of strain localization in dense sand. *Math. Comput. Modelling*. 37, Nos 5–6, 497–506.

(92) di Prisco, C., Imposimato, S. & Aifantis, E. C. (2002). A viscoplastic constitutive model for granular soils modified according to non-local and gradient approaches. *Int. J. Numer. Anal. Methods Geomech.* 26, 121–138.

(93) Dolezalová, M., Hladík, I. and Zemanová, V. (2001). Stability analysis of a motorway embankment on soft subsoil using *FEM*, *FLAC* and limit equilibrium methods. *FLAC and Numerical Modelling in Geomechanics–Proceedings of the Second International FLAC Symposium*, Lyon, France, pp. 125-132.

(94) Dounias, G. T., Potts, D. M. & Vaughan, P. R. (1988). Finite element analysis of progressive failure: two case studies. *Comput. Geotech*, 6, 155-175.

(95) Dounias, G. T., Potts, D. M. & Vaughan, P. R. (1989). *Numerical stress analysis of progressive failure and cracking in embankment dams.* Report to the Department of the Environment, Contract No. PECD 7/7/222, Building Research Establishment.

(96) Dounias, G. T., Potts, D. M. & Vaughan, P. R. (1996). Analysis of progressive failure and cracking in old British dams. *Géotechnique*, 46, No. 4, 621-640.

(97) Duncan, J. M. (1996). State of the art: limit equilibrium and finite element analysis of slopes. *J. Geotech. Eng.*, *ASCE* 122, No.7, 577–596.

(98) Dunlop, P. & Duncan, J. M. (1970). Development of failure around excavated slopes. *J. Soil Mech. Found. Div., ASCE* 96, No. 2, 471-493.

(99) Eid, H. T. (1996). *Drained shear strength of stiff clays for slope stability analyses*. PhD thesis, Univ. of Illinois at Urbana-Champaign, Ill.

(100) Eigenbrod, K. D. (1975). Analysis of the pore pressure changes following the excavation of a slope. *Can. Geotech. J.* 12, No. 3, 429-440.

(101) Farrar, D. M. (1990). *Observations of slope drainage at Romford, Essex*. Research Report 302, Transport & Road Research Laboratory, Crowthorne.

(102) Fellenius, W. (1936). Calculation of the stability of earth dams. *Proc. 2nd Congr. Large Dams, Washington DC* 4.

(103) Finno, R. J. & Rhee, Y. (1993). Consolidation, pre- and post-peak shearing responses from internally instrumented biaxial compression device. *Geotech. Test. J. AST.* 16, No. 4, 496–509.

(104) Fleischer, S. (1972). Scherbruch und Schergleitfestigkeit von Bindigen Erdstoffen. *Neue Bergbautechnik* 2, No. 2, 98-99. Freiburg: Mining Academy.

(105) Gajo, A. and Muir Wood, D. (2001). A new approach to anisotropic, bounding surface plasticity: general formulation and simulations of natural and reconstituted clay behaviour. *International Journal for Numerical and Analytical Methods in Geomechanics*, Vol. 25, pp. 207-241.

(106) Gens, A. & Alonso, E. E. (2006). Aznalcóllar dam failure. Part 2: Stability conditions and failure mechanism. *Geótechnique.* Vol. 56, No. 3, 185–201.

(107) Georgiannou, V. N. and Burland, J. B. (2001) A laboratory study of post-rupture strength. *Géotechnique*, 51, No. 8, 665–675.

(108) Georgiannou, V. N. (2003) Tunnelling through varying soil conditions in north-west Greece. *Proceedings of the Institution of Civil Engineers, Geotechnical Engineering,* 156, Issue GE2, 97–104.

(109) Georgiannou, V. N. & Burland, J. B. (2006). A laboratory study of slip surface formation in an intact natural stiff clay. *Geótechnique.* Vol. 56, No. 8, 551–559.

(110) Gibson, R. E. & Anderson, W. F. (1961). In-situ measurement of soil properties with the pressuremeter. *Civ. Engng Public Works Rev.*, 56, 615-618.

(111) Gilbert, R. B., Long, J. H., Moses, B. E. (1996). Analytical model of progressive slope failure in waste containment systems. *Int J Numer Anal Methods Geomech*. 20(1):35–56.

(112) Griffiths, D. V. and Lane, P. A. (1999) Slope stability analysis by finite elements. *Géotechnique*, 49, No. 3, 387–403.

(113) Guan, Z., Jiang Y. and Tanabasi Y. (2007). Ground reaction analyses in conventional tunnelling excavation. *Tunnelling and Underground Space Technology*, Volume 22, Issue 2, 230-237.

(114) Hammoud, I. & Schafl, P. (2001). Experiments on small-scale models and comparison with calculations with the finite difference method (*FLAC*). *FLAC and Numerical Modelling in Geomechanics–Proceedings of the Second International FLAC Symposium*, Lyon, France, pp. 215-222.

(115) Hashiguchi, K. (1980). Constitutive equations of elastoplastic materials with elasticplastic transition. *Journal of Applied Mechanics, ASME*, Vol. 47, pp. 266-272.

(116) Hashiguchi, K. (1985). Two- and three-surface models of plasticity. *Proceedings of the 5th International Conference on Numerical Methods in Geomechanics*, Nagoya, pp. 285-292.

(117) Hashiguchi, K. (1989). Subloading surface model in unconventional plasticity. *International Journal of solids and structures*, Vol. 25, pp. 917-945.

(118) Hashiguchi, K., Saitoh, K., Okayasu, T., and Tsutsumi, S. (2002). Evaluation of typical conventional and unconventional plasticity models for prediction of softening behaviour of soils. *Géotechnique*, 52, No. 8, 561–578.

(119) Hashiguchi, K. and Ueno, M. (1977). Elastoplastic constitutive laws of granular materials. *Constitutive equations of soils*, *Proceedings of the 9th International Conference on Soil Mechanics and Foundation Engineering*, Special session 9, Tokyo, pp. 73-82.

(120) Henkel, D. J., and Skempton, A. W. (1955). A landslide at Jackfield, Shropshire, in heavily overconsolidated clay. *Géotechnique*, 5, 131–137.

(121) Henkel, D. J. (1957). Investigations of two long term failures in London clay slopes at Wood Green and Northolt. *Proc., 4th Int. Conf. on Soil Mechanics and Foundation Engineering*, 2, 315–320.

(122) Hight, D. W. (1982). A simple piezometer probe for the routine measurement of pore pressure in triaxial tests on saturated soils. *Géotechnique*, 32, No. 4, 396-401.

(123) Hight, D. W., Bond, A. J. & Legge, J. D. (1992). Characterization of the Bothkennar clay: an overview. *Géotechnique*, 42, No. 2, 303-347.

(124) Hill, R. (1958). A general theory of uniqueness and stability in elastic-plastic solids. *J. Mech. Phys. Solids*, 6, 236–249.

(125) Houlsby, G. T. & Withers, N. J. (1988). Analysis of the cone pressuremeter test in clay. *Géotechnique*, Vol. 38, No. 4, 575-587.

(126) Hughes, J. M. O., Wroth, C. P. & Windle, D. (1977). Pressuremeter tests in sands. *Géotechnique*, Vol. 27, No. 4, 455-477.

(127) Hutchinson, J. N. (1987). Mechanisms producing large displacements in landslides on pre-existing shears. *Mem. Geol. Soc. of China*, 9, 175-200.

(128) Hutchinson, J. N. (1988). Morphology and geotechnical parameters of landslides in relation to geology and hydrogeology. *Proc. 5th Int. Symp. Landslides, Lausanne* 1, 3-35, Balkema, Rotterdam.

(129) Itasca *FLAC* Manual (2005). Minneapolis: Itasca Consulting Group, Inc.

(130) Iwan, W.D. (1967). On a class of models for the yielding behavior of continuous and composite systems. *Journal of Applied Mechanics, ASME*, Vol. 34, pp. 612-617.

(131) James, P. M. (1970). *Time effects and progressive failure in clay slopes*. PhD thesis, Univ. of London, London.

(132) Janbu, N. (1968). Slope stability computations. *Soil Mech. Found. Engng Report*. Trondheim: Technical University of Norway.

(133) Janbu, N. (1977). Slopes and excavations in normally consolidated and lightly overconsolidated clays. *Proc., 9th Int. Conf. in Soil Mechanics and Foundation Engineering*, Tokyo, 2, 549–566.

(134) Jardine R.J. (1985). Investigations of pile-soil behaviour with special reference to the foundations of offshore structures. PhD thesis, Imperial College, University of London, London, UK.

(135) Jardine R.J. (1992). Some observations on the kinematic nature of soil stiffness. *Soils and Foundations*, Vol. 32, No. 2, pp. 111-124.

(136) Jardine, R.J, Gens, A., Hight, D.W. and Coop, M.R. (2004) Developments in understanding soil behaviour. Keynote paper. *Advances in Geotechnical Engineering. Proc Skempton Memorial Conference*. Pub Thomas Telford, London, pp. 103-207

(137) Jardine, R.J., Potts, D.M., Fourie, A.B. and Burland, J.B. (1986). Studies of the influence of non-linear stress-strain characteristics in soil-structure interaction. *Géotechnique*, Vol. 36, No. 3, pp. 377-396.

(138) Jardine, R.J., Potts D.M., St. John, H.D. and Hight, D.W. (1991). Some practical applications of a non-linear ground model. *Proceedings of the 10th European Conference on Soil Mechanics and Foundation Engineering*, Florence, Vol. 1, pp. 223-228.

(139) Jiang, M.J. and Shen, Z.J. (1995). Expansion of cylindrical cavity of materials with strain-softening behaviour. *Chinese Journal of Geotechnical Engineering*, 17(4), 10-19.

(140) Jiang, M.J. and Shen, Z.J. (1996a). Unified solution to expansion of cylindrical cavity for geomaterials with strain-softening behaviour. *Rock and Soil Mechanics*, 17(1), 1-8.

(141) Jiang, M.J. and Shen, Z.J. (1996b). Expansion of cylindrical cavity with elastic-brittle-plastic softening and shear dilation behaviour. *Journal of Hohai University*, 24(4), 1-8.

(142) Jiang, M.J. and Shen, Z.J. (1996c). Computation and analysis on bearing capacity of foundation with strain-softening behaviour. *Journal of Nanjing Hydraulic Research Institute*, No.1, 42-47.

(143) Jiang, M.J. and Shen, Z.J. (1997). On expansion of cylindrical cavity with linear softening and shear dilation behaviour. *Chinese Journal of Rock Mechanics and Engineering*, 16(6), 550-557.

(144) Johnson, K. A. & Sitar, N. (1990). Hydrologic conditions leading to debris-flow initiation. *Can. Geotech. J.* 27, No. 6, 789-801.

(145) Kanji, M. A. (1974). The relationship between drained friction angles and Atterberg limits of natural soils. *Géotechnique*, 24, No.4, 671–674.

(146) Kavvadas, M. and Amorosi, A. (2000). A constitutive model for structured soils. *Géotechnique*, Vol. 50, No. 3, pp. 263-273.

(147) Kenney, T. C. (1969). Stability of natural slopes and embankment foundations. *Proc., 7th Int. Conf. in Soil Mechanics and Foundation Engineering,* Mexico, 3, 381–385.

(148) Kenney, T. C. (1977). Residual strengths of mineral mixtures. *Proc. 9th Int. Conf. Soil Mech.*, 1, 155-160.

(149) Krieg, R.D. (1975). A practical two surface plasticity theory. *Journal of Applied Mechanics, ASME*, Vol. 42, pp. 641-646.

(150) Kwasniewski, M.A. & Wang, J.-A. (1999). 3D numerical modelling and study of mine tremors induced by coal mining in the vicinity of major faults - A case study. *FLAC and Numerical Modelling in Geomechanics–Proceedings of the First International FLAC Symposium*, Minneapolis, Minnesota, pp. 379-388.

(151) Laflamme, J. F. et al. (2001). Simulation of pore pressures of the Saint-Hilaire test excavation.

(152) Laigle, K. (2003). A new viscoplastic model for rocks: application to the Mine-by-Test of AECL-URL. *FLAC and Numerical Modelling in Geomechanics–Proceedings of the Third International FLAC Symposium*, Sudbury, Ontario, pp. 35-43.

(153) Laigle, K. and Saitta, A. (2003). Numerical simulation of radial bolting: Application to the Tartaiguille railway tunnel. *FLAC and Numerical Modelling in Geomechanics–Proceedings of the Third International FLAC Symposium*, Sudbury, Ontario, pp. 153-160.

(154) Law, K.T. (1981). Effect of stress path geometry on soil brittleness. *Géotechnique*, 31, No.2, 279–287.

(155) Leroueil, S. & Marques, M. E. S. (1996). State of the art on the importance of strain rate and temperature effects in geotechnical engineering. *Proc. ASCE Conv., Washington,* Geotechnical Special Publication No. 61, 1-60.

(156) Leroueil, S. (1998). Contribution to the round table: peculiar aspects of structured soils. *Proc. 2nd Symp. Geotech. Hard Soils-Soft Rocks, Napoli* 3, 1669-1678.

(157) Leroueil, S (2001). Natural slopes and cuts movement and failure mechanisms. *Géotechnique*, 51, No. 3, 197-243.

(158) Leroueil, S. & Vaughan, P. R. (1990). The general and congruent effects of structure in natural soils and weak rocks. *Géotechnique*, 40, No. 3, 467-488.

(159) Li, T.L. Chen L.W., Yu M.H., Fan W. (2004). Unified solution of elastic-plastic surrounding rocks of cavity considering material softening. *Journal of Chang'an University (Natural Science Edition)*, 24(3), 48-52.

(160) Liang, F.Y., Chen, L.Z. (2004). Analytical solution to cavity expansion in strain-softening soils with Tresca yield criterion and its application. *Rock and Soil Mechanics*. Vol. 25, No.2, 261-265.

(161) Lo, K. Y. and Lee, C. F. (1973a). Stress analysis and slope stability in strain-softening materials. *Géotechnique*, 23, No. 1, 1-11.

(162) Lo, K. Y. and Lee, C. F. (1973b). Analysis of progressive failure in clay slopes. *Proc. 8th Int. Conf. Soil Mech. Found. Engng, Moscow* 1, 251-258.

(163) Lowe, J. & Karafiath, L. (1960). Stability of earth dams upon drawdown. *Proc. 1st Pan-Am. Conf. Soil Mech. Found. Engng*, 537-552.

(164) Lupini, J. F., Skinner, A. E. & Vaughan, P. R. (1981). The drained residual strength of cohesive soils. *Géotechnique* 31, No. 2, 181-213.

(165) Maksimovic, M. (1989). On the residual shearing strength of clays. *Géotechnique*, 39, No.2, 347–351.

(166) Marti, J., and Cundall, P. A. (1982). Mixed discretization procedure for accurate solution of plasticity problems, *Int. J. Num. Methods and Anal. Methods in Geomech.*, 6, 129-139.

(167) Matsumoto, T. and Ko, H. Y. (1982). Finite element analysis of strain-softening soils. *Proceedings of the 4th International Conference on Numerical Methods in Geomechanics*, Edmonton, Canada, Vol. 1, pp. 213-222.

(168) Mayne, P.W. (1980). Cam-Clay Predictions of Undrained Shear Strength. *Journal of the Geotechnical Engineering Division, ASCE*, GT106, 1219-1242.

(169) Mayne, P. W. (1991). Determination of OCR in clays by piezocone tests using cavity expansion and critical-state concepts. *Soils Found.*, Vol.31, No. 2, 65-76.

(170) Mesri, G., and Abdel-Ghaffar, M. E. M. (1993). Cohesion intercept in effective stress-stability analysis. *J. Geotech. Eng.*, 119, No.8, 1229–1249.

(171) Mesri, G., and Cepeda-Diaz, A. F. (1986). Residual shear strength of clays and shales. *Géotechnique*, 36, No.2, 269–274.

(172) Mesri, G., and Shahien, M. (2003). Residual Shear Strength Mobilized in First-Time Slope. *Journal of Geotechnical and Geoenvironmental Engineering*, 129, No.1, 12–31.

(173) Monnet, J., & Allagnat, D. (2006). Interpretation of pressuremeter results for design of a diaphragm wall. *Geotechnical Testing Journal*, 29(2), 126-132.

(174) Morgenstern, N. R. (1989). Recent experience with dam foundations on clay-shale in western Canada. Special Lecture, *Proc., 12th Int. Conf. on Soil Mechanics and Foundation Engineering*, 4, 2201–2208.

(175) Morgenstern, N. R. (1990). Instability mechanisms in stiff soils and weak rocks. *Proc. 10th Southeast Asian Geotech. Conf., Taipei* 2, 27-36.

(176) Morgenstern, N. R. and Price, V. E. (1965). The analysis of the stability of general slip surfaces. *Géotechnique*, 15, No. 1, 79-93.

(177) Morgenstern, N. R. and Simmons, J. V. (1982). Analysis of the movements of Gardiner Dam. *Proceedings, 4th International Conference on Numerical methods in Geomechanics, Edmonton, Alta*, vol. 3, 1003-1027.

(178) Morgenstern, N. R. & Tchalenko, J. S. (1967). Microscopic structures in kaolin subjected to direct shear. *Géotechnique*, 17, 309-328.

(179) Mroz, Z. (1967). On the description of anisotropic workhardening. *Journal of the Mechanics and Physics of Solids*, Vol. 15, pp. 163-175.

(180) Mroz, Z. Norris, V.A. and Zienkiewicz, O.C. (1978). An anisotropic hardening model for soils and its application to cyclic loading. *International Journal for Numerical and Analytical Methods in Geomechanics*, Vol. 2, pp. 203-221.

(181) Mroz, Z. Norris, V.A. and Zienkiewicz, O.C. (1979). Application of an anisotropic hardening model in the analysis of elastoplastic deformation of soils. *Géotechnique*, Vol. 29, No. 1, pp. 1-34.

(182) Mroz, Z. Norris, V.A. (1982). Elastoplastic and viscoplastic constitutive models for soils with application to cyclic loading. *Soil Mechanics-Transient and Cyclic Loads*, G.N. Pande and O.C. Zienkiewicz (eds.). John Wiley and Sons Ltd.

(183) Nakano, R. (1979). Geotechnical properties of mudstone of Neogene Tertiary in Japan with special reference to the mechanism of squeezing swelling rock pressure in tunneling. *Proceedings*, *International Symposium on Soil Mechanics, Oaxaca, Mexico,* vol. 1, pp. 75-92.

(184) Nemčok, A., Pašek, J. & Rybář, J. (1972). Classification of landslides and other mass movements. *Rock Mechanics* 4, 71-78.

(185) Ng, C.W.W. and Lings, M.L. (1995). Effects of modelling soil nonlinearity and wall installation on back-analysis of deep excavation in stiff clay. *Journal of geotechnical engineering*, Vol. 121, pp. 687-695.

(186) Ninis, N. (1990). Private communication.

(187) Olalla, C. & Cuéllar, V. (2001). Failure mechanism of the Azanalcóllar Dam, Seville, Spain. *Géotechnique*, 51, No.5, 399-406.

(188) Parry, R. H. G. (1972). Some properties of heavily overconsolidated Oxford clay at a site near Bedford. *Géotechnique*, 22, 485–507.

(189) Palmer, A. C. & Mitchell, R. J. (1972). Plane-strain expansion of a cylindrical cavity in clay. Stress-strain behaviour of soils: *Proceedings of the Roscoe Memorial Symposium*, Cambridge, pp. 588-599.

(190) Peck, R. B. (1967). Stability of natural slopes. *J. Soil Mech. Found. Div., Am. Soc. Civ. Eng.*, 93, SM4, 403–417.

(191) Perry, J. (1989). *A survey of slope condition on motorway earthworks in England and Wales*. Research Report 199, Transport & Road Research Laboratory, Crowthorne.

(192) Picarelli, L. (1991). Resistenza e meccanismi di rottura nei terreni naturali. Convegno dei ricercatori sul tema: Deformazioni in prossimita della rottura e resistenza dei terreni naturali e delle rocce, Ravello 2, II.7-II.61.

(193) Picarelli, L (2000). Mechanisms and rates of slope movements in fine grained soils. *Int Conf Geotech Geol Eng GeoEng* 2000, 1:1618–1670.

(194) Picarelli, L., Leroueil, S., Urciuoli, G., Guerriero, G., & Delisle, M. C. (1997). Occurrence and features of shear zones in clay. *Proc 4th Int Workshop on Localization and bifurcation theory for soils and rocks*, Gifu, Japan, pp259–269.

(195) Picarelli, L. & Olivares, L. (1998). Ingredients for modelling the mechanical behaviour of intensely fissured clay shales. *Proc. 2nd Symp. Geotech. Hard Soils-Soft Rocks, Napoli* 2, 771-780.

(196) Pietruszczak, St. & Mroz, Z. (1981) Finite element analysis of deformation of strain-softening materials. *Int. J. Numer. Meth. Eng.,* 17, 327-334.

(197) Potts D. M. (2003) Numerical analysis: a virtual dream or practical reality? (42nd Rankine Lecture). *Géotechnique*, 53, No. 6, 535–573.

(198) Potts, D. M., Dounias, G. T. & Vaughan, P. R. (1987). Finite element analysis of the direct shear box. *Géotechnique*, 37, No. 1, 11-23.

(199) Potts, D. M., Dounias, G. T. & Vaughan, P. R. (1990). Finite element analysis of progressive failure of Carsington embankment. *Géotechnique*, 40, No. 1, 79-102.

(200) Potts, D. M., Kovacevic, N., and Vaughan, P. R. (1997). Delayed collapse of cut slopes in stiff clay. *Géotechnique*, 47, No.5, 953–982.

(201) Potts, D.M. and Zdravkovic, L. (1999). *Finite element analysis in geotechnical engineering: theory*. Thomas Telford, London.

(202) Potts, D.M. and Zdravkovic, L. (2001). *Finite element analysis in geotechnical engineering: application*. Thomas Telford, London.

(203) Prevost, J.H. (1977). Mathematical modelling of monotonic and cyclic undrained clay behaviour. *International Journal for Numerical and Analytical Methods in Geomechanics*, Vol. 1, pp. 195-216.

(204) Prevost, J.H. (1978a). Anisotropic undrained stress-strain behavior of clays. *Journal of the Geotechnical Engineering Division*, *ASCE*, GT8, Vol. 104, pp. 1075-1090.

(205) Prevost, J.H. (1978b). Plasticity theory for soil stress-strain behavior. *ASCE, EM Division*, Vol. 104, pp. 1177-1196.

(206) Puzrin, A.M. and Burland, J.B. (1998). Non-linear model of small-strain behaviour of soils. *Géotechnique*, Vol. 48, No. 2, pp. 217-233.

(207) Puzrin, A.M. and Burland, J.B. (2000). Kinematic hardening plasticity formulation of small strain behaviour of soils. *International Journal for Numerical and Analytical Methods in Geomechanics*, Vol. 24, pp. 753-781.

(208) Ramesh, C. G. & John. L. D. (1986). Piezoprobe determined coefficient of consolidation. *Soils Found.*, Vol. 26, No. 3, 12-22.

(209) Randolph, M. F., Carter, J. P. & Wroth, C. P. (1979). Driven piles in clay-the effects of installation and subsequent consolidation. *Géotechnique*, Vol. 29, No. 4, 361-393.

(210) Randolph, M. F., Dolwin, J., & Beck, R. (1994). Design of Driven Piles in Sand. *Géotechnique*, *44*(3), 427-448.

(211) Rice, J. R. (1976). The localization of plastic deformation. In: Koiter (ed.), *Proc., 14th Int. Conf. Theoretical Applied Mechanics.* North Holland.

(212) Riedel, W. (1929). Zur mechanik geologischer bruchercheinungen. *Centralbl F Mineral Geol U Pal*, pp 354–368 (referred by Skempton 1967).

(213) Roddeman, D.G. (2001). *TOCHNOG professional user's manual*. Heerlen: FEAT.

(214) Rouainia, M. and Muir Wood, D. (2000). A kinematic hardening constitutive model for natural clays with loss of structure. *Géotechnique*, Vol. 50, No. 2, pp. 153-164.

(215) Rudnicki, J. W. and Rice, J. R. (1975). Conditions for the localization of deformation in pressure-sensitive dilatant materials, *J. Mech. Phys. Solids*, 23, 371-394.

(216) Sabzalisenejani, A. & Nikraz, H. (1998). A numerical approach for the prediction of shear strength of stiff fissured clay samples based on direct shear tests and *FLAC* modelling. *Proceedings of the second international symposium on hard soils-soft rocks*, Balkema, Rotterdam.

(217) Salgado, R., Mitchell, J. K. & Jamiolkowski, M. (1997). Cavity expansion and penetration resistance in sand. *J. Geotech. Geoenviron. Engng.*, ASCE 123, No. 4, 344-354.

(218) Sandroni, S. S. (1977). The strength of London Clay in total and effective stress terms. Ph.D. thesis, University of London.

(219) Sarma, S. (1979). Stability analysis of embankments and slopes. *J. Geotech. Engng, ASCE* 105, 1511-1524.

(220) Schuller, H., Schweiger, H. F. (2002). Application of a multilaminate model to simulation of shear band formation in NATM-tunnelling. *Comput. Geotech.* 29, 501–524.

(221) Seyček, J. (1978). Residual shear strength of soils. *Bull. Int. Ass. Engng Geol*. 17, 73-75.

(222) Silvestri, V. (1980). The long term stability of a cutting slope in an overconsolidated clay. *Can. Geotech. J.*, 17, No.3, 337–351.

(223) Simpson, B. (1992). 32th Rankine Lecture: Retaining structures: displacement and design. *Géotechnique*, Vol. 42, No. 4, pp. 541-576.

(224) Simpson, B., Calabresi G., Sommer, H. and Wallays, M. (1979).´Design parameters in stiff clay´. *Proc. 7th ECSMFE,* Brighton, Vol.5, pp.91-125.

(225) Simpson, B., O'Riordan, N.J. and Croft D.D. (1979). A computer model for the analysis of ground movements in London Clay. *Géotechnique*, Vol. 29, No. 2, pp. 149-175.

(226) Skempton, A. W. (1948). The rate of softening in stiff fissured clay, with special reference to London Clay. *Proc. 2nd Int. Conf. Soil Mech. Found. Engng, Rotterdam* 2, 50-53.

(227) Skempton, A. W. (1964). Long term stability of clay slopes. *Géotechnique*, 14, No.2, 77–101.

(228) Skempton, A. W. (1966). Bedding-plane slip, residual strength and the Vaiont Landslide. *Géotechnique*, 16, No.1, 82–84.

(229) Skempton, A. W. (1967). Some observations on tectonic shear zones. *Proc 2nd Int Conf on Rock Mechanics*, Belgrade, vol. 1, pp 329–335.

(230) Skempton, A. W. (1970). First-time slides in overconsolidated clays. *Géotechnique*, 20, No.3, 320–324.

(231) Skempton, A. W. (1977). Slope stability of cuttings in brown London clay. *Proc. 9th Int. Conf. Soil Mech., Tokyo* 3, 261-270.

(232) Skempton, A. W. (1985). Residual strength of clays in landslides, folded strata and the laboratory. *Géotechnique* 35, No. 1, 3-18.

(233) Skempton, A. W., and Brown, J. D. (1961). A landslide in boulder clay at Selset, Yorkshire. *Géotechnique*, 11, No.4, 280–293.

(234) Skempton, A. W. & Petley, D. J. (1967). The strength along structural discontinuities in stiff clays. *Proceedings of Geotechnical Conference*, Oslo 2, 29-46. Oslo: Norwegian Geotechnical Institute.

(235) Skempton, A. W., Schuster, R. L. & Petley, D. J. (1969). Joints and fissures in the London Clay at Wraysbury and Edgware. *Géotechnique*, 19, No. 2, 205-217.

(236) Skempton A. W. & Vaughan P. R. (1993). The failure of Carsington Dam. *Géotechnique*, 43, No. 1, 151-173.

(237) Skempton A. W. & Vaughan P. R. (1994). Reply to discussion of Skempton & Vaughan (1993). *Géotechnique*, 44, No. 4, 719-740.

(238) Skinner, A. E. (1969). A note on the influence of interparticle friction on the shearing strength of a random assembly of spherical particles. *Géotechnique*, 19, No.1, 150-157.

(239) Sloan, S.W. (1987). Substepping schemes for the numerical integration of elastoplastic stress-strain relations. *International Journal for Numerical Methods in Engineering*, Vol. 24, pp. 893-911.

(240) Souley, M., Su, K., Ghoreychi, M. and Armand, G. (2003). Constitutive models for rock mass: numerical implementation, verification and validation. *FLAC and Numerical Modelling in Geomechanics–Proceedings of the Third International FLAC Symposium*, Sudbury, Ontario, pp. 71-80.

(241) Spencer, E. (1967). A method of analysis of the stability of embankments assuming parallel interslice forces. *Géotechnique*, 17, No. 1, 11-26.

(242) Stallebrass, S.E. (1990). Modelling the effect of recent stress history on the deformation of overconsolidated soils. PhD thesis, City University, London, UK.

(243) Stallebrass, S.E. and Taylor, R.N. (1997). The development and evaluation of a constitutive model for the prediction of ground movements in overconsolidated clay. *Géotechnique*, Vol. 47, No. 2, pp. 235-253.

(244) Stark, T. D., and Eid, H. T. (1994). Drained residual strength of cohesive soils. *J. Geotech. Eng.*, 120, No.5, 856–871.

(245) Stark, T. D., and Eid, H. T. (1997). Slope stability analyses in stiff fissured clays. *J. Geotech. Geoenviron. Eng.*, 123, No.4, 335–343.

(246) Sun, H. W., Wong, H. N. & Ho, K. K. S. (1988). Analysis of infiltration in unsaturated ground. *Proc. Ann. Sem. Slope Engng. in Hong Kong, Hong Kong*, 101-109.

(247) Sterpi, D. (1999). An analysis of geotechnical problems involving strain softening effects. *Int. J.Numer. Anal. Meth. Geomech.* 23, 1427–1454.

(248) Sterpi, D. (2000). Influence of the kinematic testing conditions on the mechanical response of a sand. *Comput. Geotech.* 26, 23–41.

(249) Sterpi, D. and Cividini, A. (2004). A Physical and Numerical Investigation on the Stability of Shallow Tunnels in Strain Softening Media. *Rock Mech. Rock Engng.* 37 (4), 277–298.

(250) Tarzi, A. I., Kalteziotis, N. A. & Menzies, B. K. (1982). Finite element analysis of strip footings on strain-softening clay. *Proc. Int. Symp. on Num Models in Geomechanics*, Rotterdam, 194-200.

(251) Tavenas, F., and Leroueil, S. (1981). Creep and failure of slopes in clays. *Can. Geotech. J.*, 18, No.1, 106–120.

(252) Taylor, D. W. (1948). *Fundamentals of soil mechanics*. Wiley, New York.

(253) Terzaghi, K. & Peck, R. B. (1948). *Soil mechanics in engineering practice*, 1st edn. Wiley, New York.

(254) Terzaghi, K., Peck, R. B., and Mesri, G. (1936). Stability of slopes in natural clay. *Proceedings, International Conference on Soil Mechanics*, Harvard University, vol. 1, pp. 161-165.

(255) Terzaghi, K. (1950). Mechanism of landslides. In *Application of geology to engineering practice (Berkeley volume)* (ed. S. Paige), pp. 83-123. New York: Geological Society of America.

(256) Terzaghi, K., Peck, R. B., and Mesri, G. (1996). *Soil mechanics in engineering practice*, 3rd Ed., Wiley, New York.

(257) Tika, T. E., Vaughan, P. R., & Lemos, L. J. L. J. (1996). Fast shearing of pre-existing shear zones in soil. *Géotechnique*, 46, No. 2, 197-233.

(258) Tsige, M., González de Vallejo, L., Doval, M., Oteo, C. and Barba C. (1995). Microfabric of Guadalquivir blue marls and its engineering geological significance. Int. Assoc. of Engineering Geology. Balkema, Vol. II. 695-704.

(259) Tsige, M. y González de Vallejo, L. (1996). Microfábrica de las arcillas azules del Guadalquivir y su relación con los procesos de meteorización. Geogaceta 20 (8).

(260) Tsige, M. y González de Vallejo, L. (1997). Fábrica e historia geológica de las arcillas azules del Guadalquivir. Avances del Conocimiento del Terciario Ibérico. Eds. J.P. Calvo y J. Morales. pp. 228.

(261) Tsige, M. (1999). Microfábrica y mineralogía de las arcillas azules del Guadalquivir y su relación con las propiedades geotécnicas. Monografía 67, Mº de Fomento, CEDEX. 294 pp. ISBN 84-4980-426.

(262) Troncone, A. (2004). Analisi di stabilità dei pendii in terreni con comportamento strain-softening. PhD thesis, University of Calabria, Italy.

(263) Troncone, A. (2005). Numerical analysis of a landslide in soils with strain-softening behaviour. *Géotechnique*, 55, No. 8, 585–596.y

(264) Urciuoli, G. (1990). *Contributo alla caratterizzazione geotecnica delle frane dell'Appennino*, Reports of the Istituto di Tecnica delle Fondazioni e Costruzioni in Terra. Naples: Universita di Napoli Federico II.

(265) Urciuoli, G., Picarelli, L. and Leroueil, S. (2007). Local soil failure before general slope failure. Geotechnical and Geological Engineering, Vol. 25, No. 1, pp. 103-122(20).

(266) Vardoulakis, I., Sulem, J. (1995). Bifurcation analysis in geomechanics. Chapman & Hall, Glasgow.

(267) Vaughan, P. R. (1985). Pore pressures due to infiltration into partly saturated slopes. *Proc. 1st Int. Conf. Geomechanics in Tropical Lateritic and Saprolitic Soils, Brasilia* 2, 61-71.

(268) Vaughan, P. R., Dounias, G. T. & Potts, D. M. (1989). Advances in analytical techniques and the influence of core geometry on behaviour. *Proceedings of the conference on clay barriers for embankment dams*, London, pp. 35-56.

(269) Vaughan, P. R. & Hamza, M. M. (1977). Clay embankments and foundations: Monitoring stability by measuring deformations. Specialty Session 8: Deformation of earth-rockfall dams, *Proc. 9th Int. Conf. Soil Mech. Found. Engng, Tokyo*, 37-48.

(270) Vaughan, P. R., Hight, D. W., Sodha, V. G. & Walbancke, H. J. (1978). Factors controlling the stability of clay fills in Britain. *Clay fills*, 203-217. London: Institution of Civil Engineers.

(271) Vaughan, P. R., and Walbancke, H. J. (1973). Pore-pressure changes and delayed failure of cutting slopes in overconsolidated clay. *Géotechnique*, 23, No.4, 531–539.

(272) Vaunat, J., Leroueil, S. & Faure, R. (1994). Slope movements: a geotechnical perspective. *Proc. 7th Cong. Int. Assoc. Engng Geol.*, *Lisbon*, 1637-1646.

(273) Vermeer, P. A. (1982). A simple shear band analysis using compliances, in P. A. Vermeer and H. Luger (eds), *Proc. IUTAM Conf. on Deformation and Failure of Granular Materials*, Balkema, Rotterdam, 493-499.

(274) Vermeer, P. A. and R. de Borst (1984). Non-associated plasticity for soils, concrete and rock. *Heron*, 29(3), 3-64.

(275) Vesic, A. S. (1972). Expansion of cavities in infinite soil mass. *J. Soil Mech. Found. Div.*, ASCE 98, No. SM3, 265-290.

(276) Vesic, A. S. (1977). Design of pile foundations, *Synthesis of Highway Practice* 42, Washington, DC: Transportation Research Board, National Research Council.

(277) Viggiani, G., Rampello, S. and Georgiannou, V. N. (1993). Experimental analysis of localization phenomena in triaxial tests on stiff clays. *Proc. 1st Symp. Geotech. Hard Soils-Soft Rocks*, *Athens* 2, 849-856.

(278) Viggiani, G., Finno, R. J. & Harris, W. U. (1994). Experimental observations of strain localization in plane strain compression of a stiff clay. *Proc. 3rd Int. Workshop on Localization and Bifurcation Theory for Soils and Rocks*, 180-198. Rotterdam: Balkema.

(279) Vinkler, E. & Piguet, J.P. (1999). Analysis of the long term stability of an ancient room and abandoned pillar mine: Impact of the water level. *FLAC and Numerical Modelling in Geomechanics–Proceedings of the First International FLAC Symposium*, Minneapolis, Minnesota, pp. 245-253.

(280) Voight, B. (1973). Correlation between Atterberg plasticity limits and residual shear strength of natural soils. *Géotechnique*, 23, No. 2, 265-267.

(281) Wang, J.L. & Xiong J.H. (1999). An analytical solution to cylindrical cavity expansion in softening soil mass. *Chinese Journal of Applied Mechanics*, 16(4), 58-63.

(282) Ward, W. H., Marsland, A. & Samuels, S. G. (1965). Properties of the London Clay at the Ashford Common shaft: in-situ and undrained strength tests. *Géotechnique*, 15, No. 4, 321-344.

(283) Webb, D. L. (1964). The mechanical properties of undisturbed samples of London Clay and Pierre shale. PhD thesis, University of London.

(284) Wesley, L. D. (2002). Geotechnical characterization and behaviour of allophone clays. *Proc. Int. Workshop on Characterisation and Engineering Properties of Natural Soils, Singapore*, 2, 1379-1399.

(285) White, D. J., & Bolton, M. D. (2004). Displacement and strain paths during plane-strain model pile installation in sand. *Géotechnique, 54*(6), 375-397.

(286) Whittle, A.J. (1993). Evaluation of a constitutive model for overconsolidated clays. *Géotechnique*, Vol. 43, No. 2, pp. 289-313.

(287) Whittle, A.J., Hashash Y.M.A. and Whitman R.V. (1993). Analysis of a deep excavation in Boston. *Journal of the Geotechnical Engineering Division, ASCE*, Vol. 119, No. 1, pp. 69-90.

(288) Wilkins, M. L. (1964). "Fundamental Methods in Hydrodynamics," in *Methods in Computational Physics*, Vol. 3, pp. 211-263. Alder et al., Eds. New York: Academic Press.

(289) Wolle, C. M. (1998). Landslides in Serra do Mar, Southeastern Brazil. Short course on '*The geotechnical characterization of slope movements in the Brazilian context*', COPPE, Federal University of Rio de Janeiro.

(290) Wood, D. M. (1990). *Soil Behaviour and critical state soil mechanics*. Cambridge University Press, Lodon.

(291) Wood, D. M., Jendele, L., Chan, A. H. C. & Cooper, M. R. (1995). Slope failure by pore pressure recharge: numerical analysis. *Proc. 11th Eur. Conf. Soil Mech. Found. Engng,* Copenhagen 6, 1-8.

(292) Wroth, C. P. (1972). Some aspects of the elastic behaviour of overconsolidated clay. *Proc. Roscoe Memorial Symp*., Foulis, 347-361.

(293) Yavuz, H. and Fowell, R.J. (2001). Softening effect of coal on the design of yield pillars. *FLAC and Numerical Modelling in Geomechanics–Proceedings of the Second International FLAC Symposium*, Lyon, France, pp. 313-320.

(294) Yoshida, N., Morgenstern, N.R. and Chan, D.H. (1991). Finite element analysis of softening effects in fissured, overconsolidated clays and mudstones. *Can. Geotech. J.,* 28, 51-61.

(295) Yu, H. S. (1990). Cavity expansion theory and its application to the analysis of pressuremeters. PhD thesis, University of Oxford, UK.

(296) Yu H.S. (2000). Cavity Expansion Methods in Geomechanics. Dordrecht: Kluwer.

(297) Yu H.S. (2006). Plasticity and Geotechnics. Springer Publishers.

(298) Zabala, F. and Alonso, E. E. (2011). Progressive failure of Aznalcóllar dam using the material point method. *Géotechnique*, Vol. 61, No. 9, pp795–808.

(299) Zdravkovic, L., Potts, D.M and Jardine, R.J. (2001). A parametric study of the pull-out capacity of bucket foundations in soft clay. *Géotechnique*, Vol. 51, No. 1, pp. 55-67.

(300) Zdravkovic, L., Potts, D.M and Hight, D.W. (2002). The effect of strength anisotropy on the behaviour of embankments on soft ground. *Géotechnique*, Vol. 52, No. 6, pp. 447-457.

(301) Zheng J.J., Peng H.N. and Chong J. (2004). *Acta Mechanica Solida Sinica*, Vol. 17, No. 4, 353-360.

(302) Zhu H. & Yin Z.Z. (1996). Finite element analysis of pile driving effect. *Journal of Hohai University*, 24(1), 56-61.

(303) Zienkiewicz O. C., Valliapan, S. and King, I. P. (1968). Stress analysis of rock, as a 'no-tension' material. *Géotechnique*, 18, No. 1, 56-66.

Appendix I. Definitions of stress and strain variables

Stress is a second order tensor which is defined by six components. The effective stress tensor is given as:

$$\sigma' = \begin{bmatrix} \sigma_x' & \tau_{xy} & \tau_{xz} \\ \tau_{yx} & \sigma_y' & \tau_{yz} \\ \tau_{zx} & \tau_{zy} & \sigma_z' \end{bmatrix} \tag{I.1}$$

where $\tau_{xy} = \tau_{yx}$, $\tau_{xz} = \tau_{zx}$ and $\tau_{yz} = \tau_{zy}$.

The stress tensor can be divided into two components, the volumetric component and the deviatoric component as follows:

$$\sigma' = \begin{bmatrix} \sigma_x' & \tau_{xy} & \tau_{xz} \\ \tau_{yx} & \sigma_y' & \tau_{yz} \\ \tau_{zx} & \tau_{zy} & \sigma_z' \end{bmatrix} = \begin{bmatrix} p' & 0 & 0 \\ 0 & p' & 0 \\ 0 & 0 & p' \end{bmatrix} + \begin{bmatrix} \sigma_x' - p' & \tau_{xy} & \tau_{xz} \\ \tau_{yx} & \sigma_y' - p' & \tau_{yz} \\ \tau_{zx} & \tau_{zy} & \sigma_z' - p' \end{bmatrix} \tag{I.2}$$

In the above equation p' is the mean effective stress:

$$p' = \frac{\sigma_x' + \sigma_y' + \sigma_z'}{3} \tag{I.3}$$

Eq. (I.2) can be rewritten as follows:

$$\sigma' = p'\boldsymbol{I} + s \tag{I.4}$$

Where σ' is the effective stress tensor, p' is the mean effective stress, s is the deviatoric stress tensor and $\boldsymbol{I}$ is the second-rank identity tensor (the tensor quantities are represented by bold-faced characters).

It is common to represent the state of stress with three stress invariants, the mean effective stress, p', the deviatoric stress, J or q and the Lode's angle, θ. The mean effective stress, p', can be calculated from Eq. (I.3). The deviatoric stress, J or q, and the Lode's angle, θ, are defined as follows:

$$\begin{aligned} J &= \left[\frac{1}{2}(s:s)\right]^{1/2} \\ &= \left[\frac{1}{2}\left(\left(\sigma_x' - p'\right)^2 + \left(\sigma_y' - p'\right)^2 + \left(\sigma_z' - p'\right)^2 + 2\tau_{xy}^{\,2} + 2\tau_{yz}^{\,2} + 2\tau_{zx}^{\,2}\right)\right]^{1/2} \end{aligned} \tag{I.5}$$

$$q = \sqrt{3}J \tag{I.6}$$

$$\theta = -\frac{1}{3}\sin^{-1}\left[\frac{3\sqrt{3}}{2}\frac{\det(s)}{\left[\left[\frac{1}{2}(s:s)\right]^{\frac{1}{2}}\right]^3}\right] \tag{I.7}$$

where det(s) is the determinant of the deviatoric stress tensor s and can be given as:

$$\det s = \begin{vmatrix} \sigma_x' - p' & \tau_{xy} & \tau_{xz} \\ \tau_{yx} & \sigma_y' - p' & \tau_{yz} \\ \tau_{zx} & \tau_{zy} & \sigma_z' - p' \end{vmatrix} \tag{I.8}$$

or

$$\begin{aligned} \det s = &\left(\sigma_x' - p'\right)\left(\sigma_y' - p'\right)\left(\sigma_z' - p'\right) - \left(\sigma_x' - p'\right)\tau_{yz}^2 - \left(\sigma_y' - p'\right)\tau_{zx}^2 \\ &- \left(\sigma_z' - p'\right)\tau_{xy}^2 + 2\tau_{xy}\tau_{yz}\tau_{zx} \end{aligned} \tag{I.9}$$

These three invariants can be expressed in terms of the principal effective stresses σ_1', σ_2' and σ_3' as follows:

$$p' = \frac{\sigma_1' + \sigma_2' + \sigma_3'}{3} \tag{I.10}$$

$$J = \sqrt{\frac{1}{6}\left[\left(\sigma_1' - \sigma_2'\right)^2 + \left(\sigma_2' - \sigma_3'\right)^2 + \left(\sigma_3' - \sigma_1'\right)^2\right]} \tag{I.11}$$

or

$$q = \sqrt{\frac{1}{2}\left[\left(\sigma_1' - \sigma_2'\right)^2 + \left(\sigma_2' - \sigma_3'\right)^2 + \left(\sigma_3' - \sigma_1'\right)^2\right]} \tag{I.12}$$

$$\theta = -\tan^{-1}\left(\frac{2b-1}{\sqrt{3}}\right) \tag{I.13}$$

where

$$b = \frac{\left(\sigma_2' - \sigma_3'\right)}{\left(\sigma_1' - \sigma_3'\right)} \tag{I.14}$$

The principal stresses can be expressed in terms of these alternative invariants using the following equation:

$$\begin{Bmatrix} \sigma_1' \\ \sigma_2' \\ \sigma_3' \end{Bmatrix} = p' \begin{Bmatrix} 1 \\ 1 \\ 1 \end{Bmatrix} + \frac{2}{\sqrt{3}} J \begin{Bmatrix} \sin\left(\theta + \frac{2\pi}{3}\right) \\ \sin\theta \\ \sin\left(\theta - \frac{2\pi}{3}\right) \end{Bmatrix} \tag{I.15}$$

The above three quantities, p', J or q, and θ, have a geometrical significance in principal effective stress space. Fig. I.1a shows the principal effective stress space with the space diagonal ($\sigma_1' = \sigma_2' = \sigma_3'$) and a deviatoric plane (defined as any plane perpendicular to the space diagonal). Fig. I.1b shows the projection of the principal stress space onto the deviatoric plane. It can be seen that the mean effective stress, p', is a measure of the distance of the current deviatoric plane from the origin along the space diagonal. The deviatoric stress, q or J, is a measure of the distance of the current stress state from the space diagonal in the deviatoric plane. Finally the Lode's angle, θ, defines the orientation of the stress state within the deviatoric plane, and varies between +30° (which corresponds to triaxial extension, $\sigma_1' = \sigma_2' \geq \sigma_3'$ and b = 1) and -30° (which corresponds to triaxial compression, $\sigma_1' \geq \sigma_2' = \sigma_3'$ and b = 0).

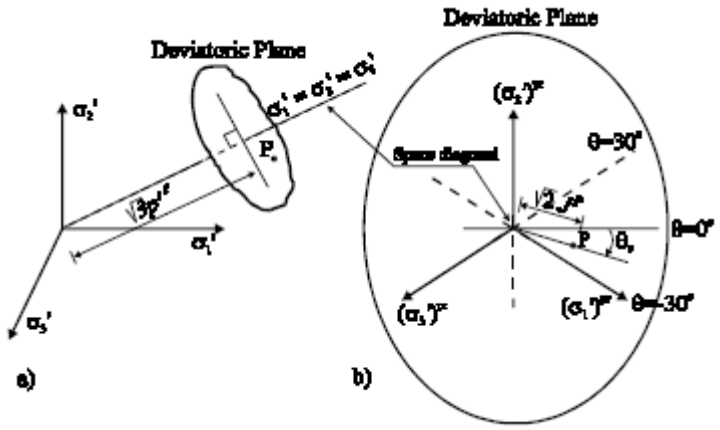

Fig. I.1 (a) Principal stress space and (b) deviatoric plane (Potts and Zdravkovic, 1999)

The three stress invariants, p', J or q and θ are commonly used in order to define the stress state of a loaded body. However, although they define the overall magnitude of the stress state, they do not provide any information on the direction of the planes on which the principal effective stresses act. This is not necessary if the material considered is isotropic, in which case the material properties are the same in all directions. However, if the material considered is anisotropic (i.e. its properties are directional dependent), then the direction of the principal effective stress planes becomes significant and the use of just the three stress invariants, p', J or q and θ is not sufficient. This is the reason why these stress invariants have been used extensively in the formulation of isotropic constitutive models, whereas in the case of anisotropic constitutive models the formulation usually involves the calculation of the whole stress tensor.

Strain, like stress, is a second order tensor, defined by six components as:

$$\varepsilon = \begin{bmatrix} \varepsilon_x & \frac{1}{2}\gamma_{xy} & \frac{1}{2}\gamma_{xz} \\ \frac{1}{2}\gamma_{xy} & \varepsilon_y & \frac{1}{2}\gamma_{yz} \\ \frac{1}{2}\gamma_{zx} & \frac{1}{2}\gamma_{zy} & \varepsilon_z \end{bmatrix} \tag{I.16}$$

where $\gamma_{xy} = \gamma_{yx}$, $\gamma_{xz} = \gamma_{zx}$ and $\gamma_{yz} = \gamma_{zy}$.

The strain tensor can be divided into two components, the volumetric and deviatoric components:

$$\varepsilon = \begin{bmatrix} \varepsilon_x & \tfrac{1}{2}\gamma_{xy} & \tfrac{1}{2}\gamma_{xz} \\ \tfrac{1}{2}\gamma_{xy} & \varepsilon_y & \tfrac{1}{2}\gamma_{yz} \\ \tfrac{1}{2}\gamma_{zx} & \tfrac{1}{2}\gamma_{zy} & \varepsilon_z \end{bmatrix} = \begin{bmatrix} e_v & 0 & 0 \\ 0 & e_v & 0 \\ 0 & 0 & e_v \end{bmatrix} + \begin{bmatrix} \varepsilon_x - e_v & \tfrac{1}{2}\gamma_{xy} & \tfrac{1}{2}\gamma_{xz} \\ \tfrac{1}{2}\gamma_{xy} & \varepsilon_y - e_v & \tfrac{1}{2}\gamma_{yz} \\ \tfrac{1}{2}\gamma_{zx} & \tfrac{1}{2}\gamma_{zy} & \varepsilon_z - e_v \end{bmatrix} \quad \text{(I.17)}$$

In the above equation e_v is equal to:

$$e_v = \frac{1}{3}\left(\varepsilon_x + \varepsilon_y + \varepsilon_z\right) = \frac{1}{3}\varepsilon_v \quad \text{(I.18)}$$

Eq. (I.17)can be rewritten as:

$$\varepsilon = \frac{1}{3}\varepsilon_v \boldsymbol{I} + e_s \quad \text{(I.19)}$$

In the above equations ε is the strain tensor, ε_v is the volumetric strain and e_s is the deviatoric strain tensor.

The strain invariants corresponding to the previously described stress invariants are the volumetric strain, ε_v, given by Eq. (I.18) and the deviatoric strain E_d, if the stress invariant J is chosen, or ε_s, if the stress invariant q is used. These are defined from the following equations:

$$\begin{aligned} E_d &= \left[2\left(e_s : e_s\right)\right]^{1/2} \\ &= \left[2\left(\left(\varepsilon_x - e_v\right)^2 + \left(\varepsilon_y - e_v\right)^2 + \left(\varepsilon_z - e_v\right)^2 + \frac{1}{2}\gamma_{xy}{}^2 + \frac{1}{2}\gamma_{yz}{}^2 + \frac{1}{2}\gamma_{zx}{}^2\right)\right]^{1/2} \end{aligned} \quad \text{(I.20)}$$

$$\varepsilon_s = \frac{1}{\sqrt{3}} E_d \quad \text{(I.21)}$$

The above equations are expressed in terms of the principal strains, ε_1, ε_2 and ε_3 as follows:

$$\varepsilon_v = \varepsilon_1 + \varepsilon_2 + \varepsilon_3 \quad \text{(I.22)}$$

$$E_d = \frac{2}{\sqrt{6}}\left[\left(\varepsilon_1 - \varepsilon_2\right)^2 + \left(\varepsilon_2 - \varepsilon_3\right)^2 + \left(\varepsilon_3 - \varepsilon_1\right)^2\right]^{1/2} \quad \text{(I.23)}$$

$$\varepsilon_s = \frac{\sqrt{2}}{3}\left[\left(\varepsilon_1 - \varepsilon_2\right)^2 + \left(\varepsilon_2 - \varepsilon_3\right)^2 + \left(\varepsilon_3 - \varepsilon_1\right)^2\right]^{1/2} \quad \text{(I.24)}$$

- **Triaxial stress space**

In triaxial stress space the most commonly adopted stress and strain invariants are the mean effective stress, p', the shear stress, q, the volumetric strain, ε_v, and the shear strain, ε_s. In this case of axially symmetric conditions, they are expressed as:

$$p' = \frac{1}{3}\left(\sigma_a' + 2\sigma_r'\right) \tag{I.25}$$

$$q = \sigma_a' - \sigma_r' \tag{I.26}$$

$$\varepsilon_v = \varepsilon_a + 2\varepsilon_r \tag{I.27}$$

$$\varepsilon_s = \frac{2}{3}\left(\varepsilon_a - \varepsilon_r\right) \tag{I.28}$$

where σ_a' and σ_r' are the axial and radial effective stresses and ε_a and ε_r are the axial and radial strains respectively.

For triaxial conditions the increments of stresses are related to the increments of strains as follows:

$$\begin{Bmatrix} d\varepsilon_v \\ d\varepsilon_s \end{Bmatrix} = \begin{bmatrix} 1/K & 1/J_{qp} \\ 1/J_{pq} & 1/3G \end{bmatrix} \begin{Bmatrix} dp' \\ dq \end{Bmatrix} \tag{I.29}$$

where K is the bulk modulus, G is the shear modulus and the parameters J_{qp} and J_{pq} are coupling moduli that express the cross dependence of the volumetric strain on the shear stress, q, and of the shear strain on the mean effective stress, p'. Hence, the shear modulus G can be calculated from a test where $dp' = 0$ and the bulk modulus K can be calculated from a test where $dq = 0$:

$$3G = \frac{dq}{d\varepsilon_s} \tag{I.30}$$

$$K = \frac{dp'}{d\varepsilon_v} \tag{I.31}$$

For any other stress path the cross coupling of the shear and volumetric components does not allow direct calculation of the bulk and shear moduli. For a material that is elastic and isotropic $J_{qp} = J_{pq} = \infty$, and the shearing and volumetric components are essentially decoupled. In this case the bulk and shear moduli, K and G, can be calculated from any stress path directly from Eq. (I.30) and Eq. (I.31). Moreover for such a material K and G are related through the Poisson's ratio, μ:

$$G = \frac{3\left(1-2\mu\right)}{2\left(1+\mu\right)}K \tag{I.32}$$

For undrained conditions, where there is no volume change, the undrained modulus, E_u, can be calculated as follows (for an elastic isotropic material):

$$E_u = 3G \tag{I.33}$$

Appendix II. Derivatives of stress invariants

The derivatives of stress invariants which have been depicted in 0 are given below.

- **For mean total stress**

$$\left\{\frac{\partial p}{\partial \sigma}\right\}=\frac{1}{3}\{1 \quad 1 \quad 1 \quad 0 \quad 0 \quad 0\}^T \tag{II.1}$$

- **For mean effective stress**

$$\left\{\frac{\partial p'}{\partial \sigma'}\right\}=\frac{1}{3}\{1 \quad 1 \quad 1 \quad 0 \quad 0 \quad 0\}^T \tag{II.2}$$

- **For deviatoric stress**

$$\left\{\frac{\partial J}{\partial \sigma'}\right\}=\frac{1}{2J}\{\sigma_x^{'}-p' \quad \sigma_y^{'}-p' \quad \sigma_z^{'}-p' \quad 2\tau_{xy} \quad 2\tau_{yz} \quad 2\tau_{zx}\}^T \tag{II.3}$$

- **For Lode's angle**

$$\left\{\frac{\partial \theta}{\partial \sigma'}\right\}=\frac{\sqrt{3}}{2\cos 3\theta J^3}\left[\frac{\det s}{J}\left\{\frac{\partial J}{\partial \sigma'}\right\}-\left\{\frac{\det s}{\partial \sigma'}\right\}\right] \tag{II.4}$$

where $\det s$ is given as Eq. (I.8) or Eq. (I.9).

In addition, the derivatives of J and θ above are expressed in terms of effective stress. If total stresses are replaced by effective stresses, the same expressions are obtained, i.e. $\left\{\frac{\partial J}{\partial \sigma}\right\}=\left\{\frac{\partial J}{\partial \sigma'}\right\}$ and $\left\{\frac{\partial \theta}{\partial \sigma}\right\}=\left\{\frac{\partial \theta}{\partial \sigma'}\right\}$.

Appendix III. Specification of strength parameters and softening rate

Potts et al. (1990) devised a reasonable method to obtain the strength parameters and relevant softening rates required in one-stage softening model. They got the peak strength of intact yellow clay from laboratory tests. And the residual strength was determined by shear box tests on specimens including the shear surface from the actual failure. Afterwards they found in trial trench that discontinuous solifluction shears were over about 40% of the whole length investigated and this was assumed to be representative of the yellow clay below the dam prior to failure. In line with this concept, a representative average strength could be deduced by adding the shear stress vs. horizontal displacement curves for intact specimens and specimens with shear in proportion 3:2 (seen in Fig. III.1). The same approach was used to calculate the initial peak strength parameters for yellow clay.

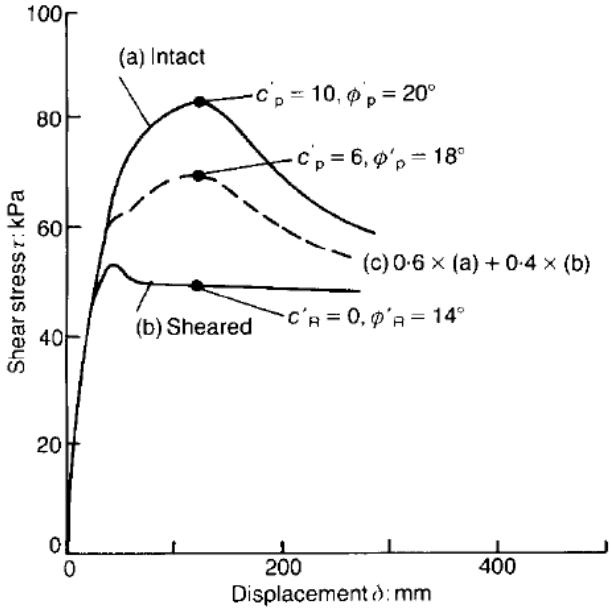

Fig. III.1 Average strength of yellow clay with 60% intact and 40% sheared: $\sigma'_n = 200$ kPa with 1 m thick element (after Skempton, 1985)

They also stated that the rate at which strength drops from peak to residual with strain or displacement is a major uncertainty. Failure in the finite element solution concentrates in half the thickness of an element, which is 0.5 m for the yellow clay. The stress-displacement relationship of such a layer is determined by the strain-softening function adopted, and this needs to simulate the stress-displacement relationship of the real shear zone. However, the latter is not easy to acquire. The assumptions made for ϕ' are shown in Fig. III.2; c' decreases linearly in the same way. The line Y_1 is thought to represent a reasonable assumption. And they also

mentioned that the initial part of the post-peak curve has the most influence on progressive failure.

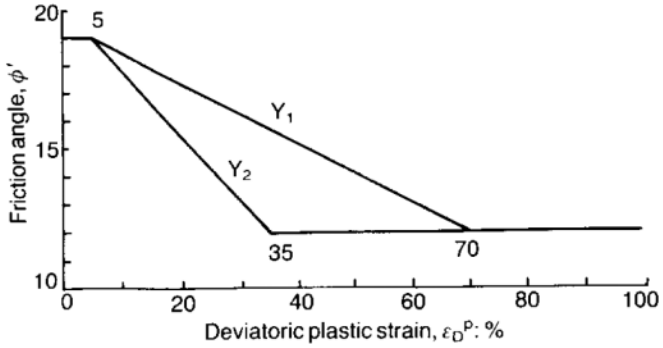

Fig. III.2 Assumption for post-peak decrease of ϕ' with plastic strain for yellow clay (Potts et al. 1997)

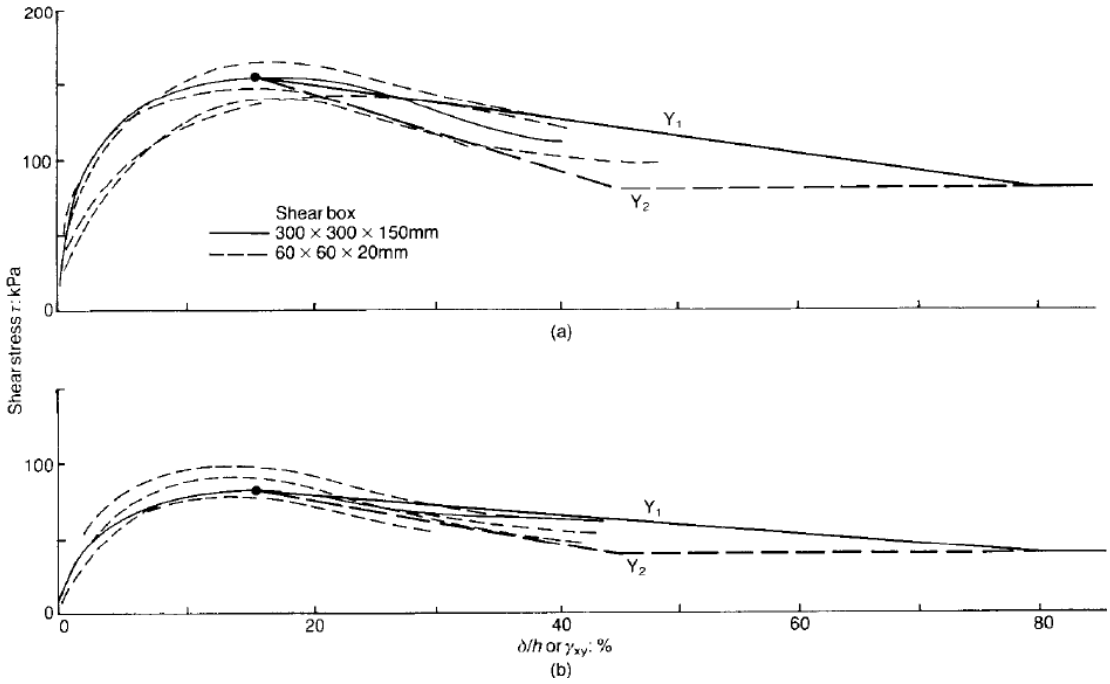

Fig. III.3 Comparison of post-peak stress-displacement assumption for yellow clay with direct shear box tests: (a) $\sigma_n' = 400$ kPa ; (b) $\sigma_n' = 200$ kPa (Potts et al. 1997)

The only test data with which this assumption may be compared is that from direct shear box tests. Fig. III.3 shows that the comparison is reasonable. It may be noted that the curves of stress against average strain for 20 mm and 150 mm thick shear box specimens are similar indicating that the same curve may apply to a 500 m thick layer. Y_2 was used to examine the influence of the rate of post-peak softening assumed. This implies that the shear strain keeps similar for specimens with different sizes.

The representative values of strength parameters and softening rates for yellow clay are given as $c_p' = 6$ kPa, $\phi_p' = 19°$, $c_r' = 0$ kPa, $\phi_p' = 12°$, $\varepsilon_{DP}^P = 5\%$ and $\varepsilon_{DR}^P = 70\%$.

Chen et al. (1992) also deduced the softening parameters by fitting the shear stress versus shear strain curves although hyperbolic softening model was applied in their analysis.

Appendix IV. Procedure to obtain theoretical shear stress vs. shear strain curve for the two-stage softening model

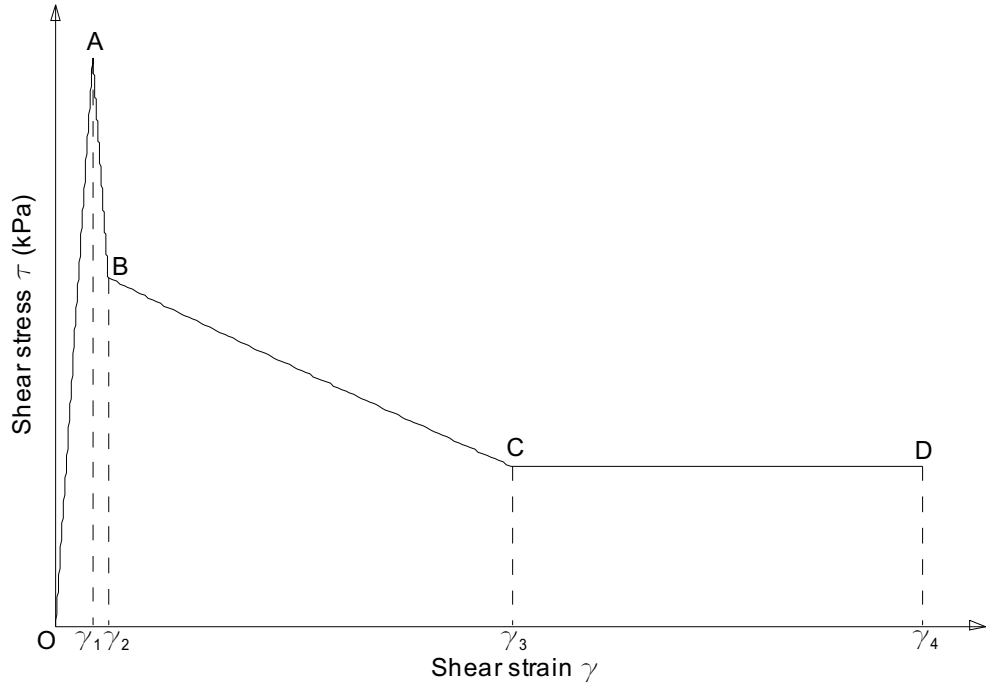

Fig. IV.1 Schematic shear stress vs. shear strain curve with two-softening model

The procedure to obtain shear stress vs. shear strain curve is based on Fig. IV.1. O-A section denotes elastic and the shear stress can be calculated by

$$\tau = G\gamma \tag{IV.1}$$

where G is the shear modulus and given by Eq.(4.2).

A is the peak point indicating the beginning of plasticity. At peak state, the shear stress can also be calculated using peak strength parameters via

$$\tau = c_p^{'} + \sigma_n^{'} \tan(\phi_p^{'}) \tag{IV.2}$$

By equalising Eqs. (IV.1) and (IV.2), the shear strain at peak state can be obtained from

$$\gamma_1 = (c_p^{'} + \sigma_n^{'} \tan(\phi_p^{'})) / G \tag{IV.3}$$

A-B is the first softening section with point B being the post-rupture strength point. With $\gamma_p = 0$, the shear strain at B can be acquired by

$$\gamma_2 = \gamma_1 + \gamma_{pr} \tag{IV.4}$$

And the shear strength can be calculated using mobilised strength parameters by

$$\tau = c_1^{'}(\gamma) + \sigma_n^{'} \tan(\phi_1^{'}(\gamma)) \tag{IV.5}$$

In terms of the description in Section 3.5, $c_1^{'}(\gamma)$ and $\phi_1^{'}(\gamma)$ can be formulated as

$$c_1^{'}(\gamma) = c_p^{'} - \frac{c_p^{'} - c_{pr}^{'}}{\gamma_{pr}}(\gamma - \gamma_1) \tag{IV.6}$$

$$\phi_1^{'}(\gamma) = \phi_p^{'} - \frac{\phi_p^{'} - \phi_{pr}^{'}}{\gamma_{pr}}(\gamma - \gamma_1) \tag{IV.7}$$

B-C is the second softening section with point C being the beginning of residual state. The shear strain at C can be calculated by

$$\gamma_3 = \gamma_1 + \gamma_r \tag{IV.8}$$

And the shear strength can be calculated using mobilised strength parameters by

$$\tau = c_2^{'}(\gamma) + \sigma_n^{'} \tan(\phi_2^{'}(\gamma)) \tag{IV.9}$$

In terms of the description in Section 3.5, $c_2^{'}(\gamma)$ and $\phi_2^{'}(\gamma)$ can be formulated as

$$c_2^{'}(\gamma) = c_{pr}^{'} - \frac{c_{pr}^{'} - c_r^{'}}{\gamma_r - \gamma_{pr}}(\gamma - \gamma_2) \tag{IV.10}$$

$$\phi_2^{'}(\gamma) = \phi_{pr}^{'} - \frac{\phi_{pr}^{'} - \phi_r^{'}}{\gamma_r - \gamma_{pr}}(\gamma - \gamma_2) \tag{IV.11}$$

Finally C-D represents the residual state and the residual shear stress can be calculated from

$$\tau = c_r^{'} + \sigma_n^{'} \tan(\phi_r^{'}) \tag{IV.12}$$

In summary, the shear stress for all the four sections can be expressed in a general function of shear strain and effective normal stress as given by

$$\tau(\gamma, \sigma_n^{'}) = \begin{cases} G\gamma & , \quad 0 \le \gamma < \gamma_1 \\ c_p^{'} - \dfrac{c_p^{'} - c_{pr}^{'}}{\gamma_{pr}}(\gamma - \gamma_1) + \sigma_n^{'} \tan(\phi_p^{'} - \dfrac{\phi_p^{'} - \phi_{pr}^{'}}{\gamma_{pr}}(\gamma - \gamma_1)) & , \quad \gamma_1 \le \gamma < \gamma_2 \\ c_{pr}^{'} - \dfrac{c_{pr}^{'} - c_r^{'}}{\gamma_r - \gamma_{pr}}(\gamma - \gamma_2) + \sigma_n^{'} \tan(\phi_{pr}^{'} - \dfrac{\phi_{pr}^{'} - \phi_r^{'}}{\gamma_r - \gamma_{pr}}(\gamma - \gamma_2)) & , \quad \gamma_2 \le \gamma < \gamma_3 \\ c_r^{'} + \sigma_n^{'} \tan(\phi_r^{'}) & , \quad \gamma_3 \le \gamma \end{cases} \tag{IV.13}$$

When the values of effective normal stress $\sigma_n^{'}$ and γ_4 are set, the shear stress is only the function of shear strain and then can be plotted in shear stress vs. shear strain curve. It should be declared here that the shear stress corresponds to the shear strength value using mobilised strength parameters.